ACCURACY IMPROVEMENT OF TERRESTRIAL MOBILE LiDAR SYSTEM IN ENGINEERING SURVEYS

GUANNAN LIU

A THESIS SUBMITTED TO THE
FACULTY OF GRADUATE STUDIES
IN PARTIAL FULFILLMENT OF THE
REQUIREMENTS FOR THE DEGREE OF
MASTER OF SCIENCE

GRADUATE PROGRAM IN EARTH AND SPACE SCIENCE
YORK
UNIVERSITY
TORONTO,
ONTARIO

AUGUST 2015

Abstract

In this thesis, a number of effective algorithms and strategies were developed to improve the accuracy of terrestrial mobile LiDAR solutions in the field of engineering surveys. A detailed analysis for error budget of the terrestrial mobile LiDAR system has been presented in order to well interpret the effects of individual error sources.

Firstly, the 3D conformal coordinate transformation (3DCCT) through Least Squares Method (LSM) was applied by employing the GCPs incorporating with feature constraints. Secondly, the multistrip adjustment (MA) algorithm was developed by taking advantage of the overlapped data strips and the repeated data acquisition over the same survey area using both of tie points and tie features. Lastly, the boresight angles of a terrestrial LiDAR system was preliminarily calibrated by using the planar and/or line features of two scans acquired during consecutive runs in opposite driving directions at the post-processing stage proposed by Keller et al. (2013).

Acknowledgments

First and foremost, I would like to express my sincere gratitude to my distinguished supervisor Dr.-Ing. Jian-Guo Wang and co-supervisor Dr. Baoxin Hu, for their guidance, enlightenment and insight suggestions during my master study in Earth and Space Science (ESS) at York University. Their continuous encouragement and supports create a stimulating academic environment that I appreciated. I am extremely impressed by their energy, patient, enthusiasm and keen into current LiDAR technology with the engineering survey applications that greatly inspired me.

My heartfelt appreciations are also extended to the members of my defense committee, Dr. Costas Armenakis, Dr. Baoxin Hu and Dr. Aijun An, for their scientific suggestions, valuable insights, warm encouragements and constructive challenges they raised, also Mr. Ron Berg at Ministry of Transportation, Ontario (MTO) for his valuable comments and suggestions throughout the research. They all made my graduate research study the most enriching professional experience I have had thus far.

I also appreciate the financial support received from various sources, including Ontario Graduate Scholarship (OGS) provided by the Ministry of Training, Colleges and Universities of Ontario, MTO Highway Infrastructure Innovation Funding Program 2012, and Natural Sciences and Engineering Research Council (NSERC). I also would like to thank Optech Inc., Canada for its in-kind contribution in support of LiDAR data acquisition and processing.

In this genuine research collaboration, the individuals who have contributed in different ways to the research are gratefully acknowledged. Especially, the warmest

thanks go out to all the faculty and student members in the Earth Observation Laboratory of York University, who helped me with the algorithm design, programming and field data acquisition, such as, Dr. Jili Li, Mr. Aaron Judah, Mrs. Wen Zhang, Dr. Kongwen Zhang, Mr. Henry Mak, Mr. Kun Qian and Mr. Damir Gumerov. I also want to particularly thank Mr. Tyler Kou and Mr. Michael Leslar from Optech Inc., Canada who kindly assisted me with the data collection and processing, which made this research started on time. In addition, I take this opportunity to express gratitude to all of the faculty members at the Department of Earth and Space Science and Engineering (ESSE) for their help and support.

Finally, I owe my deepest gratitude to my parents, my mother, Aimin Zhao and my father, Xiaowei Liu, for their love, patient, encouragement and understanding that have allowed me to achieve my dreams. Without their support in my life through faith and sacrifice, this wonderful experience and research work would not have been possible. Most importantly, I would like to thank for everything they have meant for me throughout my life.

Table of Contents

List of Tables

List of Figures

List of Acronyms

2D	2-dimensional
3D	3-dimensional
3DCCT	3D Conformal Coordinate Transformation
ALS	Airborne Laser Scanning
DMI	Distance Measurement Indicators
DTM	Digital Terrain Model
ECEF	Earth-centered Earth Fixed
EDM	Electronic Distance Measurement
GCPs	Ground Control Points
GNSS	Global Navigation Satellite System
GPS	Global Position System
IMU	Inertial Measurement Unit
LiDAR	Light Detection And Ranging
LSM	Least Squared Method
MA	Multistrip Adjustment
MTO	Ministry of Transportation, Ontario
POS	Position and Orientation System
PRF	Pulse Repetition Frequencies
RMS	Root Mean Square
RTK	Real Time Kinematic
SBET	Smoothed Best Estimated Trajectory
TLS	Terrestrial Laser Scanning
VRS	Virtual Reference System
WGS84	World Geodetic System 1984

1 Introduction

1.1 Background and Research Motivations

During the past two decades, significant progress has been made in the laser ranging and scanning technology (known as LiDAR, stands for **Li**ght **D**etection **A**nd **R**anging). The first functioning lasers were used for medical purpose that was invented by Arthur Schawlow and Charles Townes in 1958. Moreover, NASA made the first use of laser in the scientific topographic mapping of ice-covered areas since the late 70's (Krabill et al., 1984) in the field of remote sensing. Although the invention of laser technique dates back to the early 1960s, the introduction of direct georeferencing and general advancements in computer technologies enabled the development of the first commercial LiDAR product evolving from the defense industry in about 1994. The laser scanners were mounted onto the moving airborne and spaceborne platforms that led to the current LiDAR systems, which takes full advantages of the most recent technological advances in Global Position System (GPS), Inertial Navigation, laser scanning, digital imaging, and data processing methods and software.

The outcome of various commercial products has marked turning point of LiDAR from theoretical and laboratory research to application-oriented research and industry development (Grejner-Brzezinska, 2001; Pfeifer and Briese, 2007; Shan and Toth, 2008; Petrie, 2010; Puente et al., 2011). Moreover, 3D data acquisition for both topographic and artificial objects has been revolutionized. In contrast to the traditional terrestrial surveying and photogrammetry data acquisition techniques, the laser scanning could rapidly scan a scene such as rock slope and outcrop, building, bridge and other natural

and man-made objects over large areas, which allows the user to collect high accurate data of required ground points within very short period of time. The Optech Lynx V200 mobile mapping system, for instance, can acquire up to 2,000 points per second. In the most advanced commercial LiDAR systems, the data rate is typically 50,000 - 200,000 measurements per second. The point-based output from a LiDAR instrument is commonly referred to as "point cloud", which contains the visual (i.e., intensity) and metric (i.e., *XYZ* geospatial coordinates) information. Then the *XYZ*-coordinates of the backscattered echoes for each laser pulse can be calculated by combining the laser range, scan angle, georeferenced position of laser sensor and orientation of the laser platform from GNSS and IMU integrated kinematic positioning and navigation systems. Furthermore, the LiDAR point clouds are processed to extract the information such as discontinuity orientation, length, spacing, roughness, block size and so on, which ultimately depend on applications. The point clouds are also often processed to generate 3D model of the scanned scene.

LiDAR data can be collected from airborne (e.g., wing aircraft or helicopter) or terrestrial vehicles. In terrestrial geospatial data acquisition, the LiDAR unit could be over either the fixed points (i.e., static), usually on a tripod, or mounted on moving platforms (i.e., mobile), such as a van, a truck and a train. The general operation principles and the data processing workflows are very similar or almost identical for airborne and terrestrial mobile LiDAR systems. The data acquired via airborne laser scanning is stripwise with a typical strip length of 20km. The terrestrial laser scanner is not looking primarily vertical but generating a panoramic field of view. Moreover, the

point density is much higher than the one enabled by airborne LiDAR system since the range to the target is much shorter. In addition, a mobile terrestrial LiDAR system can cover much larger areas than a static terrestrial LiDAR system.

The terrestrial mobile LiDAR system as a novel mapping instrument has been introduced to Geomatics Engineering since 2000. Especially in the past few years, a great variety of application-oriented case studies have progressively been advancing this technique in term of its practicability, efficiency, and performance (Slob and Hack, 2004; Durrieu et al., 2008; Hofmann and Brenner, 2009; Jaakkola et al., 2010; Sherif et al., 2011). As engineering projects become more and more complex, it is important to take full advantages of innovative techniques for quality control and time reduction of project cycles. Laser scanning is such a technique that has high potential over the traditional surveying techniques such as total station and aerial photogrammetry for providing accurate as-built surveys with high-resolution 3D models, which could allow engineers extract all the required features, decreasing or eliminating the need for surveyors to return to the sites for additional measurements. Plenty of case studies have been completed in many surveying tasks towards advancing this technique in term of its efficiency and performance (Mensi, 2003; Goulette et al., 2006; Gräfe, 2008; Jaakkola et al., 2008; Glennie, 2009; Lato et al., 2009; Ussyshkin, 2009).

Therefore, the attractive achievements have promoted LiDAR technique in engineering applications and exploited its potential to generate engineering products from traditional digital surface/elevation model to 3D models for general geospatial database, urban planning, transportation corridor surveys, engineering design, rail surveys, utility

mapping and structure inspection, monitoring and management etc. Specifically, the use of terrestrial mobile LiDAR technique provides a good opportunity to revolutionize transportation corridor surveys. As a quick, automatic and efficient surveying method, it can reduce lane closures, which can decrease the safety risk, and increase productivity compared with traditional surveying instruments in emergency management. In addition to its use for 3D modeling in mapping, it has also shown great potential in high accuracy engineering surveying, for example, its use in as-built surveying, structure inspection and deformation monitoring. The more mature airborne LiDAR market is experiencing high growth over the recent years, which helps the relatively new terrestrial mobile LiDAR technique get accepted by the community of professional surveyors as an efficient solution in order to survey large areas. However, to make it qualified as a standard method for engineering surveys with other existing instruments standing side by side in a complementary way, more effort is demanded to improve the positioning accuracy of LiDAR points and to standardize the procedures of mobile LiDAR survey from mission planning, data acquisition, and processing to the end products due to the accuracy and resolution requirements exceed airborne technologies.

Different operational conditions may deliver LiDAR products of different qualities in terms of geospatial accuracy. There are now a variety of terrestrial LiDAR manufacturers available on the markets which are designed to meet the requirements of the specific applications. Ingensand (2006) summarized the accuracies of those systems, such as Leica, Optech, Riegel, Trimble, Zoller+Fröhlich and so on. It concluded that most scanners can measure the distances to objects up to several hundred meters with the

single-point accuracy of 1.4mm to 1.5cm at 50m range. The instrument manufactures may use the best or averaged performance for their technical specifications. Hence, a user or a specific field of application may perform comprehensive performance studies with the available instruments or systems in order to confirm the released product accuracy specification. The positioning accuracy of the Optech Lynx Mobile Mapper V200, a survey grade system for engineering surveys was assessed by Hu, et al (2012). Three tests under different environmental conditions were performed for relatively complicated urban scenes, a stretch of a main urban street and a stretch of a major road. On one hand, the absolute accuracy assessment was evaluated using the targets on walls and the natural objects on hard surfaces that were independently surveyed using a total station system and RTK GPS on the basis of the high accuracy engineering geodetic control network. On the other hand, the relative accuracy was evaluated based on the measured linear features in the scenes using steel tapes. Under good GPS conditions without using any ground control point for geo-referencing, the Lynx system demonstrated to have achieved an absolute accuracy of ±4.4cm vertically and ±6.0cm horizontally at the 95% confidence level. The horizontal positional accuracy of the well-designed targets was higher than the one of the natural targets on the scene. The relative accuracy achieved by the Lynx Mobile Mapper V200 was within ±3.65cm at the 95% confidence level. In summary, the achieved accuracies by the Lynx Mobile Mapper were lower than the required accuracy stated in the Engineering Survey Manual of Ministry of Transportation of Ontario (MTO, 2006): “in general, the minimum positional accuracy of topographic detail features with respect to the nearest project control is: 2 centimeters horizontal and vertical for hard

constructed surfaces such as pavement, concrete, gravel, culverts etc., and 5 to 10 centimeters horizontal and vertical for natural original ground features.

Yousif (et al., 2010) also summarized that some of LiDAR systems in their current terrestrial LiDAR Mobile Mapping System (MMS) resulted in high quality of positioning accuracies that range from 3cm for StreetMapper, 5cm for Lynx and 10cm for FGI Roamer under clear sky conditions or in buildings-free area. In addition, the GPS measurements suffered from multipath effect as the vehicle passed through the urban areas. The multiple signals were reflected by nearby buildings as an inevitable scenario in urban environments. As a result, the StreetMapper accuracy could drop down to 50cm. Furthermore, the accuracies of several mobile LiDAR systems were also evaluated in terms of generating digital terrain models of pavement surfaces by Yen et al (2010). It was concluded that the best accuracy of mobile LiDAR data did not meet the required accuracy, 7mm vertically for hard surface as specified in Surveys Manual for road pavement. Thus, it indicated that the LiDAR point cloud may not always satisfy the desired accuracy unless additional refinements were introduced during or after the field data acquisition.

In addition, the accuracies of mobile LiDAR products were closely linked to the quality of practical executions reflected from such as the quality of the GPS base station, data acquisition configuration, and data processing etc. To ensure the high quality of the solutions provided by a terrestrial mobile LiDAR system, the importance of framing authoritative guidelines for user community is well recognized due to lack of professional standards to regulate the use of mobile LiDAR in engineering applications (Ussyshkin,

2009; Caltrans, 2012).

Especially, just around the time as I started my graduate studies in 2012, “Improving the Accuracy of Mobile LiDAR for MTO Engineering Surveys” was listed as Topic #15 under MTO Highway Infrastructure Innovation Funding Program 2012, which was the continuation of a previous research project: “Performance and potentials of ground LiDAR (mobile and static) in engineering surveying and highway design” under Topic #15: Applying LiDAR Technologies to MTO Engineering Surveys and Highway Design, supported by MTO Highway Infrastructure Innovation Funding Program 2010 and completed by our Earth Observation Laboratory at York University.

In summary, further effort was highly demanded for the accuracy improvement of mobile LiDAR solutions in Engineering Surveying. At the same time, this offers not only challenges, but also opportunities as well. Therefore, the main objective of this research is to study how to improve the point cloud accuracy of terrestrial mobile LiDAR system in order to satisfy the accuracy specifications in engineering surveys.

1.2 Literature Review

Based on the general survey of the LiDAR technology as in Section 1.1 and directly inspired by the proposed topic under the MTO Highway Infrastructure Innovation Funding Programs, the subject of my graduate research centers on attempting to improve the overall accuracy of terrestrial mobile LiDAR solution towards better satisfying and serving the high demand of the terrestrial LiDAR products for high accuracy Engineering Surveying.

All general aspects of terrestrial mobile LiDAR technique have been explored in terms of error sources in order to clearly define the research objectives, know the problems, and conceptually design the research strategies. In addition, the potential problem-solving strategies, particularly those developed and being used for the airborne LiDAR technique along with certain relevant remarks have been overviewed that may imply the potential adaption to my research subject or certain challenges and difficulties my research may have to face or overcome.

1.2.1 Issues

The main error sources in the generated point cloud of a LiDAR instrument arise from both the systematic and random errors associated with the system parameters and measurements. A detailed analysis of error budget with airborne laser scanning systems has been performed in Huising and Pereira (1998), Baltsavias (1999), Schenk (2001), Filin (2003a and 2003b), Toth and Csanyi (2007), Zhi and Zhong (2008) and Habib et al. (2009). The systematic errors are due to the biases in the lever arm and boresight angle calibration and measurements (e.g., ranges and mirror angles), while the random errors

are due to the uncertainty of the sensor's measurements, such as position and orientation observations from the GPS/IMU component, ranging, angular and lever arm (Habib et al., 2009). Terrestrial LiDAR systems share the similar working principle with airborne systems but have been expected to deliver their point clouds at higher accuracy. Lichti et al. (2004) presented a full error budget after random error sources for directly georeferenced terrestrial laser scanners. It indicated that insufficient attention has been given to many error sources that contribute to the uncertainty of the LiDAR datasets. Therefore, a detailed analytical analysis on the terrestrial mobile LiDAR system has been introduced in Chapter 2 of this study in order to interpret the effects of individual error sources.

The Optech Lynx Mobile Mapper V200, which consists of two LiDAR sensors, four calibrated passive imaging cameras, and an Applanix POS LV system for direct georeferencing, was used in this research. It is capable of collecting rich survey-grade LiDAR and image data from a land vehicle moving at normal speed on local streets, and on highways as well. The precision and accuracy of the generated 3D model of a mobile LiDAR system is subject to many factors that may bring on errors. Among them are the uncertainties of the direct geo-referencing component based on GNSS-aided inertial integrated navigation system (Applanix POS LV), the LiDAR ranging and angular measurements, the calibrated lever arms and boresight angles between the LiDAR sensors and the POS LV system, the calibrated lever arms between the primary GPS receiver and the IMU sensor, and the baselines between the base and rover GPS receivers. On one hand, the absolute accuracy depends on the quality of the POS trajectory resulted

from the GPS-aided inertial systems (often also equipped with a DMI (Distance Measurement Indicator) sensor). The residual errors on the lever arms and the boresight angles and any other estimated parameter should also be considered. On the other hand, the relative accuracy represents the quality of the results locally, not with respect to the global georeference and mainly depends on the accuracy of the laser scanners themselves and the vehicle dynamics in real time as well. Hence, the uncertainty in 3D positions obtained by the Lynx system is mainly caused by the uncertainties introduced in the georeferencing process by the on-board POS LV system and by the LiDAR sensors themselves. The effect analysis of these two error sources on the LiDAR solution from our aforementioned individual studies (Hu et al., 2012) indicated that the positioning accuracy of a terrestrial mobile LiDAR system was significantly affected by the quality of its georeferencing component. As a result, the key to improve its overall accuracy is to reduce the uncertainty of the georeferencing process. In addition, to achieve the required accuracy in engineering surveys by a survey-grade LiDAR system, other factors, such as system lever arm, extended GPS base lines, and boresight calibration need to be considered too. In this study, the error propagation was performed for the directly georeferenced kinematic laser scanning point clouds to provide sufficient understanding of two types of the error sources mentioned above. Moreover, the effects of various error sources on the 3D positions of LiDAR point clouds with both of the best calibration accuracies and the relative low calibration accuracies were reported in Hu et al (2013) and Leslar et al (2013). This study concluded that the contributions of the uncertainties in the trajectory positions to the errors in the LiDAR 3D positions were higher than any

other factors in both scenarios. Thus, the study also verified that the accuracy of a terrestrial mobile LiDAR system was significantly affected by the accuracy of its direct georeferencing process.

1.2.2 Current Approaches and Contributions

1.2.2.1 Utilization of Ground Control Points and Feature Constraints

Due to the expectation of terrestrial mobile LiDAR products for much higher accuracy compared with the airborne LiDAR products and also the high accuracy requirements in Engineering Surveys, the situation with terrestrial mobile LiDAR products can be more complicated in practice. The use of ground control information is desirable because it can provide an absolute reference of the data as applications demanding the highest accuracy require the elimination of some of the remaining systematic errors. Thus, using additional control points is an effective way to remove some of the leftover systematic errors and to improve the absolute accuracies of terrestrial mobile LiDAR solution, compensate for sensor modeling errors, or make up the GPS outages. Toth (et al, 2005 & 2007) used LiDAR-specific ground targets to provide quality control for airborne applications that demanded for centimeter accuracy in large scale mapping for engineering applications. Extensive simulations were performed to determine the most favorable LiDAR target design. Results confirmed that the optimal target is rotation invariant, circular-shaped, elevated from the ground and a 1m circle radius can provide sufficient accuracy from a point density of about 5 pts/m^2. In addition, the two-concentric-circle design (the inner circle with one-half the radius of the

outer circle) with different coatings provided considerable accuracy improvements in the horizontal position. Thus, the vertical accuracy of the road was estimated at the 3-5 cm level by modeling the road surface with a plane. Moreover, a dense and well-distributed network of control is needed to maintain this extreme high accuracy. In principle, employing more control points could achieve higher accuracy, but setting up those control points was very costly. For example, Zampa et al, (2009) set up six base stations and a number of ground control points at an interval of 50 to 80 m along a 60 km highway road under surveying. Even though the positioning accuracy of LiDAR solution was improved to 2cm level, the associated cost for setting up these control points was so high that the benefit of a mobile LiDAR system as a cost-effective solution was significantly compromised. Therefore, the cost of installing and surveying the targets is the limitation of commercial consideration, which is only affordable for applications requiring the highest accuracy. Thus, the existing characteristic points, such as building and window corners, could be employed as absolute control information to reduce the cost and/or authority request for setting up targets in the field. In addition, optimizing the density and ideal distribution of the control points were also investigated in order to efficiently and effectively employ those measurements.

Barber (et al, 2008) outlined a study of geometric validation of a ground-based mobile laser scanning system (StreetMapper) using control points. The measurement accuracy was assessed through check points determined using conventional surveying techniques at the same time as the laser scanning survey was conducted. The Real Time Kinematic (RTK) GPS survey was carried out to introduce about 200 control points. In

addition, static differential GPS observations for at least 15 min were performed to supplement the RTK measurements. With the help of GPS technique only, the accuracy of control points could achieve ±3.5cm horizontally and ±6.5cm vertically at the 95% confidence level. The RMS errors of check points were found in the order of 3cm vertically and approximately 10cm horizontally. Thus, it indicated that the use of high accuracy ground control points was essential in order to provide reliable absolute georeference for LiDAR point cloud.

The associated cost for setting up these control points was so high that the benefit of a mobile LiDAR system as a cost-effective solution could significantly be compromised. Therefore, the geospatial locations of the existing characteristic (natural and/or artificial) points, such as the corners of buildings, windows, traffic lights and signs and pavement markings etc., were applied in my research as absolute control information to reduce even to eliminate the cost and/or access authorization request for setting up targets in field. The total station and GPS technique were applied to determine the coordinates of such control points. A straight thought would be to take advantages of the mathematic relationships of the common points through their coordinates surveyed as GCPs using geodetic instruments and delivered as LiDAR solution. If there was no error in these coordinates, they should be identical theoretically. Thus, the 3D conformal transformation was applied to model some of the systematic errors.

In addition, the results from the error analysis (Hu et al, 2013) indicated that the effects of some of the systematic errors may not be uniform in the LiDAR solutions with a large dataset due to the complicated nonlinear functional relationships with respect to

many different error sources. Thus, the 3D conformal transformation may not be valid for a large stretch of data. Therefore, it is necessary to segment the LiDAR strip into multiple smaller stretches and to piecewise determine the 3D conformal transformation parameters for each segment in order to compensate for the different natures and amplitudes of the error effects. Since the effects of the systematic errors in the 3D LiDAR solution may not be uniform in horizontal and vertical directions for a given scene, the ground control points were categorized into different groups according to their location or geometric information, such as, building and ground types.

Employing more control points could achieve higher accuracy, but setting up those control points was very costly. On one hand, it is desirable to choose natural targets placed not too far from each other and well distributed spatially to ensure that the transformation based on the targets indeed improves the LiDAR data accuracy. On the other hand, the required number of GCPs could be reduced or the shortage even the absence of GCPs may be compensated for in some areas with the aid of feature constraints to achieve the minimal required accuracy. Therefore, the optimization usage of the control points in terms of density and ideal distribution will be analyzed in order to efficiently and effectively employ those measurements.

The target-based georeferencing methods may not exploit the full accuracy potential of the terrestrial mobile LiDAR data. The geodetic surveying of GCPs naturally introduces the systematic errors, which might exceed the internal error of the laser scanner instrument (Akca 2010). Moreover, the control points must be maintained stably during the data acquisition process. Thus, besides ground control points, other measures

were also investigated accordingly, such as linear features, planar patches and vertical angles etc. The implementation of these constraints may reduce the number of GCPs and/or may make up for the absence of GCPs in some areas, and could also compensate some of the angular systematic errors.

The linear features have recently been proposed as an alternative to ground control points (Gruen et al, 2004; Filin 2003a; Habib et al, 2005; Dold et al, 2006; Jaw et al, 2008; Bosché 2012). In addition, various algorithms of co-registration of 3D points, lines and surfaces have been proposed and various variants have been integrated in registration processes (Besl et al, 1992; Zhang 1994; Gueziec et al, 1994; Habib et al, 1999; Wyngaerd et al, 1999; Fitzgibbon 2003; Park et al, 2003; Gruen et al, 2005; Kraus et al, 2006; Akca 2010). However, it only provided the relative 3D transformation between adjacent strips, no absolute positioning measurements involved.

Therefore, in my research, the absolute position and orientation parameters of feature constraints were further constructed using the corresponding pre-surveyed coordinates of control points. Toth et al. (2007) proposed a method to survey road pavement markings using GPS VRS (Virtual Reference System) technique. Typically a point was surveyed for one minute, and the associated accuracy is about 2-3 cm horizontally and 3-6 cm vertically in general. Sufficient number of pavement markings is required with good spatial distribution in order to achieve good performance. However, this became impractical in the reality due to the cost and time-consuming work load. Therefore, the amount of surveyed points could be reduced to reasonable numbers, for example, 4 points for a 2-meter long pavement marking. Other natural objects were also

selected as planar patch or linear features in both horizontal and vertical directions, such as, traffic signs and lights, advertisement signs along the road, building facades and stop bars etc.

1.2.2.2 Utilization of Overlapped LiDAR Strips

Furthermore, inspired by the advances in airborne LiDAR technology, the multistrip adjustment (MA) algorithm in my research was developed to improve the terrestrial mobile LiDAR solutions by taking advantage of the overlapped data strips and the repeated data acquisition over the same survey area. Since the objects surveyed can be large and complex-shaped, a series of scans from various directions is necessary in order to capture the complete representation of object geometry (Reshetyuk 2006). The strip offsets of common points, features and objects provide ideal information allowing refining and improving the mobile LiDAR solution through an adjusting process for the leftover boresight and other systematic errors. In other words, such discrepancies are caused by missing or improperly employed calibration and operational procedures. Thus, the misalignment between overlapping strips usually produces the problems in extracting meaningful information and affects the quality of the final product (Lee et al., 2007).

The difficulty of implementing strip adjustment comes primarily from the irregular point distribution of LiDAR system. In other words, the same object space is randomly sampled in the spatial domain in each strip (Shan and Toth, 2008). In the past, several strip adjustment methods have been developed (Kilian et al., 1996; Crombaghs et al., 2000; Maas, 2000; Maas, 2002; Filin 2003b; Kornus et al., 2003; Bretar et al., 2004;

Vosselman, 2004; Filin et al., 2004; Kager, 2004; Pfeifer et al., 2005; Kersting et al., 2008; Yousif et al., 2010) for evaluating and improving the quality of airborne LiDAR data. In Kilian et al. (1996), an adjustment procedure similar to the photogrammetric strip adjustment was introduced using tie points. However, the identification of distinct points, such as building corners, is quite difficult and not reliable due to the irregular nature of the airborne LiDAR footprints. Then, Maas (2000 & 2002) suggested to establish the correspondence between the discrete points in one LiDAR strip and TIN patches in the other one. Kersting (et al., 2008) proposed an algorithm that used linear features to measure and adjust for the discrepancies between the overlapping LiDAR data strips. The linear features were chosen as conjugate features because they could be accurately extracted from man-made structures in urban area and extracted more easily than the point features. Even though the terrestrial mobile LiDAR mapping system is fairly new, quality improvement of LiDAR data becomes increasingly critical. Yousif (et al., 2010) illustrated the theory of data assimilation to enhance the 3D georeferencing accuracy as well as to fine-tune the radiometric intensity by means of exploiting the correlation between two oppositely-collected datasets over the same study area. The purpose of data assimilation is to combine two different datasets or models of the same phenomenon in order to achieve the best estimate of the true states.

It was worth mentioning that most of the developed algorithms only use tie points, which could reduce or eliminate the relative discrepancies between overlapping strips in the boresight angles and/or measurements on the point cloud. However, they could not address which strip should be selected as a base reference and cannot identify what

corresponding impact on the absolute accuracy of the final merged strip they have. Then the use of some type of ground control information is desirable. Therefore, the multistrip adjustment (MA) algorithm was proposed in this study by aligning the adjacent strips using both of tie points and tie features. It was designed to minimize the impact of some of the systematic errors in the LiDAR system parameters by improving the compatibility among the overlapping strips. In other words, the offsets of common points, features and objects from overlapping strips could contain ideal information about the leftover boresight and other systematic errors to refine and improve the mobile LiDAR solution. Moreover, inspired by the utilization of feature constraints developed for 3DCCT, the similar straight line and planar patch features were employed in the MA algorithm as the tie features. In comparison with the use of GCPs, this approach is more economic and easily to be made automatically or semi-automatically. Surely, more overlapped data strips will definitely increase the available data volume and measurement redundancy.

1.2.2.3 Preliminary Calibration of Boresight Angles

Lastly, the terrestrial mobile LiDAR system consists of three main sensors: GPS receivers, IMU and laser scanner(s). In general, the errors can arise from individual sensor calibrations, lack of sensor synchronization and misalignments between the different sensors (Shan and Toth, 2008). An integrated GPS-aided inertial navigation system with high performance could provide accurate georeferencing information for the LiDAR data acquisition platform. Therefore, the proper calibration of the entire system including individual and inter-sensor calibration is essential. The need for accurately

evaluating the angular misalignments between the axes of a LiDAR sensor and an IMU, commonly known as the boresight angles, arise from the fact that the coordinates of LiDAR points are the solutions made by the laser scanning unit with respect to the direct-georeferencing system. The spatial and angular relationship between the IMU and laser scanner body frames could be the largest source of systematic errors, and thus, it must be determined before the system can be effectively utilized (Burman, 2000). However, under the operational circumstances, the values of the boresight angle misalignments are never accurately known but could only be estimated. Furthermore, the parameters could change over a relatively short time period (Pothou et al, 2009). Poor boresight estimation could seriously degrade the accuracy of point cloud among overlapping strips for the common objects.

A lot of studies have been performed to investigate the effect and the elimination of boresight angle misalignments in airborne laser scanning systems (Burman, 2000; Filin, 2001; Schenk, 2001; Toth et al, 2001; Toth, 2002; Friess, 2006; Skaloud et al, 2006; Pothou et al, 2007; Habib et al, 2007; Pothou et al, 2008 and 2009). However, the methods of data acquisition are inevitable different with terrestrial laser scanning (TLS) systems from airborne laser scanning systems even though their working principles are similar (Rieger et al., 2010). For instant, an area of interest can be easily scanned from different flight directions during the airborne laser scanning survey. However, the TLS systems are lack of flexibility in scanning the same objects multiple times from various directions due to the limited angular field-of-view. In addition, current calibration techniques require the access to the LiDAR system parameters and the raw observations,

such as, position and orientation of platform, scan angles of a laser beam and laser scanning ranges. Unfortunately, the raw observations are not usually available to the end users (Bang et al., 2009). Moreover, some of the methods rely on the accurate absolute coordinates of retro-reflective targets (i.e., GCPs) or scanning objects of known size and position from different driving directions and distances. The disadvantages of all these techniques were lack of flexibility and demanding more efforts on preparing the special test sites. Therefore, Keller et al. (2013) proposed a new cost-effective method for calibrating the boresight angles of terrestrial mobile LiDAR system by using the planar and/or line features of two scans acquired during consecutive runs in opposite driving directions at the post-processing stage. These parameters can be used to improve the accuracy of subsequently collected LiDAR data. Thus, the boresight angles of Lynx V200 mobile LiDAR system was calibrated by implementing this approach in this study.

1.3 Research Questions and Design of Experiments

To achieve my research goal, the following specific research objectives are determined:

(1) Provide a summary of the research results on "Error Analysis of Terrestrial Mobile LiDAR System" achieved by York's Earth Observation Laboratory, in which the author as one of the key members participated in 2010 and 2011.

(2) Utilize the 3D conformal coordinate transformation (3DCCT), or the 7 parameter similarity transformation, to model some of the potential systematic errors in terrestrial LiDAR systems for their solution refinement or adjustment

by using ground control points (GCPs) incorporating with linear and/or planar features and by implementing various strategies, such as, segmental 3D conformal transformations, deployment of categorical GCPs and making effort for a possible diminution in GCPs. In addition, the feature constraints could be categorized into horizontal directional (e.g., pavement markings) and vertical directional (for example, traffic light and signs) features so that one can analyze how the different types of features contribute to the accuracy improvement in 2D horizontal and vertical directions.

(3) Develop the multistrip adjustment (MA) algorithm to refine the alignment and georeferencing of terrestrial LiDAR point clouds by taking advantages of the overlapped data strips and the repeatedly acquired datasets in the same working area with the help of tie points and tie features. The refined solution of this approach was further compared by using two strips with having the same driving direction against the one using the two strips with having the opposite driving directions. In addition, the 3DCCT was applied to single strip in order to check the accuracy improvement from the MA process with dual strip scenario. Moreover, by reducing number of the GCPs, the refined solution was analyzed to conclude whether the accuracy of terrestrial mobile LiDAR solution was improved with involving the tie points and features to make up the lack of GCPs in some areas.

(4) Develop the preliminary boresight calibration process for terrestrial mobile LiDAR systems to enhance the other quality improvement procedures

mentioned above by using linear and/or planar facades of two scans acquired during consecutive runs in the opposite driving directions as proposed by Keller et al. (2013) and come up with the practical plan. The refined solution was compared by executing the 3DCCT and MA approaches using both of the original LiDAR data and the calibrated data. Finally, the practical protocol of post-processing procedures for a more efficient and cost-effective implementation of the proposed algorithms for performance improvement of terrestrial mobile LiDAR solutions was suggested based on aforementioned experimental results.

All of the proposed problem-solving plans will first be theoretically described and then tested out through real test datasets. The results will be then concretely analysed in the comparative way for potential combination of different approaches and strategies proposed in this research.

1.4 Thesis Outline

The thesis is organized as follows:

The introduction is followed by Chapter 2 Error Analysis of Terrestrial Mobile LiDAR System that summarizes the assessment results of positioning accuracy of the Lynx V200 Mobile Mapper manufactured by Optech Inc. for engineering surveys. Furthermore, the error budget is derived for terrestrial mobile LiDAR systems based on the error propagation theory in order to provide sufficient understanding of the error sources. In Chapter 3, the methodologies of the 3DCCT on the basis of Least Squares

Method (LSM), the multistrip adjustment algorithm and preliminary boresight calibration were presented.

In Chapter 4, the 3DCCT algorithm was firstly implemented with the experiment area in the head quarter office building of Optech Inc., which is a relative simple scenario. Furthermore, the proposed algorithm was validated with another dataset located around Black Creek Pioneer Village, Ontario, that is, under the real highway/urban environment. Then, in Chapter 5, the multistrip adjustment (MA) algorithm was performed by using overlapping strips and was validated with the same study area of Chapter 4. The boresight angles of Lynx mobile LiDAR system were calibrated by applying the raw measurements of scanned objects/facades with different orientations from the overlapping strips in Chapter 6.

Lastly, Chapter 7 provides the conclusions to the work and future recommendations. The important outcome of the research is summarized. Then some recommendations for the future development based on this research are briefly elucidated.

2 Error Analysis of Terrestrial Mobile LiDAR System

2.1 Overview

In comparison with the airborne LiDAR technique, the terrestrial mobile LiDAR, as a 3D mapping platform possesses high potential to meet the overall high accuracy requirement in Engineering Surveying (Puente, 2011; Haalaa, 2008; Morgan, 2009). It has been demonstrated that terrestrial mobile LiDAR systems can be superior to the traditional surveying instruments in practice. In addition, the commercial market shows the high demand for such a system for engineering surveys. However, the LiDAR technique has not been authoritatively regulated as a standard methodology against the existing technical specification in Engineering Surveying, which imposes limitation on the operational use of LiDAR instruments (Uddin et al., 2001). Hence, comprehensive professional studies of its performance together with specifying of application-oriented appropriate field procedures are imperatively needed in order to make it qualified as a standard method with other existing instruments standing side by side in a complementary way.

This chapter will present the error analysis on terrestrial mobile LiDAR measurements from the following aspects:

i. Summary of the accuracy assessments from the literature and our research,

ii. Error budget and the impacts of individual error sources.

2.2 Accuracy Assessment

In a previous study at York's EOL (Earth Observation Laboratory) Laboratory supported by MTO Highway Infrastructure Innovation Funding Program in 2010, the research entitled "Performance and potentials of ground LiDAR (mobile and static) in engineering surveying and highway design" was conducted (Hu et al., 2012), in which accuracy assessment of terrestrial LiDAR products by taking the Optech Lynx Mobile Mapper V200 (kinematic) and IRILS 3D (static) for the MTO engineering surveys was introduced. A Lynx Mobile Mapper V200 (Figure 2-1) consists of two laser scanners, four digital cameras and one Applanix POS LV420. The system can be operated with respect to a specific GPS reference station. The command and control unit in the vehicle controls two laser scanning sensors and four optional passive imaging cameras. Each camera is individually addressable, with independent scalable frame sizes and coverage areas. The operator controls the system through a laptop. The laser scanners collect data at the measurement rate of up to 500 kHz and the scan frequency of up to 200 Hz. The general technical specification is listed in Table 2-1.

Table 2-1: Technical specification of Optech Lynx Mobile Mapper V200 system

Parameter	Lynx V200
Number of LiDAR sensors	1 ~ 2
Camera support	Up to 2 cameras
Maximum range	200m, 20%
Range precision	8mm, 1σ (Under test conditions)
Absolute accuracy	±5cm, 1σ (Under test conditions)
Laser measurement rate	75 – 500kHz programmable
Measurement per laser pulse	Up to 4 simultaneous
Scan frequency	80 – 200 Hz programmable
Scanner field of view	360° without obscurations
Power requirements	12VDC, 30A max. draw
Operating temperature	-10 °C to + 40° C (extended range
Storage temperature	-40°C to + 60°C
Laser classification	IEC/CDRH Class 1 eye-safe
Vehicle	Fully adaptable to any vehicle

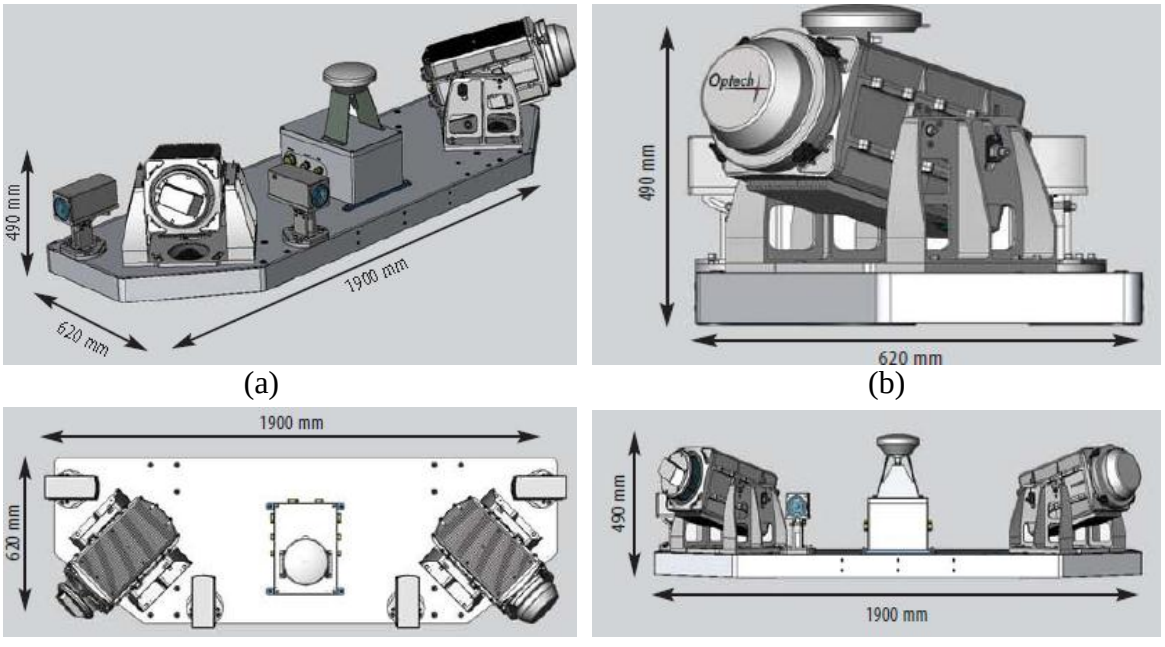

(a) (b)

(c) (d)

Figure 2-1: Overview of Optech Lynx Mobile Mapper V200 system platform. (a) The side view of the platform consisting of two laser scanners, four digital cameras and Applanix POS LV420 GPS-aided Inertial and Integrated Navigation system. (b) Close view of laser scanner sensor with the dimensions. (c) Top view of the platform. (d) Front view of the platform.

To analyze the characteristics of errors in the 3D positions of LiDAR points (i.e., the difference between LiDAR coordinates and pre-survey ones), a number of the overall quantitative indexes were used inclusive of the minimum, maximum, mean, standard deviation and RMS (root mean square). Additionally, statistical tests were employed to determine if the errors were significantly biased and if the errors were significantly larger than the requirement. Specifically, a ***t***-test statistics (Neter et al, 1988) was built up to test if the mean value was significantly different from zero. Furthermore, a χ^2-test was constructed to statistically conclude if the standard deviation or RMS of a group of measurement samples was significantly larger than the specified accuracy requirement. All of the statistic tests in the accuracy assessment were performed at the 5% significance level of Type I Error.

Three kinematic tests in different environments (Figure 2-2) were performed, covering complex urban scenes (York Boulevard on the Keele's campus of York University), a stretch of a main urban street (Steeles Avenue West in Toronto with the speed limit of 60 km/h), and a stretch of a major regional road (Highway 7 in York Region with the speed limit of 80 km/h). The GPS station on the roof of Optech headquarter building was used as a base station for reaching the RTK solution of the vehicle's trajectories. The vehicle was repeatedly driven on the test scenes at the different combination of the laser PRFs (pulse repetition frequencies) and mirror speeds for the purpose of finding the optimal configuration settings. The overview of three scanned scenes was presented in Figure 2-3.

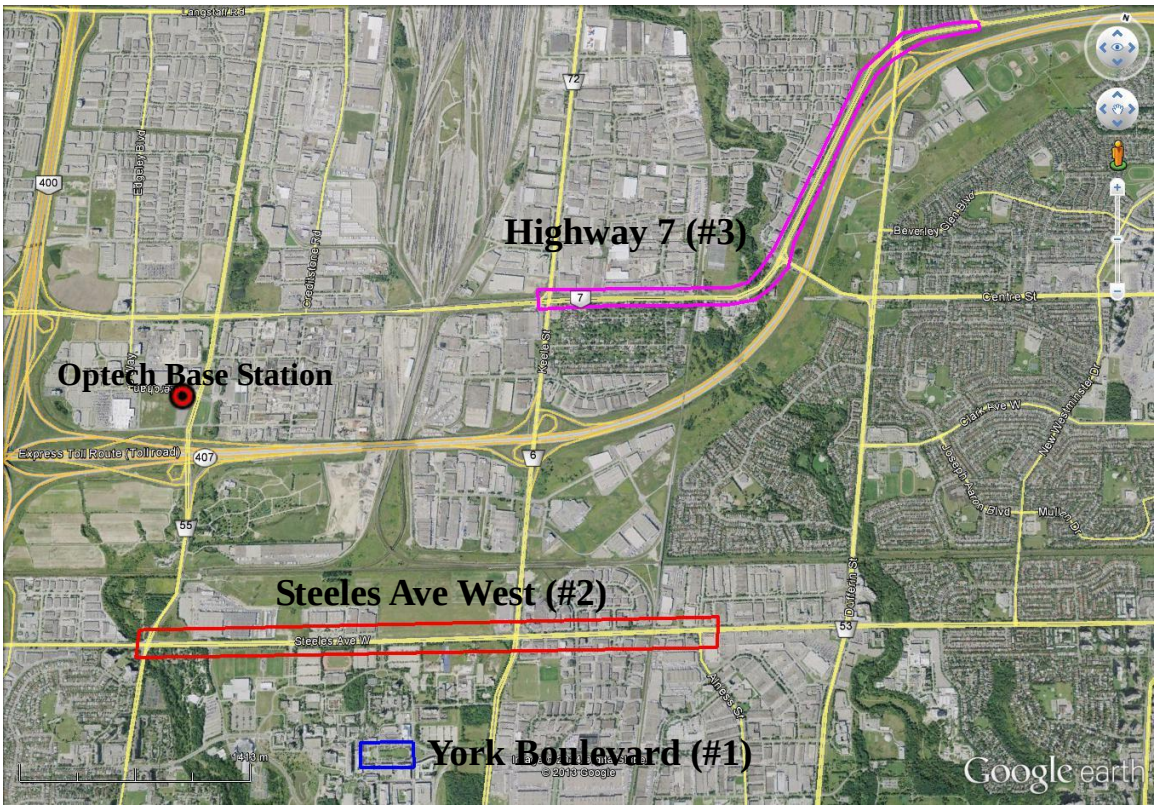

Figure 2-2: The overview of three study areas relative to the Optech GPS reference station in the city of Vaughan, Ontario Canada. The blue color represented the York Boulevard testing case. The red color indicated a main urban street scenario at Steeles Ave West. A part of the regional road Highway 7 testing case was marked as pink color.

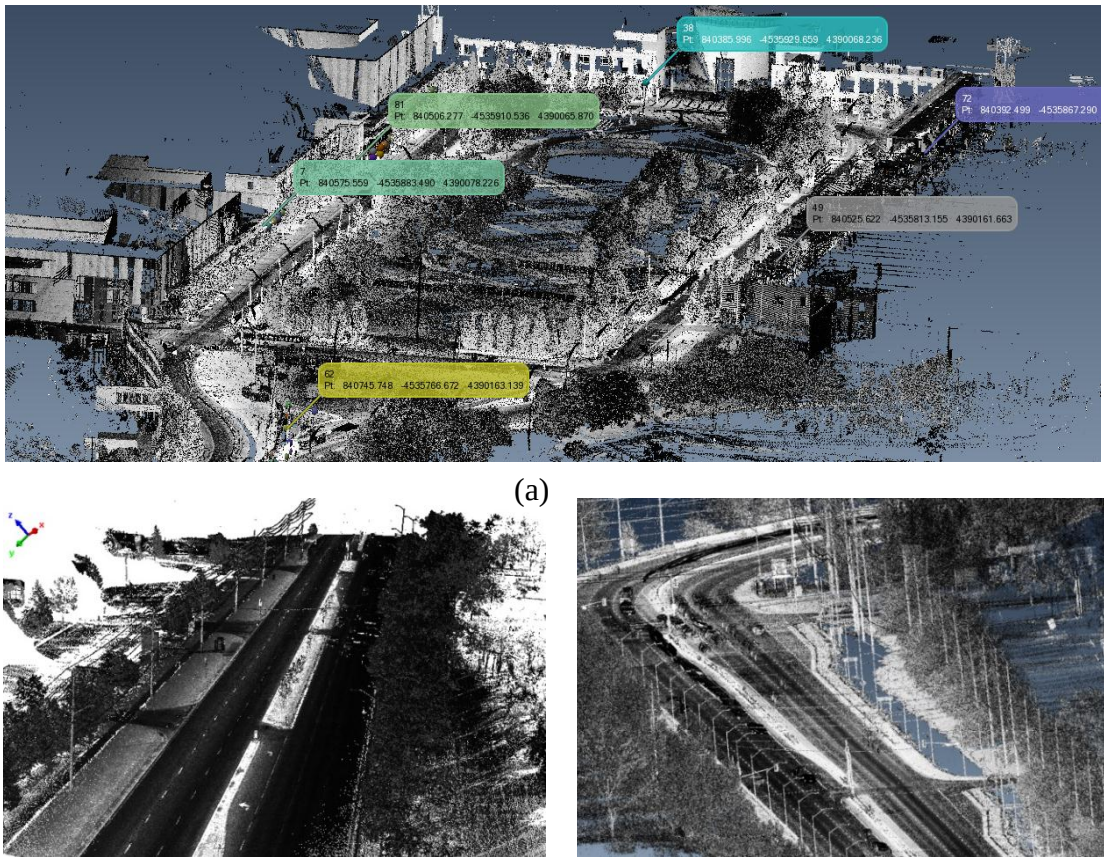

(a)

(b) (c)

Figure 2-3: The overview of three scanned scenes: (a) a complicated urban environment at York Boulevard on the Keele's Campus of York University, (b) a part of the scanned Steeles Avenue West between Keele Street and Jane Street in Toronto, and (c) a part of the scanned Highway 7 between Keele Street and Langstaff Road in the city of Vaughan [Hu, et al, 2012].

The absolute accuracy was determined against the coordinate measurements of the targets on walls and the natural objects on hard surfaces that were independently surveyed using a total station system and RTK GPS on the basis of the high accuracy engineering control network. The target is a square-shaped plate that was made of the cardboard with the dimension of 25 cm (Figure 2-4(a)). The black and white colored quadrants provided high contrast for a better recognition of the targets by the LiDAR instruments and human eyes. Because the paint coating is not reflective, a 6cm by 6cm Leica reflective sticker was laid on its center. Natural objects (e.g., traffic light, sign) were selected in order to avoid getting any complication due to the authority request for setting any target plate on private properties (Figure 2-4(b)). The relative accuracy was obtained based on the measured linear features in the scenes using steel tapes.

The quality of the mobile LiDAR solution is undoubtedly affected by the quality of the POS SBET (smoothed best estimated trajectory) solution because the geospatial coordinates of the point cloud are based on the direct georeferencing data and the lever arms and boresight angles among the GPS, IMU and DMI sensors. The absolute accuracy of a point cloud is not with respect to the POS system or the LiDAR sensor itself, but with respect to the GPS reference station. Hence, one has to take account into the effect of the uncertainty of the POS solution in the absolute accuracy assessment in order to further study what accuracy of the used Optech mobile LiDAR system is achievable. The York Boulevard test as a complicated urban scene was illustrated as an example (Figure 2-5). The accuracy of the corresponding SBET (direct georeferencing) solution resulted from the POS system for Strip 10 of this testing case is shown in Figure 2-6. The target

points scanned by the LiDAR system were presented in accordance with RMS errors to exam any abnormal phenomena.

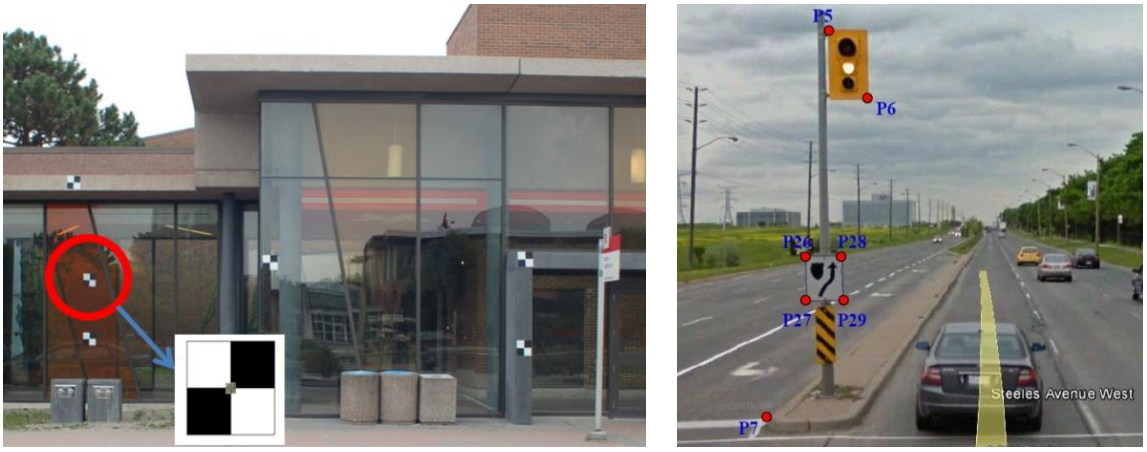

(a) (b)

Figure 2-4: (a) Reflective on-scene target stickers. (b) Existing characteristic points. [Hu et al., 2012]

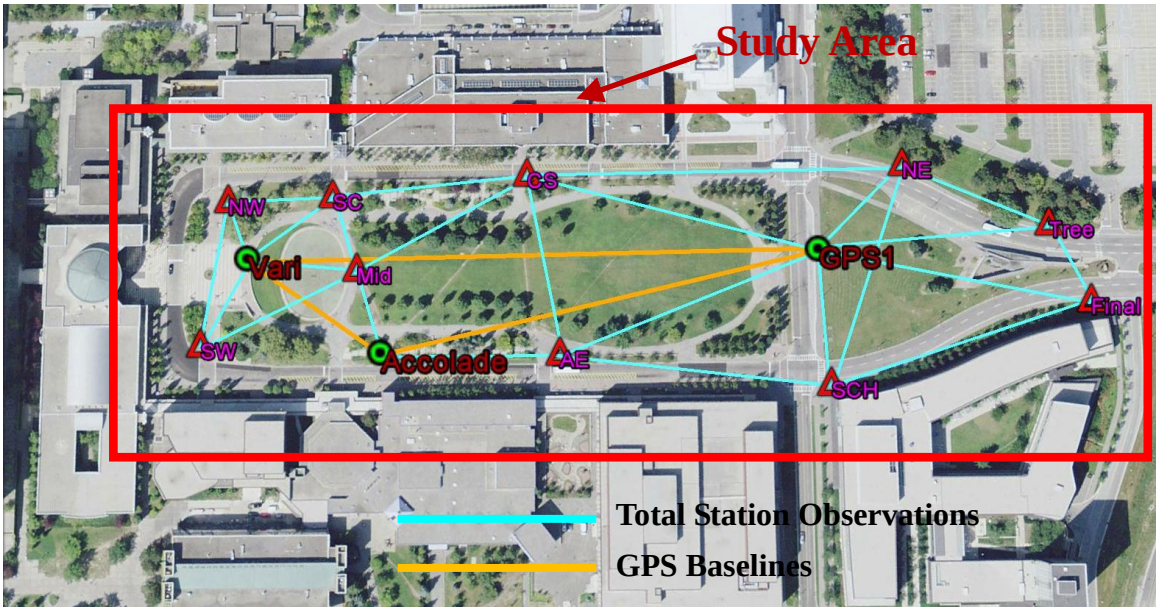

Figure 2-5: The overview of the study area of York Boulevard on the Keele's Campus of York University. The Optech Lynx V200 mobile mapping vehicle was driving on the York Boulevard circle with the laser PRF of 75kHz and mirror speed of 100Hz. The red rectangle presented the scanned areas of the mobile mapping system.

Obviously, the overall error budget of mobile LiDAR system is composed of two major contributions: the uncertainty on the POS trajectory (SBET solution) and the uncertainty brought by the LiDAR sensors. If a POS system is used as the project control, one has to split these two error sources. However, the POS system provides the LiDAR system with a moving trajectory, not the fixed control points. As a result, the error contribution in the total error budget between the POS system and the LiDAR sensor cannot easily be separated. Therefore, in order to appropriately investigate the accuracy level that one may expect from a mobile LiDAR system, it would be reasonable to consider the total uncertainty contributed by both of the POS system and the LiDAR sensors together: $\sigma_{total}^2 = \sigma_{LiDAR}^2 + \sigma_{POS}^2$ in components, 2D horizontal or 3D. Based on the quality of the POS trajectory from two terrestrial mobile LiDAR tests at York Boulevard (named as Test One) and on Steeles Avenue West (named as Test Two), the average accuracy (1σ) of the POS solutions was ±1.5cm in north and east, and ±2.0cm in vertical. So, one has $\sigma_{POS\_Horizontal}^2 = 4.5cm^2$ and $\sigma_{POS\_Vertical}^2 = 4.0cm^2$. By taking the uncertainty of the POS solution into consideration together with the 2cm horizontal and vertical accuracy (95% confidence level) for the location of the topographic features on hard surfaces, the accepted accuracy level for a mobile LiDAR system can be considered as ±4.7cm horizontally and ±4.4cm vertically at the 95% confidence level, which is called the extended accuracy criterion.

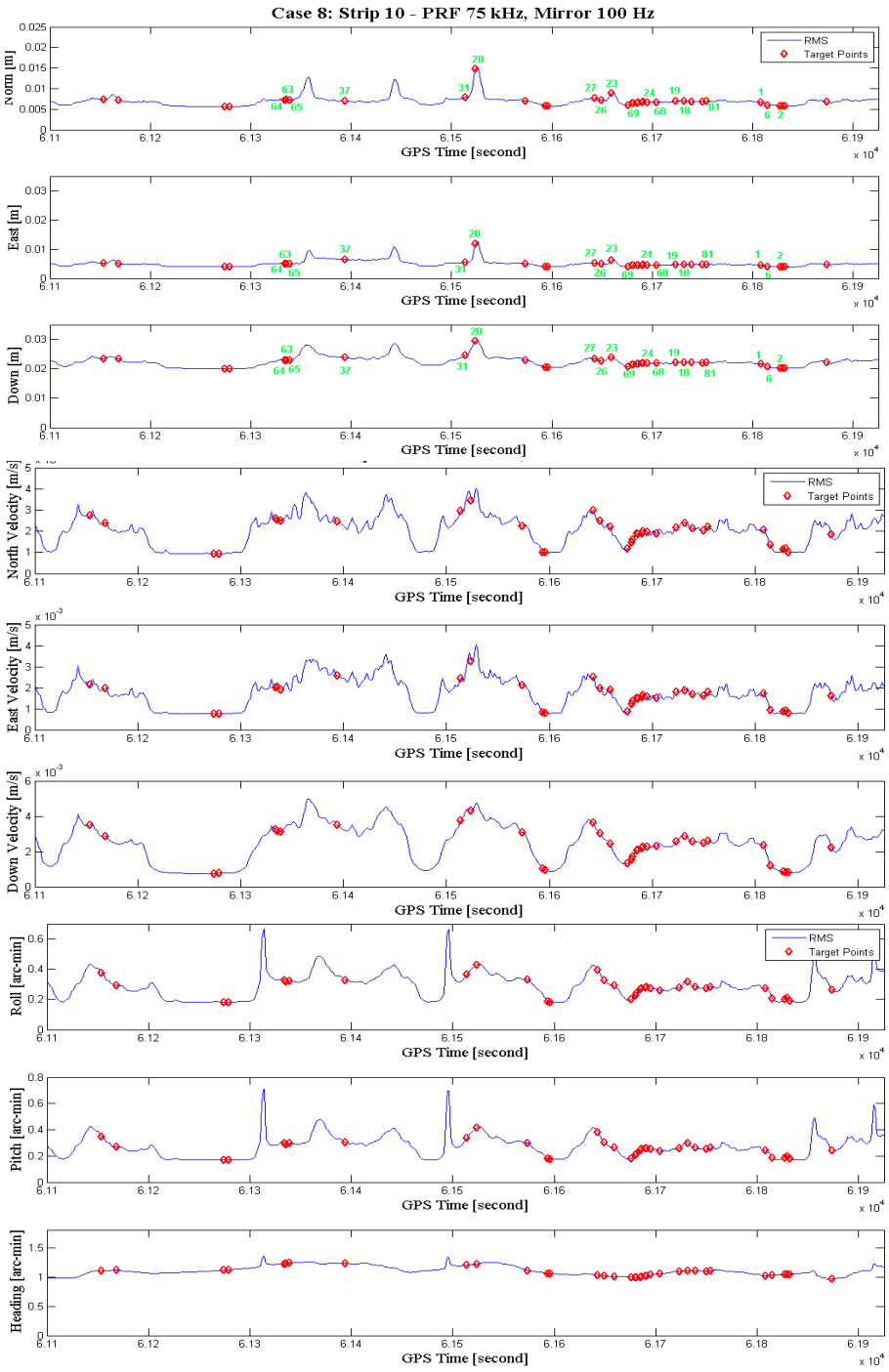

Figure 2-6: The SBET performance for Strip 10 of York Lanes testing case. The RMS error of the position (north, east and down), orientation (roll, pitch and heading) and velocity (north, east and down) versus GPS time were presented in blue lines. The target points were plot in red diamond based on the GPS time [Hu, et al, 2012].

Under good GPS conditions without using any ground control point in geo-referencing process, the absolute position errors from the mobile Lynx system, in general, statistically suffer from a few of centimeters offsets for an urban environment like York Lanes at York University. The achieved accuracies were up to ±3.2cm vertically and ±3.4cm horizontally based on the χ^2-test at the 5% significance level of Type I Error. The achieved accuracies were lower than the required 2cm horizontal and vertical at the 95% confidence level for the location of the hard surface topographic features, for example, defined by MTO. Considering the uncertainty introduced by the POS system, the total error budget in the mobile Lynx system was within the extended accuracy criterion (±4.7 cm and ±4.4 cm for horizontal and vertical accuracy, respectively). A similar performance by the Lynx mobile LiDAR system was achieved in a typical urban area, for instance, along the Steeles Avenue in GTA. The absolute accuracies were lower with natural targets on the scene than with the well-designed sticker targets. It was worth mentioning that the errors may partially be introduced in identifying of those characteristic points. Specifically, it demonstrated an achieved absolute accuracy of ±4.4cm vertically and ±6.0cn horizontally at the 95% confidence level. Moreover, these achieved accuracies could not satisfy the specific MTO accuracy requirements, even if the extended accuracy criterion was applied [Hu, et al, 2012].

In term of the relative accuracy of the Lynx Mobile Mapper system, the errors between their field measured linear features and the identified values from the kinematic LiDAR data did not show a significant bias based on our studies using 50 linear features in the scene at York Boulevard [Hu, et al, 2012]. The standard deviation of the errors with

these 50 linear features was ±3.56cm (1σ), and was not statistically acceptable against the required accuracy of 4cm at the confidence level of 95%. For the test sites along the Steeles Avenue West, the RMS values from the differences were as small as 2.0cm in one test area and 2.5cm in another test area. The results based on the test on a stretch of a major regional road (Highway 7 in York Region) showed that the coordinates of 53 selected characteristic points and 56 selected linear feature dimensions obtained from the LiDAR point clouds were not significantly different when the driving speed changed from 70 km/h to 80 km/h and even further to 90 km/hr. The χ^2-test also concluded that the sample standard deviations and RMS horizontally and vertically met the expected accuracy (2.8cm) at the 95% confident level for the differences of a point location among various vehicle speeds. However, the standard deviation based on the differences of the selected feature dimensions among three speeds did not achieve the required accuracy of 4cm at the 95% confidence level.

On the basis of the analysis in the different instrument settings of laser scanners, the laser PRF of 200 kHz is sufficient to accurately characterize the scene close to the vehicle for the complex urban environment (speed limit of 40 km/h) where the buildings are on one-side of the road and a main urban road such as Steeles Avenue (speed limit of 60 km/h). But, a higher data rate (such as 500 kHz) is recommended in order to capture the scene on both sides of the road while the mobile mapping system was being driven in one direction. In addition, the mirror speed within the range from 80 Hz to 200 Hz has a limited effect on the LiDAR solution. Therefore, it demonstrated that the accuracies of mobile LiDAR products were also closely linked to the quality of practical executions

reflected from such as the GPS base station setting up, data acquisition configuration, and data processing etc.

It is worth mentioning that the accuracies of several terrestrial mobile LiDAR systems were evaluated in aspects of DTM (digital terrain model) generation of pavement surfaces for California Department of Transportation by Yen et al (2010). Their results showed that for the best scenario under the right conditions and with good methodology, the average offset between the mobile LiDAR data and the control determined by static LiDAR instruments or by the traditional survey methods was within 1cm. They concluded that the accuracy of the best mobile LiDAR data could not satisfy the required accuracy, 7mm vertical for hard surface, specified in Surveys Manual for pavement in California of United States.

Both of the abovementioned studies demonstrated that more effort is demanded towards improving of the positioning accuracy of terrestrial mobile LiDAR solutions. The key to the improvement of the overall performance partially depends on the accuracy improvement of the direct georeferencing process. In addition to the POS georeferencing solution, it also relies on the utilization of ground control points, linear, planar and/or spatial features in the scene. This can be achieved by developing image-aided georeference methods. It obviously becomes very essential for a mobile system to be able to maintain the expected solution quality in poor or none-GNSS environments that cannot be avoid in urban area.

2.3 Error Budget of a Terrestrial Mobile LiDAR System

In order to well interpret the effects of individual error sources on the terrestrial mobile LiDAR results, a detailed analytical analysis on them has been introduced in this study. The mobile mapping systems consist of integrated laser scanner, digital camera, GNSS-aided inertial position and orientation systems. From the perspective of a system, there are two major contributors to the solution quality with terrestrial LiDAR products: the direct-georeferencing component and the LiDAR instrument itself, as described above. The former consists of a position and orientation system (e.g. Applanix POS LV system), which is normally a GNSS (Global Navigation Satellite System) aided inertial integrated navigation system. The later measures the distances from the sensor to the scanned target and records the rotating angles of the laser beam while the former provides the position and orientation of the moving instrument platform. Thus, the accuracy of LiDAR point clouds depends on the quality in terms of reliability and accuracy of the vehicle trajectory. However, the position and orientation system provides the mobile LiDAR system with a moving trajectory, not the fixed control points through a traditional control network. As a result, both of the direct georeferencing system and the LiDAR sensors together make up the total error budget.

Figure 2-7 illustrates how the 3D position of a target point *P* is determined by a terrestrial mobile LiDAR system. Mathematically, it consists of the following portions:

- The absolute position of the integrated GNSS-aided inertial position and orientation system.
- The relative position between the IMU and the laser scanner.

- The relative position between the laser scanner and the target point *P*.

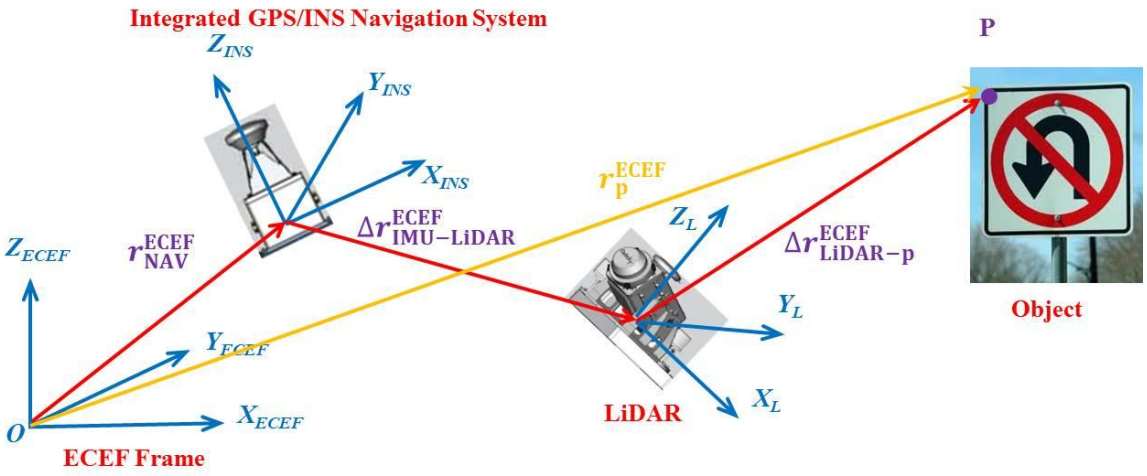

Figure 2-7: Geometry of the 3D position of a scanned target *P* determined by direct georeferencing process of a terrestrial mobile LiDAR system.

The error analysis reported from the aforementioned individual study (Hu et al., 2012) concluded that the positioning accuracy of a terrestrial mobile LiDAR system was significantly affected by the accuracy of its direct georeferencing component. As a result, the key to improve its overall accuracy is to reduce the uncertainty in the direct georeferencing of the LiDAR points. In addition, to achieve the required accuracy in engineering surveys by a survey-grade LiDAR system, other factors, such as system lever arms precision, extended GPS baselines, and boresight angles calibration need also to be considered.

Direct georeferencing is the process of determining the time-variable spatial position of points scanned by a mobile LiDAR sensor with reference to a local or a global coordinate system. The most common equipment for direct georeferencing is a combination of GNSS receiver and an IMU in accordance with POS (position and

orientation system). The GPS antenna is typically mounted on top of the vehicle and the IMU is rigidly mounted to the sensor platform. At present, the GPS-aided inertial integrated navigation system is the key component in terrestrial LiDAR mapping sensors for direct georeferencing, which is responsible for taking the position and orientation measurements. The IMU makes capable of computing the accurate position and velocity, thus filling the gap between GPS measurements or during GPS outages, while the GPS measurements, in turn, continually calibrate the systematic errors of the IMU. The direct georeferencing process involves a few of transformations between different coordinate systems.

The position vector r_p^{ECEF} of a target point *P* in ECEF (Earth-centered Earth Fixed) frame is given by:

$$\begin{aligned} r_p^{ECEF} &= r_{NAV}^{ECEF} + \Delta r_{IMU-LiDAR}^{ECEF} + \Delta r_{LiDAR-p}^{ECEF} \\ &= r_{NAV}^{ECEF} + R_{NAV}(B,L)R(r,p,h)l_{IMU-LiDAR}^{b} + \\ &+ R_{NAV}(B,L)R(r,p,h)R(\theta_1,\theta_2,\theta_3)R(\alpha,\beta)d_{LiDAR-p} \end{aligned} \tag{2.1}$$

wherein are

r_{NAV}^{ECEF} - the 3×1 absolute position vector of the integrated GPS/INS navigation component in ECEF frame,

$\Delta r_{IMU-LiDAR}^{ECEF}$ - the 3×1 incremental position vector from the IMU center to LiDAR center in ECEF frame,

$\Delta r_{LiDAR-p}^{ECEF}$ - the 3×1 incremental position vector from LiDAR center to point p in ECEF frame,

$R_{NAV}(B,L)$ - the 3×3 rotation matrix from the local geodetic coordinates to the ECEF Cartesian coordinates,

B and *L* - the latitude and longitude of the center of integrated GPS/INS navigation component, respectively,

$R(r,p,h)$ - the 3×3 roll-pitch-heading rotation matrix from the IMU body frame to

the local geodetic frame (North-East-Up),

$R(\theta_1, \theta_2, \theta_3)$ - the 3×3 boresight-angle rotation matrix from the LiDAR body frame to the IMU body frame,

$l^b_{IMU-LiDAR}$ - the 3×1 lever arm vector from the IMU center to the LiDAR center in the IMU body frame,

α , β - the horizontal and vertical angles with respect to the LiDAR center in the LiDAR body frame, and

$d_{LiDAR-p}$ - the range from the LiDAR center to target point p .

It becomes evident that all of the terms on the right hand side of the equation are contaminated by errors. Thus, the effects of the individual random errors on the target coordinates can be analyzed by applying the principle of error propagation. As a result, the effect of small differential errors on the target coordinates can be observed on the output coordinates of laser scanner by the solution of a set of linear equations (Glennie, 2007). For seeking the error propagation, its total differential equation is derived as follows:

$$\begin{aligned} dr_p^{ECEF} &= dr_{NAV}^{ECEF} + d\Delta r_{IMU-LiDAR}^{ECEF} + d\Delta r_{LiDAR-p}^{ECEF} \\ &= dr_{NAV}^{ECEF} + \left[R_{NAV}(B,L)l_1^b + R_{NAV}(B,L)R(\theta_1,\theta_2,\theta_3)l_2^b\right]d\dot{R}(r,p,h)(dr,dp,dh)^T + \\ &+ R_{NAV}(B,L)R(r,p,h)dl_1^b + R_{NAV}(B,L)R(r,p,h)R(\theta_1,\theta_2,\theta_3)dl_2^b + \\ &+ R_{NAV}(B,L)R(r,p,h)l_2^b d\dot{R}(\theta_1,\theta_2,\theta_3)(d\theta_1,d\theta_2,d\theta_3)^T \end{aligned} \quad (2.2)$$

wherein are

$l_1^b = l_{IMU-LiDAR}^b$ - the 3×1 lever arm vector from the IMU center to the LiDAR center in the IMU body frame,

$l_2^b = l_{LiDAR-p}^b = R(\alpha,\beta)d_{LiDAR-p}$ - the 3×1 incremental position vector from the LiDAR center to the target point p in the LiDAR body frame,

$d\dot{R}(r,p,h)$ and $d\dot{R}(\theta_1,\theta_2,\theta_3)$ - the Jacobian Matrix.

Equation (2.2) is the differential equation with respect to the laser scanner measurements, the POS solution (i.e., the position and orientation), and the mounting parameters (e.g., boresight angles, lever arms) that allow having sufficient understanding how the individual error sources affect the coordinates of a LiDAR target in general. Further, the error sources can be classified into two groups: the relative errors from the laser scanner system and the absolute errors from the direct georeferencing component.

The lever arms between an IMU sensor and a LiDAR sensor could be accurately determined by the LiDAR manufacturer. In addition, the zero error is the systematic bias in a LiDAR range measurement in order to account for the distance traveled by the laser pulse from the laser emitter to the focusing mirror and the distance traveled by the returning pulse from the focusing mirror to the receiver. The size of these range corrections varies with the LiDAR system design and configuration. Thus, a simulation was implemented in Hu et al (2013) to study the effects of the uncertainties on three groups of factors: IMU positions (*X*, *Y*, *Z* coordinates), IMU orientations (roll, pitch, and heading); LiDAR measurements (vertical and horizontal angles, ranging distance), and LiDAR range zero error; the lever arms and boresight angles between the IMU and LiDAR sensors. Two scenarios were simulated, one as the ideal case having the best calibrations of the last two groups of factors and the other with the relatively low calibration accuracies. For both cases, the uncertainties associated with the vehicle trajectory (i.e., the first group of the factors) were extracted from the Applanix POS SBET solution of a real dataset under the condition with good GPS coverage. The

following points were deducted:

(1) The contributions to the errors in the LiDAR 3D positions made by the position uncertainties of the trajectory were higher than the ones made by any other factors in both scenarios. Thus, it verified that the accuracy of a terrestrial mobile LiDAR system was significantly affected by the accuracy of its direct georeferencing component.

(2) The accuracies of the boresight angles and lever arms between the IMU and the LiDAR sensors were dominant factors affecting the accuracy of the final solutions for the scenario with less accurate calibration parameters. Therefore, it indicated that an accurate calibration of the LiDAR instrument for the lever arms and the boresight angles is essential for obtaining high accurate LiDAR 3D positions.

(3) The contributions of each group of factors were not uniform across the whole scene except for the orientations (roll, pitch and heading) from direct georeferencing process. It was worth mentioning that the large errors occurred in the areas above the road surface. Thus, caution should be taken in any further refinement of the LiDAR measurements. The 3DCCT commonly used to improve the LiDAR positioning accuracy with the help of ground control points may not be sufficient or valid for a large stretch of data collected with nonlinear vehicles trajectory. That is, the seven parameter conformal transformation may not be able to well compensate for the residual systematic errors.

3 Methodology for the Accuracy Improvement of Terrestrial Mobile LiDAR

3.1 Overview

Three techniques were proposed and implemented for accuracy improvement of terrestrial mobile LiDAR solutions in this research: seven parameter 3D conformal coordinate transformation (3DCCT), multistrip adjustment and preliminary LiDAR boresight calibration process, which were individually tested, analysed, and further applied in a complementary way.

As the essential technique, the 3DCCT on the basis of the Least Squares Method (LSM) was developed as conditional adjustment with parameters by employing the ground control points (GCPs) and feature constraints (straight lines/planar patches) towards the accuracy improvement of terrestrial mobile LiDAR solutions. Its general mathematical model and stochastic model along with geometrical constraints are summarized in Section 3.2. In addition, five associated strategies were developed to study the feasibility and effects of the proposed method in different ways:

1) Segmental 3D conformal coordinate transformation (3DCCT).
2) Categorization of GCPs concerning horizontal and vertical accuracy improvements.
3) Utilization of feature constraints incorporating with the GCPs.
4) Categorization of feature constraints concerning horizontal and vertical accuracy improvements.

5) Usage optimization of GCPs and feature constraints toward reducing the number of required GCPs or compensating for the shortage even the absence of GCPs in some area.

Furthermore, the multistrip adjustment (MA) algorithm was designed to refine the georeferencing of terrestrial LiDAR point clouds by taking advantages of the overlapped data strips and the repeatedly acquired datasets in the same working area with the help of tie points and tie features. The general mathematical model and stochastic model are summarized in Section 3.3.

Lastly, Section 3.4 presents a preliminary boresight calibration process of terrestrial mobile LiDAR systems used to enhance the other quality improvement procedures mentioned above by using linear and/or planar features of two scans acquired during consecutive runs in the opposite driving directions as proposed by Keller et al. (2013) and comes up with practical considerations about how to optimally utilize different accuracy improvement approaches supplementary for the better efficiency and effectiveness.

3.2 3D Conformal Coordinate Transformation (3DCCT) on the Basis of Least Square Principle

3.2.1 General Algorithmic Description

The performance of a terrestrial mobile LiDAR system is subject to various factors to satisfy the typical engineering surveying standard as previously discussed in section 2.3. Therefore, the key to the overall accuracy improvement is how to reduce the comprehensive influence of all the remaining systematic errors in the georeferencing process, in the sensor calibration for lever arms, boresight angles and any other remaining systematic errors with individual sensors in general.

Firstly, using ground control points (GCPs) is an effective way to remove some of the leftover systematic errors and improve the absolute accuracies of terrestrial mobile LiDAR solutions, or make up for poor GPS performance, even GPS outages. Even though the positioning accuracy of LiDAR solution could significantly be improved to a specific level, the associated cost for setting up these control points was so high that the benefit of a mobile LiDAR system as a cost-effective solution could significantly be compromised. Therefore, the geospatial locations of the existing characteristic (natural and/or artificial) points, such as the corners of buildings, windows, traffic lights and signs and pavement markings etc., could be employed as absolute control information to reduce even to eliminate the cost and/or access authorization request for setting up targets in field. The total station and GPS technique were applied to determine the coordinates of such control points.

A straight thought would be to take advantages of the mathematic relationships of the common points through their coordinates surveyed as GCPs using geodetic instruments and delivered as LiDAR solution. This mathematic relationship is the 3DCCT because it preserves angles and shape of objects and results in parameters to adjust the effects of the remaining systematic errors in LiDAR solution.

However, the error effects in the LiDAR solutions, specifically the coordinates of individual LiDAR points, are non-uniform because of the orientation and boresight angles based on the aforementioned error analysis (refer to equation (2.1) and (2.2)). Thus, the 3D conformal transformation may not be valid for a large stretch of data. Moreover, the errors in the 3D LiDAR positioning may not be uniform in horizontal and vertical directions for a given scene. Therefore, two strategies were implemented in accordance with control points:

(1) Piecewise segment the LiDAR strip into small stretches and model the 3D conformal transformations separately for each segment,

(2) Categorize the ground control points into different groups according to their location or geometry information, such as, building and ground types concerning horizontal and vertical accuracy improvements.

Secondly, in addition to control points, other measures were investigated toward the accuracy improvement of LiDAR solutions, such as linear features and planar patches because of their low cost and easy implementation. A few studies have been proposed to adjust the discrepancies between the overlapping strips using the conjugate features. As a result, some of the systematic errors, such as the leftover attitude or boresight angles,

could be removed to a certain level. However, it could only describe the relative 3D transformation between adjacent strips, because no absolute positioning measurements are involved. Thus, in my research, the absolute position and orientation parameters of feature constraints were determined using the corresponding pre-surveyed coordinates of control points. In addition, the number of the surveyed points could be decreased to a reasonable number to reduce cost and work load. For example, 4-5 points may be needed for 2-meter long pavement markings. Other characteristic objects were also selected as planar patches or linear features in both horizontal and vertical directions, such as traffic signs and lights, advertisement signs along the road, building facades and stop bars etc.

Lastly, employing more control points could achieve higher accuracy, but setting up those control points was very costly. Thus, it is necessary to optimize the usage of the control points in terms of density and ideal distribution in order to efficiently and effectively employ those measurements. On one hand, it is desirable to choose natural targets placed not too far from each other and well distributed spatially to ensure that the transformation based on the targets indeed improves the LiDAR data accuracy. On the other hand, the required number of GCPs could be reduced or the shortage even the absence of GCPs may be compensated for in some areas with the aid of feature constraints to achieve the minimal required accuracy.

The seven parameter 3DCCT was developed in the form of the conditional adjustment with parameters and geometrical constraints. The software implementation is illustrated in Figure 3-1. The pre-surveyed coordinates of GCPs and their corresponding geo-referenced coordinates extracted from LiDAR point cloud were used as input. Then a

user has the options to use either only GCPs or GCPs incorporating with the feature constraints. The τ-test statistics was utilized to test if a control point or a feature constraint is a potential outlier. Moreover, the *F*-test statistics was constructed to test the consistency among all of the observations. The variance components for the coordinates pre-surveyed and extracted from the LiDAR solution were then estimated. Finally, the accuracies of the LiDAR solutions before and after the adjustment were assessed using the extra GCPs which were not used in 3DCCT. The mathematical and stochastic models will be introduced in the following subsections.

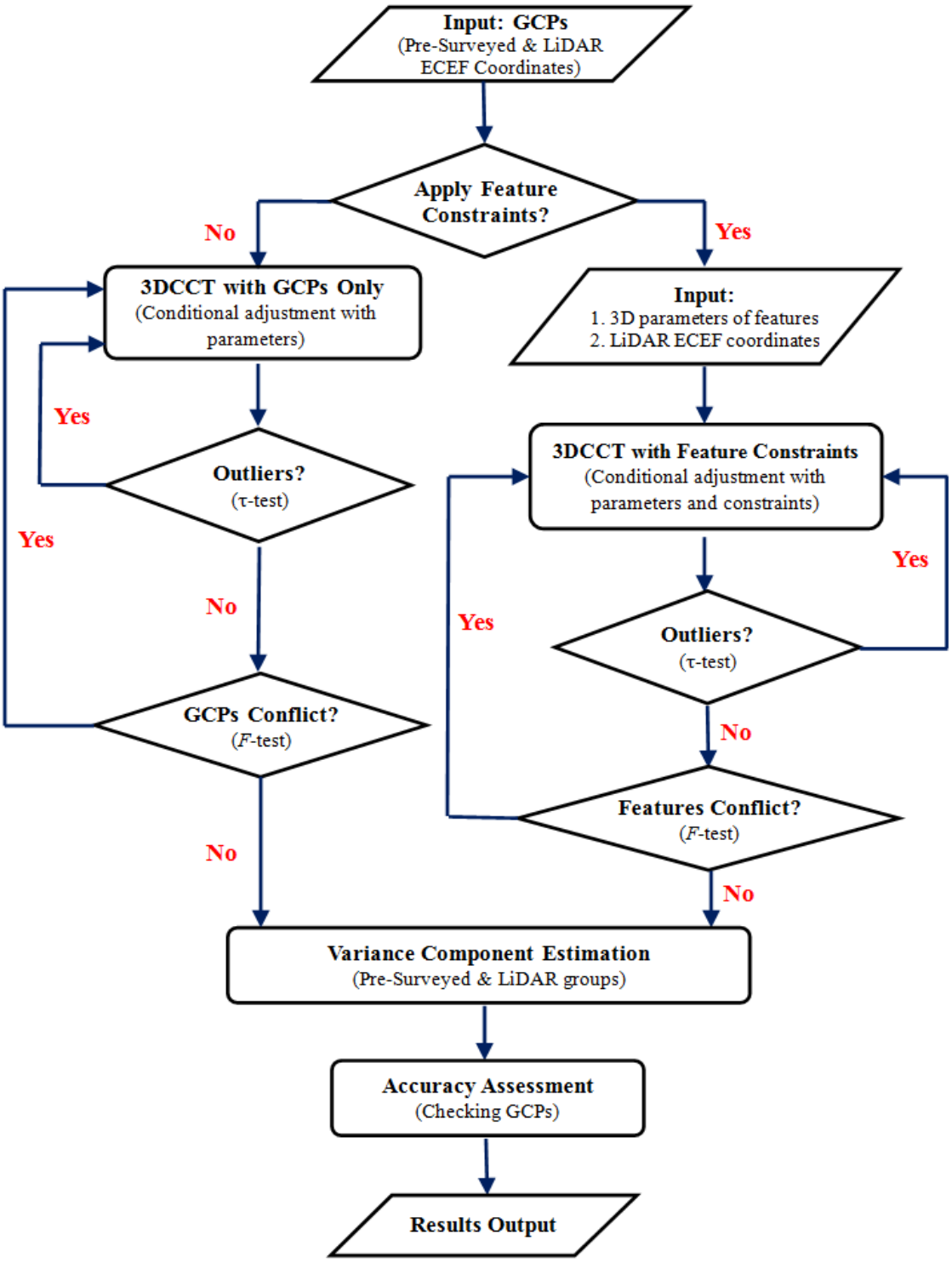

Figure 3-1: Flowchart of 3D conformal coordinate transformation (3DCCT) with Least Square Method (LSM)

3.2.2 Utilization of Ground Control Points

The introduction of ground control points (GCPs) is an effective way to remove some of the leftover systematic errors and to improve the overall accuracies of terrestrial mobile LiDAR solutions, or make up for the poor GPS performance, even the GPS outages as well. Thus, the selected in-scene characteristic points were served as GCPs in this study. In principle, it is desirable to choose natural targets placed not too far from each other and well distributed spatially to ensure that the transformation based on the targets indeed improves the LiDAR data accuracy. On one hand, their coordinates are determined on the basis of a 3D geodetic control network through conventional surveying techniques. On the other hand, the on-board POS system provided the absolute position and orientation of the working platform to enable the conversion of the local coordinates of LiDAR point into the global reference frame as stated in equation (2.1).

Assume to have the pre-surveyed coordinates $(X,Y,Z)_i^G$ and the geo-referenced LiDAR coordinates $(x,y,z)_i^{LiDAR}$ for ground point *i*. If there was no error in these coordinates, they should be identical theoretically. The 3D conformal transformation was applied to model some of the potential systematic errors. A 3D conformal transformation preserves angles and geometry of the objects being transformed, which uses three translations, three rotations and one scale factor. This transformation is assumed to be valid between the 3D points from different measurement groups. The ground control points were used to detect some of the biases or inconsistencies in the LiDAR data. Since no biases are assumed to exist in the LiDAR solution ideally, the initial approximations of these parameters could be considered as zeroes for three translations and three

rotations and one for the scale factor, respectively. The conditional equation for control point *i* is expressed as follow:

$$\begin{bmatrix} X \\ Y \\ Z \end{bmatrix}_i^G = \begin{bmatrix} X_{Tr} \\ Y_{Tr} \\ Z_{Tr} \end{bmatrix} + s \bullet R(\theta_1, \theta_2, \theta_3) \bullet \begin{bmatrix} x \\ y \\ z \end{bmatrix}_i^{LiDAR} \tag{3-1}$$

wherein

X_{Tr}, Y_{Tr}, Z_{Tr} are the three translation parameters;

s is the scaling factor;

θ_1, θ_2 and θ_3 are the three rotation angles;

and the rotation matrix $R(\theta_1, \theta_2, \theta_3)$ is computed as follows:

$$R(\theta_1, \theta_2, \theta_3) = R^T(\theta_3) R^T(\theta_2) R^T(\theta_1) = \begin{bmatrix} r_{11} & r_{12} & r_{13} \\ r_{21} & r_{22} & r_{23} \\ r_{31} & r_{32} & r_{33} \end{bmatrix} =$$

$$= \begin{bmatrix} \cos\theta_2 \cos\theta_3 & \sin\theta_1 \sin\theta_2 \cos\theta_3 - \cos\theta_1 \sin\theta_3 & \cos\theta_1 \sin\theta_2 \cos\theta_3 + \sin\theta_1 \sin\theta_3 \\ \cos\theta_2 \sin\theta_3 & \sin\theta_1 \sin\theta_2 \sin\theta_3 + \cos\theta_1 \cos\theta_3 & \cos\theta_1 \sin\theta_2 \sin\theta_3 - \sin\theta_1 \cos\theta_3 \\ -\sin\theta_2 & \sin\theta_1 \cos\theta_2 & \cos\theta_1 \cos\theta_2 \end{bmatrix}$$

(3-2)

The ECEF coordinates were used to represent the locations of the common points, either their pre-surveyed coordinates based on the geodetic control network, or their corresponding coordinates from the georeferenced LiDAR point cloud. As usual, the accuracy associated with these ECEF coordinates were given in terms of standard deviations in the local north-east-up frame for a better readability. That is, in order to easier represent the error components of the LiDAR solution, the local north-east-up

coordinates calculated with respect to the GPS base station, specifically the Optech GPS reference station used in the tests, were directly used in the 3D conformal transformation (Molodensky Model). That is, the relative coordinates of the common points with respect to a specific point in case only the local differences with respect to a specific point between two coordinate systems are concerned. Moreover, the calculation speed could be increased with the relative small numbers of local north-east-up coordinates instead of ECEF coordinates.

Each control point allows constructing three equations so that a minimum of three such common points, which are not on a straight line, are required to determine the seven parameters. The additional points lead to an overdetermined system, so the least square method can be employed to uniquely estimate the parameters. Here, the mathematical model is specifically in the form of the conditional adjustment with parameters using both of the pre-surveyed and the LiDAR coordinates as measurements, and the 7 parameters as unknowns. Thus the residuals of six coordinates for each point can be used to evaluate how well the transformed LiDAR coordinates fit its pre-surveyed coordinates. The linearized observation equations for each control point *i* are derived as:

$$A_i v_i + B_i \delta X = W_i \tag{3-3}$$

with

$$A_i = \begin{bmatrix} -1 & 0 & 0 & sr_{11} & sr_{12} & sr_{13} \\ 0 & -1 & 0 & sr_{21} & sr_{22} & sr_{23} \\ 0 & 0 & -1 & sr_{31} & sr_{32} & sr_{33} \end{bmatrix},$$

$$W_i = \begin{bmatrix} -X_{Tr} - s(r_{11}x_i + r_{12}y_i + r_{13}z_i) + X_i \\ -Y_{Tr} - s(r_{21}x_i + r_{22}y_i + r_{23}z_i) + Y_i \\ -Z_{Tr} - s(r_{31}x_i + r_{32}y_i + r_{33}z_i) + Z_i \end{bmatrix},$$

$$B_i = \begin{bmatrix} 1 & 0 & 0 \\ 0 & 1 & 0 \\ 0 & 0 & 1 \\ r_{11}x_i + r_{12}y_i + r_{13}z_i & r_{21}x_i + r_{22}y_i + r_{23}z_i & r_{31}x_i + r_{32}y_i + r_{33}z_i \\ s(r_{13}y_i - r_{12}z_i) & s(r_{23}y_i - r_{22}z_i) & s(r_{33}y_i - r_{32}z_i) \\ \cos\theta_3(r_{31}x_i + r_{32}y_i + r_{33}z_i)s & \sin\theta_3(r_{31}x_i + r_{32}y_i + r_{33}z_i)s & -s\begin{pmatrix} x_i\cos\theta_2 \\ +y_i\sin\theta_1\sin\theta_2 \\ +z_i\cos\theta_1\sin\theta_2 \end{pmatrix} \\ -s(r_{21}x_i + r_{22}y_i + r_{23}z_i) & s(r_{11}x_i + r_{12}y_i + r_{13}z_i) & 0 \end{bmatrix}^T,$$

$v_i = [v_{X_i} \quad v_{Y_i} \quad v_{Z_i} \quad v_{x_i} \quad v_{y_i} \quad v_{z_i}]^T$, and

$\delta X = [\delta X_{Tr} \quad \delta Y_{Tr} \quad \delta Z_{Tr} \quad \delta s \quad d\theta_1 \quad d\theta_2 \quad d\theta_3]^T$.

The results from the aforementioned error analysis (Hu et al, 2013) indicated that the effects of the remaining systematic errors may not be uniform in the LiDAR solutions with a large dataset due to the complicated nonlinear functional relationships with respect to so many different error sources. Thus, the 3D conformal transformation may not be valid for a large stretch of data. Therefore, it is necessary to segment the LiDAR strip into multiple smaller stretches and to piecewise determine the 3D conformal transformation parameters for each segment in order to compensate for the different natures and amplitudes of the error effects. Since the effects of the systematic errors in the 3D LiDAR solution may not be uniform in horizontal and vertical directions for a given scene, the ground control points were categorized into different groups according to their location or

geometric information, such as, building and ground types. Therefore, two strategies were further developed:

- Piecewise 3D conformal transformations
- Categorization of ground control points (GCPs)

In principle, employing more control points could potentially achieve higher accuracy, but setting up those control points was very costly (Zampa et al, 2009). On this account, the benefit of using a mobile LiDAR system for a cost-effective solution could significantly be degraded. Therefore, a study for finding practical configuration on optimizing the density and ideal distribution of control points was performed in this study and is presented in this section. Especially, the required number of the GCPs may be reduced or the absence of GCPs in some areas could be compensated by involving the linear or planar feature constraints to achieve the minimal required accuracy.

The general mathematical model of conditional adjustment with parameters can be expressed as follows:

$$F\left(L+V, X^{(0)}+\delta X\right)=F\left(L, X^{(0)}\right)+\left.\frac{\partial F}{\partial L}\right|_{L, X^{(0)}} V+\left.\frac{\partial F}{\partial X}\right|_{L, X^{(0)}} \delta X \tag{3-4}$$

wherein $F(L, X)$ is the *r*-dimensional nonlinear functions of X and L; $\hat{X}=X^{(0)}+\delta\hat{X}$, $\hat{L}=L+V$; $X^{(0)}$, $\delta\hat{X}$ are the *u*-dimensional approximate parameter vector and its correction vector, respectively; L, V are the *n*-dimensional observation vector and its correction (residual) vector. In this specific application, the pre-surveyed and LiDAR coordinates of ground control points were both considered as measurements. In addition, the LiDAR coordinates of line and planar features were used as measurements. Thus, the

linearized observation equations were derived as:

$$AV + B\delta\hat{X} + W = 0 \tag{3-5}$$

wherein $A = \left.\frac{\partial F}{\partial L}\right|_{L,X^{(0)}}$; $B = \left.\frac{\partial F}{\partial X}\right|_{L,X^{(0)}}$; $W = -F\left(L, X^{(0)}\right)$.

The goal function is to minimize the sum of the squares of the residuals in order to determine the best estimates of the parameters with the aid of Lagrange Multiplier vector *K* as:

$$G = V^T PV - 2K^T\left(AV + B\delta\hat{X} + W\right) = \min \tag{3-6}$$

Then one assigns the partial derivative vector of goal function (3-6) with respect to *V* and $\delta\hat{X}$ to zero to yield the normal equation system:

$$\begin{bmatrix} A & B & 0 \\ P & 0 & A^T \\ 0 & 0 & B^T \end{bmatrix}\begin{bmatrix} V \\ \delta\hat{X} \\ K \end{bmatrix} = \begin{bmatrix} W \\ 0 \\ 0 \end{bmatrix} \tag{3-7}$$

The solution of the conditional adjustment with parameters can be derived by solving the normal equation system (3-7):

$$\begin{cases} \delta\hat{X} = N_{bb}^{-1} B^T N_{aa}^{-1} W \\ K = N_{aa}^{-1}\left(W - B\delta\hat{X}\right) \\ V = P^{-1} A^T K \end{cases} \tag{3-8}$$

wherein $N_{aa} = AP^{-1}A^T$; $N_{bb} = B^T N_{aa}^{-1} B$.

Blunder detection can be carried out before or as part of the least-squares adjustment based on the analysis of the residuals. In order to test if a control point or a feature measurement *i* is a potential outlier, the τ test statistics (Caspary, 2009) is applied as

follows:

$$T_i = \frac{v_i}{\hat{\sigma}_0 \sqrt{q_{ViVi}}} \sim \tau_{n-r} \tag{3-9}$$

wherein T_i is the standardized residual; v_i is the residual of the measurement *i*; $\hat{\sigma}_0$ is the posteriori variance of unit weight; q_{ViVi} is the cofactor of v_i; τ_{n-r} denotes the τ test statistics with $n-r$ degrees of freedom; n and r are the total number of measurements and parameters, respectively. It is related to the student *t*-test by

$$\tau_{n-r} = \frac{\sqrt{n-r} \bullet t_{n-r-1}}{\sqrt{(n-r-1)+t_{n-r-1}^2}} \tag{3-10}$$

For an infinite degree of freedom the τ distribution converges toward the student distribution or the standardized normal distribution, i.e., $\tau_\infty = t_\infty = n(0,1)$. This blunder rejection procedure is under the hypothesis $v_i \sim n(0, \hat{\sigma}_{v_i}/\hat{\sigma}_0)$. If $|T_i| \geq c$, then the original hypothesis is rejected, i.e., the observation is flagged for further investigation and possible rejection. The critical value *c* is based on a preselected significant level.

In the linear model of parameter estimation, the a posteriori variance factor $\hat{\sigma}_0^2$ is an estimator for the common variance level of the observations (Bähr et al, 2007). It often serves as well as plausibility check for the assumptions made to a priori variance factor σ_0^2. If the relations of variance levels among the observations themselves are assumed to be known, one could consider the cofactor matrix $D(L)$ as given whereas σ_0^2 is estimated using the measurement residuals. In practice, however, an appropriate choice of $D(L)$ is not always obvious. Thus, variance component estimation renders

possible to estimate different levels of variances for multiple sets of observations. In this study, the pre-surveyed and LiDAR coordinates were considered as two groups of uncorrelated observations. Based on the accuracies of field survey and Lynx V200 mobile mapping system, a priori standard deviation of ±3mm and ±1.5cm of each component direction were selected for pre-surveyed and LiDAR groups, respectively.

Helmert (1907) proposed an approach to estimate the variance components. Many methods have been made to develop the optimal estimator for variance and covariance component since then. However, they required a considerable amount of computing time, which can be fatal for adjustment problems of high dimensions. Thus, the simple estimators based on Helmert's method have been applied by neglecting the postulates of statistical optimality and approximating the theoretical estimates. The most popular simplification of Helmert's algorithm for variance component estimation (group *i*) was developed on the basis of the measurement redundant contribution by Förstner (1979) as follows:

$$\hat{\sigma}_{0_i}^2 = \frac{V_i^T P_i V_i}{\sum r_{ii}} \tag{3-11}$$

wherein $\boldsymbol{V}_{\mathrm{i}}$ and r_{ii} are the redundant index and the residual vector of measurement group i, respectively. With a measurement group containing only one measurement, the smaller the redundant index of a measurement is, the bigger the minimal detectable outlier becomes. That is, more difficult an outlier can be detected.

A posteriori variance $\hat{\sigma}_0^2$ was the estimation of a priori variance σ_0^2 on the basis of the observations. Thus, both variances should be equal in the sense of statistics. The

formulation of the alternative hypothesis is:

$$H_0: \quad \hat{\sigma}_0^2 = \sigma_0^2 \tag{3-12}$$

$$H_1: \quad \hat{\sigma}_0^2 \neq \sigma_0^2 \tag{3-13}$$

The null hypothesis states that the posteriori variance of unit weight statistically equals the pre-given one whilst its alternative means that they are not statistically equal to each other. Under the assumption that the residuals are distributed normally, $V^T PV$ has a χ^2 distribution with $n-r$ degrees of freedom. Thus, the χ^2 test was performed to find out whether the least-squares adjustment is distorted or not (Leick, 2004) as:

$$\chi^2 = \frac{V^T PV}{\sigma_0^2} = \frac{\hat{\sigma}_0^2}{\sigma_0^2}(n-r) \sim \chi^2_{n-r} \tag{3-14}$$

If the numerical value is within the confidential region after a given significance level α as follows

$$\chi^2_{n-r,1-\alpha/2} < \chi^2 < \chi^2_{n-r,\alpha/2} \tag{3-15}$$

the null hypothesis is accepted. The significance level α is the probability of the Type I error for the incorrect rejection of a true null hypothesis.

The sequential group solution of the conditional adjustment with parameters can be formulated for two uncorrelated measurement groups, with the second group containing one or more measurements. In the application here, both groups share the common set of seven transformation parameters. Thus, one can process any group of measurements sequentially. Firstly, the linearized observation equations for n_1 measurements in group 1 can be expressed as:

$$A_1 V_1 + B_1 \delta X^{(1)} + W_1 = 0 \tag{3-16}$$

with $$L_1 \sim N\left(\tilde{L}_1, \sigma_0^2 P_1^{-1}\right) \tag{3-17}$$

The solution of (3-16) is given by

$$\delta \hat{X}^{(1)} = -(B_1^T (A_1 P_1^{-1} A_1^T)^{-1} B_1)^{-1} B_1^T (A_1 P_1^{-1} A_1^T)^{-1} W_1 \tag{3-18}$$

$$Q_{\delta \hat{X}^{(1)}} = (B_1^T (A_1 P_1^{-1} A_1^T)^{-1} B_1)^{-1} \tag{3-19}$$

$$V_1^{(1)} = -P_1^{-1} A_1^T \left(A_1 P_1^{-1} A_1^T\right)^{-1} \left(B \delta \hat{X}^{(1)} + W_1\right) \tag{3-20}$$

Then processing of the second group of n_2 measurements, is introduced using the linearized observation equation system:

$$A_2 V_2 + B_2 \left(\delta X^{(2)} + \delta X^{(1)}\right) + W_2 = 0 \tag{3-21}$$

with $$L_2 \sim N\left(\tilde{L}_2, \sigma_0^2 P_2^{-1}\right) \tag{3-22}$$

The solution of (3-21) can be derived as follows:

$$\delta \hat{X}^{(2)} = -Q_{\delta \hat{X}^{(1)}} B_2^T (A_2 Q_2 A_2^T + B_2 Q_{\delta \hat{X}^{(1)}} B_2^T)^{-1} \left(B_2 \delta X^{(1)} + W_2\right) \tag{3-23}$$

$$Q_{\delta \hat{X}^{(2)}} = -Q_{\delta \hat{X}^{(1)}} B_2^T (A_2 Q_2 A_2^T + B_2 Q_{\delta \hat{X}^{(1)}} B_2^T)^{-1} B_2 Q_{\delta \hat{X}^{(1)}} \tag{3-24}$$

$$V_2 = -P_2^{-1} A_2^T (A_2 Q_2 A_2^T + B_2 Q_{\delta \hat{X}^{(1)}} B_2^T)^{-1} \left(B_2 \delta X^{(1)} + W_2\right) \tag{3-25}$$

Since the parameter vector is updated using second group of observations, the residuals of the measurements in group 1 need to be adjusted:

$$V_1 = V_1^{(1)} + \Delta V_1 \tag{3-26}$$

wherein $\Delta V_1 = -P_1^{-1} A_1^T \left(A_1 P_1^{-1} A_1^T\right)^{-1} B_1 \delta \hat{X}^{(2)}$.

Thus, the final estimates of the parameters, their cofactor matrix and the weighted sum of the measurement residuals squared are computed as:

$$\delta\hat{X} = \delta\hat{X}^{(1)} + \delta\hat{X}^{(2)} \tag{3-27}$$

$$Q_{\delta\hat{X}} = Q_{\delta\hat{X}^{(1)}} + Q_{\delta\hat{X}^{(2)}} \tag{3-28}$$

$$V^T PV = V_1^T P_1 V_1 + V_2^T P_2 V_2 = V_1^{(1)T} P_1 V_1^{(1)} + V_X^{(2)T} P_{\delta\hat{X}^{(1)}} V_X^{(2)} + V_2^T P_2 V_2 \tag{3-29}$$

Furthermore, the *F* test statistics can be constructed to test whether the second group of observations significantly deviate the existing least-squares solution based on $V^T PV$ and the change of $V^T PV$, for which the null hypothesis (H_0) states that the second group of measurements do not significantly deviate the solution, i.e., there is no indication that the second group of measurements statistically disagree with the first group of the measurements significantly whilst the alternative hypothesis (H_1) states that the second group of measurements do not agree with the first group of measurements. That is, the F test checks the underlying assumption of homoscedasticity (i.e., homogeneity of variances) among the groups of measurements. Under the assumption that the first group of measurements is considered normal, one can make a decision if the second group of the measurements should be accepted. Accordingly, the *F* test (Leick, 2004) in sequential adjustment is performed:

$$F = \frac{\Delta\Omega^{(2)}}{\Omega^{(1)}} \bullet \frac{r_1 - t}{r_2} \sim F_{r_2, r_i - t} \tag{3-30}$$

wherein $\Omega^{(1)} = V_1^{(1)T} P_1 V_1^{(1)}$;

$$\Delta\Omega^{(2)} = V_X^{(2)T} P_{\delta\hat{X}^{(1)}} V_X^{(2)} + V_2^T P_2 V_2;$$

$$r_1 = rank(A_1), \quad r_2 = rank(A_2) \quad \text{and} \quad t = rank(B_1) = rank(B_2).$$

If the numerical value is such that $F_{r_2,r_1-t,1-\alpha/2} < F < F_{r_2,r_1-t,\alpha/2}$, then the null hypothesis is accepted, i.e., the second group of measurements did not impose any distortions on the adjustment. Since both sets of measurements were uncorrelated, then $\Omega^{(1)}$ and $\Delta\Omega^{(2)}$ are independent. In a special case, the *F*-test can be simplified to a student *t*-test if $r_2 = 1$. Therefore, the line or planar feature constraints could sequentially be tested in order to detect any inconsistency with the previous measurement group, such as the coordinates of the ground control points.

3.2.3 Utilization of Feature Constraints

The straight lines and planar patches incorporating with the ground control points were employed in the 3DCCT process in order to seek further accuracy improvement of terrestrial mobile LiDAR solutions. The linear features have recently been proposed as an alternative to GCPs due to the low cost and easy implementation (Gruen et al, 2004; Filin 2003a; Habib et al, 2005; Dold et al, 2006; Jaw et al, 2008; Bosché 2012). Moreover, it was more complicated to extract control points than linear features because these points were extracted by intersecting of three LiDAR patches, while linear features were extracted by intersecting of only two LiDAR patches (Habib et al, 2005).

A few studies have proposed to use the conjugate features to adjust the discrepancies between the overlapping strips (Besl et al, 1992; Zhang 1994; Gueziec et al, 1994; Habib et al, 1999; Wyngaerd et al, 1999; Fitzgibbon 2003; Park et al, 2003; Gruen et al, 2005; Kraus et al, 2006; Akca 2010). As a result, some of the systematic errors, such as, the leftover attitude or boresight angle errors, could be removed to a certain extend. However, it only enables the relative 3D transformation between adjacent strips, does not deliver absolute positioning information. Thus, in this research, the absolute position and orientation parameters of feature constraints were determined using the corresponding pre-surveyed coordinates of the control points. Some natural objects were selected as planar patches or linear features in both horizontal and vertical directions, such as, the pavement markings and painting lines on the ground, traffic signs and lights, advertisement signs along the road, and building facades etc. In addition, the number of the pre-surveyed points could be reduced to a reasonable number, for example, 4-5 points for a 2-meter long pavement marking.

If a LiDAR point falls on a plane or a straight line which was determined using the pre-surveyed coordinates, then the adjusted LiDAR coordinates after the 3D conformal transformation have to fall on the same feature as illustrated in Figure 3-2.

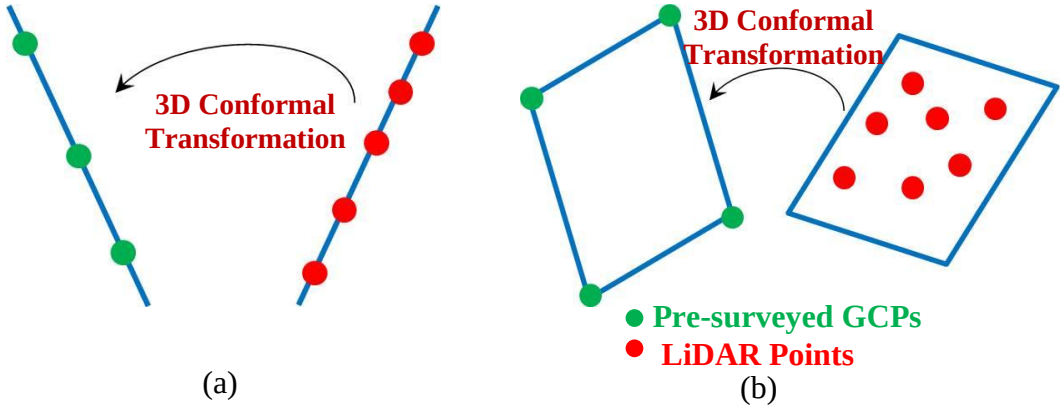

Figure 3-2: Utilization of line and plane feature constraints. The LiDAR points in green fit a line or a planar patch which is determined by the pre-surveyed control points in red. (a) Straight line feature. (b) Planar patch feature.

Firstly, the parameters of a feature were determined using the 3D best fitting of the pre-surveyed coordinates (X,Y,Z) of the control points. Assuming to have the unit vector $\vec{u}=(a_1,a_2,a_3)^T$ perpendicular to a plane, the normal form of the equation for the plane is expressed as:

$$a_1(X-X_0)+a_2(Y-Y_0)+a_3(Z-Z_0)=0 \tag{3-31}$$

with $a_1^2+a_2^2+a_3^2=1$, wherein (X_0,Y_0,Z_0) is the centroid of *n* points. The fitting plane after the least-squares principle must contain the centroid of the data points through the minimization of the sum of the orthogonal distances of the points to the plane. Because each control point generates one equation, a minimum of three points are required to solve for the three directional parameters (a_1,a_2,a_3). The linearized observation equation for a control point *i* is derived as:

$$\begin{bmatrix} a_1 & a_2 & a_3 \end{bmatrix}\begin{bmatrix} v_{Xi} \\ v_{Yi} \\ v_{Zi} \end{bmatrix}+\begin{bmatrix} X_i-X_0 & Y_i-Y_0 & Z_i-Z_0 \end{bmatrix}\begin{bmatrix} \delta a_1 \\ \delta a_2 \\ \delta a_3 \end{bmatrix}=-\begin{bmatrix} a_1(X_i-X_0)+ \\ a_2(Y_i-Y_0)+a_3(Z_i-Z_0) \end{bmatrix} \quad (3\text{-}32)$$

with $\begin{bmatrix} 2a_1 & 2a_2 & 2a_3 \end{bmatrix}\begin{bmatrix} \delta a_1 \\ \delta a_2 \\ \delta a_3 \end{bmatrix}=1-a_1^2-a_2^2-a_3^2$.

Similarly, a best fitting straight line in 3D can be derived as:

$$\frac{X-X_0}{b_1}=\frac{Y-Y_0}{b_2}=\frac{Z-Z_0}{b_3} \quad (3\text{-}33)$$

with $b_1^2+b_2^2+b_3^2=1$, wherein $\vec{u}=(b_1,b_2,b_3)^T$ is the unit vector parallel to the straight line, and (X_0,Y_0,Z_0) is the centroid of the used points. In this case, each control point provides two equations. So, a minimum of two such points are required for solving of three directional parameters. The linearized observation equation for control point *i* is derived as:

$$\begin{bmatrix} -b_2 & b_1 & 0 \\ -b_3 & 0 & b_1 \end{bmatrix}\begin{bmatrix} v_{Xi} \\ v_{Yi} \\ v_{Zi} \end{bmatrix}+\begin{bmatrix} Y_i-Y_0 & X_i-X_0 & 0 \\ Z_i-Z_0 & 0 & X_i-X_0 \end{bmatrix}\begin{bmatrix} \delta b_1 \\ \delta b_2 \\ \delta b_3 \end{bmatrix}=\begin{bmatrix} b_2(X_i-X_0)-b_1(Y_i-Y_0) \\ b_3(X_i-X_0)-b_1(Z_i-Z_0) \end{bmatrix} \quad (3\text{-}34)$$

with $\begin{bmatrix} 2b_1 & 2b_2 & 2b_3 \end{bmatrix}\begin{bmatrix} \delta b_1 \\ \delta b_2 \\ \delta b_3 \end{bmatrix}=1-b_1^2-b_2^2-b_3^2$.

Secondly, if the LiDAR point *i* fell on a plane which has analytically been determined using the pre-surveyed coordinates of the used GCPs, the adjusted coordinates $(x',y',z')_i^{LiDAR}$ of the same LiDAR point have to fall on the same plane as follows:

$$a_1(x'_i-X_0)+a_2(y'_i-Y_0)+a_3a_1(z'_i-Z_0)=0 \quad (3\text{-}35)$$

Based on equation (3-1), $(x',y',z')_i^{LiDAR}$ can be expressed in terms of the original georeferenced LiDAR coordinates $(x,y,z)_i^{LiDAR}$ as:

$$\begin{cases} x'_i = X_{Tr} + s(r_{11}x_i + r_{12}y_i + r_{13}z_i) \\ y'_i = Y_{Tr} + s(r_{21}x_i + r_{22}y_i + r_{23}z_i) \\ z'_i = Z_{Tr} + s(r_{31}x_i + r_{32}y_i + r_{33}z_i) \end{cases} \tag{3-36}$$

By substituting equation (3-36) into equation (3-35), the linearized observation equation for each LiDAR point *i* on a plan is given by

$$\overline{A}_i \overline{v}_i + \overline{B}_i \delta X = \overline{W}_i \tag{3-37}$$

wherein the matrices are defined as

$\overline{v}_i = \begin{bmatrix} v_{xi} & v_{yi} & v_{zi} \end{bmatrix}^T$;

$\overline{A}_i = \begin{bmatrix} s(a_1 r_{11} + a_2 r_{21} + a_3 r_{31}) & s(a_1 r_{12} + a_2 r_{22} + a_3 r_{32}) & s(a_1 r_{13} + a_2 r_{23} + a_3 r_{33}) \end{bmatrix}$;

$\overline{W}_i = -a_1[X_{Tr} + s(r_{11}x_i + r_{12}y_i + r_{13}z_i)] - a_2[Y_{Tr} + s(r_{21}x_i + r_{22}y_i + r_{23}z_i)] - \cdots$

$\quad - a_3[Z_{Tr} + s(r_{31}x_i + r_{32}y_i + r_{33}z_i)] + (a_1 X_0 + a_2 Y_0 + a_3 Z_0)$;

$$\overline{B}_i = \begin{bmatrix} a_1 \\ a_2 \\ a_3 \\ a_1(r_{11}x_i + r_{12}y_i + r_{13}z_i) + a_2(r_{21}x_i + r_{22}y_i + r_{23}z_i) + a_3(r_{31}x_i + r_{32}y_i + r_{33}z_i) \\ s[a_1(r_{13}y_i - r_{12}z_i) + a_2(r_{23}y_i - r_{22}z_i) + a_3(r_{33}y_i - r_{32}z_i)] \\ s\begin{bmatrix} a_1\cos\theta_3(r_{31}x_i + r_{32}y_i + r_{33}z_i) + a_2\sin\theta_3(r_{31}x_i + r_{32}y_i + r_{33}z_i) \\ -a_3(x_i\cos\theta_2 + y_i\sin\theta_1\sin\theta_2 + z_i\cos\theta_1\sin\theta_2) \end{bmatrix} \\ -s[a_1(r_{21}x_i + r_{22}y_i + r_{23}z_i) - a_2(r_{11}x_i + r_{12}y_i + r_{13}z_i)] \end{bmatrix}^T .$$

Similarly, the linearized observation equation for each LiDAR point *i* on a straight line *L* is also derived as:

$$\widetilde{A}_i \widetilde{v}_i + \widetilde{B}_i \delta X = \widetilde{W}_i \tag{3-38}$$

wherein the matrices are denoted as

$$\tilde{v}_i = \begin{bmatrix} v_{xi} & v_{yi} & v_{zi} \end{bmatrix}^T$$

$$\tilde{A}_i = \begin{bmatrix} s(a_1 r_{21} - a_2 r_{11}) & s(a_1 r_{22} - a_2 r_{12}) & s(a_1 r_{23} - a_2 r_{13}) \\ s(a_1 r_{31} - a_3 r_{11}) & s(a_1 r_{32} - a_3 r_{12}) & s(a_1 r_{33} - a_3 r_{13}) \end{bmatrix};$$

$$\tilde{W}_i = \begin{bmatrix} a_2\left[X_{Tr} + s(r_{11} x_i + r_{12} y_i + r_{13} z_i)\right] - a_1\left[Y_{Tr} + s(r_{21} x_i + r_{22} y_i + r_{23} z_i)\right] + (a_1 Y_0 - a_2 X_0) \\ a_3\left[X_{Tr} + s(r_{11} x_i + r_{12} y_i + r_{13} z_i) - a_1\left[Z_{Tr} + s(r_{31} x_i + r_{32} y_i + r_{33} z_i)\right]\right] + (a_1 Z_0 - a_3 X_0) \end{bmatrix};$$

$$\tilde{B}_i = \begin{bmatrix} -a_2 & -a_3 \\ a_1 & 0 \\ 0 & a_1 \\ \begin{bmatrix} a_1(r_{21} x_i + r_{22} y_i + r_{23} z_i) \\ -a_2(r_{11} x_i + r_{12} y_i + r_{13} z_i) \end{bmatrix} & \begin{bmatrix} a_1(r_{31} x_i + r_{32} y_i + r_{33} z_i) \\ -a_3(r_{11} x_i + r_{12} y_i + r_{13} z_i) \end{bmatrix} \\ s\begin{bmatrix} -a_2(r_{13} y_i - r_{12} z_i) \\ +a_1(r_{23} y_i - r_{22} z_i) \end{bmatrix} & s\begin{bmatrix} -a_3(r_{13} y_i - r_{12} z_i) \\ +a_1(r_{33} y_i - r_{32} z_i) \end{bmatrix} \\ s\begin{bmatrix} -a_2 \cos\theta_3(r_{31} x_i + r_{32} y_i + r_{33} z_i) \\ +a_1 \sin\theta_3(r_{31} x_i + r_{32} y_i + r_{33} z_i) \end{bmatrix} & s\begin{bmatrix} -a_3 \cos\theta_3(r_{31} x_i + r_{32} y_i + r_{33} z_i) \\ -a_1(x_i \cos\theta_2 + y_i \sin\theta_1 \sin\theta_2 + z_i \cos\theta_1 \sin\theta_2) \end{bmatrix} \\ s\begin{bmatrix} a_2(r_{21} x_i + r_{22} y_i + r_{23} z_i) \\ +a_1(r_{11} x_i + r_{12} y_i + r_{13} z_i) \end{bmatrix} & s\left[a_3(r_{21} x_i + r_{22} y_i + r_{23} z_i)\right] \end{bmatrix}^T.$$

Finally, the conditional adjustment with parameters plus additional feature constraints was applied to estimate the transformation parameters using the line and planar features (equation 3-37 & 3-38) along with the ground control points (equation 3-2). In practice, the constraints were sequentially added and tested in order to detect any potential conflict with the other applied observations and constraints. Thus, only the qualified constraints, which could pass the *F*-test, were used in the 3DCCT. In addition, the feature constraints could be categorized into horizontal directional (e.g., pavement markings) and vertical directional (for example, traffic light and signs) features so that one can analyze how the different types of features contribute to the accuracy improvement in 2D horizontal and vertical directions.

3.3 Multistrip Adjustment (MA) Algorithm

3.3.1 General Algorithmic Description

In the past few years, several approaches have been proposed for evaluating and improving the airborne LiDAR data quality by checking the compatibility of LiDAR footprints in overlapping strips. The multiple strips of data points for each scan area are often collected with airborne LiDAR missions in order to avoid gaps and reach the required point density. Since the objects surveyed can be large and complex-shaped, a series of scans from various directions is necessary in order to capture the complete representation of object geometry (Reshetyuk 2006). Thus, the performance of terrestrial mobile LiDAR system could also be improved by taking the advantage of such concept, for instant, the two or more data strips with sufficient overlapping collected from different runs.

Obviously, the adjacent LiDAR strips usually show discrepancies in overlapping areas due to the systematic errors in the LiDAR point cloud. Such discrepancies are caused by missing or improperly performing the system calibration and operation. Thus, it usually produces the problems in extracting meaningful information and affects the quality of the final product (Lee et al., 2007).

The difficulty of implementing strip adjustment comes primarily from the irregular point distribution spatially in a LiDAR point cloud. In other words, the same object space is randomly sampled in the spatial domain in each strip (Shan and Toth, 2008). In the past, several strip adjustment methods have been developed for evaluating and improving the quality of airborne LiDAR data (Kilian et al., 1996; Crombaghs et al., 2000; Maas, 2000;

Maas, 2002; Filin 2003b; Kornus et al., 2003; Bretar et al., 2004; Vosselman, 2004; Filin et al., 2004; Kager, 2004; Pfeifer et al., 2005; Kersting et al., 2008; Yousif et al., 2010). Kilian et al. (1996) presented an adjustment procedure similar to the photogrammetric strip adjustment using tie points. However, the identification of distinct points, such as building corners, is quite difficult and not reliable due to the irregular nature of the airborne LiDAR footprints. Then, Maas (2000 & 2002) suggested establishing the correspondence between the discrete points in one LiDAR strip and TIN patches in the other one. Kersting (et al., 2008) proposed an algorithm that used linear features to measure and adjust for the discrepancies between the overlapping LiDAR data strips. The linear features were chosen as conjugate features because they could be accurately extracted from man-made structures in urban area and more easily than the point features.

Even though the terrestrial mobile LiDAR mapping technique is fairly new, the refinement of terrestrial mobile LiDAR data has increasingly become critical. Yousif (et al., 2010) illustrated how to apply the theory of data assimilation to enhance the 3D georeferencing accuracy as well as fine-tuning of the radiometric intensity by means of exploiting the correlation between two oppositely-collected datasets over the same study area. The purpose of data assimilation is to combine two different datasets or models of the same phenomenon in order to achieve the best estimate of the true state.

Therefore, the multistrip adjustment (MA) algorithm was proposed as an additional tool to refine terrestrial LiDAR solutions in this research. This process attempts to align the adjacent strips using both of tie points and tie features by minimizing the impact of some of the systematic errors in the LiDAR system parameters to improve the

compatibility among the overlapped strips. In other words, the offsets of identical points, features and objects between strips could provide the ideal information allowing refining and improving mobile LiDAR solutions. Moreover, inspired by the utilization of feature constraints developed for 3DCCT, the straight line and planar patch features were also employed in the proposed MA process as the tie features.

Furthermore, most of the developed algorithms only used tie points, which could reduce or eliminate the relative discrepancies between overlapped strips in the boresight angles and measurements. However, they cannot address which strip should be selected as a reference and cannot identify what corresponding impact on the absolute accuracy of the final merged strip they have. Then the use of some type of ground control information is desirable.

The block diagram of the proposed MA algorithm is illustrated in Figure 3-3. The LiDAR solutions of two overlapped strips are firstly registered together using tie points and tie features. Once the two strips are merged together, the previously developed 3DCCT with LSM in Section 3.2 can be adapted to georeference the whole LiDAR point cloud using GCPs and geometrical feature constraints. Moreover, different features should be applied in the MA and the 3D conformal coordinate transformation to avoid the correlation. The mathematical model of MA algorithm will be introduced in the next subsection. In comparison with the 3DCCT algorithm, this approach is more economic and easier to be made automatic or semi-automatic. In addition, the number of the GCPs required in the process may be reduced through the involvement of more tie points and features.

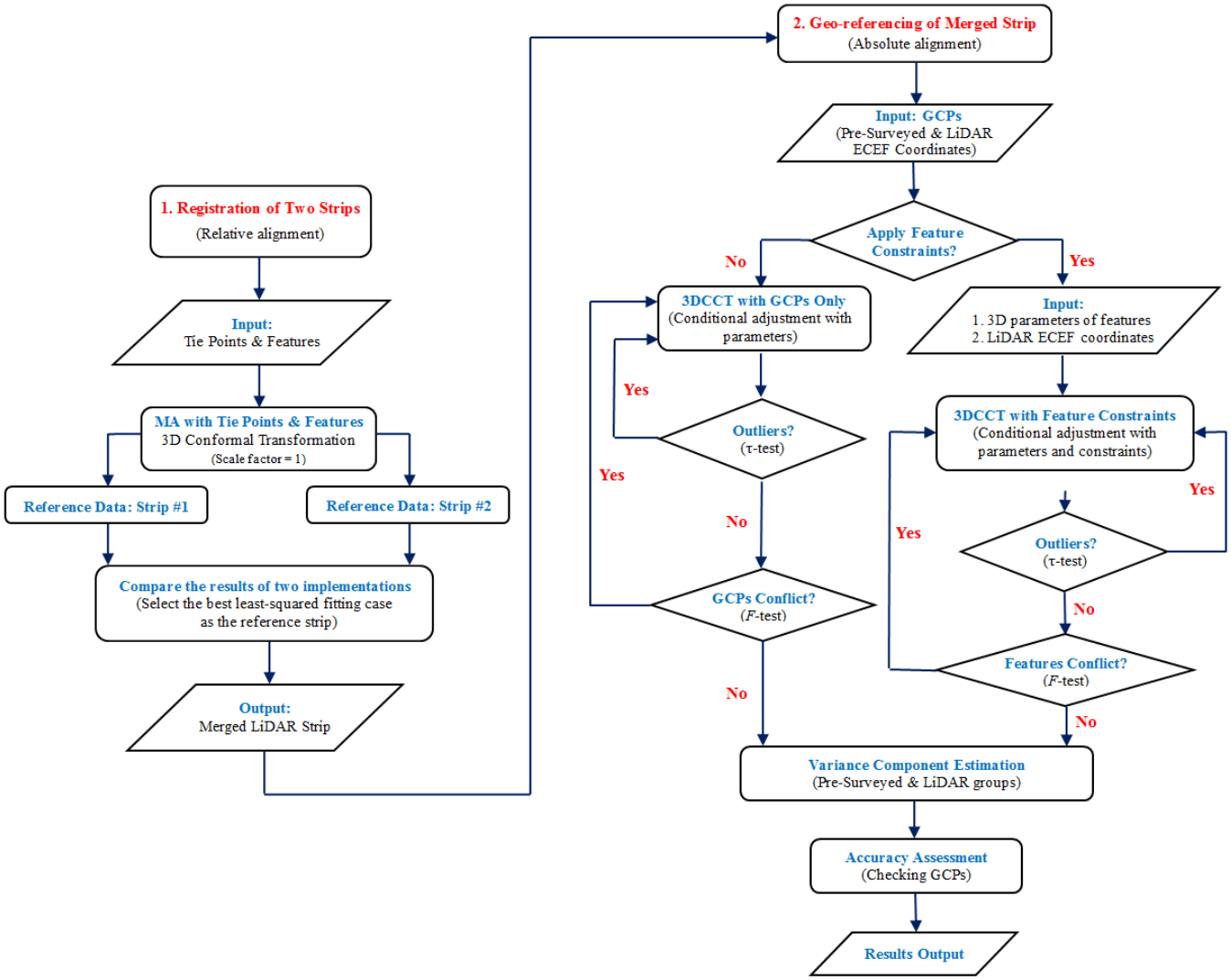

Figure 3-3: Flowchart of MA algorithm with co-registration of two strips and the georeferencing of merged strip.

3.3.2 Mathematical Model

Under the assumption that no bias in the system parameters exists, the overlapped LiDAR data strips should coincide with each other without any significant shifts or rotations to each other. Thus, the improvement of the compatibility between the overlapped data strips can be viewed as their co-alignment to a common reference frame. In other words, the strip adjustment can be thought of a refinement of the registration procedure. Assume to have a tie point *i* with its coordinates in two overlapped LiDAR point clouds as $(x,y,z)_i^1$ and $(x,y,z)_i^2$, respectively. Similar to the utilization of GCPs described in Section 3.2.2, the 3D conformal coordinate transformation is also applied to model some of the potential systematic errors. However, the scaling factor may be considered as 1 because the transformation is between the two data strips collected by the same type of the instruments (here, the Optech terrestrial LiDAR systems). With respect to one of the two involved strips, e.g., the strip 1, the mathematical equation for tie point *i* is expressed as follows:

$$\begin{bmatrix} x \\ y \\ z \end{bmatrix}_i^1 = \begin{bmatrix} X_{Tr} \\ Y_{Tr} \\ Z_{Tr} \end{bmatrix} + R(\theta_1, \theta_2, \theta_3) \bullet \begin{bmatrix} x \\ y \\ z \end{bmatrix}_i^2 \tag{3-39}$$

wherein

X_{Tr}, Y_{Tr}, Z_{Tr} are the three translation parameters;

$R(\theta_1, \theta_2, \theta_3)$ is the rotation matrix as the function of three rotation angles θ_1, θ_2 and θ_3.

Each tie point gives three equations. Thus, two such points are at least required to solve for the six parameters. The additional tie points lead to an overdetermined adjustment system in the form of the conditional adjustment with parameters so that the method of least squares is employed. Their linearized observation equations are as stated in (3-2), but replacing the scaling factor by $s = 1$.

Similar to the feature constraints described in Section 3.2.3, those characteristic objects, such as, the pavement markings and painting lines on the ground, traffic signs and lights, advertisement signs along the road, and building facades etc., can be selected as the tie features to construct the constraints. The mathematical model given in (3-31) – (3-38) for both of line and planar tie feature constraints along with the tie points together are applied to integrate the overlapped strips. Moreover, the feature constraints will sequentially be test to detect any significant conflict with the tie point measurements processed prior to them. Thus, only the qualified constraints that pass the *F*-test will be used in the adjustment process.

3.4 Accuracy Improvement with the Aid of Preliminary Calibration of Boresight Angles

As discussed in the error analysis of terrestrial mobile LiDAR systems in Section 2.3, the overall accuracy of the LiDAR solutions depends on the assembly and calibration of two components: the LiDAR units and the direct georeferencing System (GPS-aided Inertial Integrated Navigation System). The coordinates of the points in a LiDAR point cloud are the geospatial location determined by the georeferenced laser scanner.

In general, the errors can arise from individual sensor calibrations, lack of sensor synchronization and misalignments between the different sensors (Shan and Toth, 2008). An integrated GPS-aided inertial navigation system with high performance could provide accurate georeferencing information for the LiDAR data acquisition. Therefore, the proper calibration of the entire system including individual and inter-sensor calibration is essential. The need for accurately evaluating the angular misalignments between the axes of a LiDAR sensor and an IMU, commonly known as the boresight angles, arise from the fact that the coordinates of LiDAR points are the solutions made by the laser scanning unit with respect to the direct-georeferencing system. The systematic errors in the spatial and angular relationship between their own body frames could be the largest ones in the error budget, and therefore, it must be determined before the system can be effectively utilized (Burman, 2000). However, under the operational circumstances, the values of the boresight angle misalignments may never accurately be known but could only be estimated. Furthermore, the parameters could change over a relatively short time period (Pothou et al, 2009). Poor boresight estimation could seriously degrade the accuracy of

point cloud among overlapped strips for the common objects.

Discrepancies among overlapped strips occur if the point cloud is generated by the incorrect (or biased) system parameters, which can generally be modeled as the accumulated impact of some systematic errors on these strips. As a result, it is necessary to accurately compensate for the boresight misalignment in a specific terrestrial mobile LiDAR system.

The boresight angles ($\Delta\omega, \Delta\varphi, \Delta\kappa$) are the angular offsets in *X*, *Y* and *Z* directions between the scanner's body frame and the IMU body frame. The algorithms for evaluating the boresight angles have been developed and widely applied in airborne laser scanning (ALS) systems (Burman, 2000; Filin, 2001; Schenk, 2001; Toth et al, 2001; Toth, 2002; Friess, 2006; Skaloud et al, 2006; Pothou et al, 2007; Habib et al, 2007; Pothou et al, 2008 and 2009). However, the methods of data acquisition are inevitable different in the terrestrial laser scanning (TLS) systems, even though their physical working principles are similar (Rieger et al., 2010). For instant, an area of interest can be easily scanned from different flight directions during the airborne laser scanning survey. However, TLS systems are lack of flexibility in scanning the same objects multiple times from different directions due to the limited angular field-of-view. In addition, current calibration techniques require the access to the LiDAR system parameters and the raw observations, such as, the position and orientation of a platform, the commonly unavailable scan angles and laser scanning ranges (Bang et al., 2009). Moreover, some of the methods rely on the accurate absolute coordinates of the retro-reflective targets (i.e., GCPs) or the scanning objects of known size and position from different driving

directions and distances. All these techniques have been lack of flexibility and demanded more efforts on preparing the special test sites.

Accordingly, Keller et al. (2013) proposed a new cost-effective method to refine the boresight angles of TLS systems by using the planar and/or line facades of two scans acquired during consecutive runs in opposite driving directions at the post-processing stages. The calibrated boresight angles can be used to improve the accuracy of LiDAR solutions. Apparently, the calibration results for boresight angles from this approach are independent of any local behaviour because of the leftover systematic errors. Hence, it is expected that a preliminary calibration of the boresight angles before the segmental 3DCCT process will significantly enhance the entire refinement process of terrestrial LiDAR solutions.

The proposed method was inspired by the calibration procedures for multibeam sonar systems (IHO 2011). The static objects (e.g., building facades) can be scanned by a terrestrial mobile LiDAR system from several runs in the opposite directions and variable angular alignment of the laser swath. The boresight angular misalignment ($\Delta\omega, \Delta\varphi, \Delta\kappa$) between the IMU body frame and laser scanner unit could be evaluated by analyzing the discrepancies of the common targets or objects among overlapping strips. These misalignments appear with almost every TLS system due to the fact that the axes of the single unit cannot be perfectly mechanically aligned and every mechanical installation implies structural tolerance. Therefore, the poor estimation of boresight angles produces typical errors in the LiDAR point cloud.

A possible roll angle deviation ($\Delta\omega$) could result in a rotation of two scans acquired during consecutive runs in opposite driving directions as shown in Figure 3-4 (a). It causes a tilting facade parallel to the driving direction, which was supposed to be vertical. Moreover, the first facade tilts toward the vehicle, and the second facade tilts away from the vehicle. The angle between two corresponding tilting surfaces is proportional twice to the unknown roll angle deviation between the scanner and IMU with respect to the roll axis in the IMU body frame. That is, the measurement results need to be averaged for an error-free point cloud. Thus, the roll angle error can be computed as:

$$\Delta\omega = -\frac{\arccos\left(\vec{n}_1 \bullet \vec{n}_2\right)}{2} \tag{3-40}$$

wherein $\vec{n}_1$ and $\vec{n}_2$ are the unit normal vectors perpendicular to the corresponding titling surfaces, respectively.

Similarly, an error associated with the pitch angle ($\Delta\varphi$) generates the tilting facade perpendicular to the traveling direction as illustrated in Figure 3-4(b). The facade edge tilts toward the driving direction or in the opposite direction. Then, a straight line can be placed in the facade edge to determine this error, and the angle between the two straight lines corresponds to the double pitch angle deviation as:

$$\Delta\varphi = \frac{\arccos\left(\vec{u}_1 \bullet \vec{u}_2\right)}{2} \tag{3-41}$$

wherein $\vec{u}_1$ and $\vec{u}_2$ are the unit vectors parallel to the corresponding titling straight lines.

Furthermore, in the heading angle the residual error ($\Delta\kappa$) can be estimated through

passing by an object in a regular shape (e.g., circle, rectangle) on the ground from the opposite travelling directions demonstrated in Figure 3-4(c). As a result, the angle correction relative to the heading axis can be calculated as follows:

$$\Delta\kappa = \arctan\left(\frac{\Delta x}{\Delta L}\right) \tag{3-42}$$

wherein Δx is an offset to the actual position of the object and ΔL is the distance between the two trajectories from the opposite driving directions.

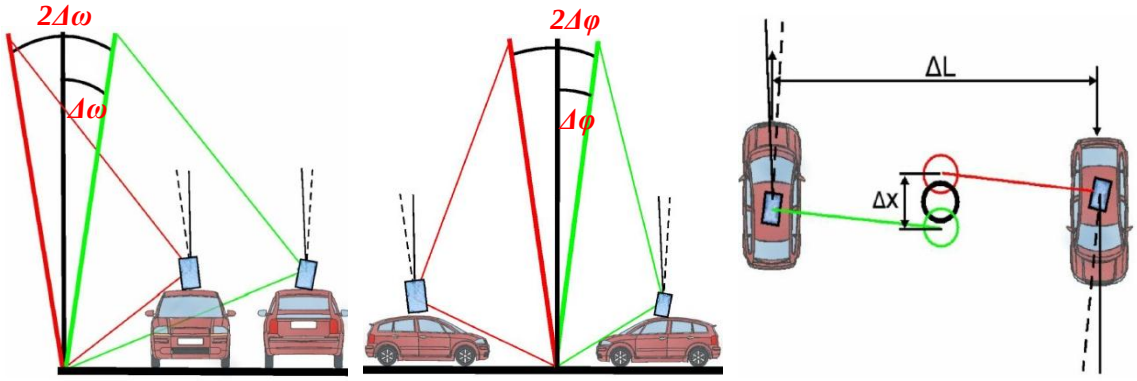

(a) (b) (c)

Figure 3-4: The field procedures of boresight angles calibration. The vehicle passes along the object or facade during consecutive runs in opposite driving directions. (a) Roll angle. (b) Pitch angle. (c) Heading angle. (Keller et al., 2013)

A common point on the common object scanned by two separate runs in the opposite driving directions will not coincide closely with each other if the boresight angles are not accurately estimated. Moreover, the significant misalignment of the overlapped strips may increase with the range as the vertical errors produced by the angular errors are proportional to the range (Chan 2011). The boresight angle calibration plays an important role in the overall quality of LiDAR point cloud because it estimates

the biases in the system parameters and measurements, which can be used to improve the quality of any subsequently collected mobile LiDAR data.

The calibration accuracy needs to be much higher than the trajectory accuracy in order to avoid significant negative influence on the final LiDAR solution because the accuracy of the trajectory is expected to be approximately 2 – 3 cm according to the SBET solution from the direct georeferencing process. Theoretically, it should be higher than the accuracy of the laser scanner. However this is considered uneconomical due to the time required and the unknown reliability and stability of the calibration itself. The boresight angles should be estimated to approximately 0.005˚ that corresponds to an accuracy of 4mm for a typical scanner distance of 50m in an urban environment. The range precision is 8mm with Lynx Mobile Mapper and 5mm with Lynx MG1, for example. Glennie (2007) found that a routine accuracy level of the boresight angles with the TITAN system by the least-squares approach is 0.001˚, 0.001˚ and 0.004˚ respectively for roll, pitch and heading. In addition, the measurements of both laser scanner and IMU system need to be timely stamped precisely.

Furthermore, the algorithm requires the usage of many planar features with different spatial orientation. They could be easily identified in the urban or sub-urban regions, where with an adequate amount of facade sections, roofs of buildings, traffic signs and pavement markings along the street containing preferably flat surfaces of variable orientation. However, not every area is adequate for carrying out a calibration of boresight angles. Obstructions of GPS signal caused by tall buildings or tree canopies can significantly degrade the accuracy of position and attitude information. Therefore, the

appropriate values of the pulse repetition frequency (PRF), the mirror scan rate and the driving speed are also essential in order to ensure the sufficient point density on the surfaces of the scanned objects.

4 Accuracy Improvement through 3D Conformal Coordinate Transformation

4.1 Overview

In this chapter, the 3DCCT on the basis of Least Squares Method (LSM) was implemented by employing the ground control points (GCPs) and feature constraints (straight lines/planar patches) towards accuracy improvement of terrestrial mobile LiDAR solutions. In addition, five strategies were applied to study the feasibility of the proposed methods:

1) Segmental 3D conformal coordinate transformation (3DCCT).
2) Categorization of GCPs concerning horizontal and vertical accuracy improvements.
3) Utilization of feature constraints incorporating with the GCPs.
4) Categorization of feature constraints concerning horizontal and vertical accuracy improvements.
5) Usage optimization of GCPs and feature constraints toward reducing the number of the required GCPs or compensating for the absence of GCPs in some area.

The headquarter office building of Optech Inc. in the City of Vaughan, Ontario, Canada was first chosen as the study area under the considerations of the research objectives, the easy access and the working safety. It focuses on the implementation of the proposed 3DCCT with LSM and the experimental analysis with this relative simple scenario. The results and the associated discussions are given in Section 4.2. In addition, more complicated testing case studies with the datasets acquired around Black Creek Pioneer Village, Ontario, Canada, were introduced (Section 4.3) to further validate the proposed algorithms and strategies.

4.2 Strategic Implementation and Experimental Results

4.2.1 General

This section presents the implementation of the proposed 3DCCT, its validation and the experimental analysis of different strategies. Accordingly, a relative simple scenario, the surroundings of the headquarter office building of Optech Inc. in City of Vaughan, Ontario, Canada was selected as the experimental study area under the considerations of the research objectives, the easy accessibility and the working safety. Four different strategies were tested to study the effectiveness and efficiency of the proposed approach:

1) **Segmental 3D conformal coordinate transformation (Section 4.2.3.1)**

   The 7 parameters of 3DCCT were separately determined for each segment in order to piecewise refine the LiDAR strip.

2) **Categorization of control points** concerning horizontal and vertical accuracy improvements **(Section 4.2.3.2)**

   The GCPs were categorized into different groups based on their location or geometry information because the effects of the remaining systematic errors may not be uniform in different parts of a LiDAR data acquisition mission (or strip).

3) **Utilization of feature constraints (Section 4.2.4)**

   In addition to the ground control points, the straight line and planar patch features were employed as geometrical constraints to strengthen the 3DCCT.

4) **Optimal usage of ground control points (Section 4.2.5)**

   The performance improvement of terrestrial LiDAR solution was investigated in terms of use of different numbers of the GCPs with linear and planar features as

constraints in order to efficiently and effectively employs the GCPs.

The strategic implementation of the seven parameter conformal coordinate transformation generally followed the workflow given in Figure 3-1. More details about the individual strategies will be involved in the relevant subsections below.

4.2.2 Studying Area and Data Acquisition

An overview of the point cloud of the test data acquired around the headquarter office building of Optech Inc. is presented in Figure 4-1 using PolyWorks Software. The top view of the entire test site is given as the left plot in Figure 4-2. Two major field tasks were performed with this test:

(1) Terrestrial mobile LiDAR data acquisition,

(2) Establishment of the 3D control network and determination of the control points and features in the ECEF coordinates system.

Figure 4-1: Overview of the scanned scene around the headquarter office building of Optech Inc., Vaughan, Ontario, Canada at the laser PRF of 500 kHz and mirror speed of 200 Hz.

4.2.2.1 Terrestrial Mobile LiDAR Data Acquisition and Processing

The mobile LiDAR data acquisition took place on April 19, 2012 by using an Optech Lynx V200 mobile mapping system sponsored by Optech Inc. The Optech Lynx V200 mobile mapping system consisted of two laser scanners, four digital cameras and one Applanix POS LV420 system. The vehicle was repeatedly driven four times both clockwise and counter-clockwise around the building at a relative constant speed of about 10km/h with the best configuration parameters of laser PRF (pulse repetition frequencies) of 500 kHz and the mirror speed of 200 Hz.

The POS LV420 component provided the direct georeferencing for the mobile LiDAR data with respect to the Optech GPS reference station. The commonly-known SBET (Smoothed Best Estimated Trajectory) solution from the POS system offers the absolute position and orientation of the working platform to convert the local coordinates of LiDAR point cloud into the global ECEF coordinates. The 2D horizontal, vertical and velocity profiles of the vehicle's trajectory are given in Figure 4-2.

Dashmap software from Optech was used to process the collected terrestrial mobile LiDAR data, and its data processing work flow is described in Figure 4-3. The corresponding SBET performance resulted from the POS LV420 is presented in Figure 4-4. It shows that the horizontal position accuracy (1σ) was better than ± 1.1cm, while the vertical accuracy (1σ) was around ± 3cm.

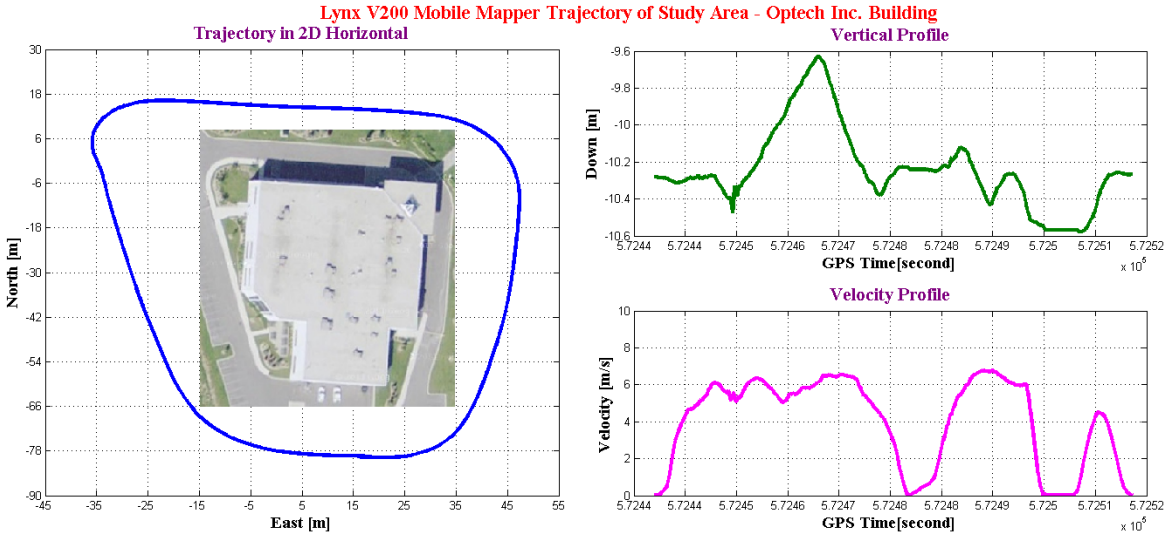

Figure 4-2: The trajectory in 2D horizontal, vertical and velocity profiles of Lynx V200 Mobile Mapper System at the studying area.

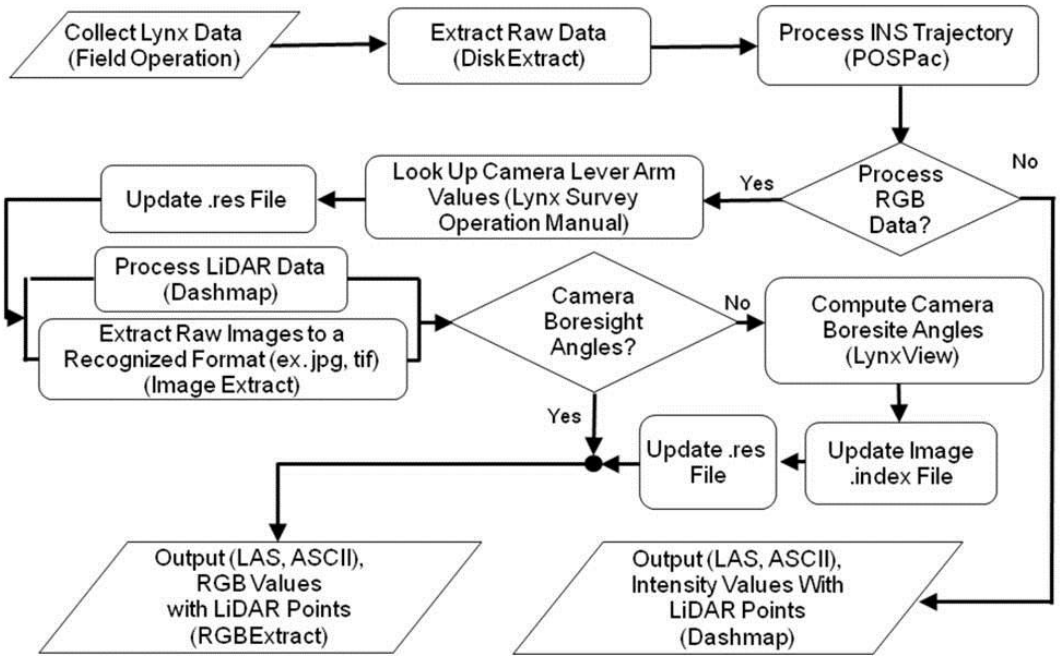

Figure 4-3: Work flow of mobile LiDAR data processing using Dashmap software.

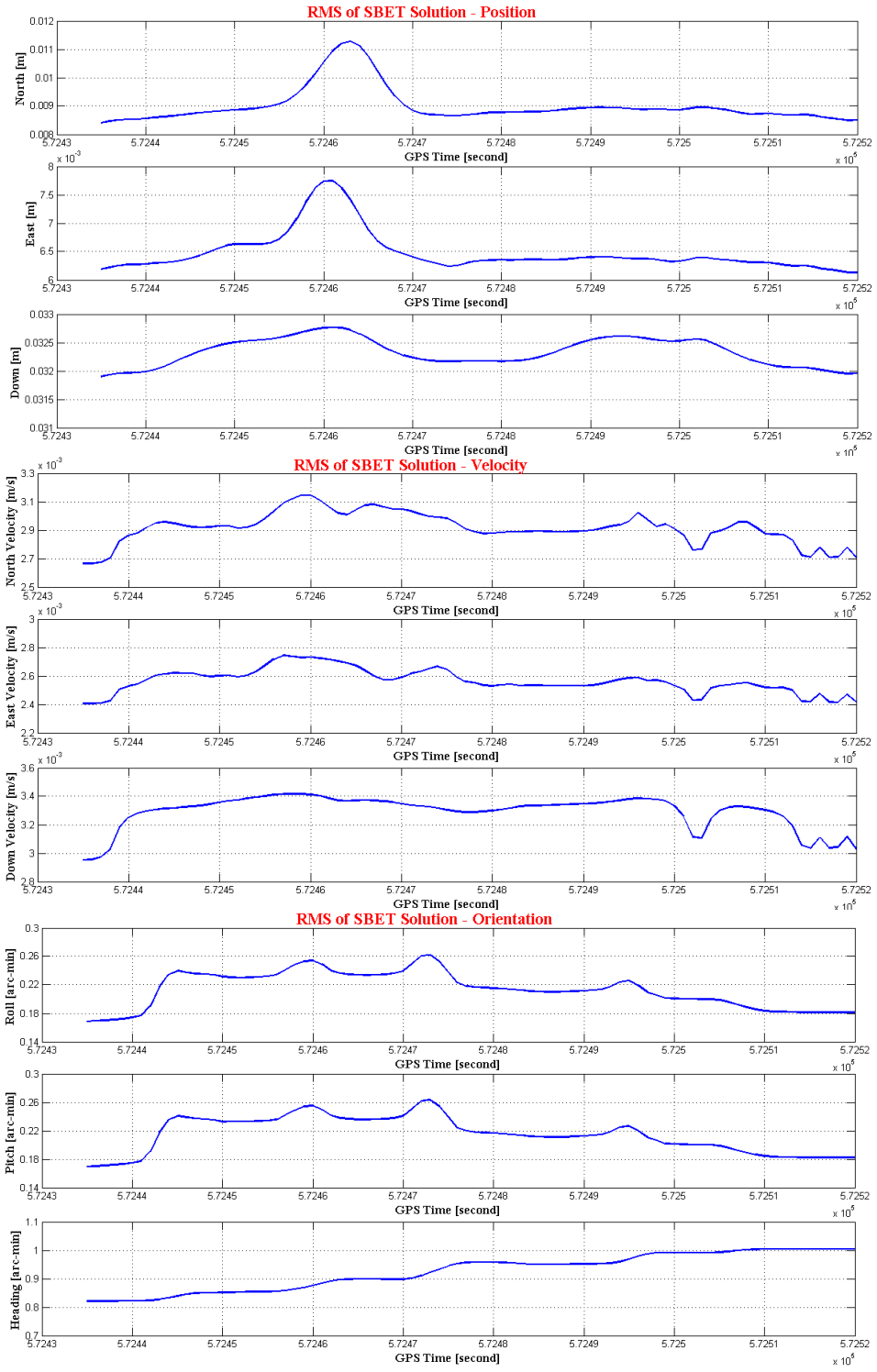

Figure 4-4: The RMS error of the position (north, east and down), orientation (roll, pitch and heading) and velocity (north, east and down) versus GPS time were presented in blue lines.

4.2.2.2 Control Network and Determination of GCPs and Features

The 3D geodetic control network built up the base on which all of the GCPs and features could be determined in the WGS84 ECEF coordinate system. It was established by using two Leica TC1800 total station systems along with a pair of Leica 1200 GPS receivers. The field work was completed in June 2012.

In the test scene, fifteen (15) control points were selected to construct the 3D geodetic control network through observing horizontal directions, vertical angles, slope distances, and GPS baselines. They were uniformly distributed in order to provide the sufficient observable access to the targets. To ensure an identical absolute position reference with the geodetic control network and the used Optech Lynx system, the Optech GPS reference station was chosen as the known initial point. The network configuration along with the GPS baseline measurements is shown in Figure 4-5.

As part of the instrument testing and calibration, the zero errors of the total stations associated with all of the targets (either the prisms or the sticker targets) were analytically determined for their EDM components using the four piers equipped with the forced centering system in the Engineering Laboratory of York University. The horizontal directions, the slope distances and the vertical angles were observed for at least three agreed full sets at each control point using the method of measurements by directions. Firstly, the station adjustment was performed to pick up the qualified measurements among all the observation sets. Then the slope distance measurements were corrected for zero error, meteorological effects concerning the pressure, temperature and humidity.

Ten control stations were occuiped twice, each for at least 15 minutes independently

by GPS receivers using the traditional static baseline approach. Together with the raw data logged at Optech reference GPS station, the post-processing resolved all the baselines at the cut-off anlge of 15° by using Lecia GeoOffice (v2.0).

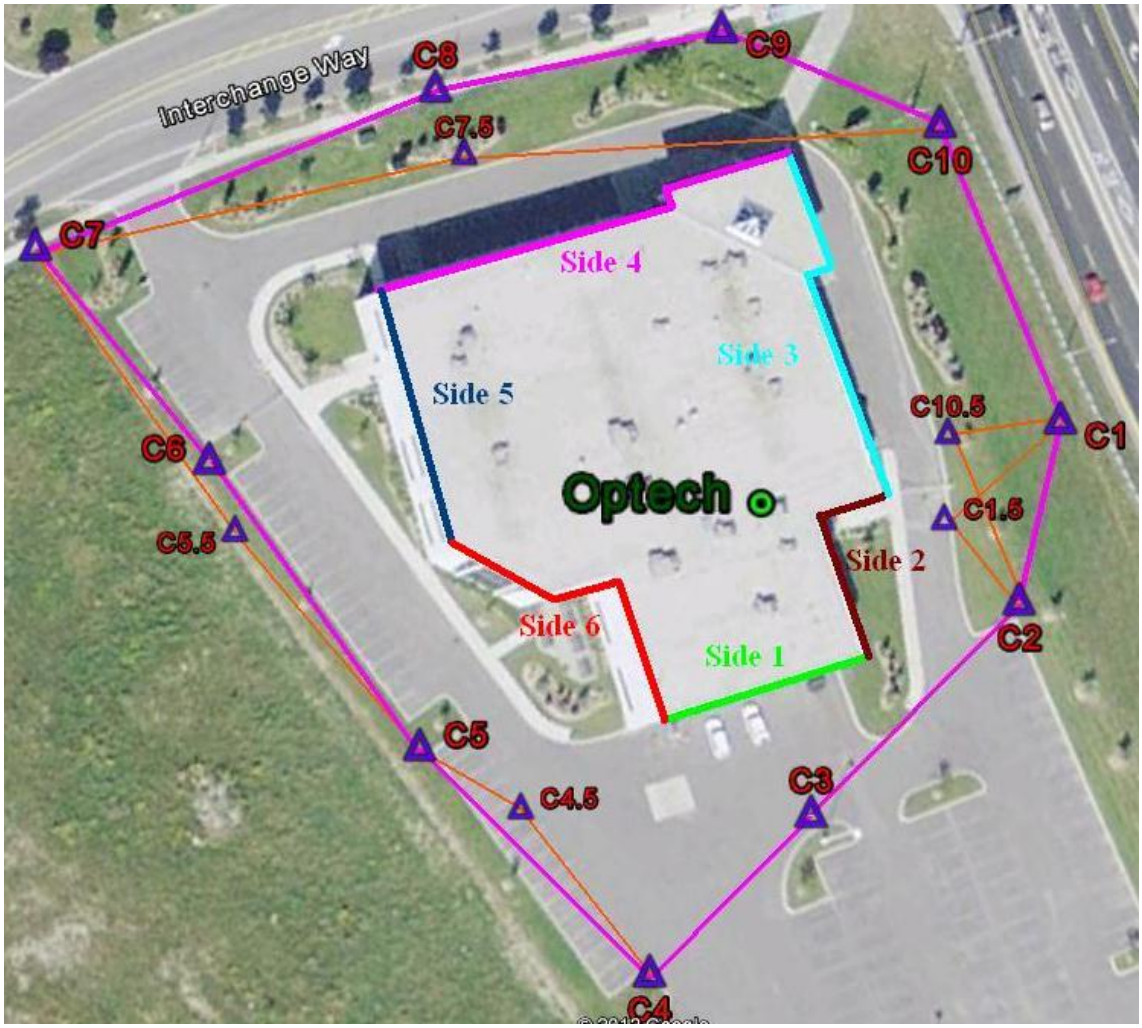

Figure 4-5: The 3D geodetic control network with the GPS baseline measurements of fifteen control points and the Optech GPS reference station. The observations were collected surround the headquarter office building of Optech Inc. in Vaughan, Ontario Canada, which was divided into six sides outlined in different colors for further data processing.

The 3D geodetic control network was adjusted using Columbus Best-Fit Computing Software, which is capable of integrating the various types of observations, inclusive of GPS baselines, horizontal directions, vertical angles, slope distances and other auxiliary data such as the instrument and target heights etc. In the 3D network adjustment, the GPS reference station at Optech was fixed as the only known point. With the 3D network adjustment, two specific issues were found and resolved as follows:

(1) Based on the pratical experience and consideration with the specific GPS receivers used in this project, the covariance matrices of individual baselines output from Leica GeoOffice were scaled by a factor of 100 to make the GPS baselines to an accuracy level of millimeters as the original variances were too optimisitc.

(2) According to the preliminary network adjustment results, most of the zenith anlges were identified as outliers because the vertical angle measurements apparently suffer from vertical refraction. Therefore, the trigonometric height differences for those sections with the rejected vertical angles were derived from their reciprocal observation and applied as measurements instead of the vertical angles.

Table 4-1 summarizes the adjusted geodetic coordinates of all the control points with the WGS84 datum. They reached the 3D postional accuracy of ±4mm (1σ) with all of the points. This accuracy level could provide realiable reference for the 3D coordinates of ground targets and features, because it was superior to the expected accuracy level of

LiDAR products of a few centimeters.

The characteristic targets and features were selected in the test scene to provide ground control points and geometrical constraints for the 3DCCT. Two types of the characteristic points around the building of Optech Inc. were chosen: the characteristic points on the building (for example, the roof corner and window corner), and the characteristic ground points located on the painting lines in the parking lot. Moreover, those ground targets were also used to determine the direction parameters of 3D lines and planar patch features. The characteristic points on north west side of the building were manually determined in point cloud (Figure 4-6).

Table 4-1: The adjusted geodetic coordinates of control points on WGS84 datum.

Station	**Latitude (N)**	**σ_N [mm]**	**Longitude (W)**	**σ_W [mm]**	**Ellipsoid Height[m]**	**σ_H [mm]**	**σ_{3D} [mm]**
C1	43 - 47 - 19.49564	1.4	79 - 31 - 27.07167	1.2	165.3221	2.5	3.1
C1.5	43 - 47 - 19.22693	1.7	79 - 31 - 27.68669	1.5	164.7455	2.6	3.4
C2	43 - 47 - 18.82524	1.4	79 - 31 - 27.74075	1.3	164.0153	2.5	3.1
C3	43 - 47 - 18.31980	1.4	79 - 31 - 29.34193	1.3	163.3035	2.5	3.1
C4	43 - 47 - 17.96290	1.4	79 - 31 - 30.51765	1.4	163.3367	2.5	3.2
C4.5	43 - 47 - 18.72493	2.5	79 - 31 - 31.03686	2.0	163.5944	2.6	4.0
C5	43 - 47 - 19.15572	1.4	79 - 31 - 31.29663	1.3	163.5611	2.5	3.1
C5.5	43 - 47 - 20.35116	1.6	79 - 31 - 31.73505	1.3	163.6636	2.5	3.2
C6	43 - 47 - 20.64020	1.5	79 - 31 - 31.89514	1.2	164.7352	2.6	3.2
C7	43 - 47 - 21.84475	1.5	79 - 31 - 32.46948	1.3	163.3915	2.4	3.1
C7.5	43 - 47 - 21.57670	1.4	79 - 31 - 29.82045	1.4	163.9123	2.5	3.2
C8	43 - 47 - 21.91644	1.3	79 - 31 - 29.84195	1.3	163.7594	2.5	3.1
C9	43 - 47 - 21.72559	1.4	79 - 31 - 28.03456	1.3	164.2299	2.5	3.1
C10	43 - 47 - 20.95281	1.4	79 - 31 - 27.00170	1.1	165.1111	2.4	3.0
C10.5	43 - 47 - 19.61899	1.7	79 - 31 - 27.73084	1.9	163.9041	2.6	3.6
Optech	**43 - 47 - 20.96747**	**-**	**79 - 31 - 29.97041**	**-**	**175.7830**	**-**	**fixed**

On one hand, the 3D ECEF coordinates of the selected targets on the building were determined using a total station system from two control points by applying 3D resection method. However, only horizontal direction and vertical angle measurements could be obtained due to the limitation of reflectance between the total station and natural targets. On the other hand, the 3D coordinates of a target on painting line were determined by using the prism mounted on a survey pole by two total station systems occupied over two control points. In this case, the slope distance measurements could be obtained to provide more redudant measurements.

Under the real working conditions in the test scene, 137 characteristic targets were surveyed in total: 86 building points and 51 ground points, which generated 12 straight line and 7 planar patch features as shwon in Figure 4-7. The number of GCPs and features surround six sides of the building are summarized in Table 4-2.

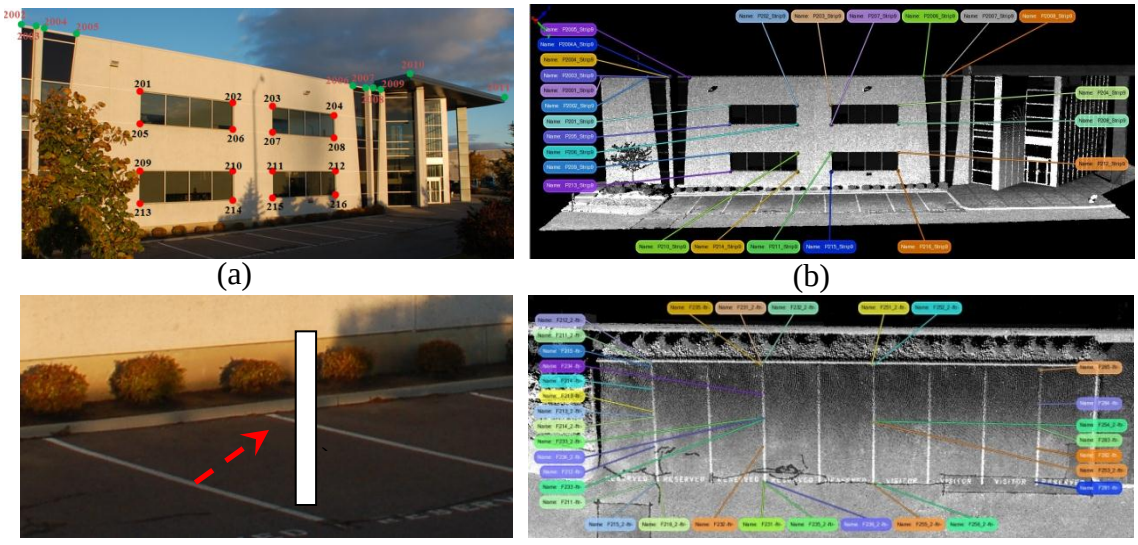

(a) (b)

(c) (d)

Figure 4-6: The location of two kind's nature points from north-west side of Optech building. (a) - (b) The window corner and roof corner from digital camera image and the corresponding LiDAR point cloud, respectively. (c) - (d) The planar patch feature extracted from painting pavements from digital camera image and the corresponding LiDAR point cloud, respectively.

The first field surveying mission of the in-scene selected characteristic targets was completed in June 2012. To validate the results of the estimated coordinates, another field surveying mission was introduced to emphasise on the north west side of the building (i.e., side 2) in June 2013. The estimated ECEF (Earth Center and Earth Fixed) coordinates of all 137 charactersitic points from six building sides were attached in Appendix A. Overall, the standard deviation in 3D was within ±6mm for all of the tragets, which satisified the design specification.

Table 4-2: The number of GCPs and features around the Optech Inc. building

Station	GCPs		Features	
	Building Type	Ground Type	Line	Plane
Side 1	12	0	0	0
Side 2	22	33	8	4
Side 3	24	18	4	3
Side 4	12	0	0	0
Side 5	14	0	0	0
Side 6	2	0	0	0
Total	**86**	**51**	**12**	**7**

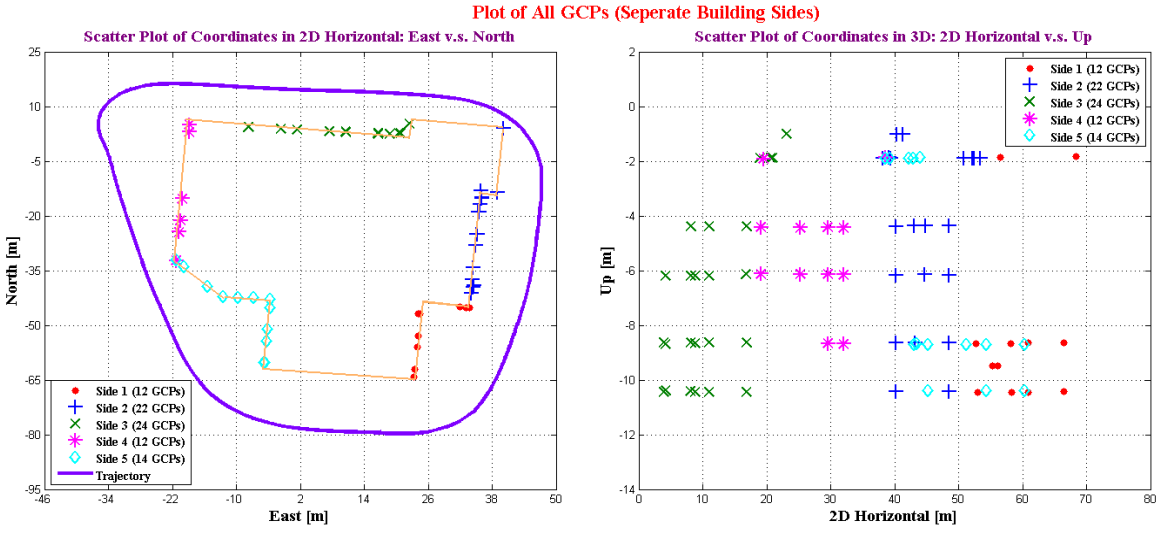

Figure 4-7: Scatter plot of GCPs and feature constraints around the Optech's building. Different colors were selected to represent the control points of individual sides in 2D Horizontal and vertical.

4.2.3 Utilization of Ground Control Points

4.2.3.1 Segmental 3D Conformal Coordinate Transformations (3DCCT)

The test data acquired around the Optech's building was divided into six parts per outer wall of the building (see Fig. 4-5). Thus, the 3DCCT parameters were determined separately for each side so as to compensate for the different natures and amplitudes of some of the systematic errors in the different parts of the LiDAR data strip. In practice, the local Noprth-East-Up coordinates of the targets with respect to the Optech GPS reference station were used in the implementation of 3D conformal coordiante transformation.

There were 86 control points evenly distributed on the six sides of the building. However, only two control points were observed on side 6 so that this side was excluded. Approximately 40 percent of the control points selected from each of the five building sides were involved in 3DCCT, and the rest GCPs were left as checking points for accuracy assessment. The numbers of the GCPs used in conformal transformations and accuracy validation are summarized in Table 4-3, whilst the scatter plot of the GCPs distribution is shown in Figure 4-8.

Table 4-3: The number of used and checking GCPs for each building side.

	# of Used GCPs	**# of Checking GCPs**
Side 1	5	7
Side 2	9	13
Side 3	10	14
Side 4	5	7
Side 5	6	8
Total	**35**	**49**

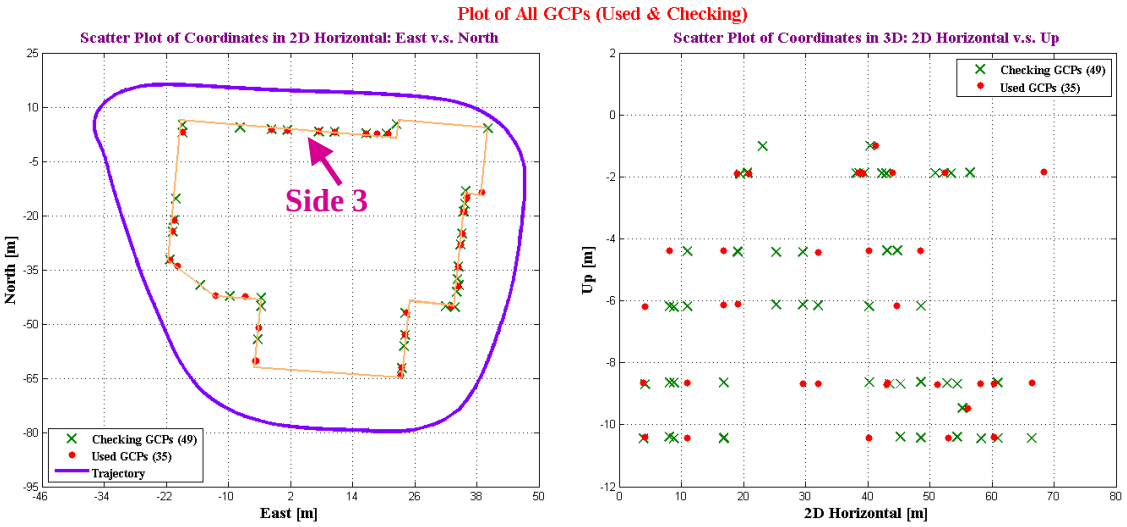

Figure 4-8: Scatter plot of 84 GCPs (49 Used in conformal transformations & 35 used in validation) distributed on five sides of testing scene in 2D horizontal and vertical.

Through the checking GCPs, the extent of the accuracy improvements was compared using all 35 GCPs from five sides together against using GCPs only from the individual sides for each building side. Building side 3 was chosen as an example to illustrate the results of this scenario, and 10 GCPs from this segment were involved in the 3D conformal transformation. Figure 4-9 represents the scatter plot of 14 checking GCPs of side 3 in both 2D horizontal and vertical. By taking the enlarged snapshots of two checking points "P308" and "P317" as examples, the adjusted LiDAR coordinates using the transformation parameters only based on 10 GCPs from side 3 (pink star) was closer to the pre-surveyed coordinates (red dot) comparing with the adjusted LiDAR coordinates using the transformation parameters based on all 35 GCPs (blue cross) in 3D. By considering the pre-surveyed coordinates as references, the differences serve as a measure of the errors in the coordinates from LiDAR data. From the numerical results in Table 4-5, even though the differences decreased for both two cases, the errors using 10

GCPs only from side 3 were smaller and the performance was improved ca. 1.5cm in 3D comparing with the ones using all 35 GCPs from five sides together.

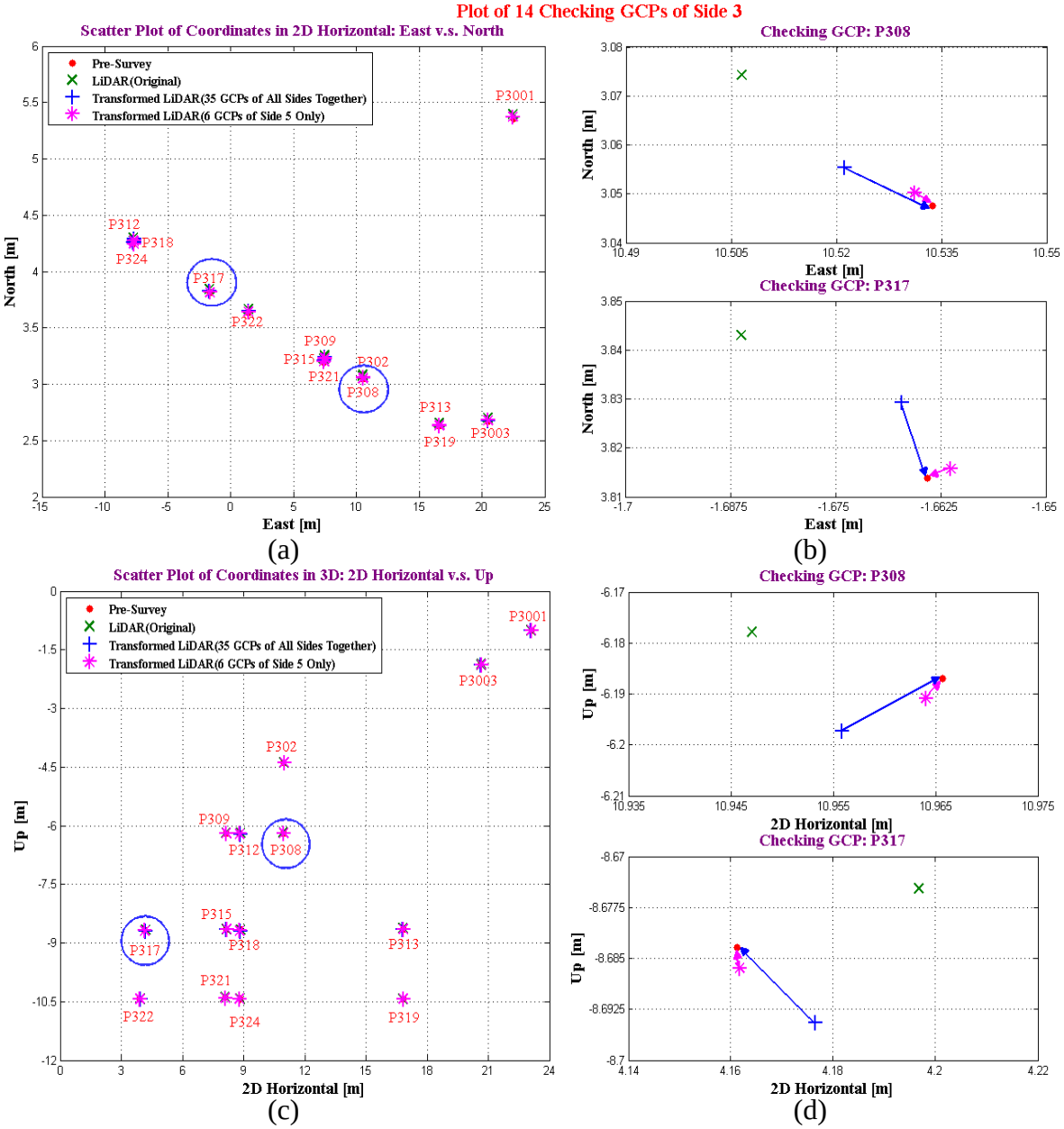

Figure 4-9: Scatter plot of 14 checking GCPs on building side 3. The adjusted LiDAR coordinates using 35 GCPs on five sides and 10 GCPs on side 3 only were presented in blue cross and pink star, respectively. (a) & (c) 2D horizontal and vertical. (b) & (d) Close-up details of "P308" and "P317".

Table 4-4: The differences between the pre-surveyed coordinates and the original LiDAR coordinates, the adjusted LiDAR coordinate using 35 GCPs and 10 GCPs, respectively, from two checking points "P308" and "P317".

ID	Original Differences [cm]					With 35 GCPs of all sides [cm]					With 10 GCPs of side 3 [cm]				
	N	E	2D	U	3D	N	E	2D	U	3D	N	E	2D	U	3D
P308	-2.68	2.72	3.82	-2.20	4.41	-0.78	1.25	**1.47**	**1.04**	**1.80**	-0.28	0.25	**0.38**	**0.39**	**0.54**
P317	-2.91	2.21	3.65	-2.23	4.28	-1.54	0.30	**1.57**	**1.11**	**1.92**	-0.18	-0.28	**0.33**	**0.30**	**0.45**

To characterize the differences between the pre-surveyed coordinates and the adjusted LiDAR coordinates (i.e., the discrepancies of the adjusted coordinates with respect to their pre-surveyed coordinates) under these two scenarios with side 3, a number of the overall quantitative indexes were calculated inclusive of the minimum, maximum, mean, standard deviation and RMS (root mean square) in Appendix B-1. Statistical tests were employed to determine if the errors were significantly biased (i.e., if the mean value was significantly different from zero), and if the errors were significantly larger than the requirements (i.e., if the standard deviation or RMS calculated from the errors was significantly larger than the given accuracy requirement).

Specifically, a *t*-test statistics (Neter et al, 1988) was built up to test if a mean error value *m* was significantly different from zero under the null hypothesis $H_0 : m = 0$ vs. the alternate hypothesis $H_a : m \neq 0$:

$$t = \frac{\hat{m}}{\hat{\sigma}_{\hat{m}}} = \frac{\hat{m}}{\hat{\sigma}}\sqrt{n} \sim t_{n-1} \tag{4-1}$$

wherein $\hat{m}$ is the mean value of a group error samples;

$\hat{\sigma}_{\hat{m}}$ is the standard deviation of mean value $\hat{m}$, where $\hat{\sigma}_{\hat{m}} = \hat{\sigma}/\sqrt{n}$;

$\hat{\sigma}$ is the standard deviation of a group error samples;

n is the number of the samples;

t_{n-1} is a t-test with the degrees of freedom of $n-1$.

Furthermore, a χ^2-test statistics (Neter et al, 1988) was constructed to statistically conclude if a sample standard deviation σ was satisfied with the specific required accuracy level under the hypothesis

$$H_0 : \sigma^2 = \sigma_0^2 \tag{4-2}$$

$$H_a : \sigma^2 > \sigma_0^2 \quad \text{or} \quad \sigma^2 \neq \sigma_0^2 \tag{4-3}$$

The χ^2 test value was denoted as

$$\chi^2 = \frac{\hat{\sigma}^2}{\sigma_0^2}(n-1) \sim \chi_{n-1}^2 \tag{4-4}$$

wherein σ_0 is a given standard deviation that indicates a required accuracy level, and χ_{n-1}^2 is the Chi-square test with the degrees of freedom of $n-1$.

According to engineering survey manuals, e.g., from Ministry of Transportation of Ontario (MTO, 2006), the **1.5*cm*** horizontal and vertical accuracy criterion at the 95% confidence level was applied in the accuracy evaluation. If the test in (4-4) is rejected at a specific error level of Type I Error, one can choose different alternate value σ_a^2, as a substitution of σ_0^2, to find the lower bound that can pass the test in (4-4), which is called the achieved accuracy with the involved samples.

Similarly, this test statistics can also be applied to the RMS value of a group of samples. All of the statistic tests in the accuracy assessment in this study were performed at the 5% significance level of Type I Error. Table 4-5 presents a summary of statistic *t*-test and alternate χ^2-test of the differences between the pre-surveyed coordinates and the

original LiDAR coordinates, the adjusted LiDAR coordinates using all 35 GCPs from five sides together and using only 10 GCPs from only side 3, respectively, with the 14 checking GCPs.

Based on the two-tailed *t*-test, the differences between the pre-surveyed and the original LiDAR coordinates contained significant biases in north, east and up directions. After the adjustment using the parameters derived from the conformal transformation, the mean of the errors became not significantly different from zero for both the scenarios using all 35 GCPs from five sides together and using 10 GCPs from side 3 only.

The achieved accuracies were ±4.1cm (horizontal) and ±2.5cm (vertical) at the 95% confidence level before the introduction of 3D conformal transformation according to the alternate χ^2-test. Using all 35 GCPs from five sides together, the vertical accuracy has improved to ±2.0cm, as it only achieved an accuracy of ±2.8cm in horizontal. Further, for case 3 where only 10 GCPs were used for side 3, the achieved horizontal accuracy was further increased from ±4.1cm to ±2.3cm, and the vertical accuracy was increased to ±1.8cm based on the χ^2-test at the 5% significant level.

The comparisons among the three testing cases indicated that the 3D conformal transformation using GCPs from side 3 only allows achieving better accuracies in both horizontal and vertical directions. In addition, the conclusions were verified through implementing the similar process and statistics tests for the rest of four building sides. Therefore, it is necessary to segment the LiDAR strip into smaller portions and determine their own transformation parameters separately. That is, the 3D conformal transformation may not be valid for a large stretch of data in practice.

Table 4-5: The statistical analysis of the differences between the pre-surveyed coordinates and the original LiDAR coordinates, the adjusted LiDAR coordinates through the 3DCCT using all 35 GCPs on five sides and 10 GCPs on side 3 only, respectively, from 14 checking GCPs on building side 3.

		Error Statistics				**Two-tailed *t*-test (α =0.05%) H_0: $\mu = 0$**			**χ^2 Test (α = 0.05%) vs. the 95% accuracy H_0: $\sigma^2 = 1.5^2 cm^2$**			**H_1: $\sigma^2 = \sigma_a^2$**		
Case No.*	Error	Mean [cm]	Stdev [cm]	RMS [cm]	f	t	$t_{f,0.025}$	Accepted (Y/N)	χ^2	$\chi^2_{f,0.05}$	Accepted (Y/N)	σ_a [cm]	χ^2	Accepted (Y/N)
1	**N**	-1.80	2.03	2.65	13	-3.31	2.160	N						
	E	1.48	1.72	2.22	13	3.21	2.160	N						
	U	-1.25	1.67	2.04	13	-2.81	2.160	N	61.73	22.36	N	**2.5**	22.22	Y
	2D(H)	2.33	2.66	3.46	13				163.63	22.36	N	**4.1**	21.90	Y
2	**N**	-0.62	1.21	1.32	13	-1.92	2.160	Y						
	E	0.65	1.38	1.48	13	1.77	2.160	Y						
	U	0.68	1.31	1.43	13	1.93	2.160	Y	38.07	22.36	N	**2.0**	21.41	Y
	2D(H)	0.90	1.83	1.98	13				77.69	22.36	N	**2.8**	22.30	Y
3	**N**	-0.46	0.99	1.06	13	-1.73	2.160	Y						
	E	-0.48	1.13	1.19	13	-1.58	2.160	Y						
	U	-0.34	1.19	1.20	13	-1.06	2.160	Y	31.57	22.36	N	**1.8**	21.93	Y
	2D(H)	0.66	1.51	1.59	13				52.41	22.36	N	**2.3**	22.29	Y

***Note:**

- Case 1: The differences between the pre-surveyed coordinates and the original LiDAR coordinates.
- Case 2: The differences between the pre-surveyed coordinates and the adjusted LiDAR coordinates derived from using all 35 GCPs on five sides.
- Case 3: The differences between the pre-surveyed coordinates and the adjusted LiDAR coordinates derived from using 10 GCPs on side 3 only.

4.2.3.2 Categorization of Ground Control Points Concerning Horizontal and Vertical Accuracy Improvements

In this section, the control points were categorized into building and ground types because the effects of some systematic errors in the 3D LiDAR positioning may not be uniform in horizontal and vertical directions. There were 38 control points for side 2 of the testing scene, including 26 building-type and 12 ground-type points, respectively. The location of two kinds of the target points were manually extracted from the LiDAR point cloud using PolyWorks software (Figure 4-10 (a) and (b)). Half of them from each type were used in 3D conformal transformation. The plot of all GCPs from side 2 of the building is presented in Figure 4-11.

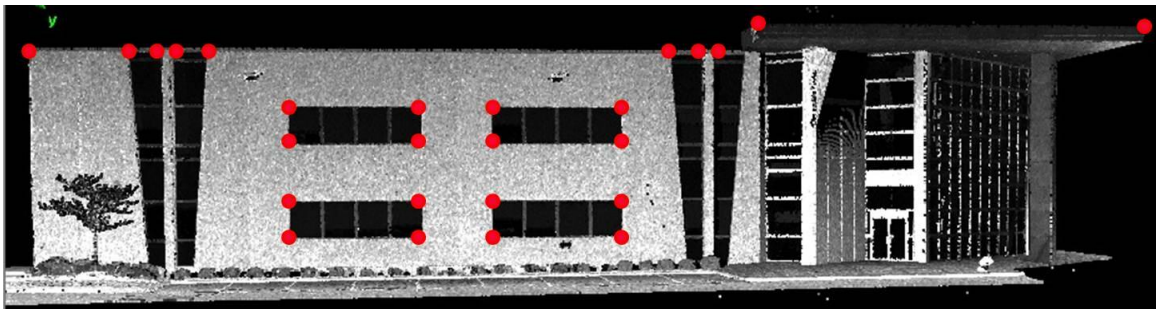

(a)

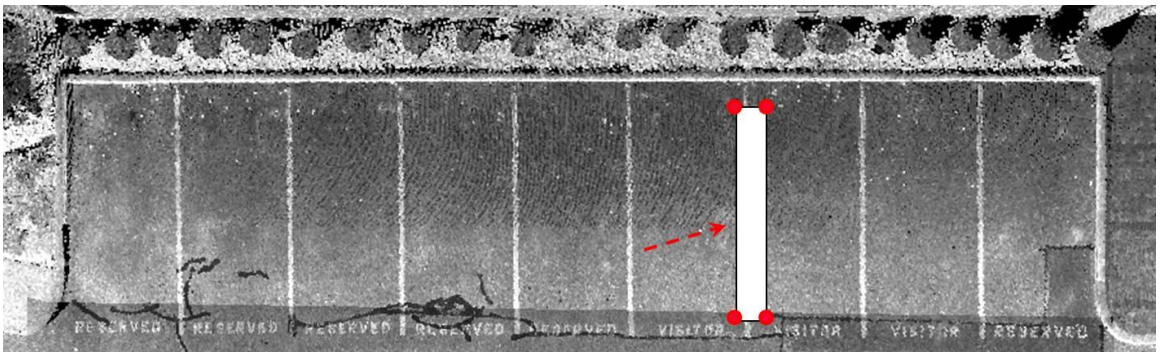

(b)

Figure 4-10: The location of two types of GCPs determined in the point cloud. (a) Building-type. (b) Ground-type.

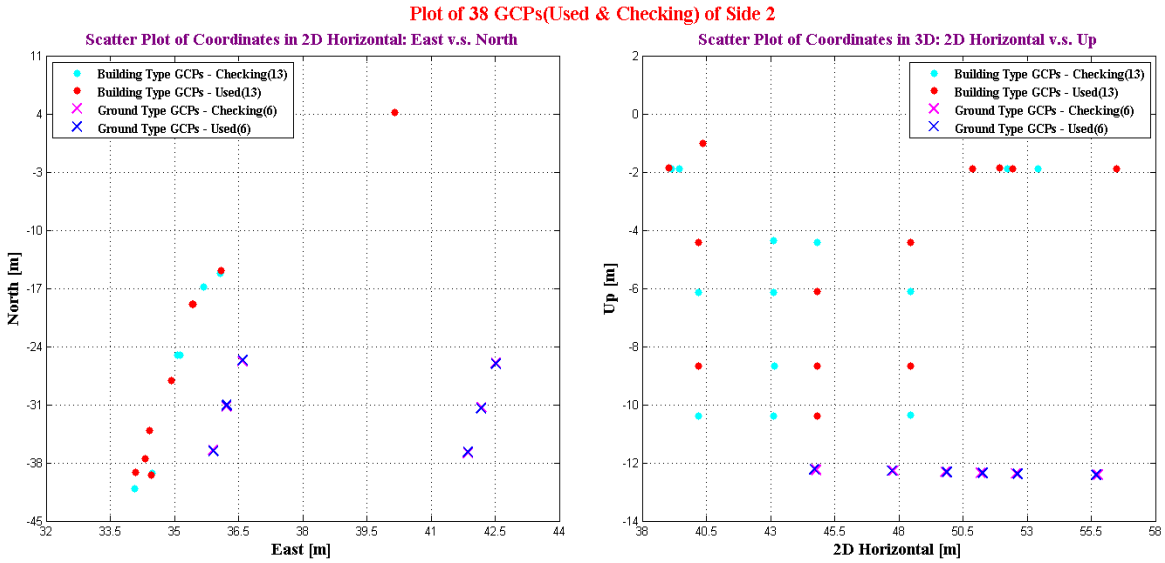

Figure 4-11: Scatter plot of 38 GCPs distributed on side 2 of testing scene in 2D horizontal and vertical. There are 26 building-type and 12 ground-type GCPs presented in dot and cross, respectively. Different colors were selected to illustrate the used and checking control points.

The performance with the checking GCPs was compared through using the same type of the GCPs against using opposite type and mixed-type of the GCPs. Figure 4-12 presents the scatter plot of 38 checking GCPs (26 building-type & 12 ground-type) on the building side 2 in both 2D horizontal and vertical directions. By taking the enlarged snapshots of two checking points "P205" (building-type) and "F251" (ground-type) as examples, the adjusted LiDAR coordinates using the parameters based on same type of GCPs was the closest ones to the pre-surveyed coordinates (red dot) in 3D, while the ones using the different type of the GCPs were the furthest, and the ones using the mixed types of the GCPs (cyan diamond) fell in between. By considering the pre-surveyed points as the reference coordinates, the coordinate differences could measure the quality of the LiDAR data. Based on the numerical results in Table 4-6, the errors just based on the 3DCCT using 6 control points on the ground were the biggest (3.63cm in 3D) for the

building-type checking GCP “P205”. Similarly, the errors based on the conformal transformation using 13 control points on the building were the largest (3.07cm in 3D) for the ground-type checking GCP “F251”. Moreover, the performance was improved by 2cm (1σ) in 3D with the same building-type GCPs.

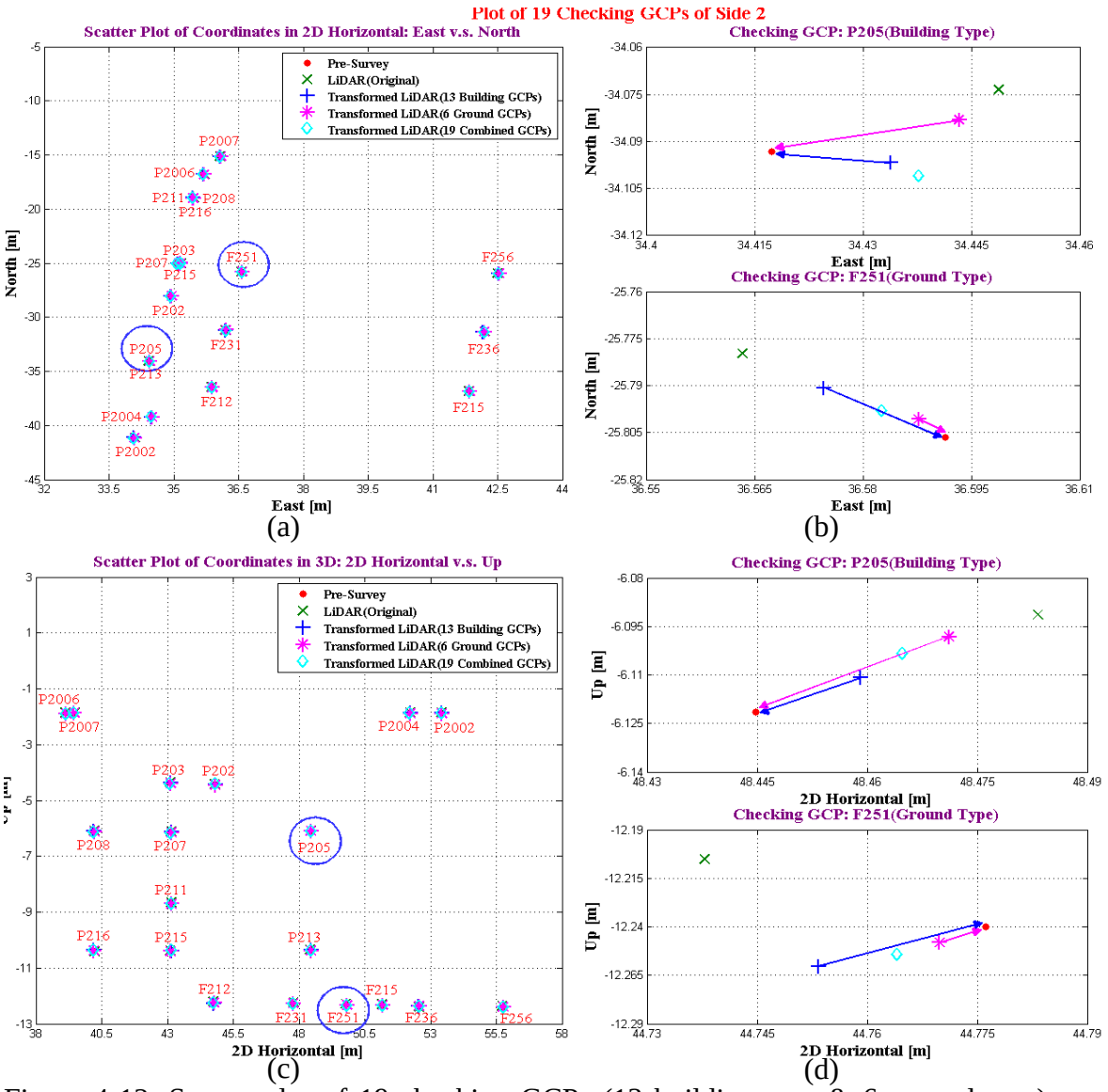

Figure 4-12: Scatter plot of 19 checking GCPs (13 building-type & 6 ground-type) on side 2. The adjusted LiDAR coordinates using 13 building-type GCPs, 6 ground-type GCPs and 19 mixed-type GCPs were presented in blue cross, pink star and cyan diamond, respectively. (a) & (c): 2D horizontal and vertical. (b) & (d): Close-up details of “P205” and “F251”.

Table 4-6: The differences between the pre-surveyed coordinates and the adjusted LiDAR coordinates using 13 building-type GCPs, 6 ground-type GCPs and 19 mixed-type of GCPs, respectively, from two checking points "P205" and "F251".

ID	With Building-type GCPs [cm]					With Ground-type GCPs [cm]					With Mixed-type GCPs [cm]				
	N	E	2D	U	3D	N	E	2D	U	3D	N	E	2D	U	3D
P205	0.36	-1.64	**1.68**	**-1.06**	**1.99**	-1.01	-2.59	**2.78**	**-2.33**	**3.63**	0.77	-2.04	**2.18**	**-1.82**	**2.84**
F251	-1.56	1.68	**2.29**	**2.04**	**3.07**	-0.56	0.37	**0.67**	**0.79**	**1.04**	-0.84	0.88	**1.22**	**1.39**	**1.85**

The building-type checking GCPs were chosen to illustrate the results under this scenario. The overall quantitative indexes inclusive of the minimum, maximum, mean, standard deviation and RMS were calculated and summarized in Appendix B-2. Furthermore, the *t*-test was constructed to determine if the errors were significantly biased and χ^2-test statistics to conclude if the standard deviation was satisfied with the required accuracy of 1.5cm. Table 4-7 presents the statistic results of different testing cases.

Based on the results of two-tailed *t*-test, the differences between the pre-surveyed and the original LiDAR coordinates contained significant biases in north, east and up directions. After the removal of some of the systematic errors based on the 3D conformal transformation, the mean value of the errors was not significantly different from zero using the same type of GCPs. However, the errors still contained significant biases if the different type of control points was used to perform the accuracy assessment, which clearly tells how important it is for us to attempt at appropriately characterize or model the effects of some of the remaining systematic errors on the LiDAR solution in order to reach accuracy improvement.

After the χ^2-test, the achieved accuracies of the original LiDAR solution were

±4.0cm (horizontal) and ±2.8cm (vertical) at the 95% confidence level of the Type I error. For case 2 where the same type of control points was used in 3DCCT, the vertical accuracy was improved up to ±1.7cm, and the achieved horizontal accuracy was ±2.2cm at the 95% confidence level. However, it only achieved an accuracy of ±3.0cm in horizontal and ±2.3cm in vertical for case 3 where the checking control points are not the same type as the control points used 3DCCT. Its performance was the worst among all the testing cases, and the adjustment could not make significant accuracy improvement. For case 4, the achieved horizontal accuracy was of ±2.6cm and vertical accuracy was of ±2.1cm after the adjustment on the basis of 19 GCPs on the ground and building based on the χ^2-test at the 95% significant level. Apparently, none of the testing cases could meet the pre-defined accuracy requirement (±1.5cm).

The comparisons among the four testing cases indicated that the adjustment after 3DCCT could achieve the best accuracy for a specific type of LiDAR points (e.g., on the building or on the ground) using the same type of control points in horizontal or vertical direction. The adjustment of a specific type of LiDAR points through the different type of GCPs may only lead to the very limited accuracy improvement. The performance of the adjusted LiDAR points using the mixed-type GCPs fell in between. Furthermore, the similar conclusions can be drawn with the ground-type checking GCPs. Hence, the categorization of the control points is necessary for ensuring an appropriate introduction of conformal coordinate transformation so that the effects of some of the remaining systematic errors can effectively be removed.

Table 4-7: The statistical analysis of the differences between the pre-surveyed coordinates and the original LiDAR coordinates, the adjusted LiDAR coordinates after the 3DCCT using 13 building-type GCPs, 6 ground-type GCPs and 19 mixed-type GCPs, respectively, from 13 building-type checking GCPs.

		Error Statistics				**Two-tailed *t*-test (α =0.05%) H_0: $\mu = 0$**			**χ^2 Test (α = 0.05%) vs. the 95% accuracy H_0: $\sigma^2 = 1.5^2 cm^2$**			**H_1: $\sigma^2 = \sigma_a^2$**		
Case No.*	Error	Mean [cm]	Stdev [cm]	RMS [cm]	f	t	$t_{f,0.025}$	Accepted (Y/N)	χ^2	$\chi^2_{f,0.05}$	Accepted (Y/N)	σ_a [cm]	χ^2	Accepted (Y/N)
1	**N**	-1.47	1.96	2.38	12	-2.71	2.179	N						
	E	-1.54	1.74	2.27	12	-3.20	2.179	N						
	U	-1.83	1.86	2.56	12	-3.55	2.179	N	70.87	21.03	N	**2.8**	20.34	Y
	2D(H)	2.13	2.61	3.29	12				145.83	21.03	N	**4.0**	20.51	Y
2	**N**	-0.10	1.02	0.98	12	-0.34	2.179	Y						
	E	-0.41	1.00	1.04	12	-1.47	2.179	Y						
	U	-0.47	1.15	1.20	12	-1.49	2.179	Y	26.96	21.03	N	**1.7**	20.99	Y
	2D(H)	0.42	1.42	1.43	12				43.17	21.03	N	**2.2**	20.07	Y
3	**N**	-0.84	1.51	1.68	12	-2.01	2.179	N						
	E	-1.76	1.24	2.12	12	-5.14	2.179	N						
	U	0.65	1.54	1.61	12	1.52	2.179	Y	48.40	21.03	N	**2.3**	20.58	Y
	2D(H)	1.95	1.95	2.71	12				81.23	21.03	N	**3.0**	20.31	Y
4	**N**	-0.09	1.24	1.19	12	-0.26	2.179	Y						
	E	-0.52	1.19	1.26	12	-1.56	2.179	Y						
	U	-0.57	1.41	1.47	12	-1.46	2.179	Y	40.50	21.03	N	**2.1**	20.67	Y
	2D(H)	0.52	1.72	1.73	12				62.96	21.03	N	**2.6**	20.96	Y

***Note:**

- Case 1: The differences between the pre-surveyed coordinates and the original LiDAR coordinates.
- Case 2: The differences between the pre-surveyed coordinates and the adjusted LiDAR coordinates derived from using 13 building-type GCPs.
- Case 3: The differences between the pre-surveyed coordinates and the adjusted LiDAR coordinates derived from using 6 ground-type GCPs.
- Case 4: The differences between the pre-surveyed coordinates and the adjusted LiDAR coordinates derived from using 19 mixed-type GCPs.

4.2.4 Utilization of Feature Constraints

By only involving ground control points, the accuracy of the adjusted solution after the seven parameters 3DCCT cannot meet the pre-defined accuracy requirement of ±1.5cm based on the previous testing results in Section 4.2.3. Thus, the straight line and plane feature constraints were added toward further accuracy improvement in this section. For building side 2 of the scanned scene, there were 8 straight lines and 4 planar patch features besides 38 pre-surveyed GCPs (26 building-type and 12 ground-type) shown in Figure 4-13. Half of them were selected as the mixed-type GCPs applied in the 3DCCT.

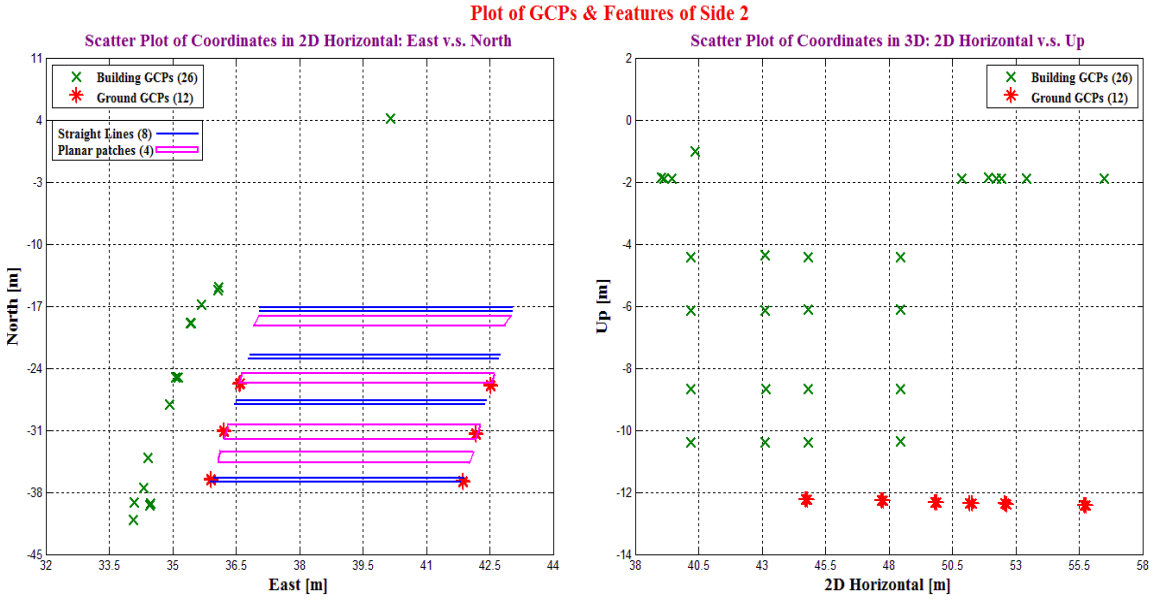

Figure 4-13: Scatter plot of 38 GCPs and 12 features distributed on building side 2 of the scanned scene in 2D horizontal and vertical.

The accuracy improvement of the 19 checking GCPs, based on the 3DCCT aided by line and planar features, was analysed. The results are partially presented in Figure 4-14. By taking the enlarged snapshots of two checking points “P205” (building-type) and

"F231" (ground-type) as examples, the adjusted LiDAR coordinates after the 3DCCT using the GCPs with the feature constraints (pink star) were closer to the pre-surveyed coordinates (red dot) in comparison with the adjusted LiDAR coordinates after the one only using the GCPs (blue cross). By taking the pre-surveyed coordinates as reference coordinates, the derived differences reflected the errors in the coordinates from the adjusted LiDAR data. Based on the numerical results in Table 4-8, the coordinate errors of the adjusted LiDAR points based on the GCPs incorporating with feature constraints were much smaller than the ones based on only the GCPs. The performance was improved by around 1cm in 3D.

Table 4-8: The differences between the pre-surveyed coordinates and the adjusted LiDAR coordinates using GCPs only and GCPs with features, from two checking points: "P205" (building-type) and "F231" (ground-type).

ID	Original Differences [cm]					With GCPs only [cm]					With GCPs and features [cm]				
	N	E	2D	U	3D	N	E	2D	U	3D	N	E	2D	U	3D
P205	-1.98	-3.14	**3.71**	**-3.01**	**4.78**	0.77	-2.04	**2.18**	**-1.82**	**2.84**	0.48	-1.34	**1.42**	**-0.87**	**1.67**
F231	1.60	2.98	**3.38**	**-2.97**	**4.50**	0.96	1.21	**1.54**	**-1.19**	**1.95**	0.75	0.65	**0.99**	**-0.78**	**1.26**

Furthermore, 15 points were chosen from each feature constraint in the original mobile LiDAR solution. The corresponding adjusted coordinates were calculated using 7 parameters derived from GCPs aided by feature constraints. The scatter plot of the original and adjusted coordinates of the LiDAR points against the pre-determined straight line #2 and planar patch #4 were illustrated as examples in Figure 4-15 and Figure 4-16, respectively. Based on the plot in 2D horizontal (Figure 4-15(b)), the adjusted coordinates using feature constraints (green cross) were closer to the pre-determined straight line comparing with their original coordinates (pink star). The similar result was achieved

according to Figure 4-16(b) for planar patch #4. In addition, the RMS was calculated using the discrepancies from the original and adjusted LiDAR points to the feature constraints, and the results were summarized in Table 4-9. The RMS after the 3D conformal transformation was much smaller than the ones from the original LiDAR solution. For example, the RMS was improved from ±4.3cm to ±2.2cm for straight line #2. Therefore, it verified that the feature constraints incorporating with GCPs could further improve the accuracy of LiDAR point cloud.

Table 4-9: RMS of original and adjusted LiDAR points to the feature constraints.

Feature	RMS (Original) [cm]	RMS (After LSM) [cm]
Straight Line #1	3.9	2.3
Straight Line #2	4.3	2.2
Straight Line #3	4.1	2.5
Straight Line #4	4.0	1.9
Straight Line #5	3.8	2.6
Straight Line #6	3.9	2.4
Straight Line #7	4.2	2.4
Straight Line #8	4.0	2.3
Plane #1	3.7	2.1
Plane #2	3.8	2.2
Plane #3	3.9	1.8
Plane #4	4.1	2.5

Appendix B-3 summarizes the calculated quantitative indexes inclusive of the minimum and maximum errors, the mean, the standard deviation and the RMS from 19 checking GCPs on the building side 2. Moreover, the *t*-test and χ^2-test were constructed, and the statistic results of the different cases are summarized in Table 4-10. Based on the two-tailed *t*-test, the differences between the pre-surveyed and the original LiDAR

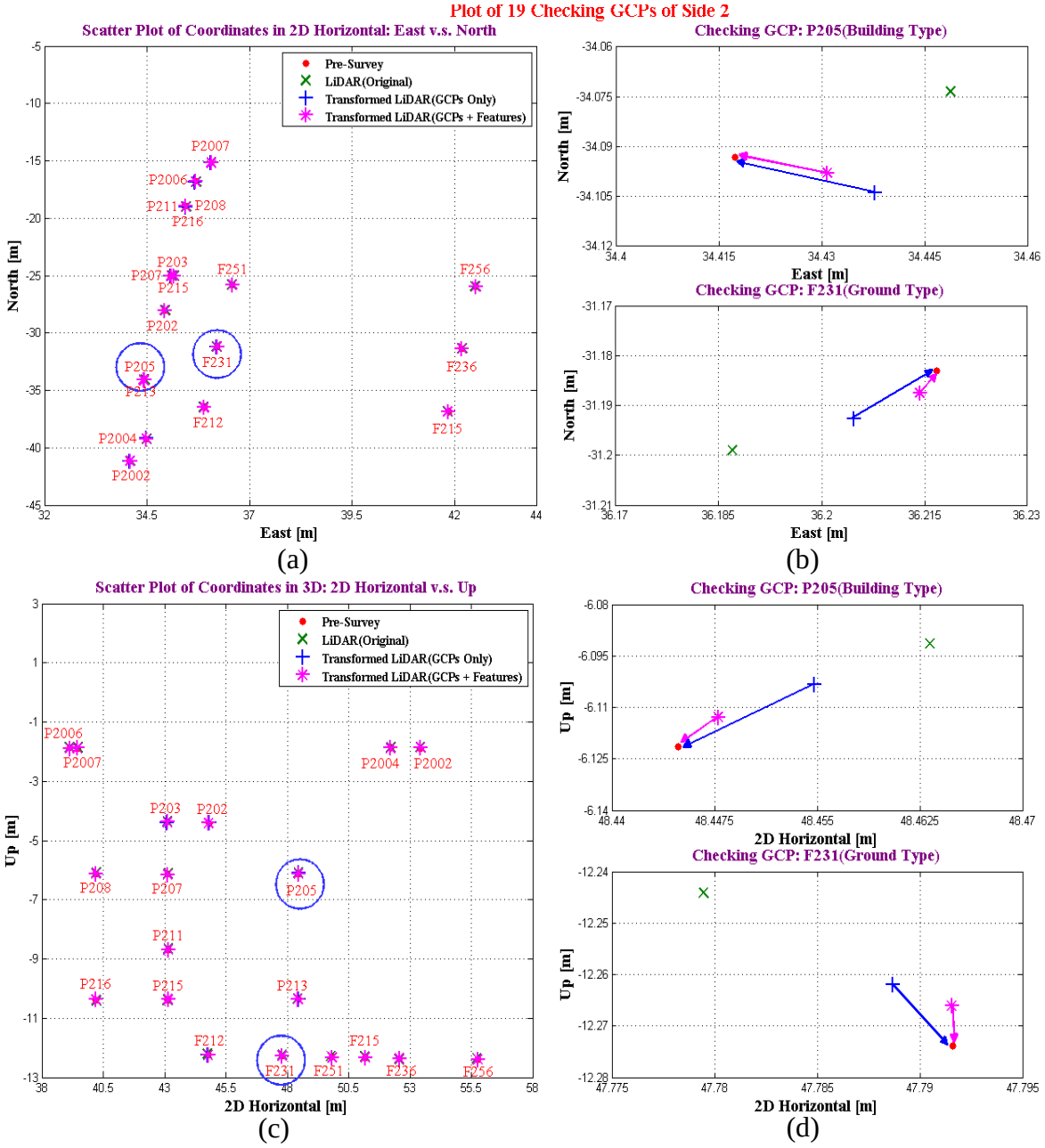

Figure 4-14: Scatter plot of 19 checking GCPs (13 building-type & 6 ground-type) on building side 2. The adjusted LiDAR coordinates using the mixed-types of GCPs with the feature constraints and using GCPs only were presented in pink star and blue cross, respectively: (a) & (c) 2D horizontal and vertical; (b) & (d) Close-up details of "P205" and "F231".

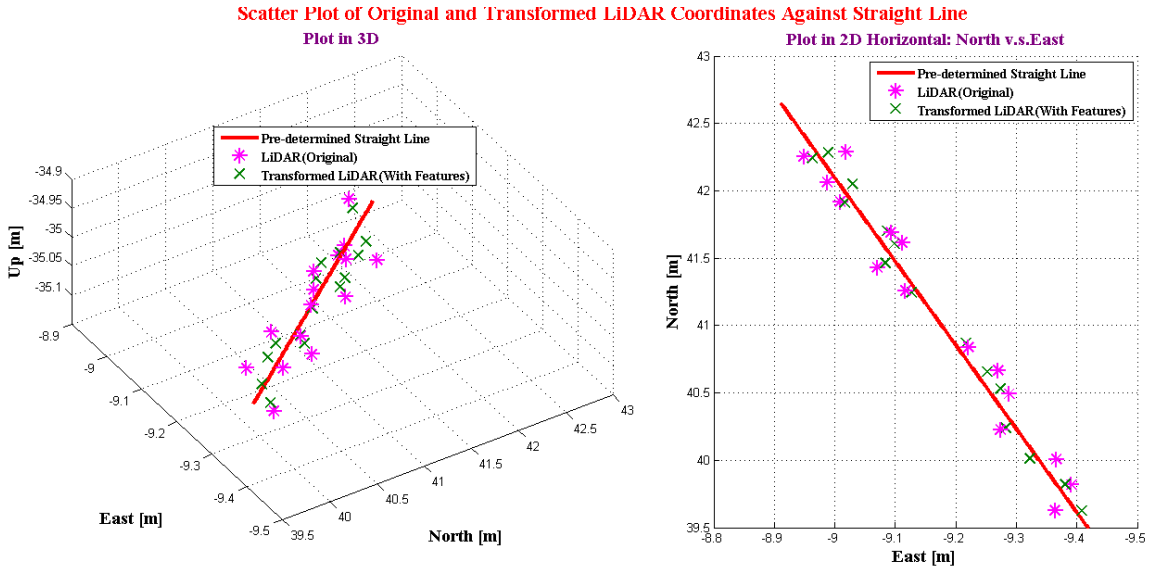

Figure 4-15: Scatter plot of 15 original and adjusted LiDAR points against a straight line constraint in 2D horizontal and 3D. The line in red was determined using pre-surveyed GCPs. 15 selected points from the original mobile LiDAR solution were presented in pink stars. The corresponding adjusted LiDAR coordinates based on the 3DCCT using GCPs incorporating with the feature constraints were presented in green cross.

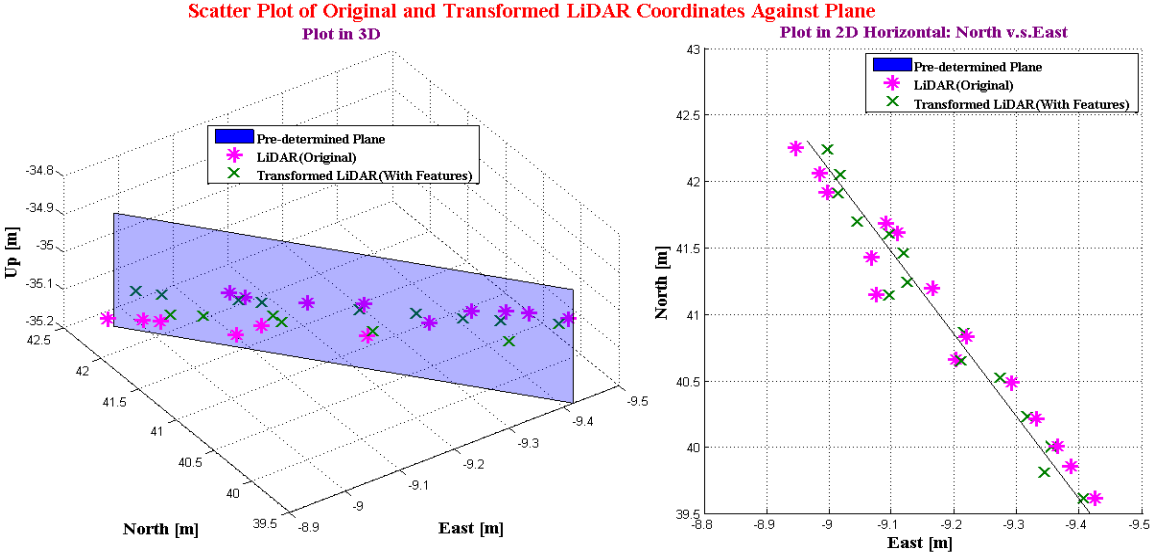

Figure 4-16: Scatter plot of 15 original and adjusted LiDAR points against a planar patch feature constraint in 2D horizontal 3D. The plane in blue was determined using the pre-surveyed GCPs. 15 selected points from the original mobile LiDAR solution were presented in pink stars. The corresponding adjusted LiDAR coordinates based on the 3DCCT using the GCPs with the help of the feature constraints were presented in green cross.

coordinates contained significant biases in north, east and up directions. After the adjustment was introduced using the parameters from the 3D conformal transformation through the GCPs only or with the help of feature constraints, the mean of the errors became insignificant from zero.

The achieved accuracies of the original LiDAR solution assessed through the checking GCPs were ±4.9cm (horizontal) and ±3.0cm (vertical) at the 95% confidence level of the Type I Error according to the χ^2-test. For case 2 where only GCPs were used in the 3D conformal transformation, the vertical accuracy was improved to ±2.2cm and the achieved horizontal accuracy became ±2.7cm at the 95% confidence level. Moreover, the achieved horizontal and vertical accuracies were further improved to ±2.2cm and ±1.7cm, respectively, for case 3 where the GCPs and the feature constraints were applied together at the same significant level as before.

Therefore, the comparisons among the three testing cases concluded that the 7 parameter conformal transformation based on GCPs aided by the straight line and plane features could further improve the accuracies of LiDAR solution in both of the horizontal and vertical directions. Especially, the horizontal accuracy was improved from ±4.9cm up to ±2.2cm (95% confidence level). Furthermore, the RMS values of the selected LiDAR points from those feature constraints were improved by around 2cm through the conformal transformation. Thus, it indicated that the feature constraints incorporating with GCPs could also improve the accuracy of LiDAR points on the features themselves.

Table 4-10: The statistical analysis of the differences between the pre-surveyed and original LiDAR coordinates, the adjusted LiDAR coordinates through the 3DCCT using GCPs only and GCPs with feature constraints, respectively, from 19 checking GCPs on building side 2.

		Error Statistics				**Two-tailed *t*-test (α =0.05%) H_0: $\mu = 0$**			**χ^2 Test (α = 0.05%) vs. the 95% accuracy H_0: $\sigma^2 = 1.5^2 cm^2$**			**H_1: $\sigma^2 = \sigma_a^2$**		
Case No.*	Error	Mean [cm]	Stdev [cm]	RMS [cm]	f	t	$t_{f,0.025}$	Accepted (Y/N)	χ^2	$\chi^2_{f,0.05}$	Accepted (Y/N)	σ_a [cm]	χ^2	Accepted (Y/N)
1	**N**	-1.49	1.82	2.32	18	-3.58	2.101	N						
	E	-1.38	2.49	2.46	18	-2.41	2.101	N						
	U	-2.15	1.94	2.86	18	-4.83	2.101	N	115.44	28.87	N	**3.0**	28.86	Y
	2D(H)	2.03	3.09	3.38	18				304.59	28.87	N	**4.9**	28.54	Y
2	**N**	0.04	1.22	1.19	18	0.13	2.101	Y						
	E	-0.21	1.20	1.19	18	-0.77	2.101	Y						
	U	-0.56	1.42	1.49	18	-1.72	2.101	Y	61.55	28.87	N	**2.2**	28.61	Y
	2D(H)	0.22	1.71	1.68	18				93.87	28.87	N	**2.7**	28.97	Y
4	**N**	-0.21	0.95	0.95	18	-0.95	2.101	Y						
	E	-0.18	1.00	0.99	18	-0.79	2.101	Y						
	U	-0.36	1.09	1.12	18	-1.43	2.101	Y	36.73	28.87	N	**1.7**	28.60	Y
	2D(H)	0.27	1.38	1.37	18				60.67	28.87	N	**2.2**	28.21	Y

***Note:**

- Case 1: The differences between the pre-surveyed coordinates and the original LiDAR coordinates.
- Case 2: The differences between the pre-surveyed coordinates and the adjusted LiDAR coordinates derived from using GCPs only.
- Case 3: The differences between the pre-surveyed coordinates and the adjusted LiDAR coordinates derived from using GCPs with feature constraints.

4.2.5 Usage Optimization of Ground Control Points

In principle, employing more control points could potentially achieve higher accuracy, but setting up those control points was very costly. For example, Zampa et al, (2009) set up six base stations and a number of ground control points at an interval of 50m to 80m along a 60km long highway under surveying. Even though the positioning accuracy of the LiDAR solution was improved to 2 cm level, the benefit of using a mobile LiDAR system for a cost-effective solution was significantly degraded. Therefore, a study for finding practical configuration on optimizing the density and ideal distribution of control points was performed in this research and is presented in this section. Especially, the number of the required GCPs may be reduced or the absence of GCPs in some areas could be compensated for by involving the linear or planar feature constraints to achieve the minimal required accuracy.

There were 38 ground control points in total for building side 2 in the scanned scene. The accuracy improvements of LiDAR solutions based on the 3D conformal transformation were compared through the checking GCPs using different number of control points (i.e., 20, 10 and 5) incorporating with the same feature constraints. Moreover, the feature constraints were sequentially tested using *F*-test to detect any inconsistency with the previous observation group, and only the qualified constraints were used in the least-squares fitting. The plot of the selected GCPs in three scenarios is presented in Figure 4-17.

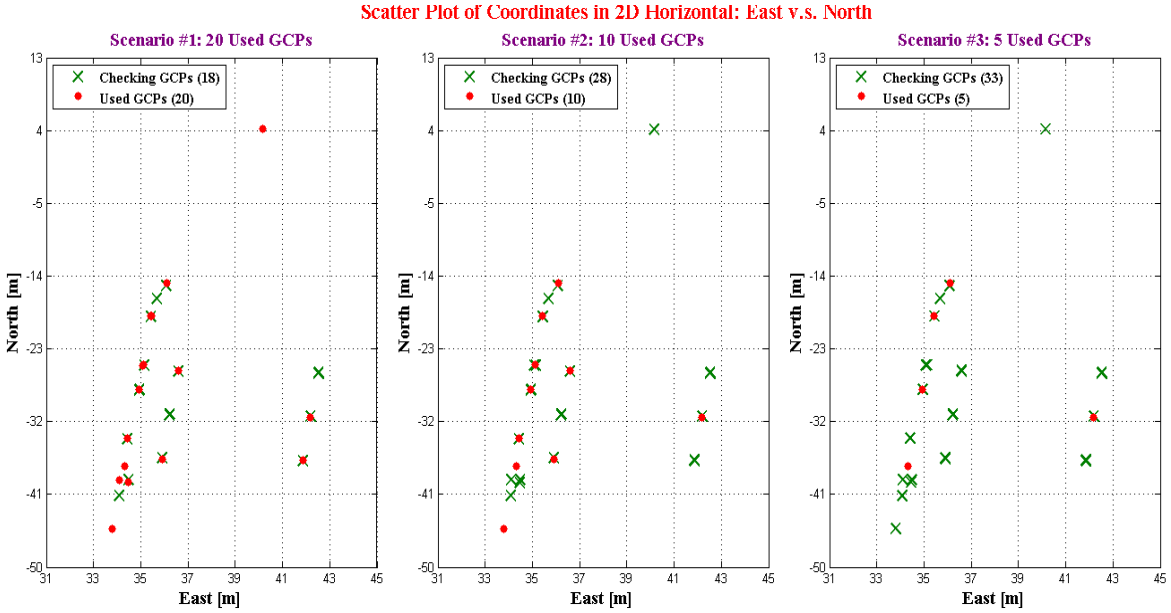

(a)

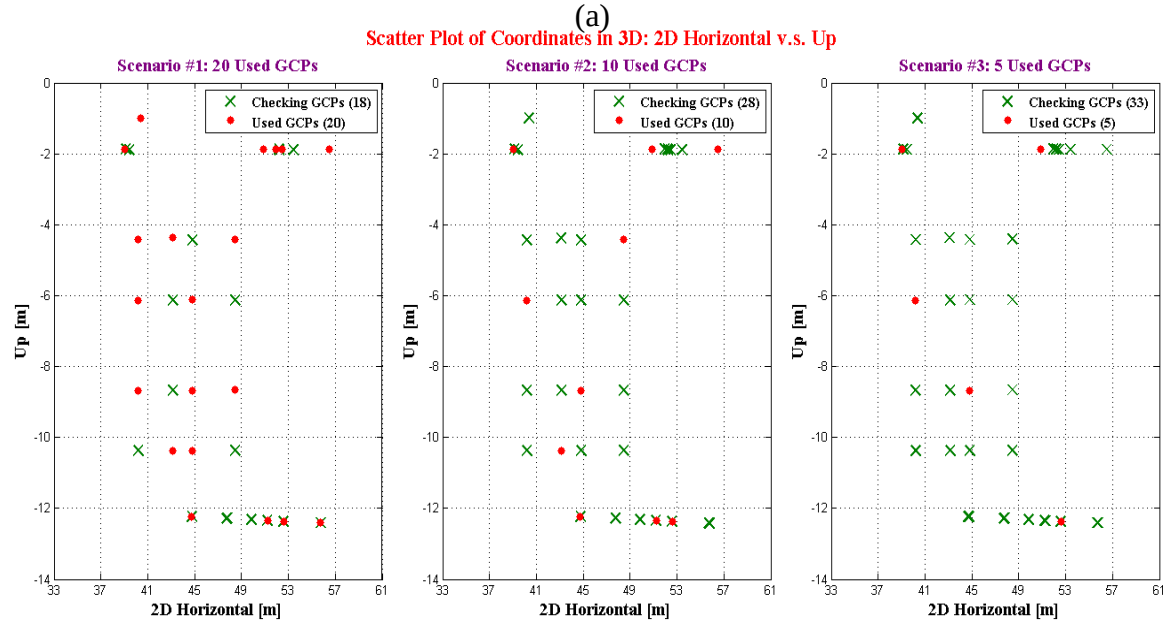

(b)

Figure 4-17: (a) Scatter plot of coordinates in 2D horizontal of scenario #1 (20 used GCPs), scenario #2 (10 used GCPs) and scenario #3 (5 used GCPs). (b) Scatter plot of coordinates in vertical.

Figure 4-18 shows the scatter plot of 18 checking GCPs in the testing scene in both 2D horizontal and 3D direction. By taking the enlarged snapshots of two checking points "P205" and "F231" as examples, the adjusted LiDAR coordinates on the basis of 20 GCPs out of 38 control points (i.e., ~50%) and 10 GCPs (i.e., ~30%) were close to each other, and they had the similar distances to the pre-surveyed coordinates (red dot). However, the corrected LiDAR coordinates on the basis of only 5 GCPs (i.e., ~10%) were the furthest among three scenarios. By considering the pre-surveyed coordinates as reference, Table 4-11 shows that the errors based on 5 GCPs were the biggest ones. The 3D error based on 10 GCPs was around 5mm bigger than the ones based on 20 GCPs.

Table 4-11: The differences between pre-surveyed coordinates and adjusted LiDAR coordinates using 20, 10 and 5GCPs, respectively, from two checking points "P205" and "F231".

ID	With 20 GCPs + Features [cm]					With 10 GCPs + Features [cm]					With 5 GCPs + Features [cm]				
	N	E	2D	U	3D	N	E	2D	U	3D	N	E	2D	U	3D
P205	0.65	-1.45	**1.59**	**-0.64**	**1.71**	0.97	-1.88	**2.12**	**-0.97**	**2.33**	1.46	-2.33	**2.75**	**-1.57**	**3.17**
F231	0.75	0.96	**1.22**	**-0.76**	**1.44**	1.03	1.35	**1.70**	**-1.10**	**2.02**	1.57	1.84	**2.42**	**-1.68**	**2.94**

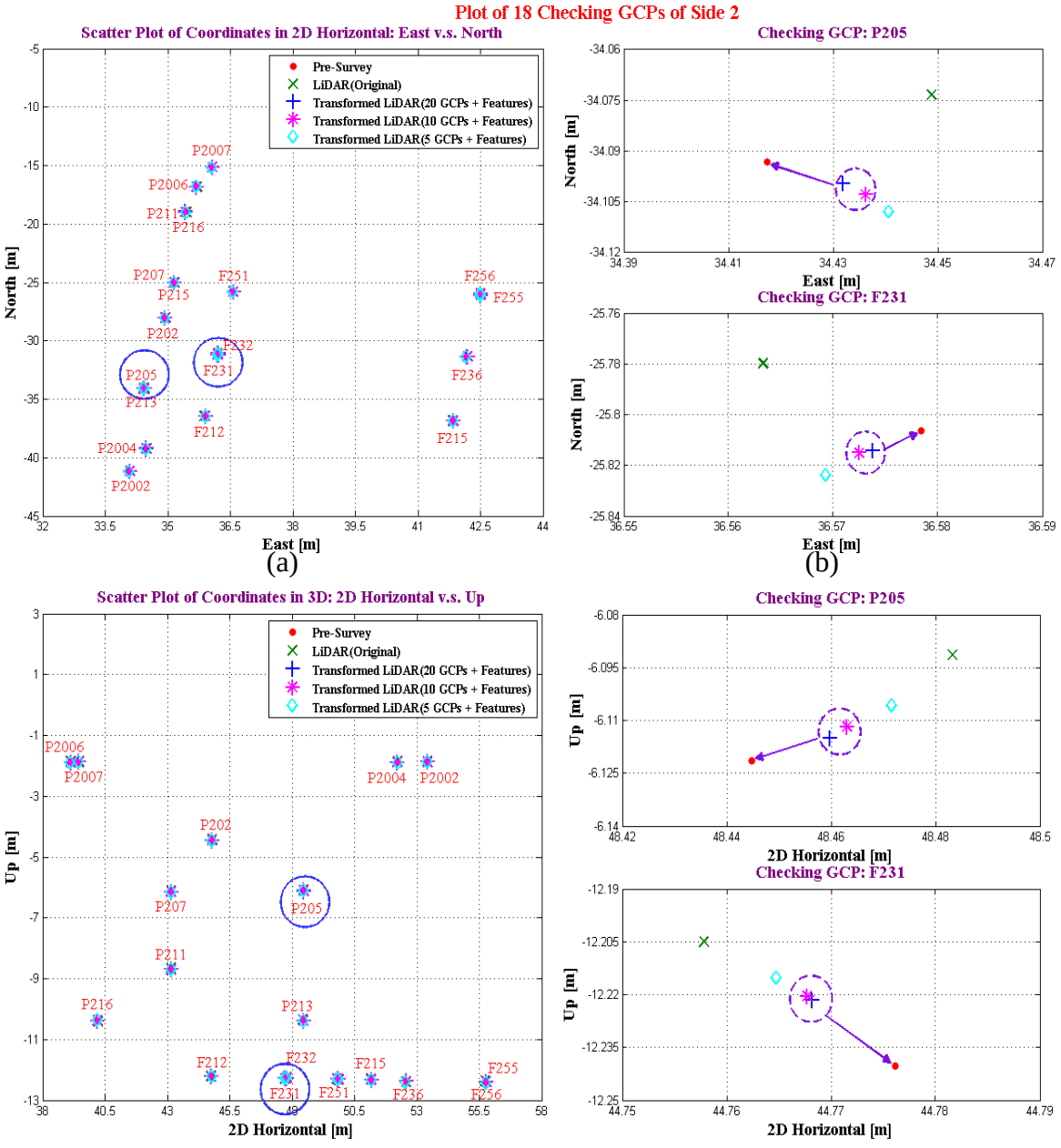

Figure 4-18: Scatter plot of 18 checking GCPs on side 2. The adjusted LiDAR coordinates using 20 GCPs, 10 GCPs and 5 GCPs aided by the same feature constraints were presented in blue cross, pink star and cyan diamond, respectively. (a) & (c) 2D horizontal and vertical. (b) & (d) Close-up details of "P205" and "F231".

Then a number of the overall quantitative indexes for 18 checking GCPs on the building side 2 were also calculated (see Appendix B-4). Furthermore, Table 4-12 summarized the statistic results of different testing cases. The *t*-test and χ^2-test were constructed to determine if the errors were significantly biased and if a sample deviation was satisfied with the pre-defined ±1.5cm accuracy level, respectively. The differences between the pre-surveyed and original LiDAR coordinates showed significant biases in north, east and up directions based on the two-tailed *t*-test. After the adjustment based on the parameters from the 3D conformal transformation, the mean of the errors was not significantly different from zero with 20 and 10 GCPs. However, the errors showed significant biases in north and east directions as only 5 GCPs were used in the 3D conformal transformation.

The achieved accuracies of the original LiDAR solution with the selected checking GCPs were ±4.7cm (horizontal) and ±3.3cm (vertical) at the 95% confidence level. It achieved the best accuracy of ±2.2cm in horizontal and ±1.8cm in vertical by using 20 GCPs (i.e., ~50%) in the 3D conformal transformation. Moreover, for case 3 where only 10 GCPs (i.e., ~30%) were applied, the achieved horizontal and vertical accuracies were ±2.5cm and ±2.1cm, respectively. Although more GCPs could achieve better accuracy, the performance would not be decreased significantly by reducing the number of GCPs down to 30 percentages of the total number of control points. Furthermore, for the test case 4 where only 5 GCPs (i.e., ~10%) were used, the accuracy became ±2.9cm horizontally and ±2.4cm vertically, which were decreased relatively significant in comparison with the other two scenarios mentioned above.

Based on the results among all test cases, using more GCPs in the solution refining process could generally achieve better accuracy in both horizontal and vertical directions. However, the overall accuracies were not decreased a lot by reducing the number of used GCPs around 30 percent of the total number (38 GCPs in this case study) aided by straight line and planar patch feature constraints. However, the 3D LiDAR positioning accuracy was decreased dramatically using only 10 percent (i.e., 5 GCPs) of total GCPs in the 3D conformal transformation. Therefore, it is necessary to select the control points efficiently and effectively by considering the project budget and minimal required accuracy.

Table 4-12: The statistical analysis of the differences between the pre-surveyed coordinates, the original LiDAR coordinates, and the adjusted LiDAR coordinates through the 3DCCT using 20, 10 and 5 GCPs aided by the same feature constraints, respectively, from 18 checking GCPs on building side 2.

		Error Statistics				**Two-tailed *t*-test (α =0.05%) H_0: $\mu = 0$**			**χ^2 Test (α = 0.05%) vs. the 95% accuracy H_0: $\sigma^2 = 1.5^2 cm^2$**			**H_1: $\sigma^2 = \sigma_a^2$**		
Case No.*	Error	Mean [cm]	Stdev [cm]	RMS [cm]	f	t	$t_{f,0.025}$	Accepted (Y/N)	χ^2	$\chi^2_{f,0.05}$	Accepted (Y/N)	σ_a [cm]	χ^2	Accepted (Y/N)
1	**N**	-1.35	1.78	2.19	17	-3.21	2.110	N						
	E	1.43	2.39	2.33	17	2.53	2.110	N						
	U	-1.76	2.09	2.68	17	-3.57	2.110	N	126.26	27.59	N	**3.3**	26.09	Y
	2D(H)	1.96	2.98	3.20	17				268.93	27.59	N	**4.7**	27.39	Y
2	**N**	0.39	1.00	1.05	17	1.66	2.110	Y						
	E	0.39	0.94	0.99	17	1.76	2.110	Y						
	U	0.16	1.17	1.15	17	0.57	2.110	Y	39.62	27.59	N	**1.8**	27.52	Y
	2D(H)	0.55	1.37	1.44	17				56.83	27.59	N	**2.2**	26.42	Y
3	**N**	0.39	1.12	1.16	17	1.48	2.110	Y						
	E	0.44	1.13	1.18	17	1.65	2.110	Y						
	U	0.09	1.36	1.33	17	0.28	2.110	Y	53.80	27.59	Y	**2.1**	27.45	Y
	2D(H)	0.59	1.59	1.65	17				76.56	27.59	N	**2.5**	27.56	Y
4	**N**	0.75	1.28	1.45	17	2.47	2.110	N						
	E	0.72	1.26	1.42	17	2.43	2.110	N						
	U	0.15	1.53	1.43	17	0.40	2.110	Y	68.00	27.59	N	**2.4**	26.56	Y
	2D(H)	1.04	1.80	2.03	17				97.61	27.59	N	**2.9**	26.11	Y

***Note:**

- Case 1: The differences between the pre-surveyed and the original LiDAR coordinates.
- Case 2: The differences between the pre-surveyed coordinates and the adjusted LiDAR coordinates derived from using 20 GCPs and features.
- Case 3: The differences between the pre-surveyed coordinates and the adjusted LiDAR coordinates derived from using 10 GCPs and features.
- Case 4: The differences between the pre-surveyed coordinates and the adjusted LiDAR coordinates derived from using 5 GCPs and features.

4.3 Refinement of Terrestrial Mobile LiDAR Solutions: Two Road Test Areas

4.3.1 General

The proposed 3DCCT and various aforementioned strategies were further applied to a much more complicated testing site located around Black Creek Pioneer Village, Toronto, Canada, which is about 3 kilometers away from the Optech GPS reference station. This test case was divided into two parts as shown in Figure 4-19 for different testing purposes:

(1) Study Area #1: The stretch of Shoreham Drive between Calumet Resident and Ian Macdonald Blvd. This test was designed to validate the algorithms and strategies under an ideal condition, that is, in a relative small area with adequate ground control points and feature constraints.

(2) Study Area #2: A loop starting from Murray Ross Parkway, heading north and turning left on Steeles Ave West, heading west and turning left on Jane Street, then heading south and turning left to Shoreham Drive, and closing back to Murray Ross Parkway again. It was designed to test the proposed strategies under a real environmental condition, that is, in a relative big area with limited ground control points and feature constraints.

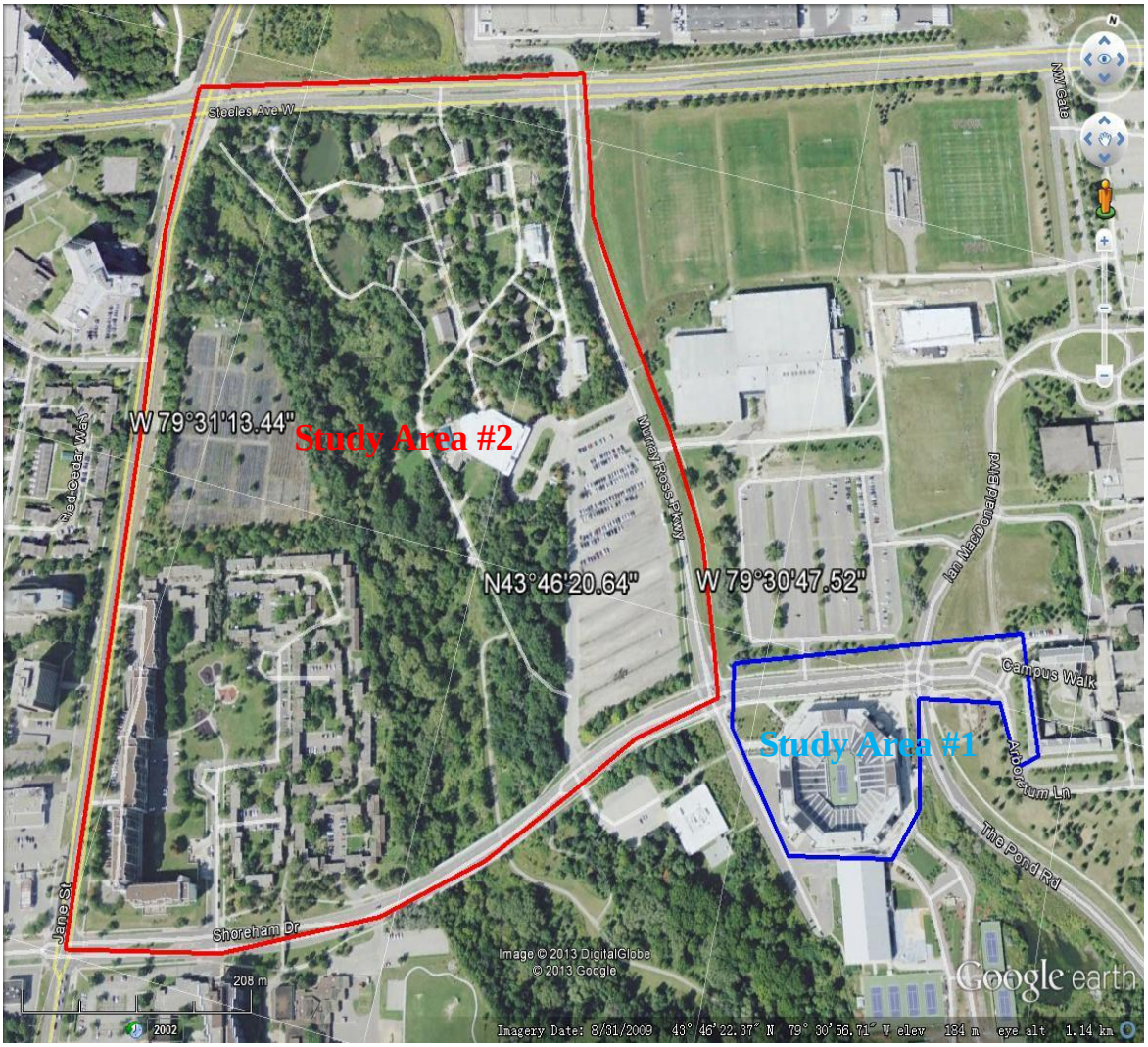

Figure 4-19: Black Creek Pioneer Village in Toronto, Canada was chosen as the testing scene for strategy validation. Study area #1: the stretch of Shoreham Drive between Calumet Resident and Ian Macdonald Blvd at York University Campus. Study area #2: the loop of Steeles Ave West – Murray Ross Pkwy – Shoreham Drive – Jane Street.

4.3.2 Results of Study Area #1

4.3.2.1 Overview

This test was used to further validate the effects of 3DCCT based on the conditional adjustment with parameters and constraints, and also the different strategies under an ideal condition towards accuracy improvement of terrestrial mobile LiDAR solutions. The same mathematical and stochastic models illustrated in Section 3.2 were applied. As with the Optech building test in Section 4.2, four different strategies were tested to study the effectiveness and efficiency:

(1) Categorization of ground control points concerning horizontal and vertical accuracy improvements (Section 4.3.2.3)

(2) Utilization of feature constraints (Section 4.3.2.4)

(3) Categorization of feature constraints concerning horizontal and vertical accuracy improvements (Section 4.3.2.5)

The feature constraints were also further categorized into two groups: horizontal direction (e.g., pavement markings) and vertical direction (e.g., traffic light and signs). The performance improvement of LiDAR solution was investigated in 2D horizontal and vertical directions by utilizing different types of features.

(4) Usage optimization of ground control points (Section 4.3.2.6)

Sponsored by Optech Inc., an Optech Lynx V200 mobile mapping vehicle equipped with two Lynx scanners and an Applanix POS system was used to acquire the LiDAR data on May 25, 2013. The Optech GPS reference station was used as the known initial point by the control network and the Optech mobile Lynx system. The field work such as

the establishment of the 3D geodetic control network and the observation of the targets were completed in August 2013.

Without any further elaboration, the accuracy criteria, the statistic tests and the approaches applied to the accuracy assessment for checking GCPs in this test were the same as the ones described in Section 4.2.3.1.

4.3.2.2 Studying Area and Data Acquisition

4.3.2.2.1 Terrestrial Mobile LiDAR Data Acquisition and Processing

With the data acquisition in Study Area #1, the vehicle started at the bus stop around Calumet Resident, was heading west on Shoreham Drive, approaching to Murray Ross Parkway, and then heading back to the start location. During the LiDAR data collection, the laser PRF (pulse repetition frequencies) of 250 kHz and the mirror speed of 200 Hz were used. The vehicle maintained the speed of 20km/h. An overview of the point cloud is presented in Figure 4-20. The 2D horizontal and vertical profiles and the velocity profile of the trajectory are given in Figure 4-21.

The accuracy performance of the corresponding SBET solution resulted from the POS LV420 is presented in Figure 4-22. It described the accuracy of the POS SBET for the position, orientation and velocity using RMS. As can be seen, the horizontal position accuracy (1σ) was better than ±1.5cm, while the vertical accuracy was about ±3cm.

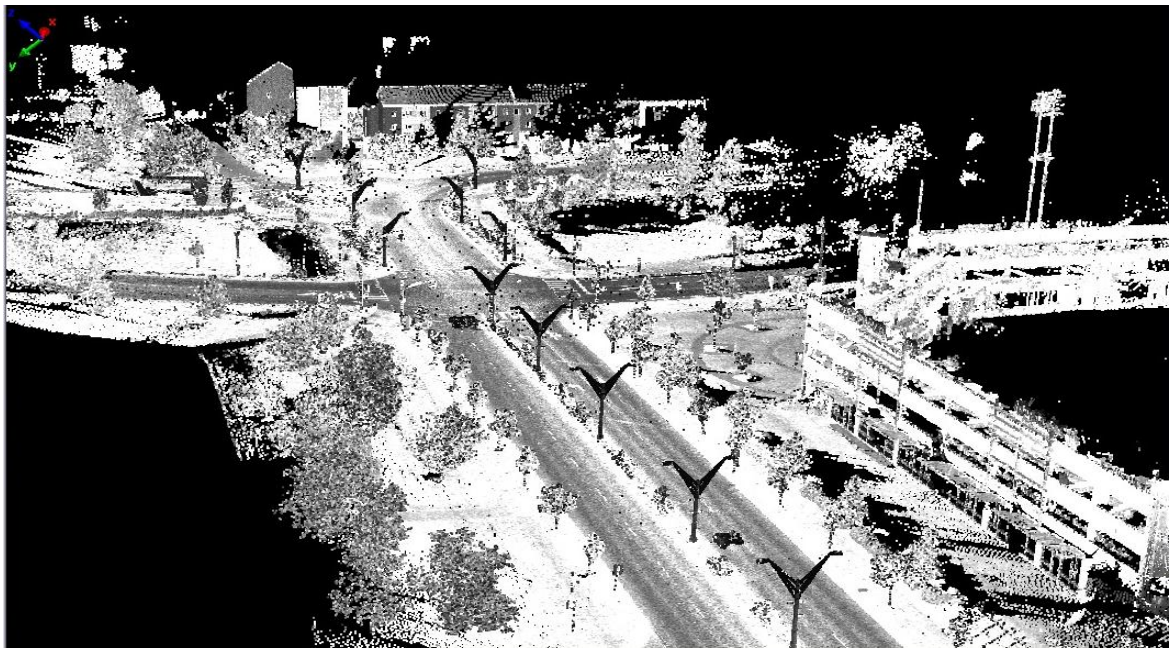

Figure 4-20: Overview of study area #1 where the stretch of Shoreham Drive between Calumet Resident and Ian Macdonald Blvd in Toronto, Canada with a laser PRF of 250 kHz and a mirror speed of 200 Hz.

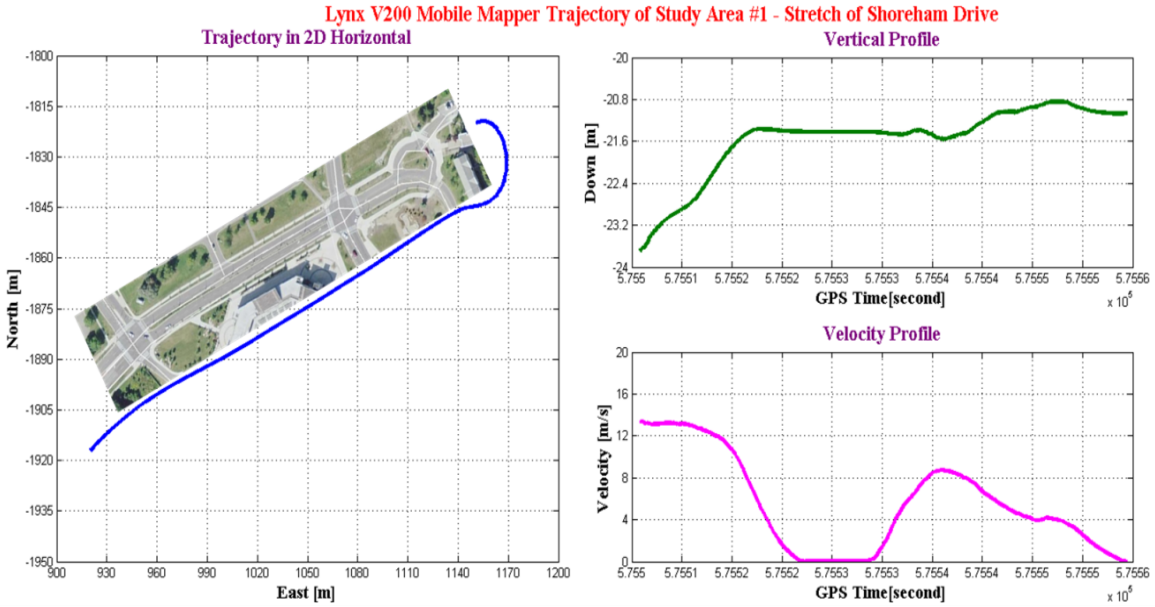

Figure 4-21: The 2D horizontal, vertical and velocity profiles of the trajectory of the collected LiDAR data in the studying area #1.

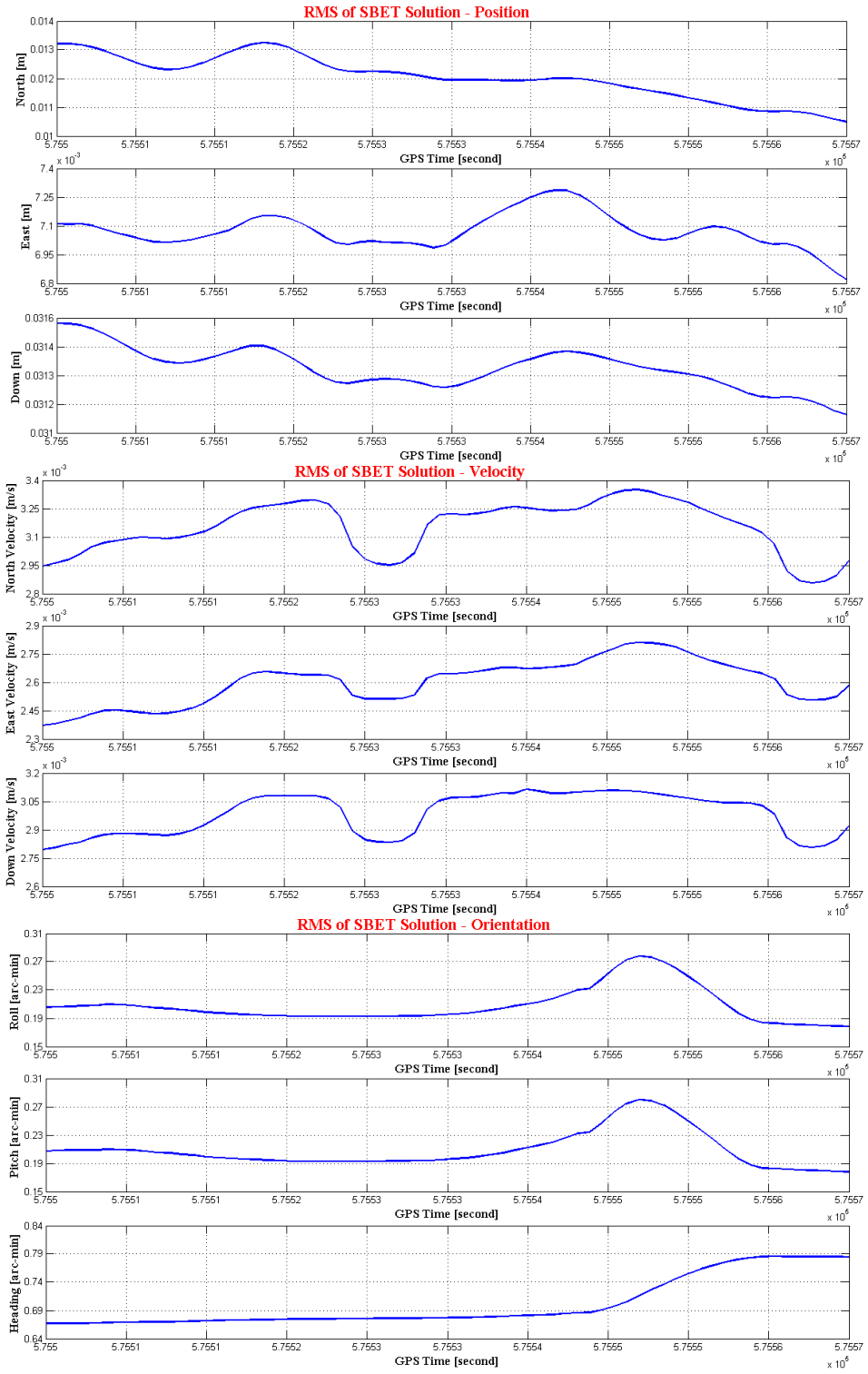

Figure 4-22: The RMS of the position (north, east and down), orientation (roll, pitch and heading) and velocity (north, east and down) versus GPS time.

4.3.2.2.2 Determination of GCPs and Features

Similarly to the geodetic control survey used in the Optech building test (Section 4.2.2.2), all of the selected control points in the validation scenes need to be determined with respect to Optech GPS reference station which is the same reference the mobile mapping vehicle used. The control network was observed using both Leica TC1800 and TCA1800 total station systems along with a pair of Leica 1200 GPS receivers. The field work was completed in August 2013.

In the test scene, two control points (O_1 and O_2) were selected to construct the GPS baselines with respect to the Optech GPS base station. Then two local traverses were established around those two control points through observing horizontal directions, vertical angles, slope distances, and GPS baselines. The network configuration is shown in Figure 4-23.

The 3D geodetic control network was adjusted by using Columbus Best-Fit Computing Software. The adjusted coordinates of all the control points on the WGS84 datum are summarized in Table 4-13. It reached the 3D postional accuracy of ±4mm (1σ) with all of the points. This accuracy level could provide realiable reference for the determination of control targets and features, as it was superior to the expected accuracy of a few centimeters with the of LiDAR products.

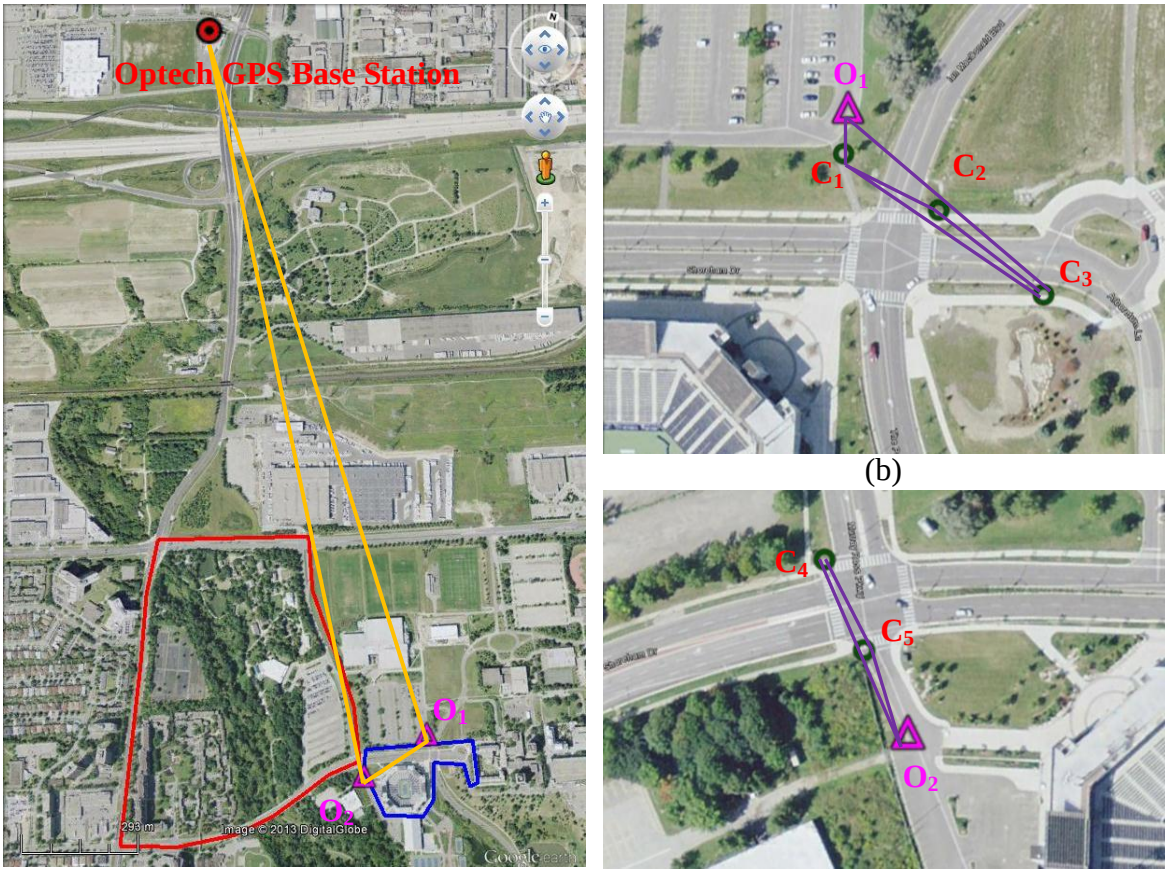

(a) (b) (c)

Figure 4-23: The 3D geodetic control network: (a) The static GPS baseline network between Optech reference station and two local control points O_1 and O_2; (b) The local traverse at control point O_1. (c)The local traverse at control point O_2.

Table 4-13: The adjusted geodetic coordinates of control points on WGS84 datum.

Station	Latitude (north)	σ [mm]	Longitude (west)	σ [mm]	Ellipsoid Height	σ [mm]	σ_{3D} [mm]
C1	43 - 46 - 21.39407	1.5	79 - 30 - 40.61881	1.0	152.7997	2.7	3.3
C2	43 - 46 - 21.64571	1.4	79 - 30 - 42.16988	2.7	152.7851	2.7	4.0
C3	43 - 46 - 20.91294	1.7	79 - 30 - 38.87012	2.9	152.8881	2.2	4.0
C4	43 - 46 - 18.27285	1.5	79 - 30 - 49.20371	2.1	150.2753	2.9	3.9
C5	43 - 46 - 19.00393	1.0	79 - 30 - 50.16291	2.2	150.4640	2.9	3.8
O1	43 - 46 - 22.11553	1.4	79 - 30 - 42.32205	2.3	152.5055	2.3	3.5
O2	43 - 46 - 17.64497	1.4	79 - 30 - 48.24151	2.5	150.3198	2.5	3.8
Optech	**43 - 47 - 20.96747**	-	**79 - 31 - 29.97041**	-	**175.7830**	-	**fixed**

The targets and feature constraints were utilized to improve the accuracy of terrestrial mobile LiDAR solution. Again, two types of the existing characteristic points were selected, which was similar to Optech building testing case (Section 4.2.2.2, Figure 4-6). One type is the points on the ground, such as pavement markings and curbs, while the other type is the points on the building corners, traffic signs, guide boards and traffic lights. Figure 4-24 gives some examples of such control points. Moreover, the painting lines, traffic lights and signs were also used as the horizontal and vertical linear feature constraints as shown in Figure 4-25.

The whole estimation process of the 3D target coordinates was the same as the one applied in Optech Building Test by using 3D resection method. In total, 76 targets were surveyed, consisted of 54 building-type control points and 22 ground-type control points (Figure 4-26). In addition, 4 horizontal and 6 vertical directional feature constraints were generated, respectively. Figure 4-27 gives an overview of all control points distributed in Study Area #1.

Figure 4-24: Examples of building (green dots) and ground (red dots) types control points.

Figure 4-25: Examples of horizontal and vertical directional feature constraints, such as, traffic light and sign, York University guideboard and stop bar on the ground.

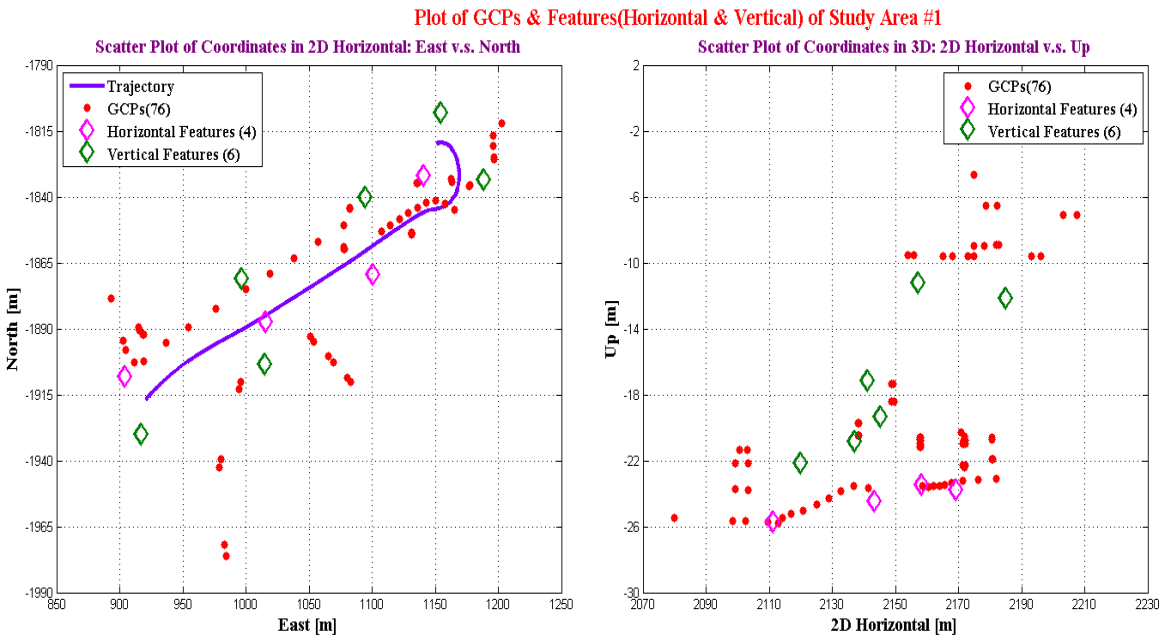

Figure 4-26: Scatter plot of 76 GCPs and 10 feature constraints in study area #1 (2D horizontal and 3D). Different colors were selected to represent building- and ground-type control points, and the horizontal and vertical directional features.

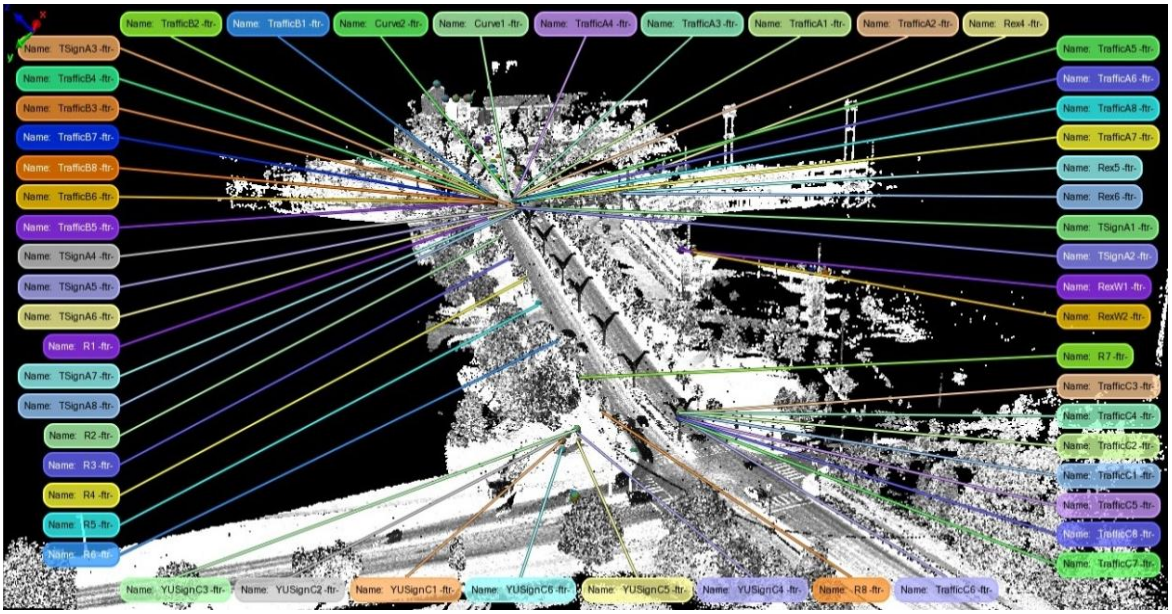

Figure 4-27: Overview of the distribution of 76 control points in study area #1 where the 200-meter stretch of Shoreham Drive was scanned between Calumet Resident and Ian Macdonald Blvd in Toronto, Canada.

4.3.2.3 Categorization of Ground Control Points Concerning Horizontal and Vertical Accuracy Improvements

Similarly to the test given in Section 4.2.3.2, the control points were categorized into building and ground types due to the fact that the effects of some of the remaining systematic errors in the 3D LiDAR solution may not be uniform in horizontal and vertical directions. Among the 76 control points in study area #1 (Figure 4-28), 54 control points were building-type and 22 were ground-type. Their locations determined by LiDAR instrument were manually extracted from the LiDAR point cloud using PolyWorks Software (Figure 4-29 (a) and (b)), respectively. Half of them from each type were used in the 3DCCT and the others were used as checking GCPs in accuracy assessment.

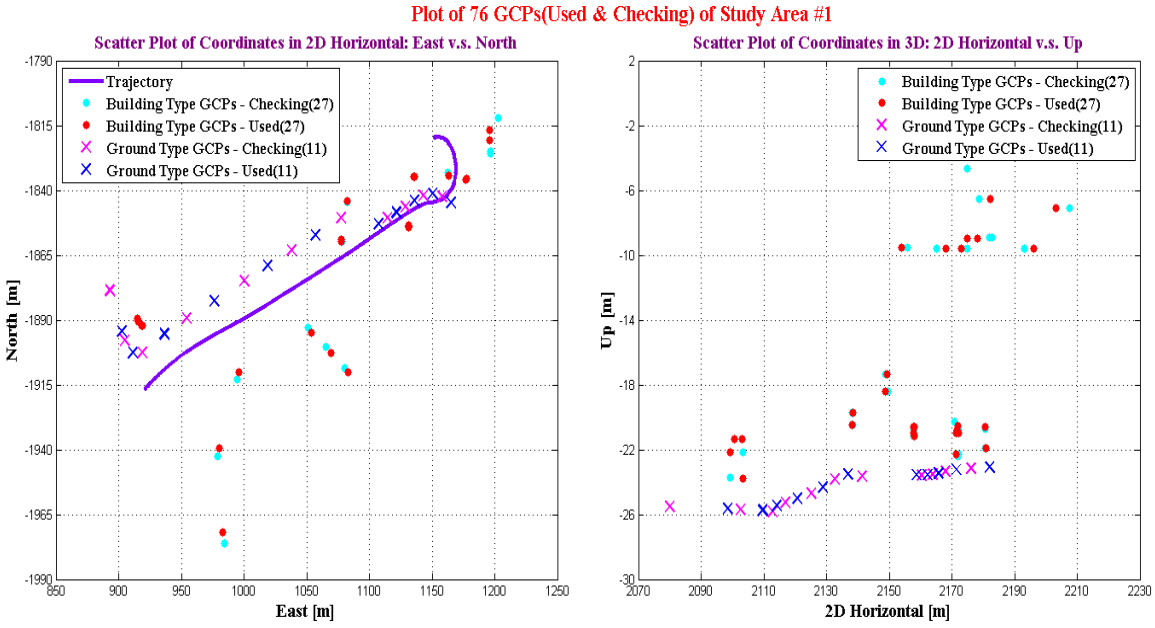

Figure 4-28: Scatter plot of 76 GCPs distributed in the test scene (2D horizontal and vertical profiles): 54 building-type GCPs as dots, and 22 ground-type GCPs as crosses. Different colors represent either the points used in conformal transformation or in the validation process, respectively.

The performance of accuracy improvement was evaluated using the checking GCPs through the comparison among the results using different types and the mixed-types of GCPs. The error analysis of 38 checking GCPs (27 building-type & 11 ground-type) and two points as examples are shown in Appendix D-1. The ground-type checking GCPs were chosen as an example to illustrate the results. Then a number of the overall quantitative indexes inclusive the minimum, maximum, mean, standard deviation and RMS are summarized in Appendix C-1. Furthermore, the *t*-test was constructed to determine if the errors were significantly biased and χ^2-test statistics was used to conclude if a sample deviation was satisfied with the specific required ±1.5cm accuracy level. The statistic results of different testing cases are presented in Table 4-14.

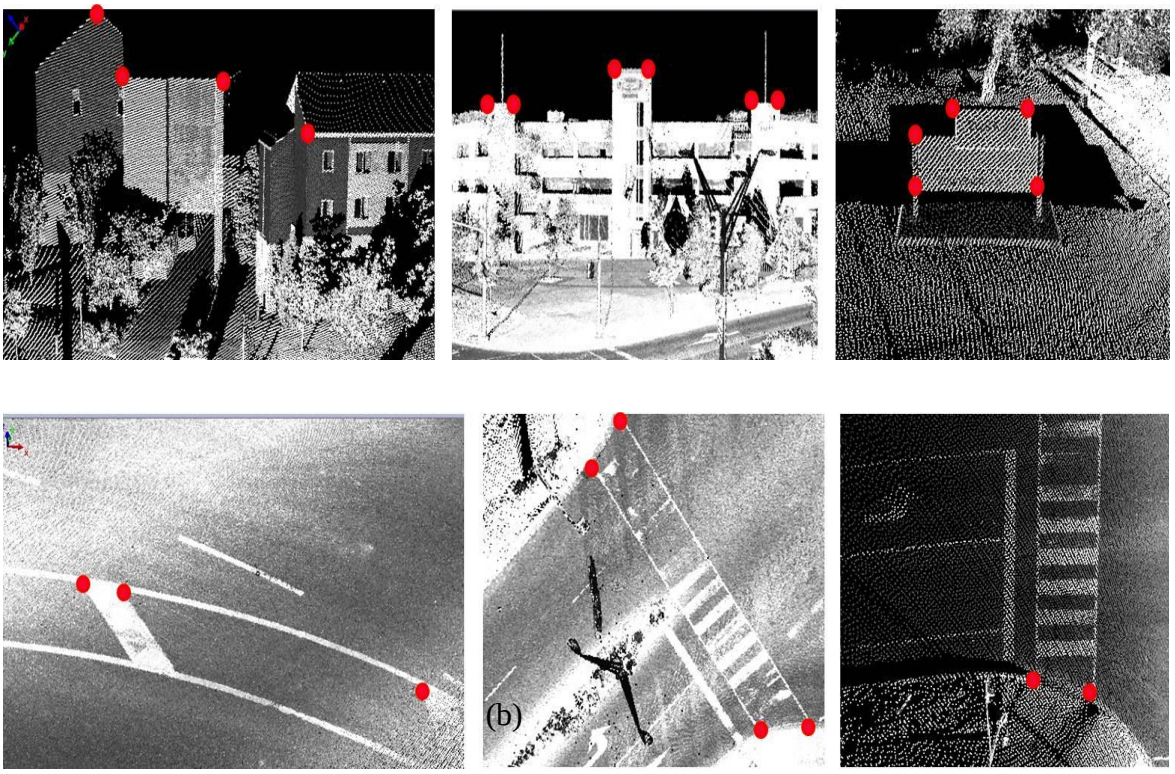

Figure 4-29: The location of two types of GCPs extracted from the point cloud: (a) building-type and (b) ground-type.

Based on the results from two-tailed *t*-test, the differences between the pre-surveyed and the original LiDAR coordinates of the checking points contained significant biases in north, east and up directions. After the adjustment based on the 3DCCT, the mean of the errors was not significantly different from zero with the same-type of GCPs as the checking points. However, the errors still contained significant biases if the different type of checking control points were considered.

The achieved accuracies were ±4.1cm (horizontal) and ±3.9cm (vertical) at the 95% confidence level after the χ^2-test before the 3DCCT adjustment. For case 3 where the same type of the control points was used in 3D conformal transformation, the vertical accuracy was improved to ±1.8cm, and the achieved horizontal accuracy was ±2.2cm at the 95% confidence level. It only achieved an accuracy of ±3.0cm in horizontal and ±2.5cm in vertical for case 2 as the different types of the control points were employed. The corresponding performance was the worst one among all the testing cases, and was not improved significantly in comparison with the original LiDAR solution. For case 4, the achieved horizontal accuracy was ±2.6cm and vertical accuracy was ±2.1cm after the 3DCCT adjustment using 38 mixed-types of GCPs based on the χ^2-test at the 5% significant level. Apparently, none of the testing cases could meet the pre-specified accuracy requirement (±1.5cm).

The comparisons among the four testing cases indicated that the 3D conformal transformation process could achieve the best accuracy using the same type of control points in both horizontal and vertical directions, respectively. While the employment of the different types of GCPs yields the worst result and the accuracy could not be

significantly improved in comparison with the original LiDAR solutions. The performance after the adjustment based on the mixed-types of GCPs fell in between. Furthermore, the conclusions were also verified through the similar process and statistic tests for the building-type checking GCPs. Therefore, concerning the horizontal and vertical accuracy improvements, the categorization of the control points is necessary. Thus, the 3DCCT parameters could separately be determined by using the same type of control points. In general, the conclusions were consistent with the ones drawn from the previous test at Optech in section 4.2.3.2.

Table 4-14: The statistical analysis of the differences between the pre-surveyed coordinates and the original LiDAR coordinates, the adjusted LiDAR coordinates after the 3DCCT using 11 ground-type GCPs, 27 building-type GCPs and 38 mixed-type GCPs, respectively, from 11 ground-type checking GCPs in Study Area #1.

		Error Statistics				**Two-tailed *t*-test (α =0.05%) H_0: $\mu = 0$**			**χ^2 Test (α = 0.05%) vs. the 95% accuracy H_0: $\sigma^2 = 1.5^2 cm^2$**			**H_1: $\sigma^2 = \sigma^2_a$**		
Case No.*	Error	Mean [cm]	Stdev [cm]	RMS [cm]	*f*	*t*	$t_{f,0.025}$	Accepted (Y/N)	χ^2	$\chi^2_{f,0.05}$	Accepted (Y/N)	σ_a [cm]	χ^2	Accepted (Y/N)
1	**N**	-1.56	1.86	2.36	10	-2.77	2.201	N						
	E	-1.25	2.05	2.32	10	-2.22	2.201	N						
	U	3.71	2.66	4.49	10	4.63	2.201	N	120.60	18.31	N	**3.9**	17.84	Y
	2D(H)	2.00	2.77	3.31	10				136.25	18.31	N	**4.1**	18.24	Y
2	**N**	-1.56	1.42	2.07	10	-3.65	2.201	N						
	E	-1.15	1.44	1.79	10	-2.65	2.201	N						
	U	-1.65	1.71	2.32	10	-3.20	2.201	N	49.76	18.31	N	**2.5**	17.91	Y
	2D(H)	1.94	2.02	2.74	10				72.84	18.31	N	**3.0**	18.21	Y
3	**N**	-0.57	1.12	1.21	10	-1.69	2.201	Y						
	E	-0.68	0.98	1.16	10	-1.93	2.201	Y						
	U	-0.21	1.24	1.20	10	-0.56	2.201	Y	26.09	18.31	N	**1.8**	18.12	Y
	2D(H)	0.89	1.49	1.67	10				39.32	18.31	N	**2.2**	18.28	Y
4	**N**	-0.57	1.38	1.43	10	-1.38	2.201	Y						
	E	-0.80	1.05	1.28	10	-2.53	2.201	N						
	U	-0.67	1.43	1.51	10	-1.55	2.201	Y	34.70	18.31	N	**2.1**	17.71	Y
	2D(H)	0.98	1.73	1.92	10				53.25	18.31	N	**2.6**	17.72	Y

***Note:**

- Case 1: The differences between the pre-surveyed coordinates and the original LiDAR coordinates.
- Case 2: The differences between the pre-surveyed coordinates and the adjusted LiDAR coordinates derived from using 27 building-type GCPs.
- Case 3: The differences between the pre-surveyed coordinates and the adjusted LiDAR coordinates derived from using 11 ground-type GCPs.
- Case 4: The differences between the pre-surveyed coordinates and the adjusted LiDAR coordinates derived from using 38 mixed-type GCPs.

4.3.2.4 Utilization of Feature Constraints

Section 4.2.4 showed that the feature constraints incorporating with GCPs could significantly improve the accuracy of LiDAR solutions. For study area #1 here, there were 5 straight lines and 5 planar patches applied together with 76 pre-surveyed GCPs (54 building-type and 22 ground-type). Half of those GCPs were selected from each type and were applied in a combined way in the 3D conformal coordinate transformation (i.e., case 4 in section 4.3.2.3). The used and the checking GCPs are plotted in Figure 4-30.

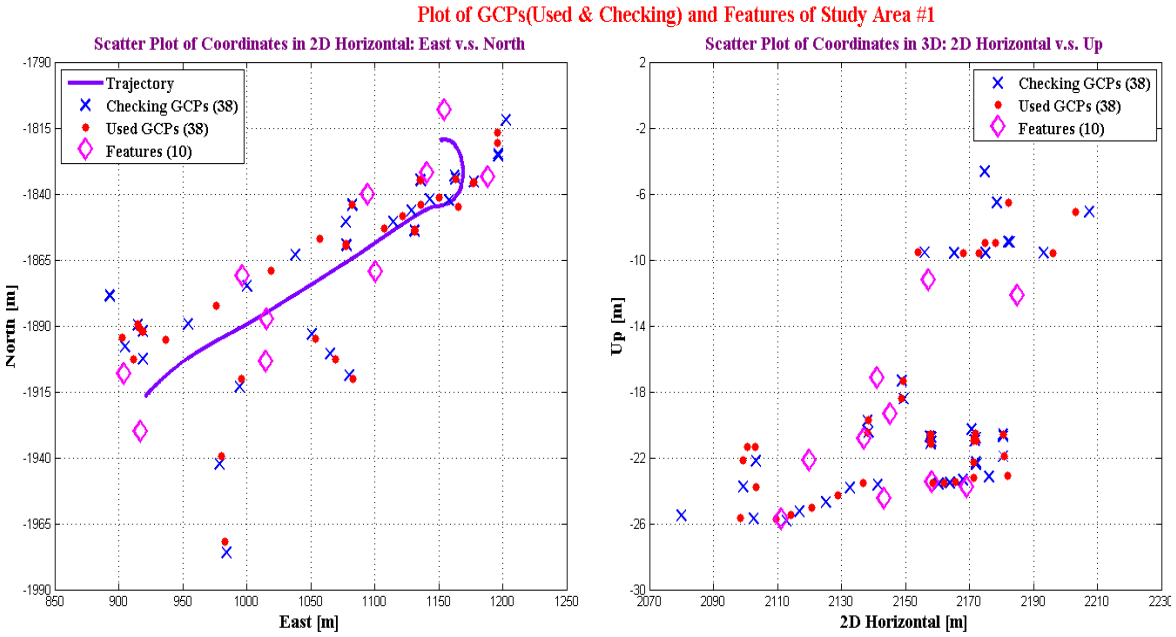

Figure 4-30: Scatter plot of 76 GCPs and 10 features in study area #1 (2D horizontal and vertical): 38 GCPs in red dot used in 3D conformal transformation, and 38 control points in blue cross used for accuracy assessment.

The extent of the accuracy improvement through the 38 checking GCPs aided by line and planar features was analyzed (Appendix D-2). In addition, the error results of

two example points "SWTraffic4" and "R11" are illustrated in the same Appendix. Appendix C-2 also summarizes the error analysis through the 38 checking GCPs in study area #1. The statistic results of the different cases using t-test and χ^2-test are listed in Table 4-15. Based on the two-tailed *t*-test, the differences between the pre-surveyed and the original LiDAR coordinates contained significant biases in north, east and up directions. After the adjustment based on the 7 parameter conformal transformation, the mean of the errors became no more significant versus zero.

The achieved accuracies of the original LiDAR solution with the checking GCPs were ±5.0cm (horizontal) and ±3.9cm (vertical) at the 95% confidence level according to the χ^2-test. For case 2 where only the GCPs were used in 3DCCT process, the vertical accuracy was improved to ±2.2cm, and the achieved horizontal accuracy was ±2.8cm at the 95% confidence level. After the additional features were applied with case 3, the achieved horizontal and vertical accuracies were further improved to ±2.3cm and ±1.8cm respectively based on the χ^2-test at the 95% significant level.

Therefore, the comparisons among the three testing cases concluded that the 7 parameter conformal transformation based on the GCPs aided by the straight line and planar features could further improve the accuracy of LiDAR solution. Especially, the horizontal accuracy was improved from ±5.0cm up to ±2.3cm. Thus, the conclusions were consistent with the previous Optech building test given in section 4.2.4.

Table 4-15: The statistical analysis of the differences between the pre-surveyed coordinates and the original LiDAR coordinates, the adjusted LiDAR coordinates after the 3DCCT using GCPs only and GCPs with feature constraints, respectively, from 38 checking GCPs in Study Area #1.

		Error Statistics				**Two-tailed *t*-test (α =0.05%) H_0: $\mu = 0$**			**χ^2 Test (α = 0.05%) vs. the 95% accuracy H_0: $\sigma^2 = 1.5^2 cm^2$**			**H_1: $\sigma^2 = \sigma_a^2$**		
Case No.*	Error	Mean [cm]	Stdev [cm]	RMS [cm]	f	t	$t_{f,0.025}$	Accepted (Y/N)	χ^2	$\chi^2_{f,0.05}$	Accepted (Y/N)	σ_a [cm]	χ^2	Accepted (Y/N)
1	**N**	-0.93	2.02	2.20	37	-2.83	2.026	N						
	E	-0.96	2.16	2.34	37	-2.75	2.026	N						
	U	4.79	2.35	5.32	37	12.54	2.026	N	350.24	52.19	N	**3.9**	51.81	Y
	2D(H)	1.34	2.95	3.21	37				574.26	52.19	N	**5.0**	51.68	Y
2	**N**	-0.33	1.20	1.23	37	-1.69	2.026	Y						
	E	-0.45	1.15	1.22	37	-2.42	2.026	N						
	U	-0.53	1.33	1.41	37	-2.46	2.026	N	111.20	52.19	N	**2.2**	51.69	Y
	2D(H)	0.56	1.66	1.73	37				181.60	52.19	N	**2.8**	52.12	Y
3	**N**	-0.23	0.96	0.98	37	-1.48	2.026	Y						
	E	-0.19	0.97	0.97	37	-1.21	2.026	Y						
	U	-0.35	1.08	1.12	37	-1.96	2.026	Y	74.32	52.19	N	**1.8**	51.61	Y
	2D(H)	0.30	1.36	1.38	37				122.54	52.19	N	**2.3**	52.12	Y

***Note:**

- Case 1: The differences between the pre-surveyed coordinates and the original LiDAR coordinates.
- Case 2: The differences between the pre-surveyed coordinates and the adjusted LiDAR coordinates derived from using GCPs only.
- Case 3: The differences between the pre-surveyed coordinates and the adjusted LiDAR coordinates derived from using GCPs and features.

4.3.2.5 Categorization of Feature Constraints Concerning Horizontal and Vertical Accuracy Improvements

In order to further analyze how the different types of features contribute to the accuracy improvement in 2D horizontal and vertical directions, here in the testing case, the feature constraints were categorized into horizontal directional (e.g., pavement markings) and vertical directional (for example, traffic light and signs) features.

The locations of the features in LiDAR point cloud identified by using PolyWorks Software are illustrated in Figure 4-32. 76 control points were evenly distributed in study area #1. Half of them were used in the 3DCCT. In addition, 4 horizontal and 6 vertical directional feature constraints were added. Figure 4-31 shows the GCPs used in the 3DCCT and the checking GCPs used in the accuracy assessment.

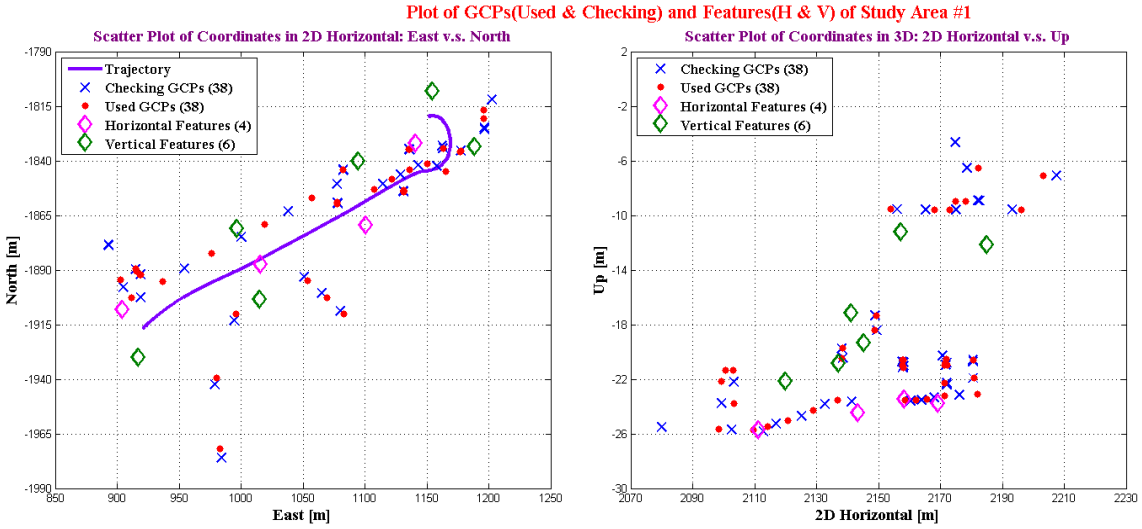

Figure 4-31: Scatter plot of 76 GCPs and 10 features distributed in study area #1. Different colors were selected to represent the checking GCPs, the GCPs, and the horizontal and vertical features used in the 3D conformal transformation.

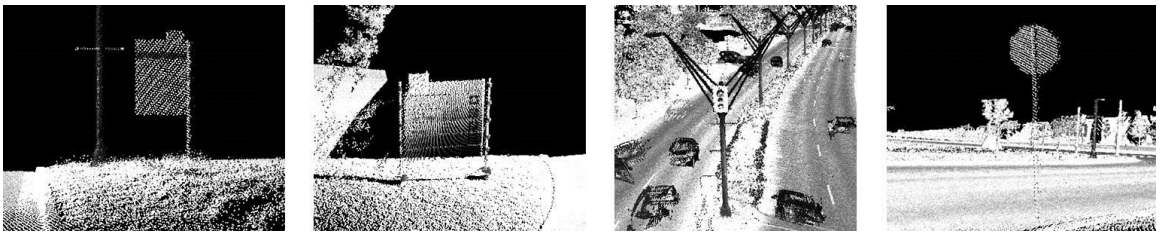

(a)

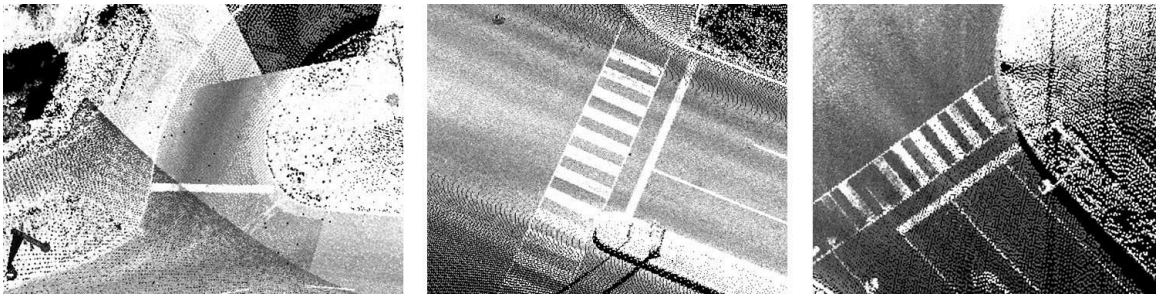

(b)

Figure 4-32: The location of two types of feature constraints extracted from the LiDAR point cloud: (a) Vertical directional features; (b) Horizontal directional features.

The effect of the LiDAR data refinement by adding feature constraints, in addition to the GCPs, was analyzed through the checking GCPs based on the 3DCCT adjustment using all the feature constraints (i.e., case 3 in Section 4.3.2.4), only four horizontal directional features, or only six vertical directional features. Figure 4-33 is the scatter plot of 38 checking GCPs horizontally and vertically. The close-up snapshots of "SWTraffic4" (building-type) and "R11" (ground-type), taken as examples from the checking GCPs, showed that the adjusted LiDAR coordinates after the 7 conformal transformation using all features (pink star), only horizontal directional features (blue cross) were close to each other, and both also closer to the pre-surveyed coordinates (red dot) than the adjusted coordinates using only vertical directional features (cyan diamond)

in horizontal direction illustrated in Figure 4-33(b). However, the adjusted LiDAR coordinates after the 3DCCT parameters based on all features (pink star) and only vertical directional features (cyan diamond) had the same distance to the pre-surveyed coordinates (red dot) in vertical direction, and they were closer than the ones using only horizontal direction features (blue cross) illustrated in Figure 4-33(d). Moreover, all three cases gained their accuracy improvements, in varying degrees, in comparison with the original LiDAR coordinates (green cross). It was worth mentioning that the best refinement was achieved using all feature constraints (pink star).

The differences between the LiDAR solutions refined in different ways and the pre-surveyed coordinates served as the best available error information to evaluate the performance of the being studied accuracy improvement approach. Based on the results in Table 4-16, the best performance came with the results using all feature constraints. On one hand, the horizontal errors after the 3DCCT adjustment using only vertical directional features were obviously bigger than the adjusted ones using all feature constraints or only horizontal directional features. On the other hand, the vertical errors after the 3DCCT adjustment using all feature constraints or only vertical directional features were smaller than the ones after the 3DCCT adjustment only using horizontal directional features.

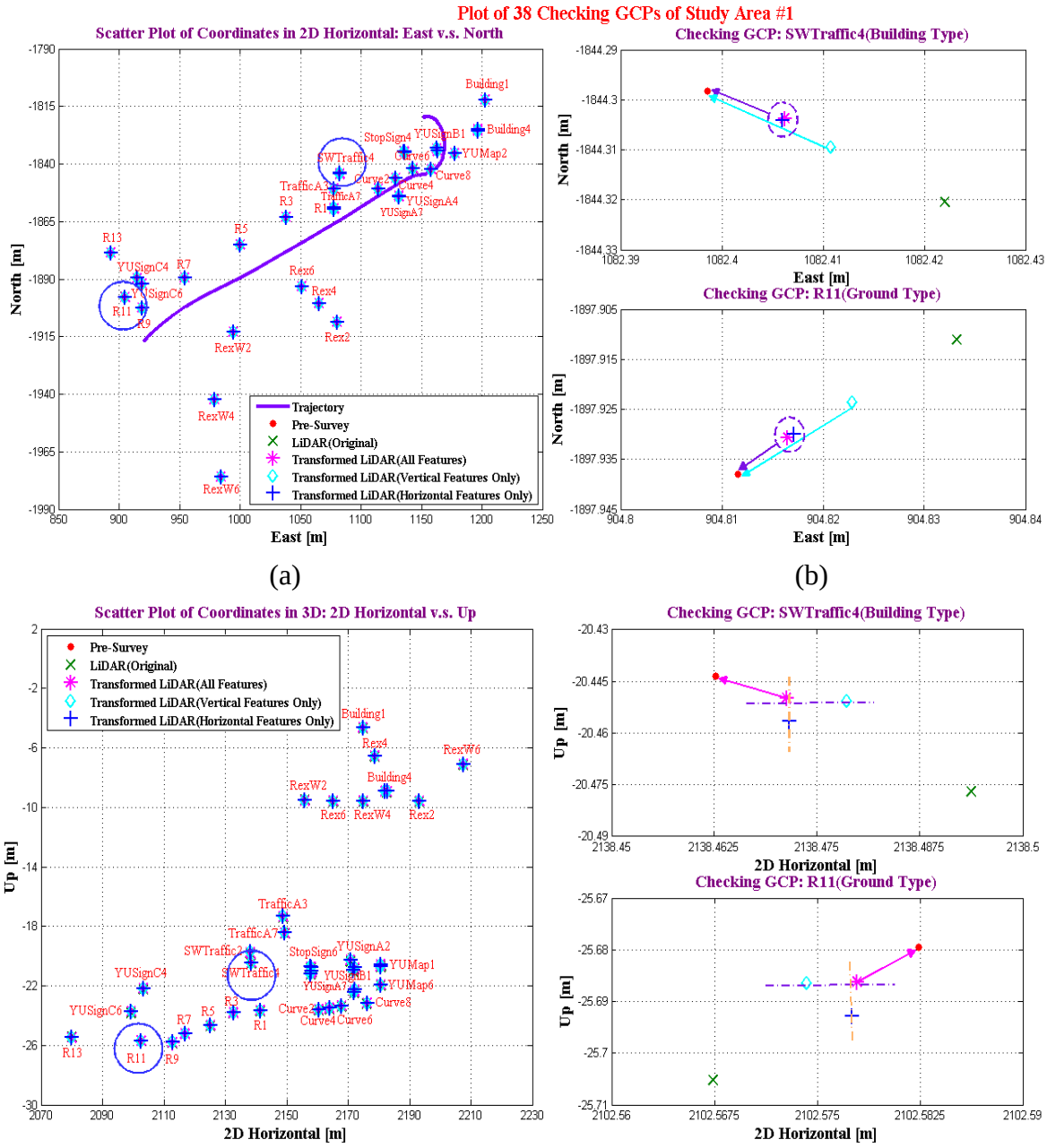

Figure 4-33: Scatter plot of 38 checking GCPs. The adjusted LiDAR coordinates using all of the feature constraints, only the vertical features, and only the horizontal features were plotted in pink star, cyan diamond and blue cross, respectively: (a) & (c) 2D horizontal and vertical; (b) & (d) Close-up details of "SWTraffic4" (building-type) and "R11"(ground-type).

Table 4-16: The differences between the pre-surveyed coordinates and the adjusted LiDAR coordinates using all of the feature constraints, using only 4 horizontal features and only 6 vertical features, respectively, from two checking points "R11" and "SWTraffic4(SW4)".

ID	With All Features [cm]					With Only Vertical Features [cm]					With Only Horizontal Features [cm]				
	N	E	2D	U	3D	N	E	2D	U	3D	N	E	2D	U	3D
SW4	0.55	-0.76	0.94	0.63	1.13	1.13	-1.22	1.66	0.70	1.80	0.60	-0.74	0.95	1.30	1.61
R11	-0.73	-0.49	0.88	0.66	1.10	-1.44	-1.13	1.83	0.69	1.96	-0.80	-0.55	0.97	1.33	1.65

Then the overall quantitative accuracy indexes with 38 checking GCPs were calculated (Appendix C-3). In the same way as above, *t*-test was constructed to determine if the errors were significantly biased, whilst χ^2-test statistics was used to conclude if the overall deviation was satisfied with the specific ±1.5cm accuracy level. The statistic results of the different testing cases are presented in Table 4-17. Based on the two-tailed *t*-test, the differences between the pre-surveyed and the original LiDAR coordinates did contain significant biases in north, east and up. After the refinement process, the mean of the errors became not significant from zero by using all feature constraints, only vertical directional features and only horizontal directional features.

The achieved accuracies of the original LiDAR solution were ±5.0cm (horizontal) and ±3.9cm (vertical) at the 95% confidence level of the Type I error based on the χ^2-test. Using all of the feature constraints, they were improved up to ±2.3cm horizontally and ±1.8cm vertically, the highest among all scenarios. For case 3 where incorporating with only vertical directional features, the achieved vertical accuracy was ±1.9cm, however

the horizontal accuracy was degraded down to ±2.6cm. For case 4 where using only horizontal directional features, the achieved horizontal accuracy remained at ±2.3cm which was compatible with the one using all feature constraints. However, the achieved vertical accuracy was just ±2.2cm according to the χ^2-test at the 95% significant level.

Comparisons among the four different testing cases indicated that the incorporation of both the horizontal and vertical directional features with the GCPs could further refine the LiDAR solutions in both of the horizontal and vertical directions. By only using one type of the feature constraints, either horizontal or vertical, the accuracy in the same direction could significantly be increased, while the accuracy in the other direction could not be improved significantly in comparison with using both of the feature types. Therefore, it is necessary to apply both of the horizontal and vertical directional feature constraints together with the GCPs for further accuracy improvement.

Table 4-17: The statistical analysis of the differences between the pre-surveyed coordinates and the adjusted LiDAR coordinates through the 3DCCT using GCPs with 10 features, 4 horizontal directional features and 6 vertical directional features, respectively, from 38 checking GCPs in Study Area #1.

		Error Statistics				**Two-tailed *t*-test (α =0.05%)** $H_0: \mu = 0$			**χ^2 Test (α = 0.05%) vs. the 95% accuracy** $H_0: \sigma^2 = 1.5^2 cm^2$			$H_1: \sigma^2 = \sigma_a^2$		
Case No.*	Error	Mean [cm]	Stdev [cm]	RMS [cm]	f	t	$t_{f,0.025}$	Accepted (Y/N)	χ^2	$\chi^2_{f,0.05}$	Accepted (Y/N)	σ_a [cm]	χ^2	Accepted (Y/N)
1	**N**	-0.93	2.02	2.20	37	-2.83	2.026	N						
	E	-0.96	2.16	2.34	37	-2.75	2.026	N						
	U	4.79	2.35	5.32	37	12.54	2.026	N	350.24	52.19	N	**3.9**	51.81	Y
	2D(H)	1.34	2.95	3.21	37				574.26	52.19	N	**5.0**	51.68	Y
2	**N**	-0.23	0.96	0.98	37	-1.48	2.026	Y						
	E	-0.19	0.97	0.97	37	-1.21	2.026	Y						
	U	-0.35	1.08	1.12	37	-1.96	2.026	Y	74.32	52.19	N	**1.8**	51.61	Y
	2D(H)	0.30	1.36	1.38	37				122.54	52.19	N	**2.3**	52.12	Y
3	**N**	-0.31	1.09	1.12	37	-1.74	2.026	Y						
	E	-0.35	1.09	1.13	37	-1.95	2.026	Y						
	U	-0.32	1.13	1.16	37	-1.78	2.026	Y	80.22	52.19	N	**1.9**	50.00	Y
	2D(H)	0.46	1.54	1.59	37				156.58	52.19	N	**2.6**	52.12	Y
4	**N**	-0.25	0.96	0.98	37	-1.61	2.026	Y						
	E	-0.19	0.97	0.97	37	-1.23	2.026	N						
	U	-0.43	1.29	1.35	37	-2.07	2.026	Y	105.37	52.19	N	**2.2**	48.98	Y
	2D(H)	0.32	1.36	1.38	37				122.37	52.19	N	**2.3**	52.05	Y

***Note:** Case 1: The differences between the pre-surveyed coordinates and the original LiDAR coordinates.
Case 2: The differences between the pre-surveyed coordinates and the adjusted LiDAR coordinates through the 3DCCT using all directional feature constraints. (i.e., case 3 of section 4.3.2.4)
Case 3: The differences between the pre-surveyed coordinates and the adjusted LiDAR coordinates through the 3DCCT using only the vertical directional features.
Case 4: The differences between the pre-surveyed coordinates and the adjusted LiDAR coordinates through the 3DCCT using only the horizontal directional features.

4.3.2.6 Usage Optimization of Ground Control Points

Similarly to the Optech building test presented in Section 4.2.5, the density of the ground control points on accuracy improvement was investigated for more efficient and effective employment of GCPs in the 3DCCT. Especially, one may reasonably reduce the number of the used GCPs and/or make up for the lack of the available GCPs in some areas by adding the linear or the planar features.

The differences of the adjusted coordinates of the checking points with respect to their pre-surveyed coordinates were compared by utilizing of different numbers of the GCPs (i.e., 50%, 30%, 20% and 10%) through incorporating with the same feature constraints. The selected GCPs in four scenarios are plotted in Figure 4-34. Again, in the LSM implementation, the feature constraints were sequentially added by using *F*-test to detect if any inconsistent existed with the previous observation group and added constraints. Only the qualified constraints were used in the least-squares for 3DCCT model. The scatter plot of 38 checking GCPs and the analysis on the error results of two example points ("SWTraffic4" and "R11") can be found in Appendix D-3.

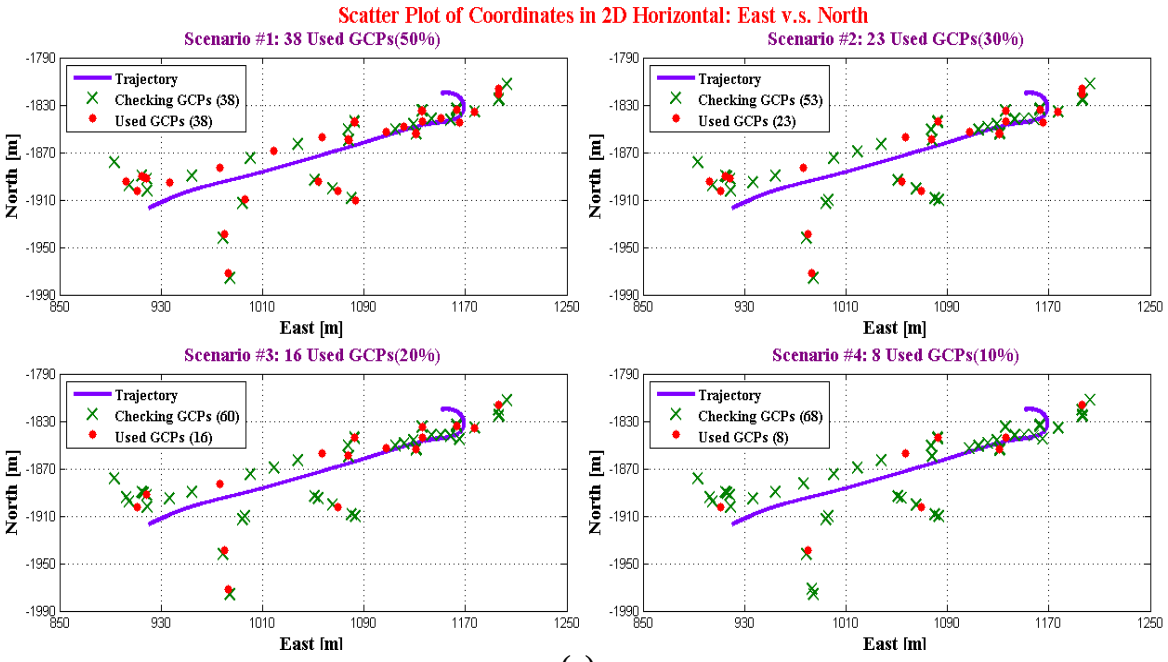

(a)

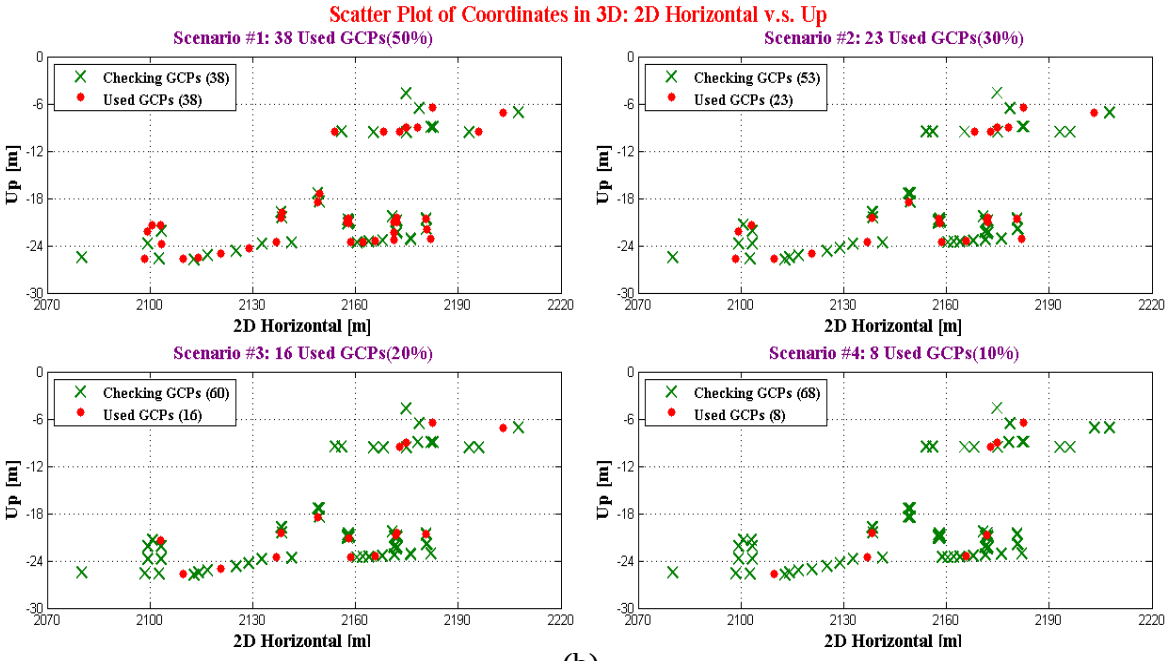

(b)

Figure 4-34: (a) Scatter plot in 2D horizontal plane: scenario #1 - 50% of GCPs used; scenario #2 - 30% GCPs used; scenario #3 - 20% of GCPs used and scenario #4 - 10% GCPs used. (b) Scatter plot in vertical.

The overall quantitative indexes, inclusive of the minimum, the maximum, the mean, the standard deviation and the RMS, for the discrepancies of 38 checking GCPs were also calculated (see Appendix C-4). Table 4-18 summarizes the statistical results of different test cases. The differences between the pre-surveyed and the original LiDAR coordinates contained significant biases in north, east and up directions based on the two-tailed *t*-test. After the adjustment based on the 3D conformal transformation, the mean of the errors with their refined coordinates became insignificant from zero for all the test cases.

The achieved accuracies of the original LiDAR solution from the checking GCPs were ±5.0cm (horizontal) and ±3.9cm (vertical) at the 95% confidence level. They became ±2.3cm in horizontal and ±1.8cm in vertical, the highest among all of the scenarios, after the 3DCCT adjustment using 38 GCPs (i.e., 50%). Moreover, the vertical accuracies were ±2.0cm and ±2.2cm for the results based on 23 GCPs (30%) and 16 GCPs (20%), respectively, with the same feature constraints. The corresponding achieved horizontal accuracies were ±2.6cm and ±2.7cm. Although more GCPs could achieve better accuracy, the performance was not decreased significantly by reducing a certain number of the GCPs, e.g., down to 20 percentages of the total number of control points in this case study. Furthermore, for test case 5 where only 8 GCPs (10%) were used in the 3D conformal transformation, the horizontal accuracy was decreased down to ±3.4cm and the achieved vertical accuracy became ±2.5cm, which were significantly decreased in

comparison with the ones from the other three scenarios.

Based on the results from all of the test cases, the more GCPs were used, the better accuracy could be achieved in both horizontal and vertical directions. However, the overall accuracies were not decreased significantly here specifically by reducing the number of the used GCPs down to between 20 and 30 percent of the total number of the GCPs aided by straight line and planar patch feature constraints. However, the 3D LiDAR positioning accuracy was decreased dramatically using only 10 percent (i.e., 8 GCPs) of the total GCPs in the 3DCCT adjustment. Therefore, it is necessary to select the control points efficiently and effectively by considering the project budget and minimal required accuracy. The conclusions from the current test are consistent with the ones from the previous Optech building test presented in section 4.2.5.

Table 4-18: The statistical analysis of the differences between the pre-surveyed coordinates and the adjusted LiDAR coordinates through the 3DCCT derived from using 38 GCPs, 23 GCPs, 16 GCPs and 8 GCPs with the same feature constraints, respectively, from 38 checking GCPs in the Study Area #1.

		Error Statistics				**Two-tailed *t*-test (α=0.05%) H_0: $\mu = 0$**			**χ^2 Test (α=0.05%) vs. the 95% accuracy H_0: $\sigma^2 = 1.5^2 cm^2$**			**H_1: $\sigma^2 = \sigma_a^2$**		
Case No.*	Error	Mean [cm]	Stdev [cm]	RMS [cm]	f	t	$t_{f,0.025}$	Accepted (Y/N)	χ^2	$\chi^2_{f,0.05}$	Accepted (Y/N)	σ_a [cm]	χ^2	Accepted (Y/N)
1	**N**	-0.93	2.02	2.20	37	-2.83	2.026	N						
	E	-0.96	2.16	2.34	37	-2.75	2.026	N						
	U	4.79	2.35	5.32	37	12.54	2.026	N	350.24	52.19	N	**3.9**	51.81	Y
	2D(H)	1.34	2.95	3.21	37				574.26	52.19	N	**5.0**	51.68	Y
2	**N**	-0.23	0.96	0.98	37	-1.48	2.026	Y						
	E	-0.19	0.97	0.97	37	-1.21	2.026	Y						
	U	-0.35	1.08	1.12	37	-1.96	2.026	Y	74.32	52.19	N	**1.8**	51.61	Y
	2D(H)	0.30	1.36	1.38	37				122.54	52.19	N	**2.3**	52.12	Y
3	**N**	-0.25	1.05	1.07	37	-1.49	2.026	Y						
	E	-0.27	1.07	1.09	37	-1.58	2.026	Y						
	U	-0.37	1.17	1.21	37	-1.97	2.026	Y	86.03	52.19	N	**2.0**	48.39	Y
	2D(H)	0.37	1.50	1.53	37				148.56	52.19	N	**2.6**	49.45	Y
4	**N**	-0.27	1.13	1.15	37	-1.48	2.026	Y						
	E	-0.31	1.11	1.14	37	-1.72	2.026	Y						
	U	-0.35	1.32	1.35	37	-1.62	2.026	Y	109.67	52.19	N	**2.2**	50.98	Y
	2D(H)	0.41	1.59	1.62	37				165.90	52.19	N	**2.7**	51.20	Y
5	**N**	-0.34	1.40	1.42	37	-1.48	2.026	Y						
	E	-0.42	1.45	1.49	37	-1.79	2.026	Y						
	U	-0.41	1.49	1.53	37	-1.70	2.026	Y	140.24	52.19	N	**2.5**	50.49	Y
	2D(H)	0.54	2.01	2.06	37				266.17	52.19	N	**3.4**	51.81	Y

***Note:** Case 1: The differences between the pre-surveyed coordinates and the original LiDAR coordinates.
Case 2: The differences between the pre-surveyed coordinates and the adjusted LiDAR coordinates using 38 GCPs and features.
Case 3: The differences between the pre-surveyed coordinates and the adjusted LiDAR coordinates using 23 GCPs and features.
Case 4: The differences between the pre-surveyed coordinates and the adjusted LiDAR coordinates using 16 GCPs and features.
Case 5: The differences between the pre-surveyed coordinates and the adjusted LiDAR coordinates using 8 GCPs and features.

4.3.3 Results of Study Area #2

4.3.3.1 Overview

The loop around Black Creek Pioneer Village in Toronto, Canada was chosen as Study Area #2. This test was designed to validate the refinement process of terrestrial LiDAR solutions after the 3DCCT using LSM and also the different strategies in the normal working environment, in other words, in a relative big area with limited ground control points and feature constraints and at the regular street speed limit. Similar to Optech building test and Study Area #1 test, two strategies were implemented by effectively and efficiently employing either GCPs or GCPs together with linear/planar feature constraints, respectively, to attain accuracy improvement of the terrestrial LiDAR solution and are summarized as follows:

1) Segmental 3D conformal coordinate transformation (Section 4.3.3.3)
2) Usage optimization of ground control points (Section 4.3.3.4)

The data acquisition in Study Area #2 was performed using the same vehicle on the same day as in Study Area #1. The Optech GPS reference station was again used as the known point in the control network and the data acquisition. Instead of using the total station system, the rapid static combined with stop-and-go GPS approach was applied to observe the GCPs. The data was a 3km long loop consisted of 135 ground control points and 8 features constraints. In addition, the accuracy criteria, the statistic test and the approaches applied to the accuracy improvement and assessment using the checking GCPs here are the same as the ones described in Section 4.2.3.1.

4.3.3.2 Studying Area and Data Acquisition

4.3.3.2.1 Terrestrial Mobile LiDAR Data Acquisition and Processing

The mobile LiDAR data was collected using the same Optech Lynx V200 mobile mapping vehicle, started from Murray Ross Parkway around the north-west corner of Rexall Tennis Center, was heading north to Steeles Ave West, made a left turn onto Steeles Ave West to west, had a second left turn onto Jane Street, then heading south to Shoreham Drive, and finally came back to the start point. LiDAR data acquisition was performed using the configuration parameters of the laser PRF of 250 kHz and the mirror speed of 200 Hz at the speed limit of 60km/h. The horizontal, vertical profiles and the velocity profile of the POS LV trajectory are given in Figure 4-35.

The overview of point cloud of the scanned scenes is shown in Figure 4-36. The performance of the direct georeferencing system resulted from POS LV420 is shown in Figure 4-37 based on the provided SBET file. As usual, the horizontal position accuracy (1σ) was better than ±2cm, while the vertical accuracy (1σ) was around ±3cm.

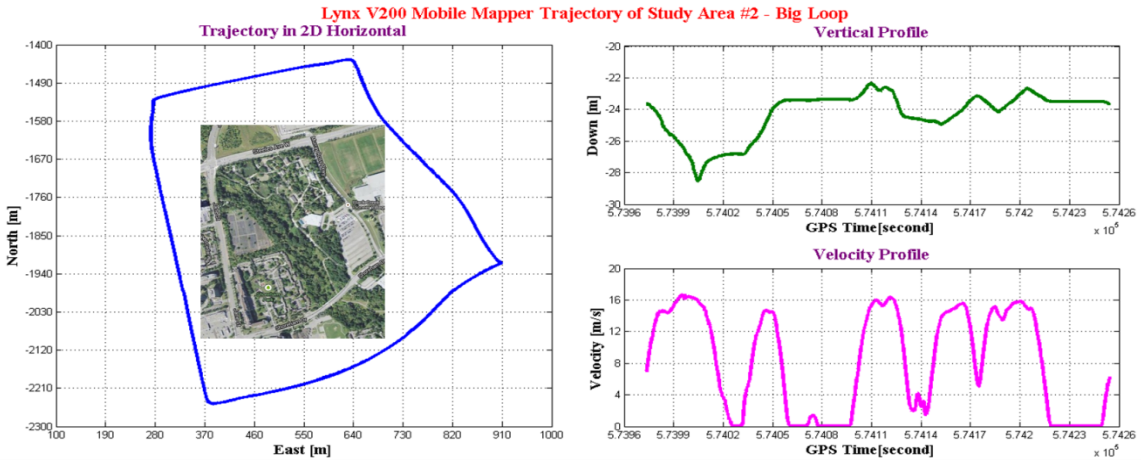

Figure 4-35: The trajectory profiles in 2D horizontal, vertical and velocity in study area #2.

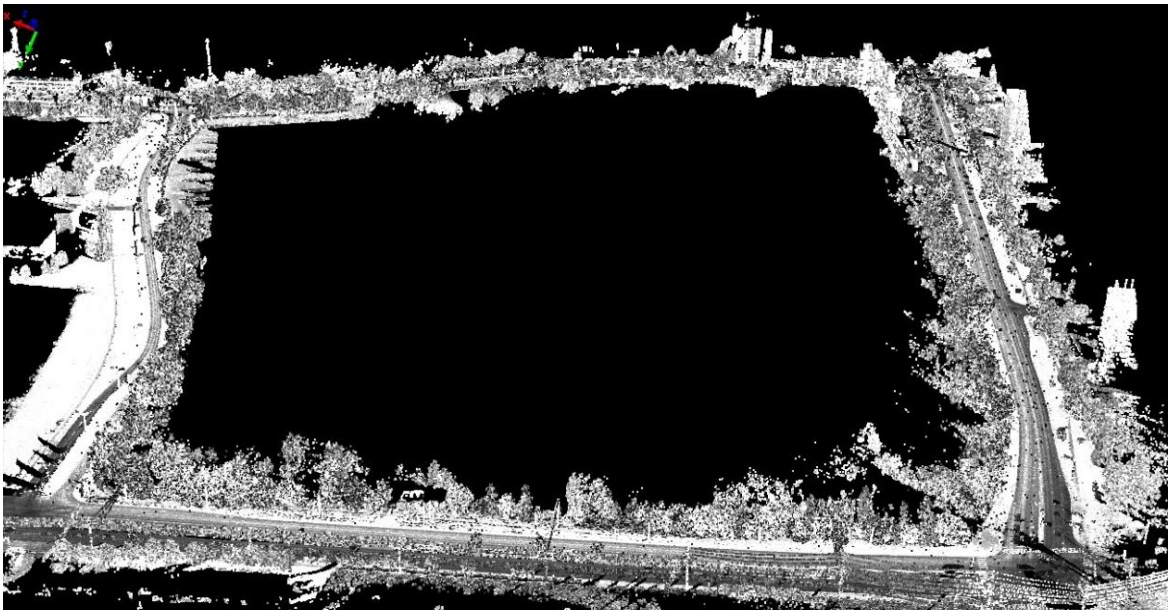

(a)

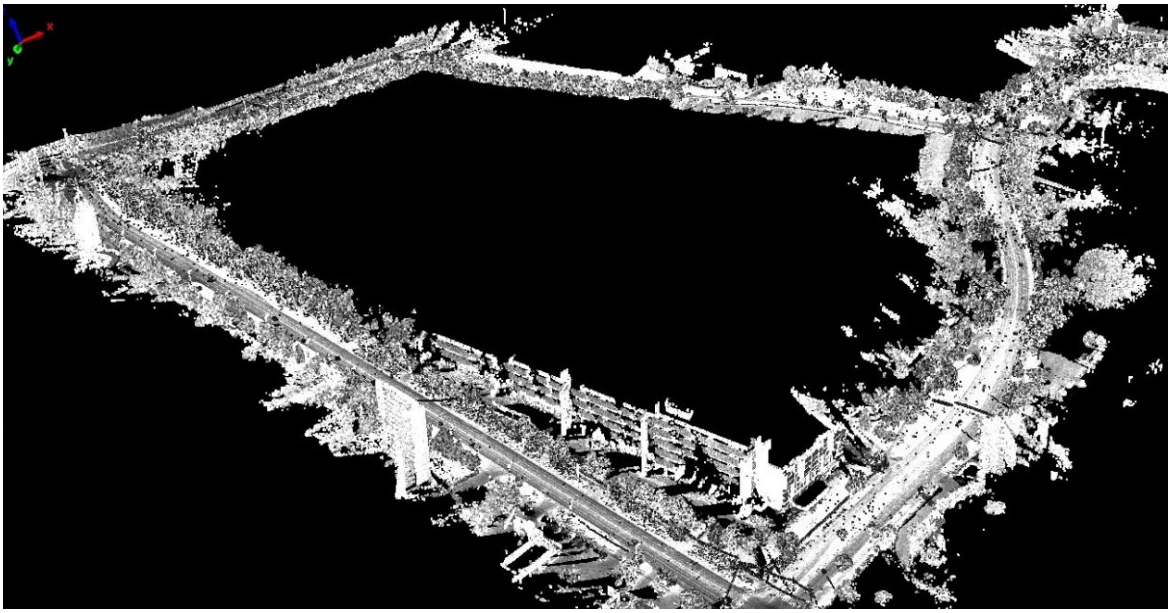

(b)

Figure 4-36: Overview of the scanned scene in study area #2 (Steeles Ave W – Murray Ross Parkway – Shoreham Dr – Jane St) in Toronto, Canada with the laser PRF of 250 kHz and the mirror speed of 200 Hz: (a) Side view (bottom up) from Steeles Ave W. (b) Side view (bottom up) from intersection of Jane St and Shoreham Dr.

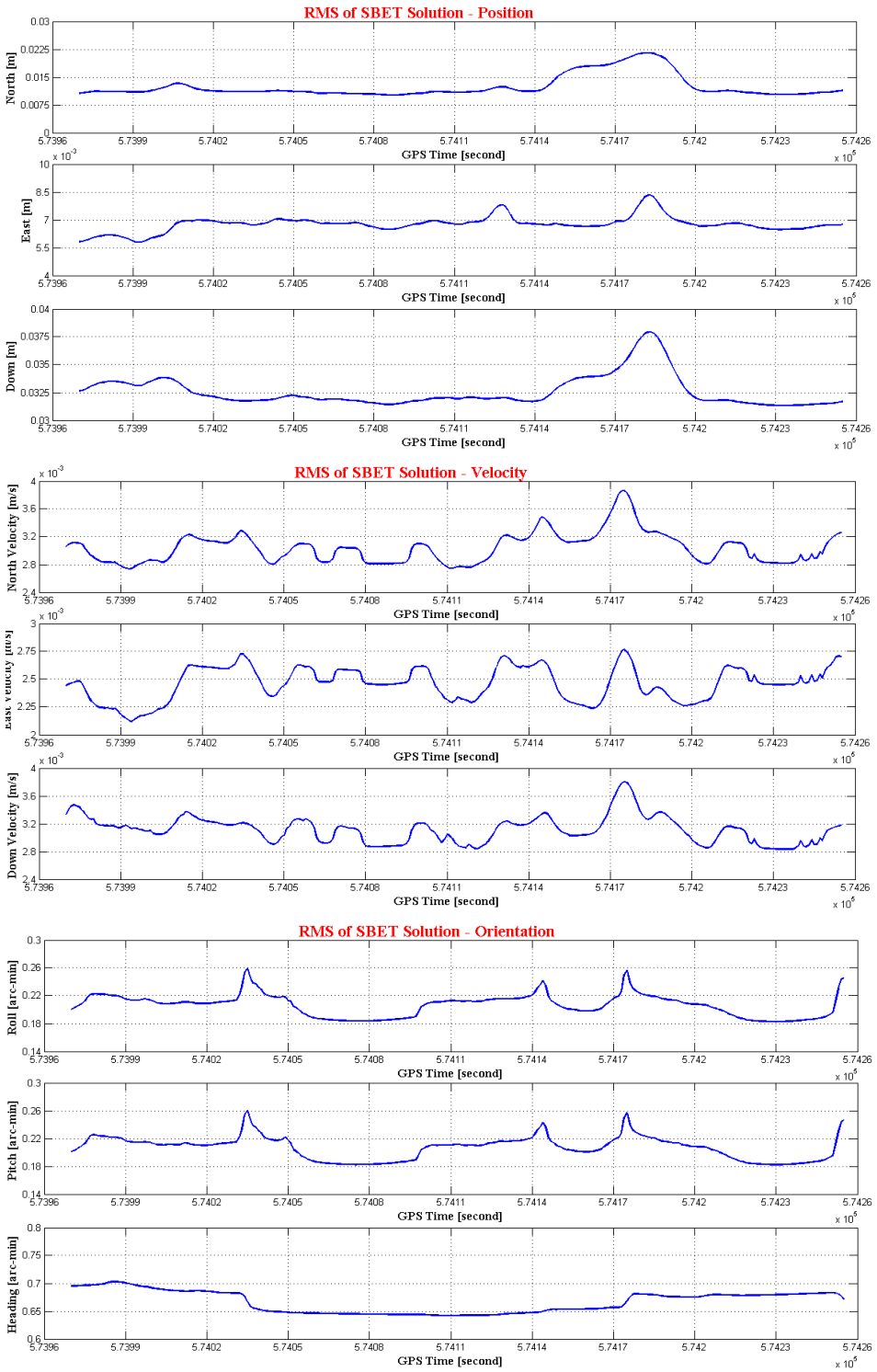

Figure 4-37: The RMS error of the position (north, east and down), orientation (roll, pitch and heading) and velocity (north, east and down) versus GPS time were presented in blue lines.

4.3.3.2.2 Determination of Coordinates of GCPs and Features

The same 3D geodetic control network as shown in Figure 4-23 in study area #1 was used. All of the selected GCPs and features were determined with respect to Optech GPS reference station, the same reference used by the mobile mapping vehicle. The control network was adjusted by using Columbus Best-Fit Computing Software. The final WGS84 coordinates of the control points can be found in Table 4-13.

Some characteristic points along the road curbs were selected as the GCPs under the consideration of realistic highway/urban environments. The separation between the GCPs is from a few meters to 50 meters in order to outline the shape of the route. In this test, only the GPS technique was applied to determine the GCPs due to the consideration of the field safety and work load. The chosen ground control points along the curbs were observed using static baseline approach (the combination of the rapid static and the stop-and-go) by setting up one GPS receiver over each control point for 5 minutes shown in Figure 4-38 (b) and (c), at the same time, set up another GPS receiver over the local control station O_1 by continually logging the data, of which O_1 was linked to the Optech base station. The overview of the GPS observation configuration is given in Figure 4-38(a).

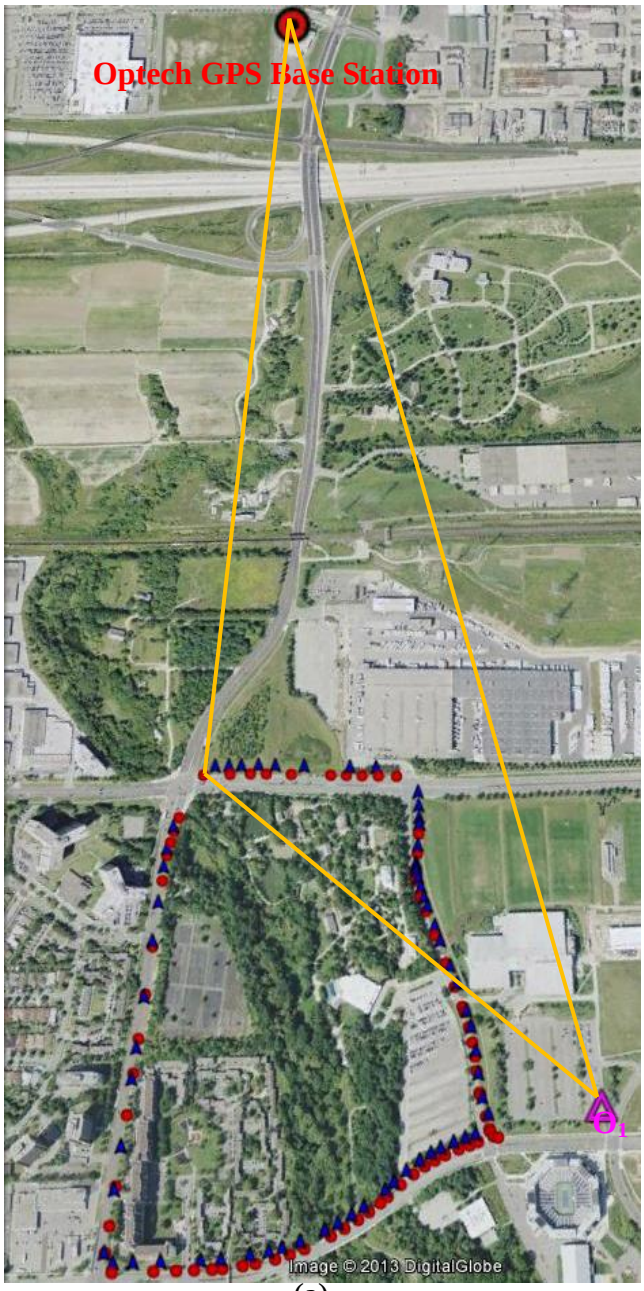

(a)

(b)

(c)

Figure 4-38: The kinematic RTK GPS approach of determination of 3D coordinates of ground control points in study area #2. (a) The overview of the GPS configuration, where the red dots represented the control points in the first run and the blue arrows represented the control points in the second run, respectively. (b) - (c) The field approach by setting up the GPS receiver on the control points that beside the road curbs.

A double-run loop measurement was also performed to guarantee the good quality of GPS observations. There were 68 GCPs in the first run and 67 GCPs determined in the second run, respectively, shown Figure 4-39. For the execution of the 3DCCT, the coordinates were calculated in local North-East-Up system based on the Optech GPS reference station. The loop was divided into four segments after the driving directions (north, west, south and east). The number of GCPs in each section is summarized in Table 4-19. The distribution of all control points in study area #2 is overviewed in Figure 4-40.

Table 4-19: The number of GCPs in study area #2

Segment	Run #1	Run #2
Segment #1(East)	23	23
Segment #2 (North)	10	8
Segment #3 (West)	13	11
Segment #4 (South)	22	25
Total	**68**	**67**

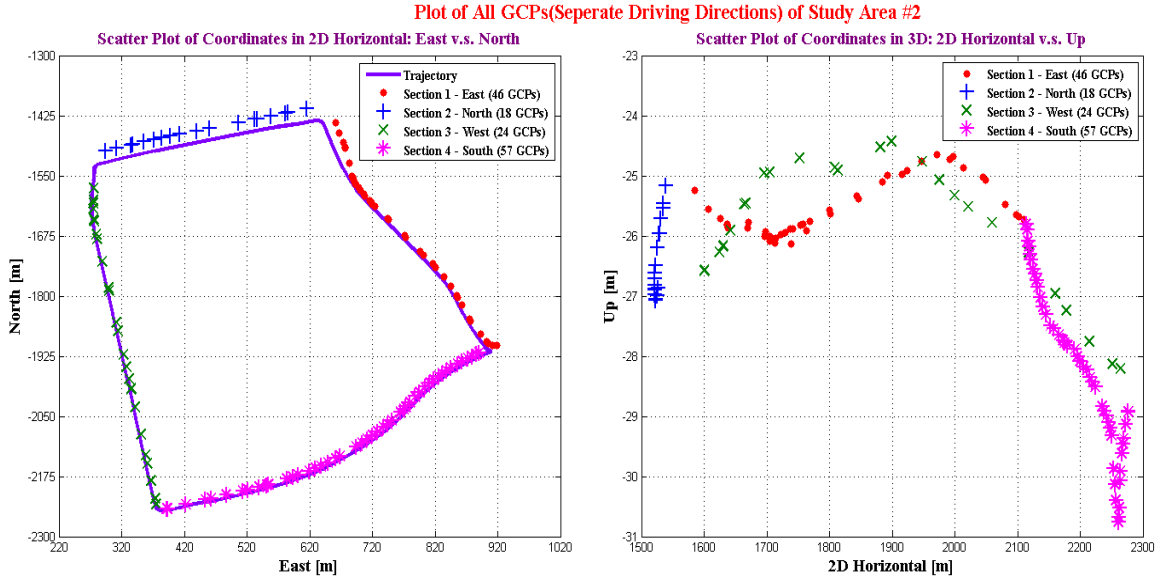

Figure 4-39: Scatter plot of 135 GCPs in study area #2 (2D horizontal and vertical).

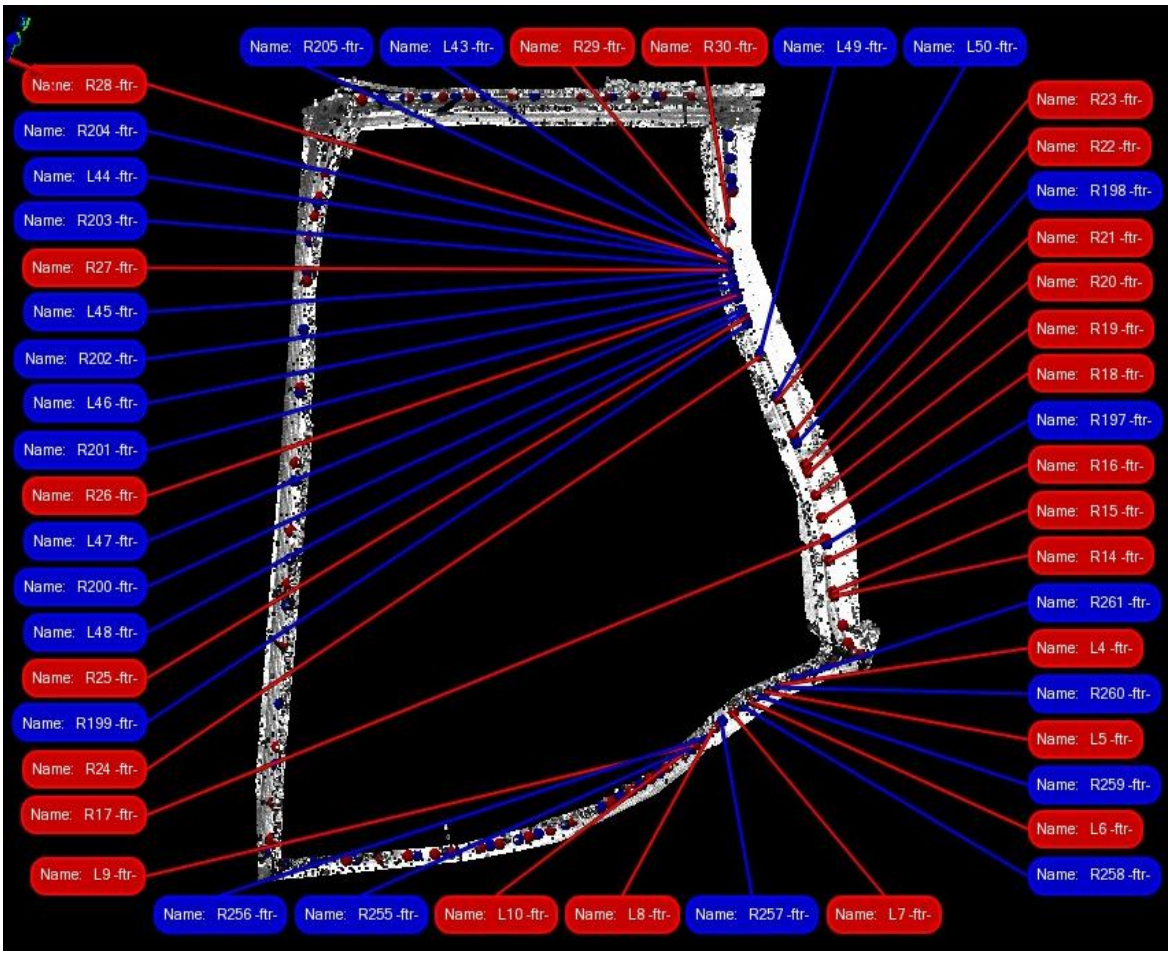

Figure 4-40: The overview of GCPs distribution from LiDAR point cloud in study area #2 (Murray Ross Pkwy – Steeles Ave. W – Jane St. - Shoreham Dr.), Toronto, Canada.

4.3.3.3 Segmental 3D Conformal Coordinate Transformation

The whole test data as a loop was divided into four segments based on the driving directions. Thus, the 3DCCT parameters were determined separately so that a better compensation may expectantly be reached for some of the left-over systematic errors in the different parts of the data strip. Then, all of the GCPs from the first run were used in 3D conformal coordinate transformation, and the GCPs from the second run were left as checking points for accuracy assessment. Figure 4-41 presents the used and checking GCPs.

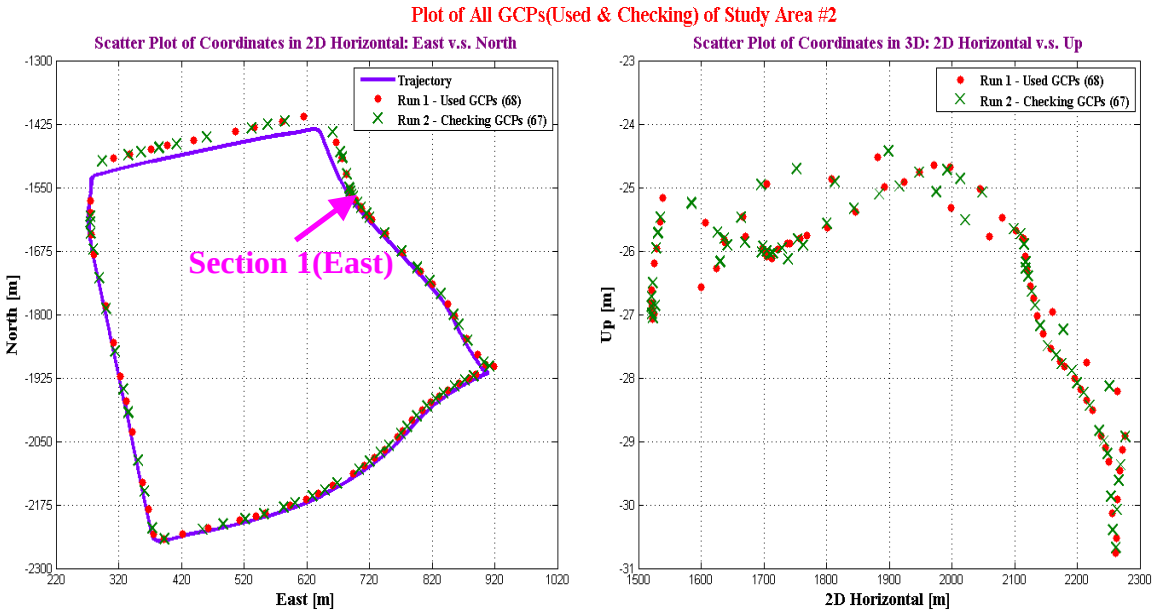

Figure 4-41: Scatter plot of 135 GCPs (65 used & 67 for checking) distributed in study area #2 from a double-run static GPS observation (2D horizontal and vertical).

For each segment, the 3DCCT was performed under two different strategies: i).

applying all of 68 GCPs from the first run to the entire data loop as a whole and ii). applying the GCPs only associated with each segment separately. As an example, the results from Segment #1 (on Shoreham Drive) is here illustrated, with which 23 GCPs were involved in the segmental 3DCCT. Figure 4-42 presents the 23 checking GCPs on Shoreham Drive in both 2D horizontal and vertical direction. Specifically by taking the enlarged snapshots of two checking points "L49" and "R14" as examples, the refined LiDAR coordinates (pink star) from its segmental refinement were clearly closer to the pre-surveyed coordinates (red dot) than the ones (blue cross) based on the whole loop integrated refinement using all 68 GCPs from first run in north, east and up. Their differences versus the pre-surveyed coordinates are given in Table 4-20. Although the differences under both of the refinement strategies became smaller against the original LiDAR solution, the ones based on the 23 GCPs only from Segment #1 were smaller and the 3D positional differences were decreased by around 1.5cm in comparison with the ones using all 68 GCPs from the first run of GPS observation.

Table 4-20: The differences between the pre-surveyed coordinates and the original LiDAR coordinates, the adjusted LiDAR coordinates using 68 GCPs from all the segments and 23 GCPs from Segment #1 only, respectively, from two checking points "L49" and "R14".

ID	Original Differences [cm]					With 68 GCPs of Run 1 [cm]					With 23 GCPs of Section 1 [cm]				
	N	E	2D	U	3D	N	E	2D	U	3D	N	E	2D	U	3D
L49	-3.42	-3.16	4.66	3.35	5.74	-1.64	-1.76	**2.41**	**1.46**	**2.81**	-0.67	-0.76	**1.01**	**0.63**	**1.19**
R14	-2.25	-3.62	4.26	3.59	5.57	-1.52	-2.02	**2.53**	**1.79**	**3.10**	-0.73	-1.21	**1.41**	**0.88**	**1.66**

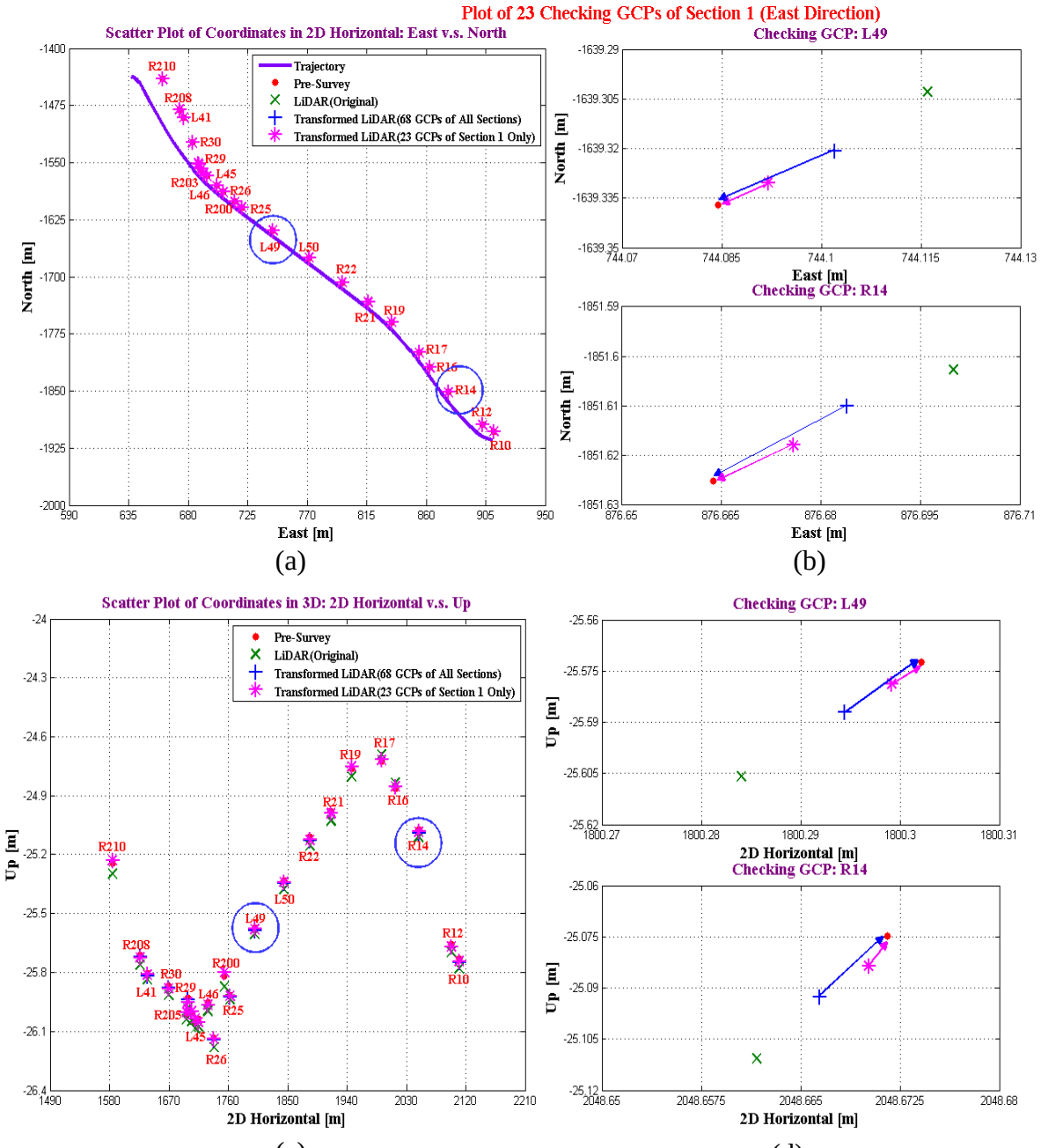

Figure 4-42: Scatter plot of 23 checking GCPs in Segment #1. The adjusted LiDAR coordinates using all 68 GCPs from the first run of GPS observation (i.e., all the segments) and 23 GCPs from Segment #1 only are presented in blue cross and pink star, respectively: (a) & (c) 2D horizontal and vertical; (b) Close-up details of "L49" and "R14".

To characterize the differences between the pre-surveyed coordinates and the adjusted LiDAR coordinates refined using two groups of the 7 conformal transformation parameters for Segment #1, the overall quantitative indexes were calculated inclusive of the minimum, maximum, mean, standard deviation and RMS (root mean square) as in Appendix C-5. A summary of the corresponding statistic *t*-tests and alternate χ^2-tests with the differences from 23 checking GCPs with respect to the pre-surveyed coordinates is presented in Table 4-21.

Based on the two-tailed *t*-test, the differences between the pre-surveyed and the original LiDAR coordinates of the checking points were significantly biased in north, east and up directions. After the segmental adjustment through the 3DCCT process using 23 GCPs associated with Segment #1 only, the mean of the coordinate differences was not significantly different from zero. However, the mean value of the coordinate differences after the adjustment process with the entire test loop using all of 68 GCPs still contained significant biases in 2D horizontal direction.

The achieved accuracies of the original LiDAR solution with the checking points were ±4.7cm (horizontal) and ±3.7cm (vertical) at the 95% confidence level according to the alternate hypothesis under the χ^2-test. Through the refinement process using all of the 68 GCPs together with the entire test data, the vertical accuracy was improved up to ±2.2cm, while it only achieved ±2.7cm in horizontal. Moreover, as the segmental

refinement process was done using 23 GCPs only with Segment #1, the achieved horizontal accuracy was further increased from ±4.7cm to ±2.3cm, and the vertical accuracy became ±1.9cm based on the χ^2-test at the 95% confidential level.

The comparisons among three different cases indicated that the segmental 3DCCT could achieve better accuracies in both horizontal and vertical directions using the GCPs only with Segment #1. In addition to this, the conclusions were confirmed through the results from the rest of three segments. Therefore, it is necessary to segment the LiDAR strip into smaller portions and introduce the 3D conformal transformation separately to each segment. In other words, the 3D conformal transformation may not be valid for a large stretch of dataset. The conclusions were consistent with the ones from the previous Optech building test shown in section 4.2.3.1.

Table 4-21: The statistical analysis of the differences between the pre-surveyed coordinates, the original LiDAR coordinates, and the adjusted LiDAR coordinates through the 3DCCT derived from using 68 GCPs from all the segments and 23 GCPs from Segment #1 only, respectively, from 23 checking GCPs with Segment #1 in Study Area #2.

		Error Statistics				**Two-tailed *t*-test (α =0.05%) H_0: $\mu = 0$**			**χ^2 Test (α = 0.05%) vs. the 95% accuracy H_0: $\sigma^2 = 1.5^2 cm^2$**			**H_1: $\sigma^2 = \sigma_a^2$**		
Case No.*	Error	Mean [cm]	Stdev [cm]	RMS [cm]	f	t	$t_{f,0.025}$	Accepted (Y/N)	χ^2	$\chi^2_{f,0.05}$	Accepted (Y/N)	σ_a [cm]	χ^2	Accepted (Y/N)
1	**N**	-1.59	2.17	2.67	22	-3.51	2.074	N						
	E	-2.05	1.95	2.82	22	-5.04	2.074	N						
	U	3.56	2.34	4.24	22	7.31	2.074	N	205.08	33.92	N	**3.7**	33.70	Y
	2D(H)	2.59	2.92	3.88	22				332.68	33.92	N	**4.7**	33.89	Y
2	**N**	-0.60	1.19	1.34	22	-2.44	2.074	N						
	E	-0.57	1.17	1.31	22	-2.32	2.074	N						
	U	0.42	1.37	1.44	22	1.46	2.074	Y	70.80	33.92	N	**2.2**	32.91	Y
	2D(H)	0.83	1.67	1.88	22				108.91	33.92	N	**2.7**	33.61	Y
3	**N**	-0.41	1.06	1.16	22	-1.87	2.074	Y						
	E	-0.34	0.93	1.02	22	-1.74	2.074	Y						
	U	0.35	1.19	1.25	22	1.41	2.074	Y	53.24	33.92	N	**1.9**	33.19	Y
	2D(H)	0.54	1.41	1.54	22				78.29	33.92	N	**2.3**	33.30	Y

***Note:**

- Case 1: The differences between the pre-surveyed coordinates and the original LiDAR coordinates.
- Case 2: The differences between the pre-surveyed coordinates and the adjusted LiDAR coordinates derived from using 68 GCPs from all the segments.
- Case 3: The differences between the pre-surveyed coordinates and the adjusted LiDAR coordinates derived from using 23 GCPs from Segment #1 only.

4.3.3.4 Usage Optimization of Ground Control Points

Similarly to the Optech building test data presented in section 4.2.5 and the validation test in study area #1 presented in section 4.3.2.6, the optimal density of the ground control points were investigated in order to efficiently and effectively employ those measurements, here even with much longer data strips in a much more realistic filed environment. As mentioned above, there were 135 control points in total in study area #2. The accuracy performance using the checking GCPs was compared among different refinement strategies in terms of six different control point separations from 25m to 200m (i.e., 25m, 50m, 75m, 100m, 150m and 200m). The plot of the selected GCPs for six scenarios is presented in Figure 4-43.

Figure 4-44 is the scatter plot of 59 checking GCPs in the test scene with the different separations. By looking into the details of two checking points “R224” and “L25” as examples, the adjusted LiDAR coordinates using the 3DCCT parameters derived from 74 GCPs (out of 135) with the separation of 25m (pink star) were the closest ones to the pre-surveyed coordinates (red dot). In addition, the refined LiDAR coordinates using the 3DCCT parameters derived from 42 GCPs with the separation of 50m (purple triangle) and from 31 GCPs with the separation of 75m (blue cross) were close to each other, i.e., they were deviated quite the same from the reference coordinates. However, the adjusted LiDAR coordinates using the 3DCCT parameters derived from 17 GCPs with the separation of 150m (yellow pentagram) and from 10 GCPs with the

separation of 200m (brown square) were much further away from their pre-surveyed coordinates than the ones from the other cases. With respect to the pre-surveyed points as the reference coordinates, the coordinate differences derived from the above mentioned various adjustments through the use of the GCPs with the different separations were used to assess how the different cases may improve the solution accuracy of the LiDAR point cloud. Based on the numerical results of two selected checking points shown in Table 4-22, the coordinate differences corresponding to the 3DCCT adjustment based on the GCPs at the separation of 25m were the smallest ones, as the adjustment based on the GCPs at the separation of 200m generated the biggest differences. Among these multiple cases, the accuracy performance with the refinement using the GCP separation of 100m was only degraded by around 1cm in 3D in comparison with the one having the separation of 25m.

Table 4-22: The differences between the pre-surveyed coordinates and the adjusted LiDAR coordinates using the GCPs separated by 25m, 100m and 200m, respectively, from two checking points "R224" and "L25".

ID	With 25m Interval [cm]					With 100m Interval [cm]					With 200m Interval [cm]				
	N	E	2D	U	3D	N	E	2D	U	3D	N	E	2D	U	3D
R224	-0.55	0.78	0.95	0.84	1.27	-1.28	1.23	1.78	1.24	2.17	-2.00	2.21	2.98	2.53	3.91
L25	0.56	0.93	1.09	0.64	1.26	1.23	1.45	1.90	1.35	2.33	2.01	2.13	2.93	2.46	3.82

The overall quantitative indexes through the coordinate differences of the checking GCPs were calculated inclusive of the minimum, maximum, mean, standard deviation and RMS (Appendix C-6). In addition, the *t*-test and χ^2-test were constructed and their

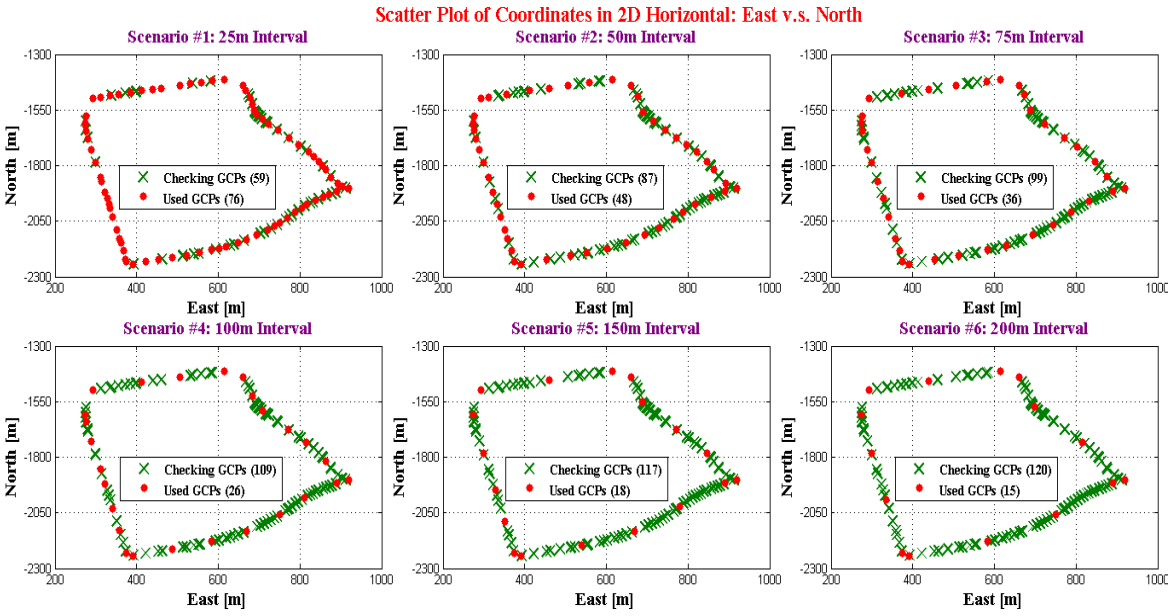

(a)

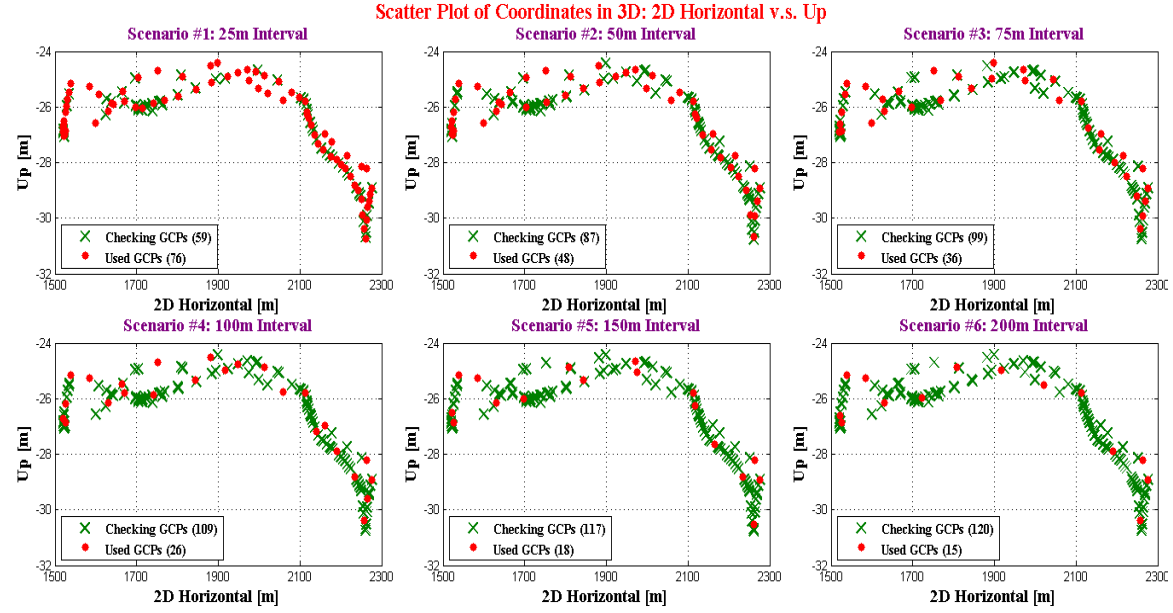

(b)

Figure 4-43: (a) Scatter plot of the GCPs in 2D horizontal for six scenarios (25m, 50m, 75m, 100m, 150m and 200m separations). (b) Scatter plot of the GCPs in vertical.

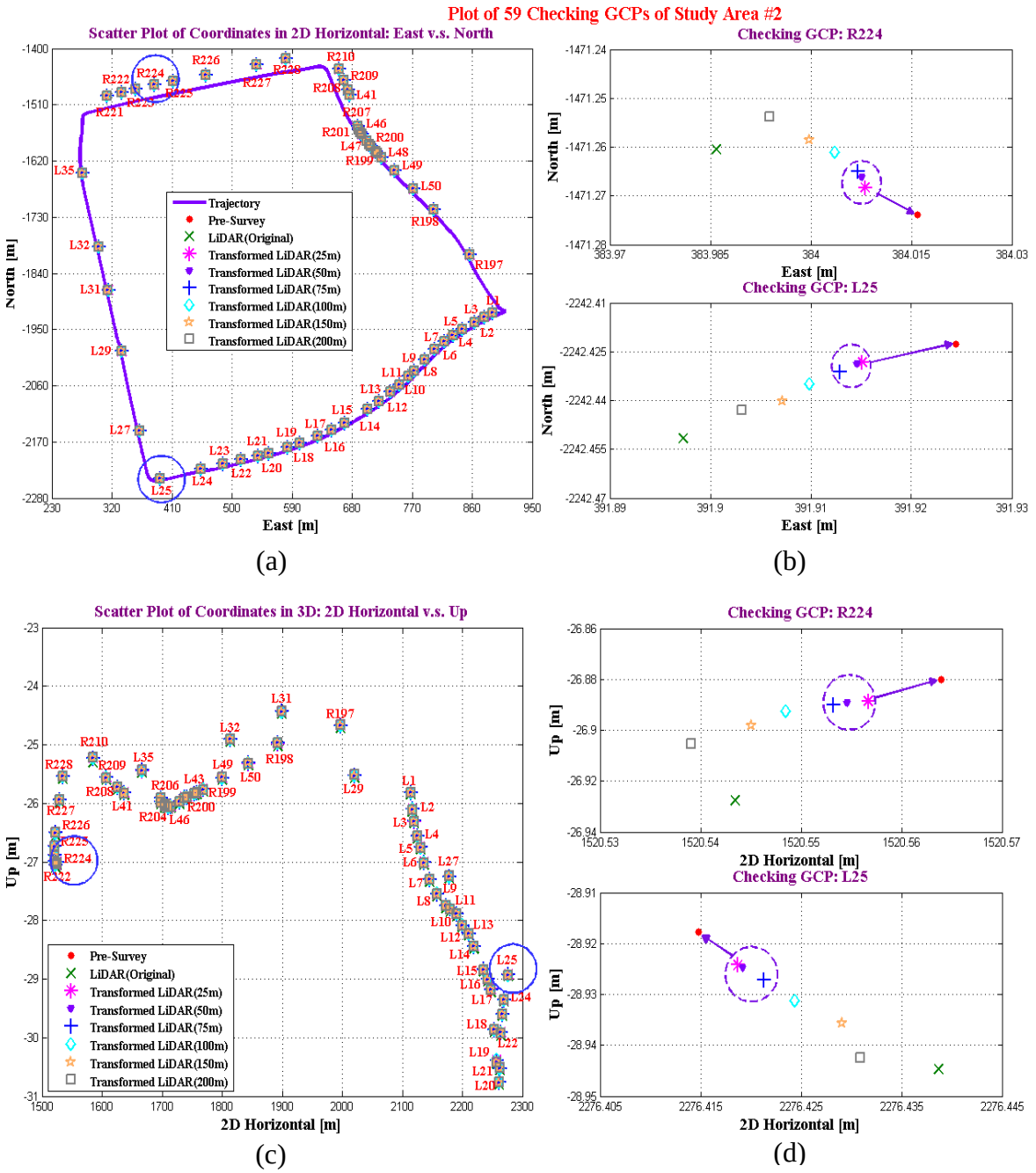

Figure 4-44: Scatter plot of 59 checking GCPs in the test scene. The adjusted LiDAR coordinates using the GCPs at the different separations of 25m, 50m, 75m, 100m, 150m and 200m were presented in pink star, purple triangle, green cross, cyan diamond, yellow pentagram and brown square, respectively. (a) & (c) 2D horizontal and vertical; (b) & (d) Close-up details of "R224" and "L25".

results are summarized in Table 4-23 for the different cases. The differences between the pre-surveyed and the original LiDAR coordinates, which were used as the direct information about the coordinate errors of the checking points, showed significant biases in north, east and up directions based on the two-tailed *t*-test. After the refining process using the 3DCCT, the mean of the coordinate differences became not significantly different from zero associated with the different GCP separations of 25m, 50m, 75m and 100m. However, the significant biases could not be removed in north, east and up direction with the refinements using the GCP separations of 150m and 200m.

The achieved accuracies of the original LiDAR point cloud were ±6.0cm (horizontal) and ±4.1cm (vertical) by using the checking points at the 95% confidence level. Among all of the scenarios, the highest accuracy, ±2.3cm in horizontal and ±2.0cm in vertical, came from the refinement by using the GCPs at the separation of 25m in the 3DCCT. Moreover, the vertical accuracy was ±2.1cm by using the GCPs at the separations of 50m and 75m, whilst the corresponding horizontal accuracies were ±2.4cm and ±2.6cm, respectively. With the case that the GCPs were used at the separation of 100m, the achieved accuracies were ±2.8cm horizontally and ±2.2cm vertically based on the χ^2-test at the 95% confidential level. Thus, the performance was not degraded a lot as the control point separation was changed from 25m to 100m. Furthermore, with the case where the GCPs were used at the separation of 150m, the achieved vertical accuracy was ±2.4cm;

however, the horizontal accuracy was decreased down to ±3.2cm at the 95% confidence level. The horizontal accuracy was further decreased down to ±3.5cm as the GCP separation was increased to 200m. With the last two cases, the 3D LiDAR positioning accuracies were decreased significantly in comparison with the other cases.

As expected, the results from all the cases showed that the smaller the separation between control points (i.e., more GCPs) is, the more accuracy improvement can be achieved through the 3DCCT. However, the overall accuracies were not degraded very significant (e.g., 5mm in horizontal direction) by utilizing the different GCP separations from 50m, 75m to 100m with the test data from Study Area #2. That is, there will be no more significant gain of the accuracy improvement once the number of control points is increased to a certain level, especially in term of the vertical accuracy. However, as the separation between GCPs was increased up to 150m, even 200m, the 3D positioning accuracy was decreased significantly. Therefore, it is necessary to optimally select the control points efficiently and effectively by considering the project budget and the minimal required accuracy. The conclusions were consistent with the ones from the analysis of Study Area #1 (Section 4.3.2.6). For example, at the 100m GCP separation using 23 GCPs out of 135 GCPs (i.e., ~20%), the accuracy performance was compatible with the performance at the 25m GCP separation using 74 GCPs (i.e., ~50%). In addition, no significant accuracy improvement was gained as the GCP separation was increased up to 200m that used only 10GCPs, lower than 10% of the total GCPs.

Table 4-23: The statistical analysis of the differences between the pre-surveyed coordinates and the adjusted LiDAR coordinates after the 3DCCT using the GCPs at the different separations of 25m, 50m, 75m, 100m, 150m and 200m with the help of the same feature constraints, respectively, from 59 checking GCPs in Study Area #2.

		Error Statistics				**Two-tailed *t*-test (α=0.05%) H_0: μ = 0**			**χ^2 Test (α=0.05%) vs. the 95% accuracy H_0: $\sigma^2 = 1.5^2 cm^2$**			**H_1: $\sigma^2=\sigma_a^2$**		
Case No.*	Error	Mean [cm]	Stdev [cm]	RMS [cm]	*f*	*t*	$t_{f,0.025}$	Accepted (Y/N)	χ^2	$\chi^2_{f,0.05}$	Accepted (Y/N)	σ_a [cm]	χ^2	Accepted (Y/N)
1	**N**	-0.35	2.45	2.45	58	-1.09	2.002	Y						
	E	0.71	2.43	2.51	58	2.26	2.002	N						
	U	3.51	2.41	4.24	58	11.21	2.002	N	572.98	76.78	N	**4.1**	76.69	Y
	2D(H)	0.79	3.45	3.51	58				1223.81	76.78	N	**6.0**	76.49	Y
2	**N**	-0.21	0.93	0.95	58	-1.69	2.002	Y						
	E	0.17	0.92	0.93	58	1.46	2.002	Y						
	U	0.19	1.16	1.17	58	1.26	2.002	Y	133.97	76.78	N	**2.0**	75.36	Y
	2D(H)	0.27	1.31	1.33	58				176.84	76.78	N	**2.3**	75.22	Y
3	**N**	-0.27	1.05	1.08	58	-1.94	2.002	Y						
	E	0.16	0.89	0.90	58	1.38	2.002	Y						
	U	0.26	1.21	1.23	58	1.67	2.002	Y	144.92	76.78	N	**2.1**	73.94	Y
	2D(H)	0.31	1.38	1.40	58				196.33	76.78	N	**2.4**	76.69	Y
4	**N**	-0.25	1.11	1.13	58	-1.71	2.002	Y						
	E	0.19	0.98	0.99	58	1.52	2.002	Y						
	U	0.31	1.23	1.26	58	1.96	2.002	Y	150.31	76.78	N	**2.1**	76.69	Y
	2D(H)	0.31	1.48	1.50	58				225.07	76.78	N	**2.6**	74.91	Y
5	**N**	-0.29	1.16	1.19	58	-1.90	2.002	Y						
	E	0.22	1.08	1.10	58	1.55	2.002	Y						
	U	0.36	1.29	1.33	58	2.14	2.002	N	164.52	76.78	N	**2.2**	76.48	Y
	2D(H)	0.36	1.59	1.62	58				259.95	76.78	N	**2.8**	74.60	Y
6	**N**	-0.37	1.34	1.38	58	-2.11	2.002	N						
	E	0.34	1.26	1.29	58	2.08	2.002	N						
	U	0.77	1.39	1.58	58	4.26	2.002	N	191.22	76.78	N	**2.4**	74.70	Y
	2D(H)	0.50	1.84	1.89	58				348.04	76.78	N	**3.2**	76.47	Y

7	**N**	-0.55	1.47	1.56	58	-2.88	2.002	N							
	E	0.43	1.35	1.41	58	2.44	2.002	N							
	U	0.67	1.46	1.60	58	3.52	2.002	N	212.26	76.78	N	**2.5**	76.41	Y	
	2D(H)	0.70	2.00	2.10	58				413.25	76.78	N	**3.5**	75.90	Y	

***Note: The error information for the coordinates of LiDAR point cloud were analysed as follows:**

- Case 1: The differences between the pre-surveyed coordinates and the original LiDAR coordinates.
- Case 2: The differences between the pre-surveyed coordinates and the adjusted LiDAR coordinates derived from the GCPs at the separation of 25m.
- Case 3: The differences between the pre-surveyed coordinates and the adjusted LiDAR coordinates derived from the GCPs at the separation of 50m.
- Case 4: The differences between the pre-surveyed coordinates and the adjusted LiDAR coordinates derived from the GCPs at the separation of 75m.
- Case 5: The differences between the pre-surveyed coordinates and the adjusted LiDAR coordinates derived from the GCPs at the separation of 100m.
- Case 6: The differences between the pre-surveyed coordinates and the adjusted LiDAR coordinates derived from the GCPs at the separation of 150m.
- Case 7: The differences between the pre-surveyed coordinates and the adjusted LiDAR coordinates derived from the GCPs at the separation of 200m.

5 Accuracy Improvement through Multistrip Adjustment (MA)

5.1 Overview

As concluded in Chapter 4, the utilization of the characterized control points incorporating with the feature constraints could significantly improve the quality of terrestrial mobile LiDAR solutions. Besides, there are still other post-processing methods with good potential for further enhancement of accuracy improvement, which are the center of Chapter 5 and Chapter 6.

On one hand, it still cannot meet the pre-defined accuracy requirement of ±1.5cm (1σ) on the hard surface in engineering surveys according to the testing results discussed in Chapter 4. Even though different strategies were tested out, the achieved horizontal accuracies were only 2.2cm (Section 4.3.2.3) by categorizing the GCPs and 2.3cm (Section 4.3.3.3) by segmenting the LiDAR strip. On the other hand, one can seek for alternative technique to further refine the terrestrial mobile LiDAR solution towards more accuracy improvement.

The next attempt, the focus of the current chapter, is to implement the multistrip adjustment (MA) by taking advantages of the overlapped data strips and/or the repeatedly acquired data over the same surveying area. Correspondingly，its effect in terms of accuracy improvement of terrestrial mobile LiDAR solutions will be analysed through

test datasets. Both of tie points and tie features could be applied to co-register the scans acquired during consecutive runs. The general mathematical model and the stochastic model for the multistrip adjustment were summarized in Section 3.3. The same test scenes (Figure 4-19) at Black Creek Pioneer Village discussed in Chapter 4 was selected for our case studies. This chapter focuses on implementing the proposed MA algorithm and studying its effect. The results were partially presented in Section 5.3.

5.2 Terrestrial Mobile LiDAR Data

The same test scenes (Figure 4-19) introduced in Chapter 4 was selected as the study area to test out the proposed multistrip adjustment (MA) algorithm. Study Area #1 was a 200m long stretch along Shoreham Drive between Calumet Resident and Ian Macdonald Blvd, a relative small area with the adequate GCPs and feature constraints. Study Area #2 was a 3-km long loop around Black Creek Pioneer Village, a more complex and relative large area with the limited number of GCPs.

The mobile LiDAR data was collected by using Optech Lynx V200 mobile mapping vehicle on May 25, 2013. The vehicle was repeatedly driven for four times on the streets forward and backward by using the same configuration parameters at the speed limit of 20km/h in Study Area #1 and 60km/h in Study Area #2, respectively. The data acquisition scenarios and configuration parameters are summarized in Table 5-1. Each strip was

further divided into two parts based on the locations of two study areas.

Table 5-1: Data acquisition scenarios and system configuration parameters of Study Areas #1 and #2.

Strip #	PRF	Mirror Rate	Time	Direction
012	250 kHz	200 Hz	12:30 ~	Forward
013	250 kHz	200 Hz	12:45 ~	Reverse
014	250 kHz	200 Hz	13:00 ~	Forward
015	250 kHz	200 Hz	13:13 ~ 13:30	Reverse

A scanned scene selected from different strips around Calumet Resident in study area #1 was first examined to study the effects of vehicle driving directions on the visibility of the merged LiDAR point clouds. It is shown that the merged strip in Figure 5-1(c) from the opposite driving directions produced a better visibility than any of the used datasets alone. For example, the missing part of the building in strip 12 was made up by the point cloud of strip 13. Moreover, the radiometric intensity was enhanced due to the more dense point cloud. However, the merged strip in Figure 5-2(c) based on the same driving direction showed no significant difference in terms of visibility.

Figure 5-1: A scanned scene around Calumet Resident in study area #1 on York's Keele campus, Toronto, Canada with the multiple data acquisition runs: (a) LiDAR point cloud of strip 12 in forward direction; (b) LiDAR point cloud of strip 13 in reverse direction and (c) the merged result based on the opposite driving directions.


(a)


(b)


(c)

Figure 5-2: A scanned scene around Calumet Resident in study area #1 on York Keele campus, Toronto, Canada with the different data acquisition runs: (a) LiDAR point cloud of Strip 12 in forward direction; (b) LiDAR point cloud of Strip 14 in forward direction and (c) the merged result based on the same driving direction.

5.3 Experimental Results and Analysis

5.3.1 Study Area #1

Parts of the three strips (Strip 12, 13 and 14) in Study Area #1 were selected to realize the Multistrip Adjustment (MA) process. The corresponding trajectory in 2D horizontal, vertical and velocity of Lynx V200 system is overviewed in Figure 5-3. The SBET performance from the direct georeferencing process using the POS LV420 is presented in Figure 5-4. As can be seen, the horizontal position accuracy (1σ) was better than ±1.5cm for all three strips, while the vertical accuracy (1σ) was between ±3cm and ±3.7cm. Specifically, the vertical accuracy of strip 13 was around 3.5cm, which was lower than the ones of the other two strips.

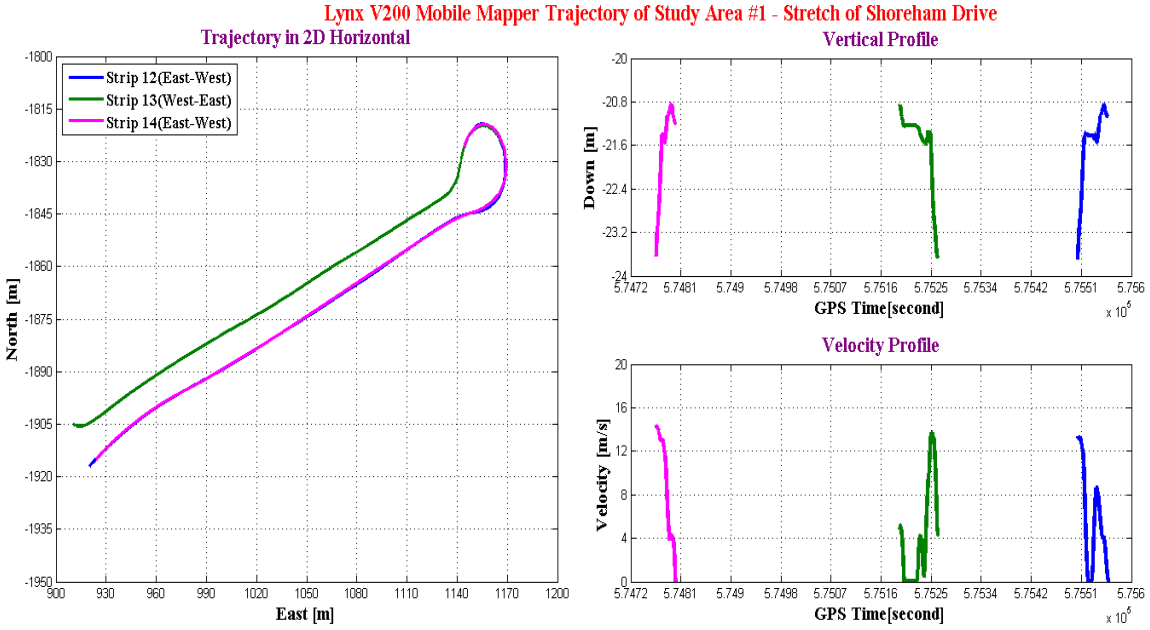

Figure 5-3: The horizontal, vertical trajectory profiles and velocity profile in study area #1 from three strips.

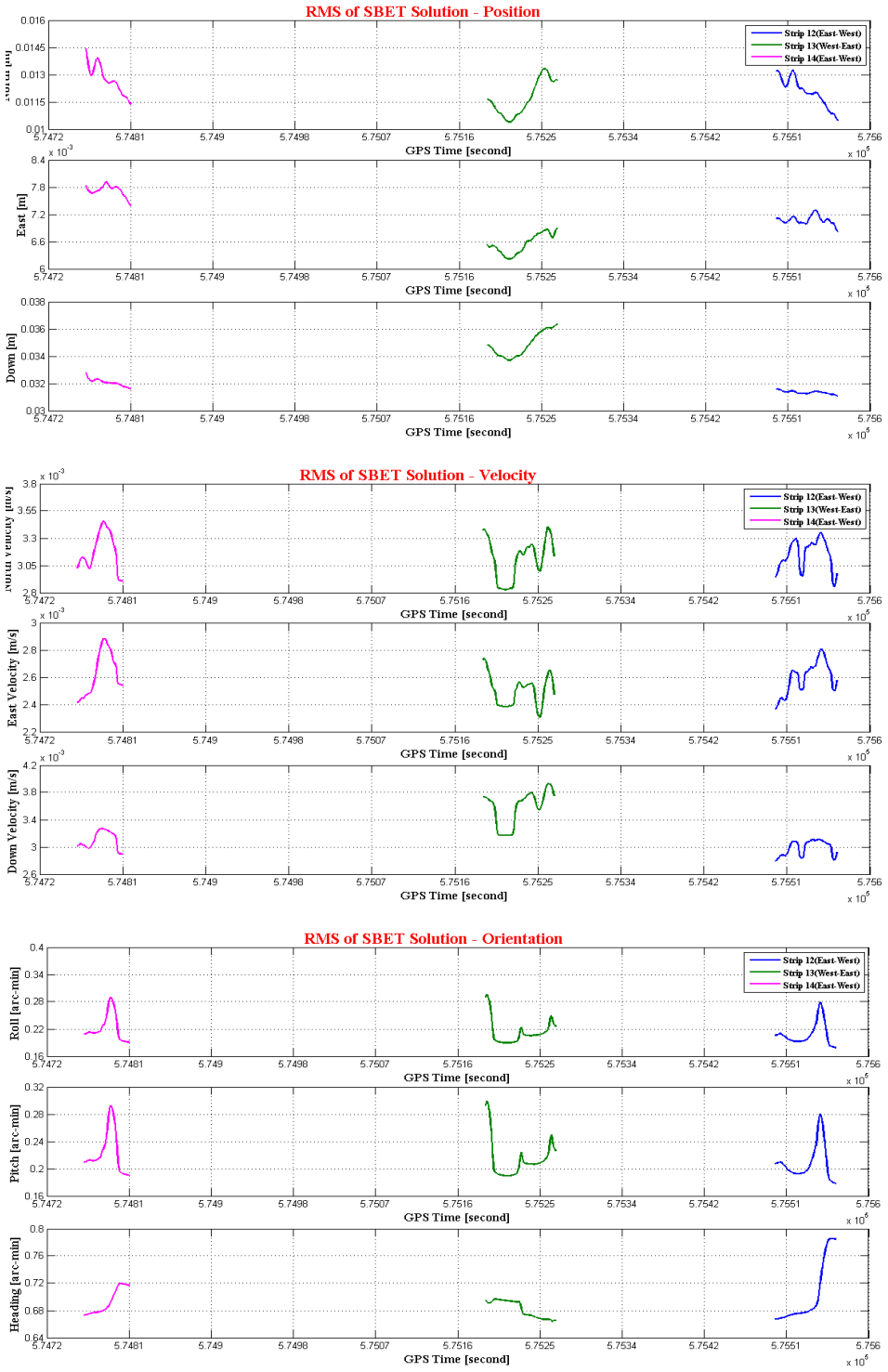

Figure 5-4: The RMS of the position (north, east and down), orientation (roll, pitch and heading) and velocity (north, east and down) versus GPS time in pink, green and blue lines for overlapped Strip 12, Strip 13 and Strip 14, respectively.

In Study Area #1, there were 10 feature constraints along with 76 pre-surveyed GCPs, of which 54 were the building type and 22 were the ground type. Half of them from each group were selected to participate in the solution refinement (Figure 5-5 (a) and (b)). The rest of 38 GCPs were used for accuracy assessment. Moreover, the adjacent strips were aligned together by using 52 tie points and 23 tie features (Figure 5-5 (c) and (d)). The local North-East-Up coordinates with respect to the Optech GPS reference station were used in the process.

The checking GCPs were used to evaluate the effects of the proposed multistrip adjustment approach using two strips with having the same driving direction against the one using the two strips with having the opposite driving directions. In addition, the 3DCCT was applied to single strip in order to check the accuracy improvement from the MA process with dual strip scenario.

Figure 5-6 gives on overview of 38 checking GCPs in Study Area #1. By taking the enlarged snapshots of two checking points “B4” (building-type) and “R3” (ground-type) as examples, then how the adjusted LiDAR solution was improved in different ways of multistrip adjustment were visually detailed. The refined coordinates using two strips in the opposite driving directions (cyan diamond) were the closest ones to the pre-surveyed coordinates (red dot) in 3D, as the ones using the single strip (pink star) were the furthest ones from the pre-surveyed coordinates, and the ones using the two strips collected in the

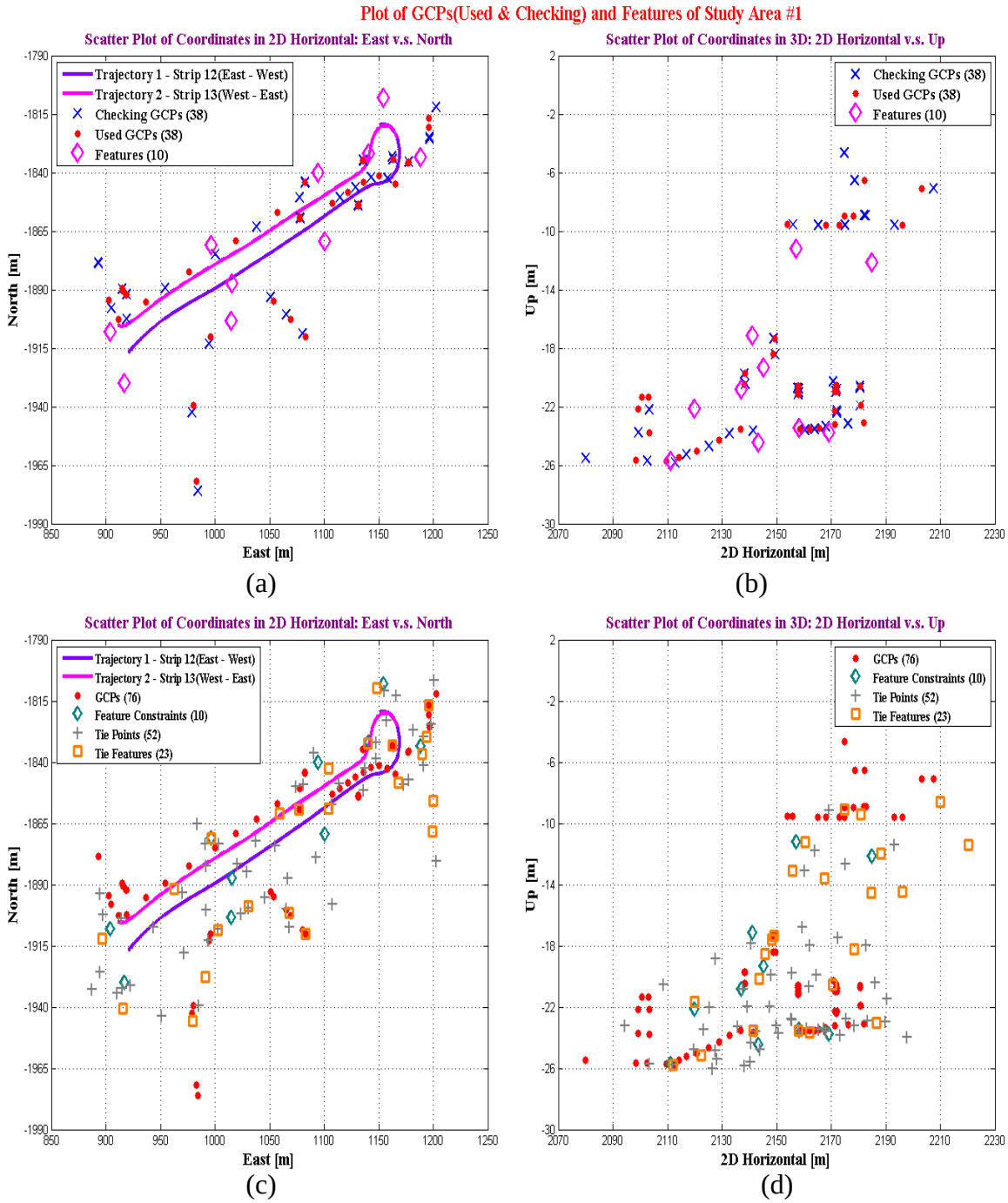

Figure 5-5: Scatter plot of 76 GCPs and 10 features distributed in study area #1: 38 GCPs in red dot used in 3D conformal transformation, and 38 control points in blue cross used for accuracy assessment; 52 tie points and 23 tie features applied in the relative alignment of the adjacent strips.

same driving direction (blue cross) fell in between. With respect to the pre-surveyed coordinates, the coordinate differences as the estimated errors for the three experiments were statistically analysed (Table 5-2). The errors using the single strip were biggest among these three experiments. Besides, the performance was not improved significantly in 3D through the adjustment of two strips in the same driving direction. However, the errors after the strip adjustment using two strips in the opposite driving directions were 1.5cm and 1.4cm in 3D at B4 and R3, clearly smaller than the errors from the other two refinement processes.

Table 5-2: The differences between the pre-surveyed coordinates and the adjusted LiDAR coordinates after 3DCCT using single strip, after MA using two strips with the opposite driving directions and two strips with the same direction, respectively, from two checking points "B4" and "R3".

ID	With Single Strip [cm]					With Opposite Direction Strips [cm]					With Same Direction Strips [cm]				
	N	E	2D	U	3D	N	E	2D	U	3D	N	E	2D	U	3D
B4	-1.93	0.94	2.15	0.73	2.27	-1.39	0.42	1.45	0.33	1.49	-1.58	0.68	1.72	0.44	1.78
R3	-1.43	0.89	1.68	-1.55	2.29	-1.01	0.44	1.10	-0.83	1.38	-1.20	0.69	1.38	-1.11	1.77

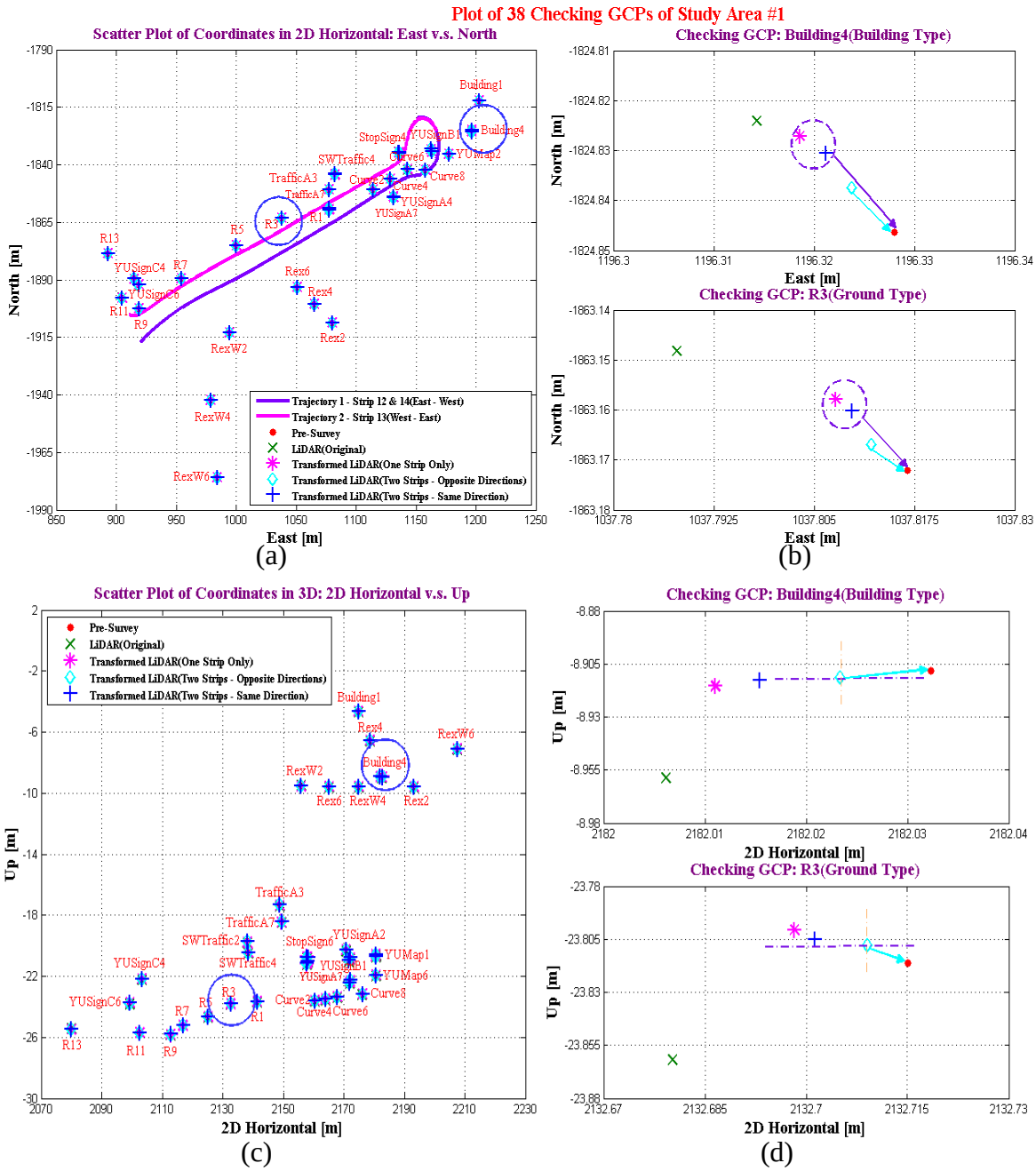

Figure 5-6: Scatter plot of 38 checking GCPs in Study Area #1. The adjusted LiDAR coordinates after 3DCCT using a single strip, after MA using two strips acquired in the opposite driving directions and in the same driving direction in pick star, cyan diamond and blue cross, respectively: (a) & (c): 2D horizontal and vertical; (b) & (d): Close-up details of "B4" and "R3".

The accuracy criteria, the statistic test and the approaches applied to the accuracy assessment through 38 checking GCPs in this test were the same as the ones described in Section 4.2.3.1. Their overall quantitative indexes were calculated (see Appendix C-7). The *t*-test statistics was used to determine if the errors were significantly biased and the χ^2-test statistics was used to conclude if a sample deviation was satisfied with the pre-defined accuracy level of ±1.5cm (1σ). The statistic results from the different test cases are presented in Table 5-4. Based on the two-tailed *t*-test, the differences, as the errors with respect to the pre-surveyed coordinates, of the original LiDAR coordinates contained significant biases in north, east and up directions. After 3DCCT using a single strip and after MA using two strips with the same and opposite driving directions, the mean of the errors became insignificant from zero.

The achieved accuracies of the original LiDAR solution based on the checking points were ±5.0cm (horizontal) and ±3.9cm (vertical) at the 95% confidence level according to the χ^2-test. For case 2, in which the single strip was used in the solution refinement process, the vertical accuracy was improved up to ±1.8cm, and the achieved horizontal accuracy reached ±2.3cm. After the multistrip adjustment with two strips driven in the same direction (case 4), the achieved horizontal accuracy was only improved to ±2.2cm. However, for case 3, in which the two strips collected in the opposite driving directions were used, the accuracies were further increased to ±2.0cm

horizontally and ±1.6cm vertically based on the χ^2-test at the 95% confidential level.

In general, the comparisons among the four test cases concluded that the multistrip adjustment process could further improve the accuracies of LiDAR solution. Especially, the best accuracy improvement came from the multistrip adjustment using two strips collected in the opposite driving directions. Furthermore, the same assessment procedures were applied to the results given by the multistrip adjustment only based on 16GCPs (i.e., 20%). The achieved accuracies for each scenario are illustrated in Table 5-3, which verified that the accuracy of the LiDAR solution was significantly improved through the strip adjustment using two strips acquired in the opposite driving directions. It was worth mentioning that the achieved accuracies were ±2.2cm in horizontal and ±1.8cm in vertical just based on 16 GCPs with two oppositely driven strips and were compatible with the scenario based on 38 GCPs with a single strip. Hence, the multistrip adjustment (MA) process could effectively enhance the accuracy improvement of terrestrial mobile LiDAR solutions even with the significantly reduced number of the GCPs, especially with involving the tie points and features to make up the lack of GCPs in some areas.

Table 5-3: The achieved accuracies for different scenarios using 38GCPs and 16GCPs.

Scenario	**Original**		**Single Strip**		**Two Strips (Opposite)**		**Two Strips (Same)**	
	V[cm]	**H_{2D}[cm]**	**V[cm]**	**H_{2D}[cm]**	**V[cm]**	**H_{2D}[cm]**	**V[cm]**	**H_{2D}[cm]**
38 GCPs (50%)	3.9	5.0	**1.8**	**2.3**	1.6	2.0	1.8	2.2
16 GCPs (20%)	3.9	5.0	2.2	2.7	**1.8**	**2.2**	2.0	2.4

Table 5-4: The statistical analysis of the differences between the pre-surveyed coordinates and the adjusted LiDAR coordinates through the 3DCCT using a single strip, through the MA process using two strips with the opposite driving directions and two strips with the same direction, respectively, from 38 checking GCPs in Study Area #1.

		Error Statistics				**Two-tailed *t*-test (α =0.05%) H_0: $\mu = 0$**			**χ^2 Test (α = 0.05%) vs. the 95% accuracy H_0: $\sigma^2 = 1.5^2 cm^2$**			**H_1: $\sigma^2 = \sigma_a^2$**		
Case No.*	Error	Mean [cm]	Stdev [cm]	RMS [cm]	f	t	$t_{f,0.025}$	Accepted (Y/N)	χ^2	$\chi^2_{f,0.05}$	Accepted (Y/N)	σ_a [cm]	χ^2	Accepted (Y/N)
1	**N**	-0.93	2.02	2.20	37	-2.83	2.026	N						
	E	-0.96	2.16	2.34	37	-2.75	2.026	N						
	U	4.79	2.35	5.32	37	12.54	2.026	N	350.24	52.19	N	**3.9**	51.81	Y
	2D(H)	1.34	2.95	3.21	37				574.26	52.19	N	**5.0**	51.68	Y
2	**N**	-0.23	0.96	0.98	37	-1.48	2.026	Y						
	E	-0.19	0.97	0.97	37	-1.21	2.026	Y						
	U	-0.35	1.08	1.12	37	-1.96	2.026	Y	74.32	52.19	N	**1.8**	51.61	Y
	2D(H)	0.30	1.36	1.38	37				122.54	52.19	N	**2.3**	52.12	Y
3	**N**	-0.21	0.85	0.87	37	-1.54	2.026	Y						
	E	-0.17	0.82	0.83	37	-1.27	2.026	Y						
	U	-0.24	0.97	0.98	37	-1.53	2.026	Y	59.18	52.19	N	**1.6**	52.02	Y
	2D(H)	0.27	1.19	1.20	37				92.39	52.19	N	**2.0**	51.97	Y
4	**N**	-0.21	0.96	0.97	37	-1.32	2.026	Y						
	E	-0.25	0.88	0.91	37	-1.74	2.026	Y						
	U	-0.28	1.07	1.09	37	-1.60	2.026	Y	72.33	52.19	N	**1.8**	50.23	Y
	2D(H)	0.32	1.30	1.32	37				111.54	52.19	N	**2.2**	51.85	Y

***Note**: Case 1: The differences between the pre-surveyed coordinates and the original LiDAR coordinates.

Case 2: The differences between the pre-surveyed coordinates and the adjusted LiDAR coordinates using a single strip (Case 3 in Section 4.3.2.4).

Case 3: The differences between the pre-surveyed coordinates and the adjusted LiDAR coordinates using two strips (driven in the opposite directions).

Case 4: The differences between the pre-surveyed coordinates and the adjusted LiDAR coordinates using two strips (driven in the same direction).

5.3.2 Study Area #2

The MA approach was further validated by selecting parts of three strips (Strip 12, 13 and 14) in Study Area #2, a more complicated and relative big area. The corresponding 2D horizontal, vertical and velocity profiles of the POS trajectory are shown in Figure 5-7. The performance of the SBET direct georeferencing solution resulted from the POS LV420 is presented in Figure 5-8, from which one can see that the position accuracies (1σ) were better than ±2cm in horizontal with all of three strips, and while the vertical accuracy was larger than ±3cm (a maximum of ±4cm with strip 14).

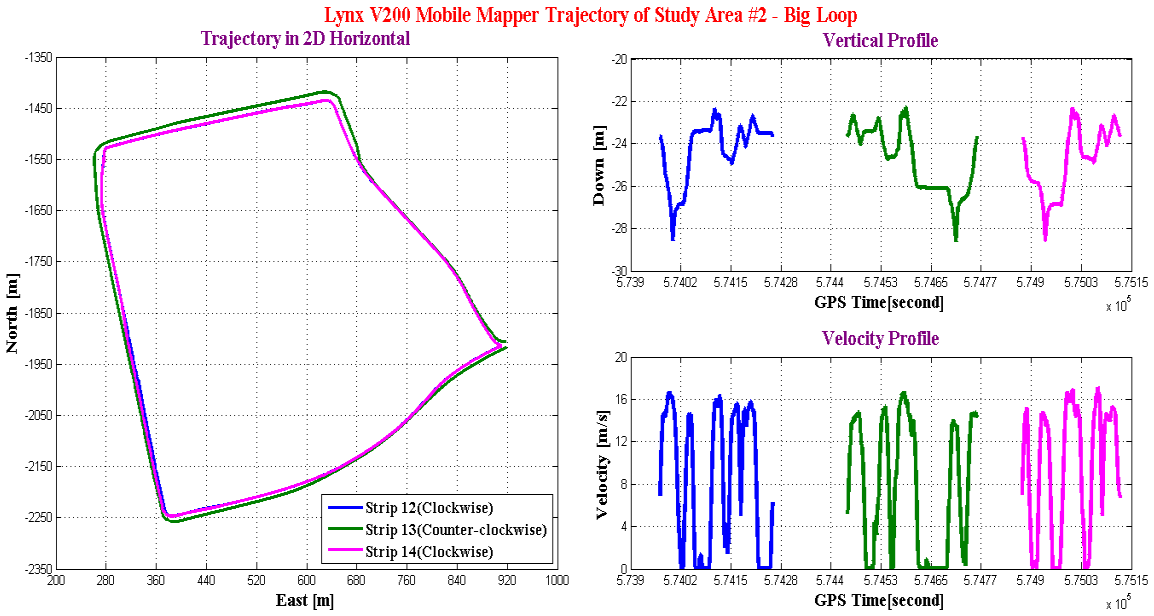

Figure 5-7: The 2D horizontal, vertical and velocity profiles of the trajectory of the three selected strips in study area #2.

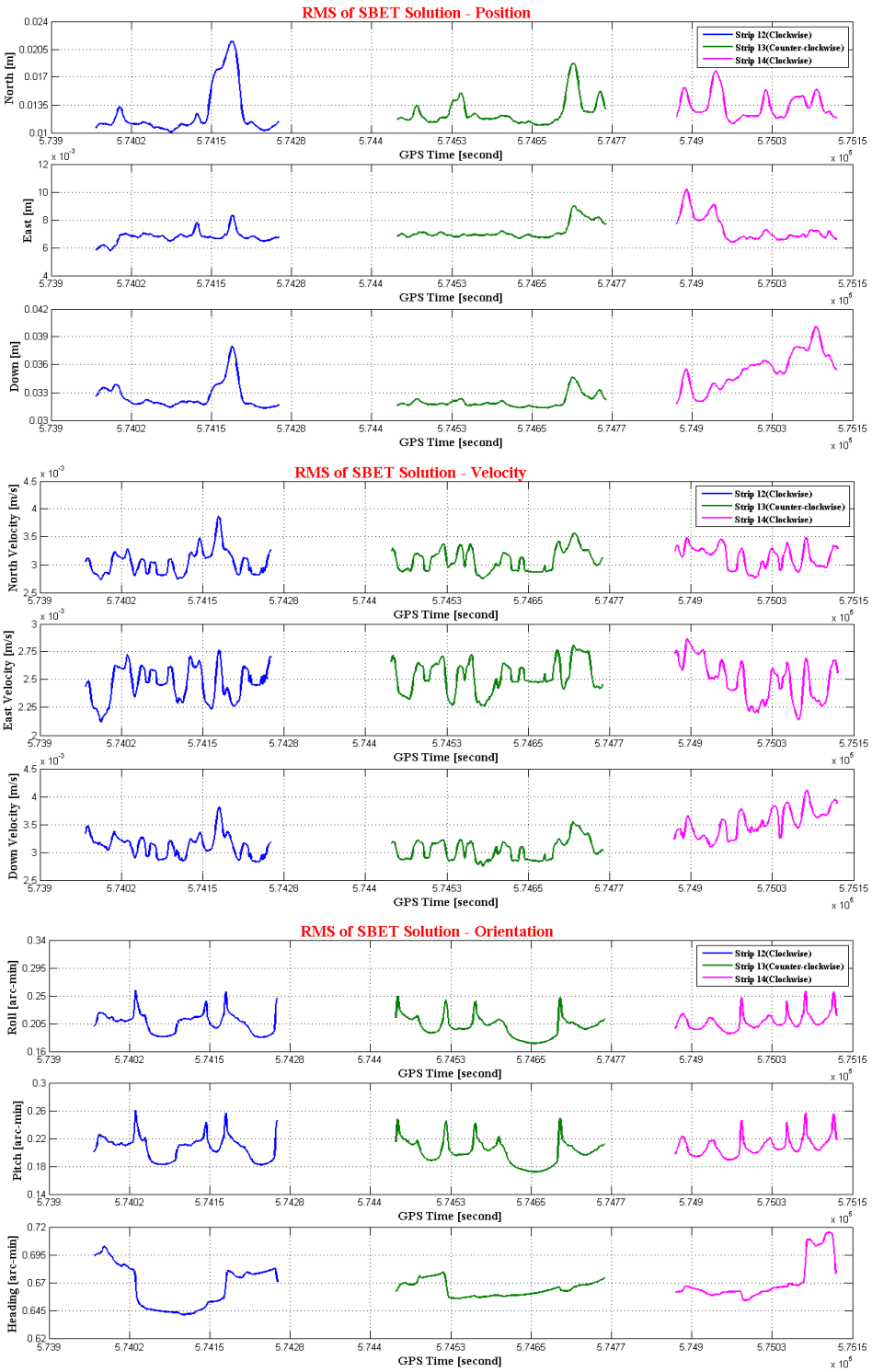

Figure 5-8: The RMS of the position (north, east and down), orientation (roll, pitch and heading) and velocity (north, east and down) versus GPS time in blue, green and pink lines for the overlapped Strip 12, Strip 13 and Strip 14, respectively.

With the test in Study Area #2, the accuracy of the terrestrial mobile LiDAR solutions could be improved by segmentally determining the 3DCCT parameters for the four segments in each driving direction in the same way as in Section 4.3.3.3. Thus, the segment on Shoreham Drive driven to the east (i.e., Segment #1) was chosen again as an example to validate the MA approach. There were 8 feature constraints together with 47 pre-surveyed GCPs distributed in the test scene, of which half of them were applied in the MA process whilst the other 23 GCPs were used in the accuracy assessment process. Moreover, the adjacent strips were aligned together by using 40 tie points and 20 tie features as presented in Figure 5-9.

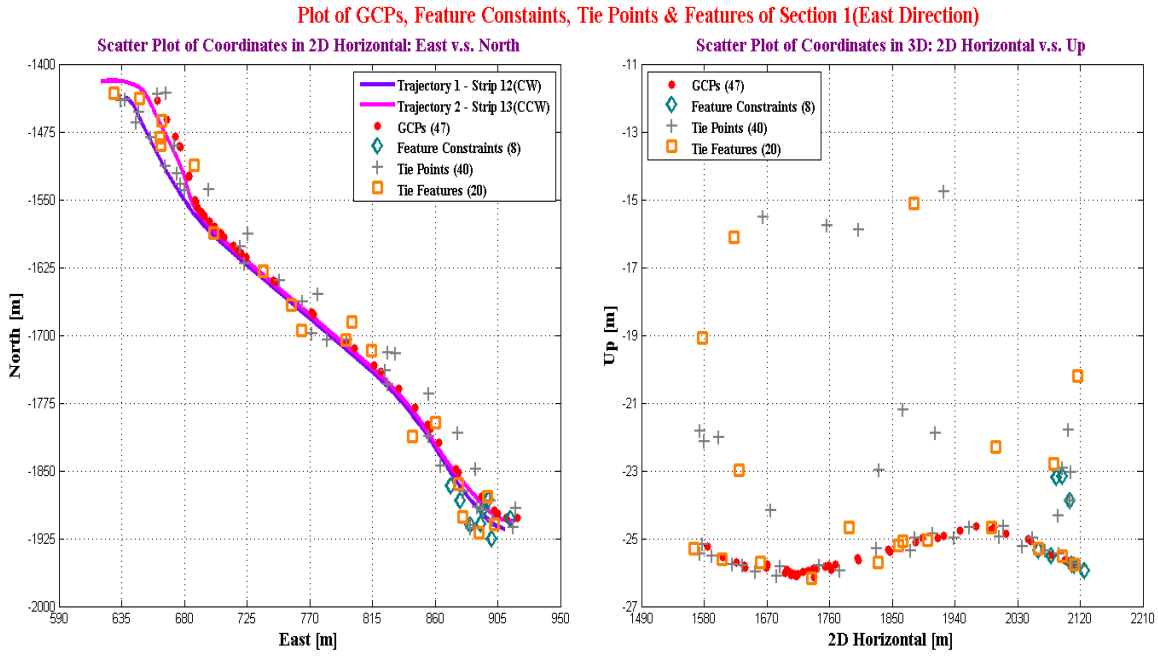

Figure 5-9: Scatter plot of 47 GCPs and 8 features distributed on Shoreham Drive (i.e., Segment 1) in study area #2 (2D horizontal and vertical): 40 tie points and 20 tie features applied in the relative alignment of the overlapped strips.

The same strategy used in Section 5.3.1 was applied to the MA process using two data strips collected in the same driving direction, and two data strips collected in the opposite driving directions as well. Their performance was compared using the checking GCPs. In addition, the 3DCCT was applied using only single strip so that the advantages of the MA approach with two overlapped strips could clearly be explored. Figure 5-10 plots 23 checking GCPs on the Segment #1 in Study Area #2 in 2D horizontal (Figure 5-10(a)) and vertical (Figure 5-10(c)) directions. Again, the enlarged snapshots of two selected checking points "R203" and "R205" were taken as examples to be specifically discussed (Figure 5-10 (b) and (d)).

Their adjusted LiDAR coordinates using two strips collect in the opposite driving directions (cyan diamond) were the closest ones to their pre-surveyed coordinates (red dot) in 3D, as their adjusted coordinates from the refined single strip (pink star) were the furthest ones, and their adjusted coordinates from the two-strip adjustment in the same driving direction (blue cross) fell in between. It was also noticed that the pink stars and the blue crosses were close to each other, i.e., the performance of the LiDAR solution was not significantly improved through the multistrip adjustment using two strips acquired in the same driving direction in comparison with the one using only single strip based on the 3DCCT adjustment. In the same way as in the above chapter, the coordinate differences of the checking GCPs with respect to their pre-surveyed coordinates were

calculated and used as the direct error information for accuracy assessment purpose.

Based on the numerical results given in Table 5-5, these errors given from the adjusted single strip were the biggest ones, while the magnitudes of the positional errors after the MA process using two strips driven in the opposite directions was improved by around 1.5cm in 3D in comparison with the errors in the single strip case. However, the same errors from the scenario with the two strips acquired in the same driving direction were reduced only by about 0.4cm.

Table 5-5: The differences between the pre-surveyed coordinates and the adjusted LiDAR coordinates after the 3DCCT using single strip, after the MA using two strips acquired in the opposite driving directions and in the same driving direction, respectively, from two checking points "R203" and "R205".

ID	With Single Strip [cm]					With Opposite Direction Strips [cm]					With Same Direction Strips [cm]				
	N	E	2D	U	3D	N	E	2D	U	3D	N	E	2D	U	3D
R203	1.88	-1.98	2.73	-1.55	3.14	1.18	-0.92	1.50	-0.75	1.67	1.56	-1.88	2.44	-1.31	2.77
R205	2.03	0.79	2.18	2.13	3.05	1.24	0.38	1.30	1.05	1.68	1.66	0.85	1.86	1.88	2.65

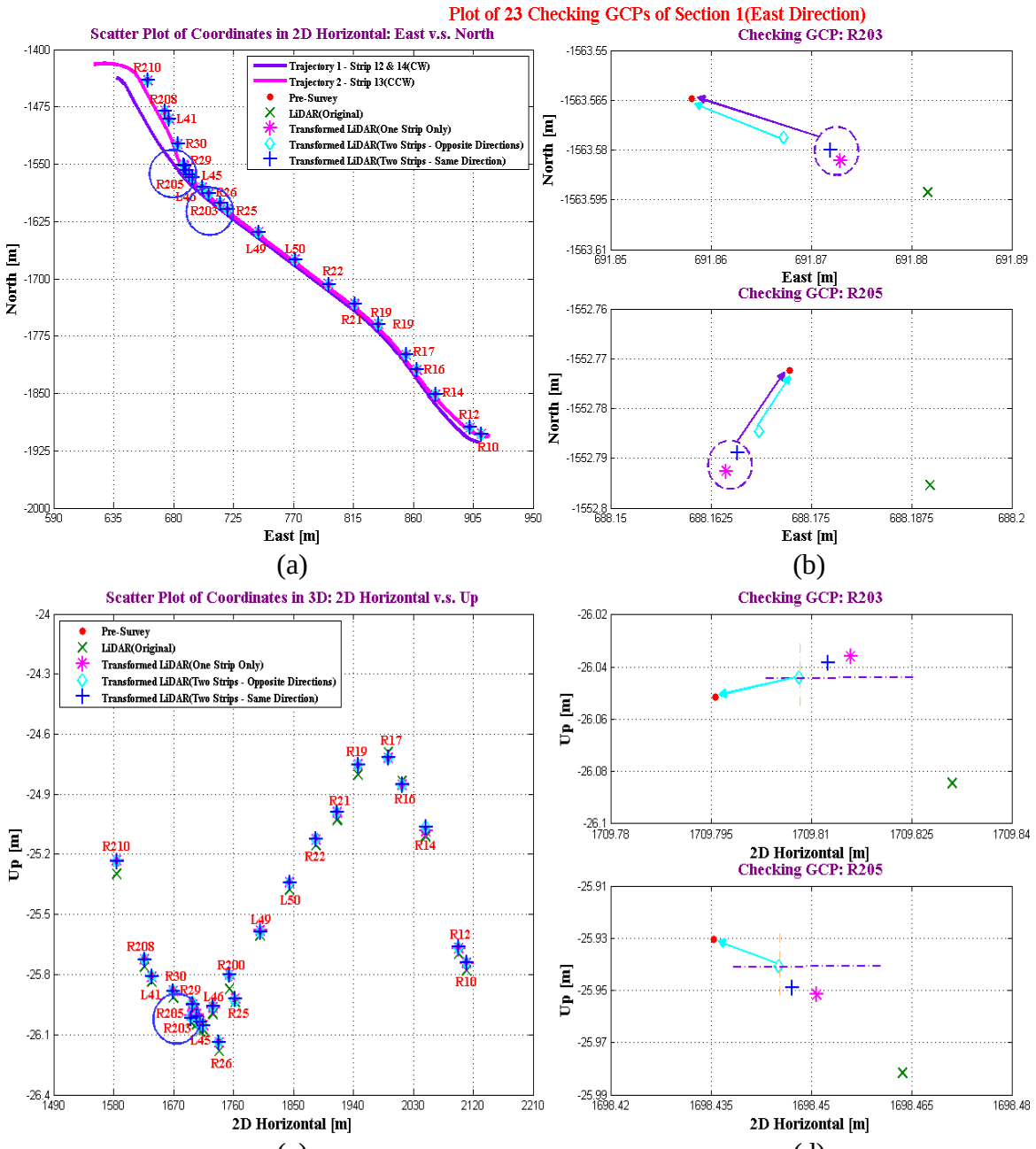

Figure 5-10: Scatter plot of 23 checking GCPs on Shoreham Drive driven to the east (i.e., Segment 1) in Study area #2. The adjusted LiDAR coordinates after 3DCCT using a single strip, after MA using two strips acquired in the opposite driving directions and in the same driving direction in pick star, cyan diamond and blue cross, respectively: (a) & (c) 2D horizontal and vertical; (b) & (d) Close-up details of "R203" and "R205".

The overall quantitative indexes, inclusive of the minimum, maximum, mean, standard deviation and RMS, for 23 checking GCPs with Segment #1 in Study Area #2 were calculated (see Appendix C-8). The *t*-test was introduced to determine if the errors were significantly biased whilst the χ^2-test statistics was to conclude if a sample deviation was satisfied with the pre-defined ±1.5cm(1σ) accuracy level. A summary of statistic *t*-test and alternate χ^2-test with the coordinate differences, against the pre-surveyed coordinates, of the original LiDAR and the adjusted LiDAR coordinates from 3DCCT adjustment using the single strip, the MA approach with two strips in the opposite driving directions and in the same driving direction is presented in Table 5-6.

Based on the two-tailed *t*-test, the coordinate differences of the original LiDAR solution contained significant biases in north, east and up directions. After the introduction of the single strip adjustment, the MA approach using two strips acquired both in the same and opposite driving directions, the mean values of the coordinate differences became insignificant from zero.

The achieved accuracies with the checking GCPs were ±4.7cm (horizontal) and ±3.7cm (vertical) at the 95% confidence level with the original mobile LiDAR solution according to the χ^2-test. Further, with case 2, in which the single strip adjustment was performed by applying the 3DCCT, the accuracies were improved to ±1.9cm vertically and ±2.3cm horizontally. Moreover, through MA approach by applying the two strips

acquired in the same driving direction (case 4); the achieved horizontal accuracy was only improved to ±2.1cm. However, with case 3, in which the two strips acquired in the opposite driving direction were used, the accuracies were further improved to ±1.9cm horizontally and ±1.6cm vertically based on the χ^2-test at the 5% significant level.

Therefore, the comparisons among the four testing cases concluded that the MA approach could further improve the accuracies of LiDAR solution. The conclusions here were consistent with the ones drawn from Study Area #1 as in Section 5.3.1. Indeed, the offsets of the common points, the common features and objects from the overlapped strips could provide the ideal information allowing refining and improving the mobile LiDAR solutions. In comparison with the use of GCPs in single strip, the MA approach is more economic and easily to be realized automatically or semi-automatically. Moreover, the number of the required GCPs may significantly be reduced or the lack of GCPs in some areas could be made up for through the involvement of tie points and features. However, more overlapped data strips will definitely increase the data volume and cost more. Therefore, an appropriate method needs to be implemented to reduce the overwhelming growth of data volume whilst improving the solution quality.

Table 5-6: The statistical analysis of the differences between the pre-surveyed coordinates and the adjusted LiDAR coordinates through the 3DCCT adjustment using a single strip, and through the MA process using two strips acquired in the opposite driving directions and in the same driving direction, respectively, from 23 checking GCPs on Segment #1 in Study Area #2.

		Error Statistics				**Two-tailed *t*-test (α =0.05%) H_0: $\mu = 0$**			**χ^2 Test (α = 0.05%) vs. the 95% accuracy H_0: $\sigma^2 = 1.5^2 cm^2$**			**H_1: $\sigma^2 = \sigma^2_a$**		
Case No.*	Error	Mean [cm]	Stdev [cm]	RMS [cm]	f	t	$t_{f,0.025}$	Accepted (Y/N)	χ^2	$\chi^2_{f,0.05}$	Accepted (Y/N)	σ_a [cm]	χ^2	Accepted (Y/N)
1	**N**	-1.59	2.17	2.67	22	-3.51	2.074	N						
	E	-2.05	1.95	2.82	22	-5.04	2.074	N						
	U	3.56	2.34	4.24	22	7.31	2.074	N	205.08	33.92	N	**3.7**	33.70	Y
	2D(H)	2.59	2.92	3.88	22				332.68	33.92	N	**4.7**	33.89	Y
2	**N**	-0.41	1.06	1.16	22	-1.87	2.074	Y						
	E	-0.34	0.93	1.02	22	-1.74	2.074	Y						
	U	0.35	1.19	1.25	22	1.41	2.074	Y	53.24	33.92	N	**1.9**	33.19	Y
	2D(H)	0.54	1.41	1.54	22				78.29	33.92	N	**2.3**	33.30	Y
3	**N**	-0.28	0.81	0.89	22	-1.67	2.074	Y						
	E	-0.24	0.86	0.92	22	-1.37	2.074	Y						
	U	0.30	1.01	1.07	22	1.42	2.074	Y	38.00	33.92	N	**1.6**	33.40	Y
	2D(H)	0.37	1.18	1.28	22				54.38	33.92	N	**1.9**	33.89	Y
4	**N**	-0.35	0.92	1.01	22	-1.84	2.074	Y						
	E	-0.34	0.92	1.01	22	-1.75	2.074	Y						
	U	0.35	1.13	1.19	22	1.50	2.074	Y	47.62	33.92	N	**1.8**	33.07	Y
	2D(H)	0.49	1.30	1.43	22				66.43	33.92	N	**2.1**	33.89	Y

***Note:** Case 1: The differences between the pre-surveyed coordinates and the original LiDAR coordinates.
Case 2: The differences between the pre-surveyed coordinates and the adjusted LiDAR coordinates using single strip (Case 3 in Section 4.3.3.3)
Case 3: The differences between the pre-surveyed coordinates and the adjusted LiDAR coordinates using two strips acquired in the opposite driving directions.
Case 4: The differences between the pre-surveyed coordinates and the adjusted LiDAR coordinates using two strips acquired in the same driving direction.

6 Accuracy improvement with the aid of preliminary calibration of boresight angles

6.1 Overview

As discussed in the error analysis of terrestrial mobile LiDAR systems in Section 2.3, the overall accuracy of LiDAR solutions depends on the assembly and calibration of two components: the LiDAR units and the direct georeferencing system (GPS-aided Inertial Integrated Navigation System, e.g., an Applanix POS System). The coordinates of the points in a LiDAR point cloud are normally the absolute geospatial locations. The boresight angular misalignments are one of the major error contributors to the systematic errors.

Discrepancies among the overlapped strips occur if the point cloud is generated by the incorrect (or biased) system parameters, which can generally be modeled as the accumulated impact of the systematic errors. Especially, the poor boresight and lever arm estimation could seriously degrade the accuracy of LiDAR solutions. As a result, it is necessary to accurately compensate for the boresight misalignments in a mobile LiDAR system.

The boresight angles ($\Delta\omega, \Delta\varphi, \Delta\kappa$) are the angular offsets in *X*, *Y* and *Z* directions between the scanner's body frame and the IMU body frame. The algorithms for evaluating the boresight angles have been developed and widely applied in airborne laser scanning (ALS) systems. However, the methods of data acquisition are inevitable different in terrestrial laser scanning (TLS) systems, even though their physical working principles are similar (Rieger et al., 2010). For instant, an area of interest can be easily

scanned from different flight directions in the airborne laser scanning survey. However, the TLS systems are lack of flexibility in scanning the same objects multiple times from various directions due to the limited angular field-of-view. In addition, current calibration techniques require the access to the LiDAR system parameters and the raw observations, such as, the position and orientation of a platform, the scanning angles and ranges. Unfortunately, the raw observations are not usually made available to the end users (Bang et al., 2009). Moreover, some of the methods rely on the accurate absolute coordinates of the retro-reflective targets (i.e., GCPs) or the scanning objects of known size and position from different driving directions and distances. All these techniques have been lack of flexibility and demanded for more efforts on preparing the special test sites.

In connection with TLS systems, Keller et al. (2013) proposed a new cost-effective method for the boresight angle refinement by using the common planar and/or line facades identified from two scans consecutively acquired in the opposite driving directions at the post-processing stage. The calibrated boresight angles can be used to improve the accuracy of subsequently collected LiDAR data. Apparently, the calibration results of boresight angles from this approach are independent of any local behaviour. Hence, it is expected that a preliminary calibration of the boresight angles before the segmental 3DCCT process will significantly enhance the entire refinement process of terrestrial LiDAR solutions.

In this chapter, the boresight angles of the used Lynx V200 mobile LiDAR system was calibrated after the approach from Keller (2013) using the same two test scenes as in Figure 4-19 introduced in Chapter 4. Refer to Section 3.4 for the general mathematical model. The implementation results with the test data are presented in Section 6.2 below.

6.2 Implementation and Results

A general flowchart about the realization of the being discussed approach is given in Figure 6-1. The same test scenes presented in Chapter 4, as Study Area #1 and Study Area #2 in Figure 4-19, were again selected as the calibration sites. Moreover, the LiDAR data: strip 12 and strip 13 collected from two consecutive runs driven in the opposite directions (Table 5-1) were selected to test out the effect of this preliminary boresight angle calibration.

A number of facade objects or sections with different spatial orientations were extracted and taken to determine the deviation of boresight angles individually using the aforementioned approach. Therein to, the determination of roll and pitch angular errors require the facades parallel (e.g., building roofs and windows along the road) with and perpendicular (e.g., traffic lights and signs) to the travelling direction, respectively. The residual error of the heading angle was estimated by driving through the objects with the regular shapes (e.g., pavement marking, sewer and sidewalk curb) on the ground. Then the raw point cloud data were re-processed by applying the calibrated boresight angles. After that, the 3DCCT on the ground of LSM for the single strip using GCPs and feature constraints, and then the MA approach with two strips using tie points and tie features were executed by applying both of the original LiDAR data and the corrected mobile LiDAR data for the calibrated boresight angular biases. Their effects were compared using the checking GCPs. The flowchart of the implementation and testing procedures of the preliminary boresight angle calibration is presented in Figure 6-1.

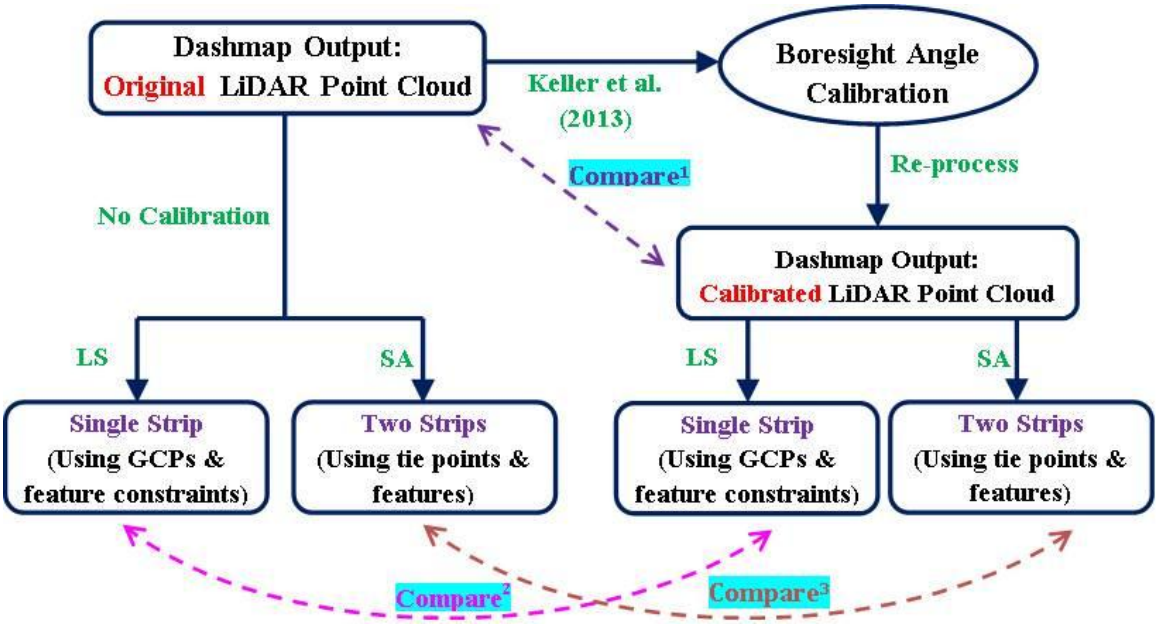

Figure 6-1: Flowchart of the preliminary boresight angle calibration.

6.2.1 Study Area #1

Part of two consecutive runs (strip 12 and 13) driven in the opposite directions in Study Area #1 were selected for the boresight angle calibration. Refer to Figure 5-3 for the corresponding horizontal, vertical and velocity profiles of the trajectory, and Figure 5-4 for the quality of the SBET solution of the POS LV420. Twenty facade objects with different spatial orientations were chosen to evaluate the errors in each of the three boresight angles individually. The calibration results of two sensors are summarized in Table 6-1.

Table 6-1: Calibration results of boresight angles for two sensors in Study Area #1.

	Sensor #1 (˚)	**Sensor #2 (˚)**
Roll	-0.013˚	0.008˚
Pitch	0.033˚	-0.026˚
Heading	-0.005˚	-0.006˚

In Study Area #1, there were 10 feature constraints along with the 76 pre-surveyed control points, of which half of them were employed as the checking points for accuracy assessment. Moreover, 52 tie points and 23 tie features identified (Figure 5-5) in the LiDAR point cloud could serve the alignment of the adjacent strips.

The results were compared through 38 checking GCPs among the different refinement strategies: the single strip 3DCCT adjustment, and the MA process with two strips using both of the original LiDAR solution and the corrected mobile LiDAR solution for the calibrated boresight-angles. By taking two checking points “Building4” (building-type) and “R3” (ground-type) as examples (Figure 6-2), the original LiDAR coordinates without the boresight angle calibration (green cross) were the furthest ones

away from the pre-surveyed coordinates (red dot) in 3D, while the adjusted LiDAR coordinates using two strips after the preliminary boresight calibration (blue pentagon) were the closest ones to them.

Moreover, the solution of the calibrated raw LiDAR coordinates (cyan diamond) was compatible with the adjusted LiDAR coordinates through the refinement using the single strip but no calibration involved (orange star). The similar situation was also observed from the coordinate differences between the adjusted LiDAR coordinates through the 3DCCT using single strip with the calibration process (brown square) and the adjusted LiDAR coordinates through the MA process using two strips without any boresight angle calibration (grey cross). The performance here was not significantly worse than the best solution (blue pentagon) which employed both of the preliminary boresight calibration and MA process with two strips. It implied that the boresight angle calibration could improve the overall quality of LiDAR solution, on one hand. On the other hand, it could simplify the post-processing procedures towards the accuracy improvement by only executing the 3DCCT with single strip instead of performing the MA process with two strips. In this way, the refinement process can be done more efficiently and cost-effectively.

The comparisons among different scenarios are presented in Figure 6-3 using the checking GCP “R3” in order to further illustrate the effect of the preliminary boresight angle calibration from various refinement strategies. Based on plots (Figure 6-2(b) and Figure 6-2(c)), it verified that the solution performance of both the raw LiDAR data and the adjusted LiDAR data through the 3DCCT using the single strip has significantly been

improved by carrying out the preliminary boresight calibration in comparison with the solution performance from the same data but without involving the boresight angle correction.

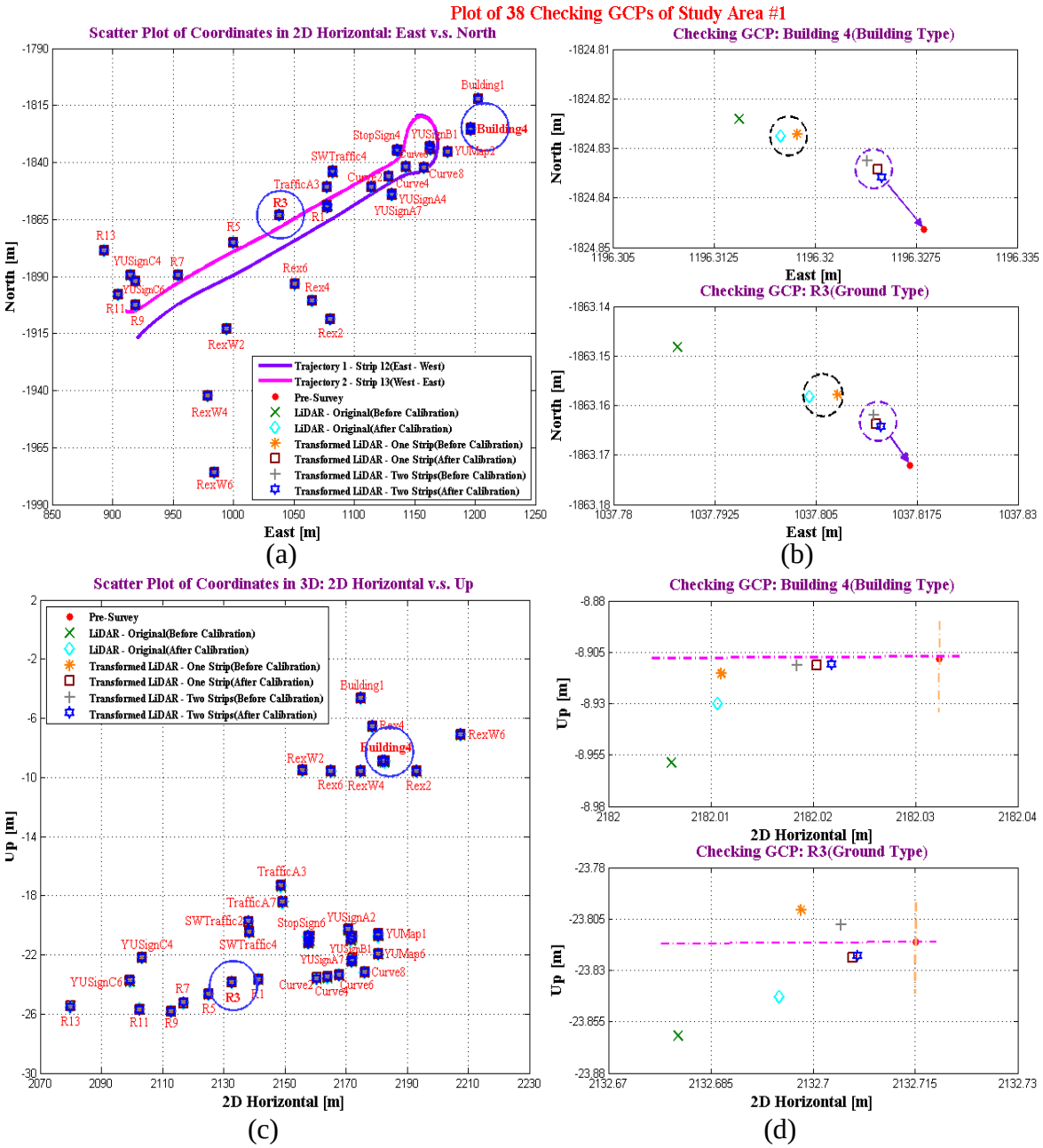

Figure 6-2: Scatter plot of 38 checking GCPs in Study Area #1 for all test scenarios: (a) & (c) 2D horizontal and vertical; (b) & (d) Close-up details of "Building4" and "R3".

In addition, the adjusted LiDAR coordinates through the refinement process using both of the single strip and two strips with the boresight angle calibration became much closer to the pre-surveyed coordinates as shown in Figure 6-3(a). However, after the preliminary boresight angle calibration, the results from the two-strip scenario have not shown a significant improvement relative to the ones using the single strip. It was noticed that the similar circumstances occur in Figure 6-3(d) where the performance of the adjusted LiDAR solution using two strips without the boresight angle correction was not degraded significantly versus the results using the same strategy but involving the boresight calibration. It indicated that some of the systematic errors could significantly been eliminated through either the MA process or the preliminary boresight calibration.

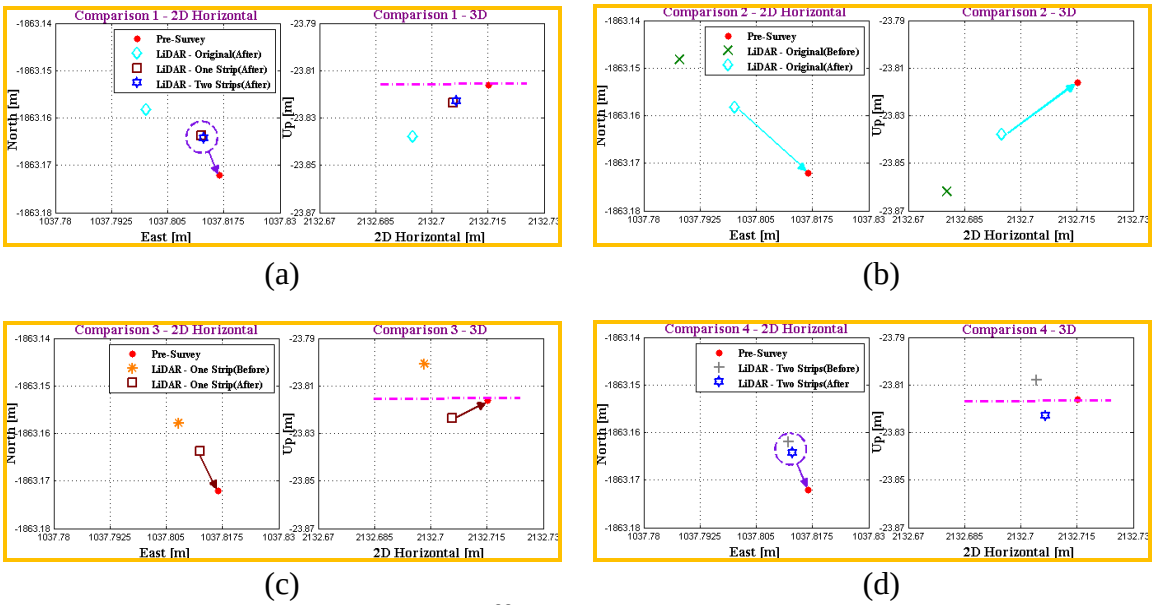

Figure 6-3: The comparison among different scenarios with the checking GCP – "R3". (a) After boresight angle calibration: the original LiDAR solution vs. the adjusted LiDAR solution using the single strip vs. the adjusted LiDAR using two strips; (b) the original LiDAR solution: before vs. after boresight calibration; (c) the adjusted LiDAR solution using the single strip: before vs. after boresight calibration; (d) the adjusted LiDAR solution using two strips: before vs. after boresight calibration.

The overall quantitative indexes, inclusive of the minimum, maximum, mean, standard deviation and RMS, were calculated (see Appendix C-9). Furthermore, the *t*-test and χ^2-test were introduced to determine if the errors were significantly biased and the sample deviation was satisfied with the specific pre-defined accuracy level of ±1.5cm, respectively, as in Table 6-3. Then the achieved accuracies from the different strategies applied before and after the boresight angle calibration are illustrated in Table 6-2. The results were consistent with the previous analysis based on the scatter plot of the checking GCPs. For boresight angle calibration, some important findings can be addressed as follows:

1. It could improve the overall quality of terrestrial mobile LiDAR solution, especially with the raw LiDAR point cloud and 3DCCT on the ground of LSM using single strip. For example, the achieved accuracy was improved significantly from ±5.0cm to ±3.9cm horizontally and from ±2.3cm to ±1.8cm vertically, respectively, at the 95% confident level.
2. Some of the systematic errors have been eliminated through the MA process as it was introduced by aligning two overlapped data strips using tie points and tie features. The accuracies were only increased from ±2.0cm to ±1.7cm in horizontal, but no improvement in vertical after the boresight angle calibration was applied additionally.
3. The solution refinement process could be simplified because one may only need to introduce the 3DCCT to the single strip instead of further introducing the MA

process to the two strips in case the preliminary boresight angle calibration was already applied before the 3DCCT adjustment.

As a result, one could choose either one of the two following strategic combinations in a more efficient and cost-effective way according to the data acquisition condition:

- Option 1: Perform the preliminary boresight angle calibration and then the 3DCCT adjustment using GCPs and features based on the single strip.
- Option 2: Introduce the MA process using two overlapped data strips without involving the preliminary boresight angle calibration. Once the two strips are merged together, apply the 3DCCT adjustment to the whole LiDAR point cloud using GCPs and geometrical feature constraints.

Table 6-2: The achieved accuracies with different strategies applied before and after the boresight angle (BA) calibration in study area #1.

Algorithm	**Before BA Calibration**		**After BA Calibration**	
	V[cm]	**H_{2D}[cm]**	**V[cm]**	**H_{2D}[cm]**
Original LiDAR point cloud	3.9	5.0	3.0	3.9
Single strip	1.8	2.3	**1.6**	**1.8**
Two strips	**1.6**	**2.0**	1.6	1.7

Table 6-3: The statistical analysis of the differences between the pre-surveyed coordinates and the original LiDAR coordinates, the adjusted LiDAR coordinates through the 3DCCT using single strip and through the MA process using two strips acquired in the opposite driving directions before and after the preliminary boresight angle calibration, respectively, from 38 checking GCPs in Study Area #1.

		Error Statistics				**Two-tailed *t*-test (α=0.05%) H_0: $\mu = 0$**			**χ^2 Test (α=0.05%) vs. the 95% accuracy H_0: $\sigma^2 = 1.5^2 cm^2$**			**H_1: $\sigma^2=\sigma_a^2$**		
Case No.*	Error	Mean [cm]	Stdev [cm]	RMS [cm]	f	t	$t_{f,0.025}$	Accepted (Y/N)	χ^2	$\chi^2_{f,0.05}$	Accepted (Y/N)	σ_a [cm]	χ^2	Accepted (Y/N)
1	**N**	-0.93	2.02	2.20	37	-2.83	2.026	N						
	E	-0.96	2.16	2.34	37	-2.75	2.026	N						
	U	4.79	2.35	5.32	37	12.54	2.026	N	350.24	52.19	N	**3.9**	51.81	Y
	2D(H)	1.34	2.95	3.21	37				574.26	52.19	N	**5.0**	51.68	Y
2	**N**	-0.49	1.52	1.58	37	-1.98	2.026	Y						
	E	-0.39	1.73	1.75	37	-1.38	2.026	Y						
	U	1.46	1.82	2.31	37	4.95	2.026	N	208.11	52.19	N	**3.0**	52.03	Y
	2D(H)	0.62	2.31	2.36	37				349.73	52.19	N	**3.9**	51.73	Y
3	**N**	-0.23	0.96	0.98	37	-1.48	2.026	Y						
	E	-0.19	0.97	0.97	37	-1.21	2.026	Y						
	U	-0.35	1.08	1.12	37	-1.96	2.026	Y	74.32	52.19	N	**1.8**	51.61	Y
	2D(H)	0.30	1.36	1.38	37				122.54	52.19	N	**2.3**	52.12	Y
4	**N**	-0.12	0.69	0.69	37	-1.12	2.026	Y						
	E	-0.21	0.80	0.82	37	-1.64	2.026	Y						
	U	-0.19	0.93	0.94	37	-1.28	2.026	Y	54.68	52.19	N	**1.6**	48.06	Y
	2D(H)	0.25	1.06	1.07	37				73.68	52.19	N	**1.8**	51.17	Y
5	**N**	-0.21	0.85	0.87	37	-1.54	2.026	Y						
	E	-0.17	0.82	0.83	37	-1.27	2.026	Y						
	U	-0.24	0.97	0.98	37	-1.53	2.026	N	59.18	52.19	N	**1.6**	52.02	Y
	2D(H)	0.27	1.19	1.20	37				92.39	52.19	N	**2.0**	51.97	Y

6	**N**	-0.07	0.66	0.66	37	-0.66	2.026	Y							
	E	-0.18	0.74	0.76	37	-1.48	2.026	Y							
	U	-0.11	0.96	0.95	37	-0.68	2.026	Y	57.92	52.19	N	**1.6**	50.90	Y	
	2D(H)	0.19	1.00	1.00	37				65.38	52.19	N	**1.7**	50.90	Y	

***Note:**

- Case 1: The differences between the pre-surveyed coordinates and the original LiDAR coordinates **before** BA calibration.
- Case 2: The differences between the pre-surveyed coordinates and the original LiDAR coordinates **after** BA calibration.
- Case 3: The differences between the pre-surveyed coordinates and the adjusted LiDAR coordinates derived from using single strip **before** BA calibration. (i.e., case 2 of section 5.3.1)
- Case 4: The differences between the pre-surveyed coordinates and the adjusted LiDAR coordinates derived from using single strip **after** BA calibration.
- Case 5: The differences between the pre-surveyed coordinates and the adjusted LiDAR coordinates derived from using two strips with opposite directions **before** BA calibration. (i.e., case 3 of section 5.3.1)
- Case 6: The differences between the pre-surveyed coordinates and the adjusted LiDAR coordinates derived from using two strips with opposite directions **after** BA calibration.

6.2.2 Study Area #2

The data segment on Shoreham Drive driven to the east (i.e., Segment #1) in Study Area #2 was again chosen as an example to validate the performance of the preliminary boresight angle calibration. Again, part of two consecutive runs (strip 12 and 13) driven in the opposite directions in Study Area #2 were selected. Refer to Figure 5-7 and Figure 5-8 for the corresponding 2D horizontal, vertical and velocity profiles of the trajectory with the Lynx V200 system and the performance of the SBET solution resulted from the POS LV420, respectively. Similar to the test data in Study Area #1, twenty facade objects with the different spatial orientations were here selected to determine the errors in three boresight angles individually. The results of two sensors are summarized in Table 6-4. The estimated error for the pitch angle was the biggest one. For the test scene, there were 8 feature constraints together with 47 pre-surveyed control points, of which half of them were employed as the checking points for accuracy assessment. Moreover, 40 tie points and 20 tie features identified (Figure 5-9) in the LiDAR point cloud served to align the adjacent strips.

Table 6-4: Calibration results of boresight angles for two laser sensors in Study Area #2.

	Sensor #1 (˚)	**Sensor #2 (˚)**
Roll	-0.012˚	0.010˚
Pitch	0.024˚	-0.028˚
Heading	-0.008˚	-0.005˚

The performance with 23 checking GCPs was used to make the comparison among the results after the introduction of 3DCCT to single strip and the introduction of MA to two strips using both of the original LiDAR data and the calibrated mobile LiDAR data for boresight angles. By taking the enlarged snapshots of two checking points “R203” and “R205” as examples (Figure 6-4), the similar conclusions were drawn through looking into the scatter plot of the checking GCPs as in Section 6.2.1. Then the comparison among different scenarios is presented in Figure 6-5 with the checking GCP “R205” to further illustrate the effect of the preliminary boresight angle calibration on the different refinement strategies.

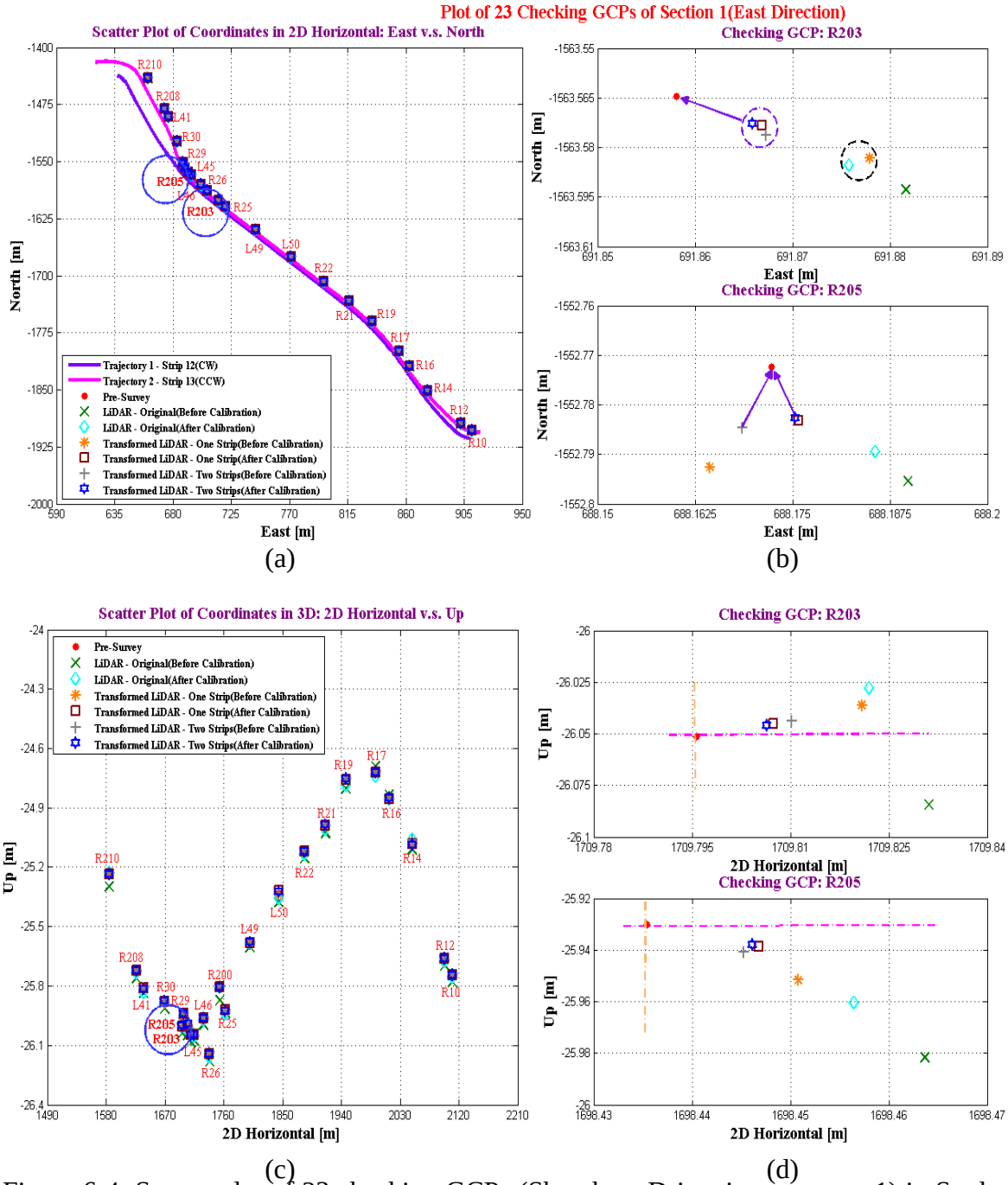

Figure 6-4: Scatter plot of 23 checking GCPs (Shoreham Drive, i.e., segment 1) in Study Area #2 for all test scenarios: (a) & (c) 2D horizontal and vertical; (b) & (d) Close-up details of "R203" and "R205".

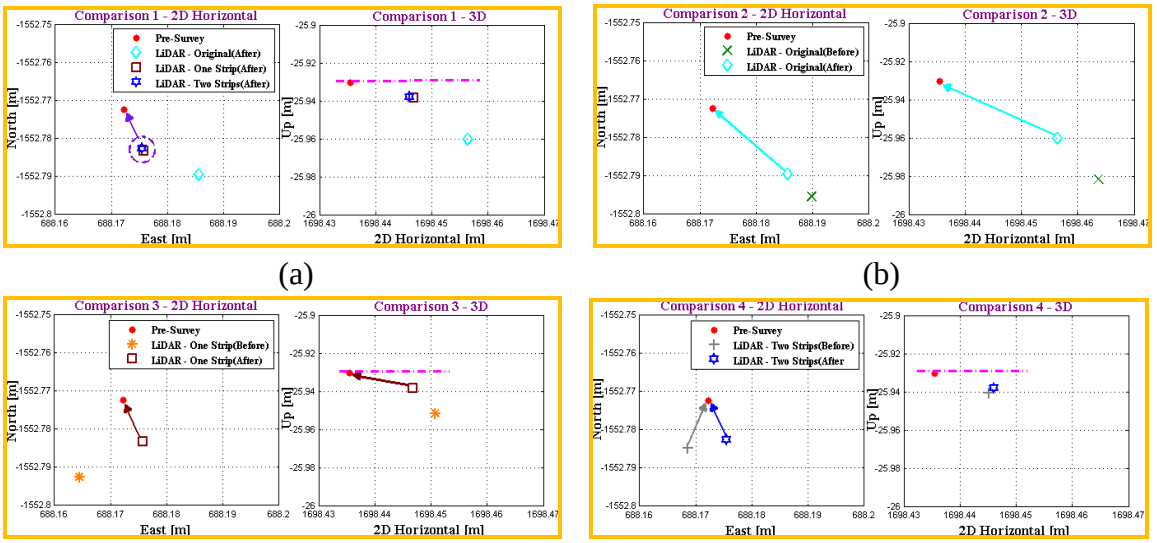

Figure 6-5: The comparison among different scenarios with the checking GCP – "R205". (a) After boresight angle calibration: the original LiDAR solution vs. the adjusted LiDAR solution using single strip vs. the adjusted LiDAR using two strips; (b) The original LiDAR solution: before vs. after boresight calibration; (c) the adjusted LiDAR solution using the single strip: before vs. after boresight calibration; (d) the adjusted LiDAR solution using two strips: before vs. after boresight calibration.

The same accuracy criteria, overall quantitative indexes and statistic test approaches were applied to the results from the checking GCPs. Refer Appendix C-10 and Table 6-6 for the details. Furthermore, the achieved horizontal and vertical accuracies for different strategies applied before and after the preliminary boresight angle calibration are illustrated in Table 6-5. The conclusions were consistent with the results derived in Study Area #1. The preliminary boresight angle calibration could improve the overall quality of original LiDAR solution. Especially, the horizontal accuracy was improved significantly from ±4.7cm to ±3.7cm and from ±2.3cm to 1.8cm through the 3DCCT

adjustment using single strip. Some of the systematic errors (e.g., biases in lever-arm, boresight angles and ranges) have been modeled in the MA process. The accuracies were only increased from ±1.9cm to ±1.6cm in horizontal, but no improvement in vertical either after the calibration. The post-processing procedures could be simplified by either applying the 3DCCT to the single strip plus the preliminary boresight angle calibration (horizontal: ±1.8cm, vertical: ±1.5cm) or applying the MA to two strips but without involving the boresight calibration (horizontal: ±1.9cm, vertical: ±1.6). None of the achieved accuracies of two options were degraded dramatically relative to the best scenario where both the preliminary boresight angle corrections and the MA were applied to two strips. The achieved horizontal and vertical accuracies became ±1.6cm and ±1.6cm, respectively.

Table 6-5: The achieved accuracies for different strategies applied before and after the boresight angle (BA) calibration with segment 1 in Study Area #2.

Algorithm	**Before BA Calibration**		**After BA Calibration**	
	V[cm]	**H_{2D}[cm]**	**V[cm]**	**H_{2D}[cm]**
Original LiDAR point cloud	3.7	4.7	2.8	3.7
Single strip	1.9	2.3	**1.5**	**1.8**
Two strips	**1.6**	**1.9**	1.6	1.6

Table 6-6: The statistical analysis of the differences between the pre-surveyed coordinates and the original LiDAR coordinates, the adjusted LiDAR coordinates through the 3DCCT using single strip and through the MA process using two strips acquired in the opposite driving directions before and after the preliminary boresight angle calibration, respectively, from 23 checking GCPs with segment 1 in Study Area #2.

		Error Statistics				**Two-tailed *t*-test (α=0.05%) H_0: $\mu = 0$**			**χ^2 Test (α=0.05%) vs. the 95% accuracy H_0: $\sigma^2 = 1.5^2 cm^2$**			**H_1: $\sigma^2 = \sigma_a^2$**		
Case No.*	Error	Mean [cm]	Stdev [cm]	RMS [cm]	f	t	$t_{f,0.025}$	Accepted (Y/N)	χ^2	$\chi^2_{f,0.05}$	Accepted (Y/N)	σ_a [cm]	χ^2	Accepted (Y/N)
1	**N**	-1.59	2.17	2.67	22	-3.51	2.074	N						
	E	-2.05	1.95	2.82	22	-5.04	2.074	N						
	U	3.56	2.34	4.24	22	7.31	2.074	N	205.08	33.92	N	**3.7**	33.70	Y
	2D(H)	2.59	2.92	3.88	22				332.68	33.92	N	**4.7**	33.89	Y
2	**N**	-0.37	1.71	1.74	22	-1.04	2.074	Y						
	E	-0.63	1.53	1.65	22	-1.96	2.074	Y						
	U	1.11	1.77	2.08	22	3.01	2.074	N	118.02	33.92	N	**2.8**	33.87	Y
	2D(H)	0.73	2.29	2.40	22				205.98	33.92	N	**3.7**	33.85	Y
3	**N**	-0.41	1.06	1.16	22	-1.87	2.074	Y						
	E	-0.34	0.93	1.02	22	-1.74	2.074	Y						
	U	0.35	1.19	1.25	22	1.41	2.074	Y	53.24	33.92	N	**1.9**	33.19	Y
	2D(H)	0.54	1.41	1.54	22				78.29	33.92	N	**2.3**	33.30	Y
4	**N**	-0.25	0.76	0.84	22	-1.58	2.074	Y						
	E	-0.20	0.78	0.84	22	-1.22	2.074	Y						
	U	0.19	0.91	0.96	22	0.98	2.074	Y	31.18	33.92	Y	**1.5**	31.18	Y
	2D(H)	0.32	1.09	1.19	22				46.41	33.92	N	**1.8**	32.23	Y
5	**N**	-0.28	0.81	0.89	22	-1.67	2.074	Y						
	E	-0.24	0.86	0.92	22	-1.37	2.074	Y						
	U	0.30	1.01	1.07	22	1.42	2.074	N	38.00	33.92	N	**1.6**	33.40	Y
	2D(H)	0.37	1.18	1.28	22				54.38	33.92	N	**1.9**	33.89	Y

6	**N**	-0.18	0.68	0.75	22	-1.29	2.074	Y							
	E	-0.12	0.72	0.77	22	-0.84	2.074	Y							
	U	0.15	0.98	1.01	22	0.72	2.074	Y	35.79	33.92	N	**1.6**	31.46	Y	
	2D(H)	0.22	0.99	1.08	22				38.28	33.92	N	**1.6**	33.64	Y	

***Note:**

- Case 1: The differences between the pre-surveyed coordinates and the original LiDAR coordinates **before** BA calibration.
- Case 2: The differences between the pre-surveyed coordinates and the original LiDAR coordinates **after** BA calibration.
- Case 3: The differences between the pre-surveyed coordinates and the adjusted LiDAR coordinates derived from using single strip **before** BA calibration. (i.e., case 2 of section 5.3.2)
- Case 4: The differences between the pre-surveyed coordinates and the adjusted LiDAR coordinates derived from using single strip **after** BA calibration.
- Case 5: The differences between the pre-surveyed coordinates and the adjusted LiDAR coordinates derived from using two strips in opposite directions **before** BA calibration. (i.e., case 3 of section 5.3.2)
- Case 6: The differences between the pre-surveyed coordinates and the adjusted LiDAR coordinates derived from using two strips in opposite directions **after** BA calibration.

7 Conclusions and Future Work

7.1 Conclusions

In this research, various algorithms and strategies were developed and applied to improve the overall accuracy of terrestrial mobile LiDAR solutions in the field of engineering surveys. A detailed analysis for error budget of terrestrial mobile LiDAR system has been presented in order to well interpret the effects of individual error sources. The Optech Lynx Mobile Mapper V200 was used in this study.

Firstly, the 3D conformal coordinate transformation (3DCCT) was proposed to improve the accuracy quality of terrestrial mobile LiDAR solutions by utilizing the ground control points aided by straight line and planar patch feature constraints. The utilization of GCPs could remove some of the leftover systematic errors and improve the absolute accuracies of terrestrial mobile LiDAR solutions, or make up for poor GPS performance and/or the GPS outages. The characteristic points, such as the corners of building, window, traffic lights and signs and pavement markings etc., were chosen as the absolute control information to eliminate the cost and/or authority request for setting up targets in field. Then the 3DCCT adjustment, which preserved angles and shape of objects, was applied to establish the relationship between the per-surveyed coordinates and the coordinates of LiDAR points. Furthermore, two strategies were implemented by: (1) Segmental 3DCCT adjustment, and (2) Categorization of GCPs concerning horizontal and vertical accuracy improvements.

The feature constraints were also applied to enhance the GCPs for further accuracy improvement of terrestrial mobile LiDAR solutions. In the research, the absolute position

and orientation parameters of features were determined using the corresponding pre-surveyed coordinates of control points. Some characteristic objects were selected as planar patch or linear features in both horizontal and vertical directions, such as, traffic signs and lights, advertisement signs along the road, building facades and stop bars etc. Moreover, the usage optimization of the control points was investigated in terms of density and ideal distribution in order to efficiently and effectively employs those measurements.

The proposed methodology has been thoroughly investigated for its accuracy through the checking GCPs based on the testing results in various environments. Different strategies were designed and first implemented with the data collected at the headquarter office building of Optech Inc. at the City of Vaughan, Ontario. Then, a more complicated and actual field site located around Black Creek Pioneer Village was selected to further validate the developed algorithms and strategies. Two study areas: i) a 200-meter stretch under an ideal condition with adequate GCPs and feature constraints; ii) a 3-kiloemter loop under a real-time condition with limited GCPs, were made available for this research. Some important findings from this research are restated below:

1. The error behaviors may change during a long data acquisition mission due to the non-uniform effects of the residual systematic errors of a terrestrial mobile LiDAR system. Thus, it is necessary to segment a long LiDAR data strip into small portions and introduce the 3DCCT adjustment separately for each segment in order to compensate for the different natures and amplitudes of the errors in the different parts

of the data strip. In other words, the best practice is to apply segmental 3DCCT to a large stretch of data.

2. The error effects in terrestrial mobile LiDAR solutions may not be uniform in horizontal and vertical directions for a given scene caused by the uncertainties in INS orientation and boresight angles between the INS and LiDAR instrument (Hu et al., 2013). Therefore, the GCPs could be categorized into different groups, e.g. in concerning accuracy improvements of points on ground surfaces or on the vertical wall surface etc., according to their location or geometry information, such as, building and ground types. Then the 3DCCT parameters were separately determined by using the same type of control points.
3. It was concluded that additional straight line and planar patch feature constraints incorporating with GCPs could further improve the accuracies of mobile LiDAR solutions. It achieved the accuracy of ±2.2cm in horizontal and ±1.7cm in vertical for the best scenario case (case 4 in Section 4.2.4) at the 95% confidence level of the Type I error. Furthermore, the feature constraints could be categorized into horizontal direction (e.g., pavement markings) and vertical direction (for example, traffic light and signs). By using only one type of feature constraints, the accuracy in that direction could be increased significantly, while the accuracy in the other direction was not be improved significantly in comparison with using both types of feature constraints. Therefore, it is necessary to apply all direction feature constraints in the 3DCCT adjustment.

4. The results in Study Area #2 (Section 4.3.3.4) indicated that using more GCPs or smaller control points interval could achieve more accuracy improvement. However, the overall performance of the LiDAR solutions were not decreased a lot by reducing the number of used GCPs between 20 and 30 percentages of the total number control points or extending the intervals to 50m, 75m and 100m with the help of straight line and planar patch feature constraints. That is, the number of control points had a limited impact on the accuracy of LiDAR points especially in term of the vertical accuracy with the GCP separation from 25m to 100m. However, the 3D LiDAR positioning accuracy was decreased dramatically by extending the intervals to 150m and 200m. Therefore, it is necessary to select the control points efficiently and effectively by considering the project budget and minimal required accuracy. Especially, the number of GCPs may be reduced or the shortage or absence of GCPs in some areas could be made up for by involving the linear or planar feature constraints.

Furthermore, inspired by the advances in airborne LiDAR technology, the multistrip adjustment (MA) process was developed to take advantage of the overlapped data strips and the repeated data acquisition over the same study area. The strip offsets of tie points and features provided the ideal information allowing refining and improving the mobile LiDAR solution by adjusting the leftover boresight and other systematic errors. Once the two strips were merged together, the 3DCCT adjustment was applied by georeferencing the whole LiDAR point cloud using GCPs and geometrical constraints. The testing results implied that:

1. The accuracy of LiDAR solutions was increased significantly by using two strips acquired in the opposite driving directions. However, the overall performance was not improved significantly with the two strips acquired in the same travelling direction. It was also worth mentioning that the merged LiDAR point cloud derived from opposite directions produced the best visibility, and the radiometric intensity was enhanced due to the more dense points. Nevertheless, the merged strips from the same driving direction showed no difference in terms of visibility relative to the individual datasets.
2. For Study Area #1 of the validation site (Section 5.3.1), the achieved horizontal accuracy was ±2.2cm and vertical accuracy was ±1.8cm by using 16 GCPs with two oppositely-driven data strips, which was compatible with the scenario by using 38 GCPs with single strip. Therefore, it indicated that the number of the required GCPs could be reduced or the shortage even the absence of GCPs in some areas could be compensated for by implementing the MA process with the tie points and tie features.

Lastly, the boresight angles of a terrestrial mobile LiDAR system could preliminarily be calibrated by applying the method in Keller et al. (2013). This technique employed raw point cloud measurements of scanned objects/facades with different orientation of two scans consecutively acquired in the opposite driving directions. Then these parameters can be used to compensate for the boresight biases in the subsequently collected LiDAR data. The poor boresight estimation could seriously degrade the quality of LiDAR solutions. As a result, the boresight angle calibration plays an important role in

the LiDAR solutions. Some important outcomes from this research are summarized as follows:

1. It could improve the overall quality of terrestrial mobile LiDAR solution, especially with the raw LiDAR point cloud and the 3DCCT adjustment using single strip. For example, in Study Area #1 (Section 6.2.1), the achieved horizontal accuracy was improved significantly from ±5.0cm to ±3.9cm (raw LiDAR point cloud, cases 1 and 2) and from ±2.3cm to ±1.8cm (3DCCT using single strip, cases 3 and 4), respectively, after the boresight angle calibration.
2. Some of the remaining systematic errors could be modeled and eliminated through the MA process using two data strips acquired in the opposite driving directions because it aligns the overlapped strips with tie points and tie features. Take Study Area #1 as a example (Section 6.2.1, cases 5 and 6), the accuracies derived through MA process only increased from ±2.0cm to ±1.7cm in horizontal, but no improvement in vertical where before and after the boresight angel calibration because the MA process and the preliminary boresight calibration have the similar function in LiDAR solution refinement in terms of modeling systematic errors.
3. The post-processing procedures could be simplified by either implementing the 3DCCT with single strip and the boresight angle calibration (horizontal - ±1.8cm, vertical - ±1.5cm in Study Area #2, Section 6.2,2, case 4) or executing the MA approach using two strips acquired in the opposite driving directions but not involving the system calibration (horizontal - ±1.9cm, vertical - ±1.6cm in Study Area #2, Section 6.2.2, case 5). None of the achieved accuracies of two options were

degraded dramatically relative to the best testing case where applying both boresight angles correction and MA process (horizontal - ±1.6cm, vertical - ±1.6cm in Study Area #2, Section 6.2.2, case 6).

The proposed algorithms in this research require the usage of many ground control points and feature constraints with different spatial orientation. They could be easily identified in the urban or sub-urban regions, where with an adequate amount of facade sections, roofs of buildings, traffic signs and pavement markings along the street containing preferably flat surfaces of variable orientation. However, not every area is adequate for carrying out a system calibration of boresight angles. Obstructions of GPS signal caused by tall buildings or tree canopy degrade the accuracy of position and attitude information significantly. Therefore, the appropriate values of pulse repetition frequency (PRF), mirror scan rate and driving speed is also essential in order to ensure the sufficient point density on the surfaces of the scanned objects. In practical, the laser PRF of 250 kHz was sufficient to accurately in the statistical sense characterize the scenes in the urban environment where the buildings are on both sides of the road. The mirror speed (within the range from 80 Hz to 200 Hz) has a limited effect on the LiDAR solution. Finally, the practical protocol of post-processing procedures for a more efficient and cost-effective implementation of the proposed algorithms for performance improvement of terrestrial mobile LiDAR solutions is suggested in Figure 7-1.

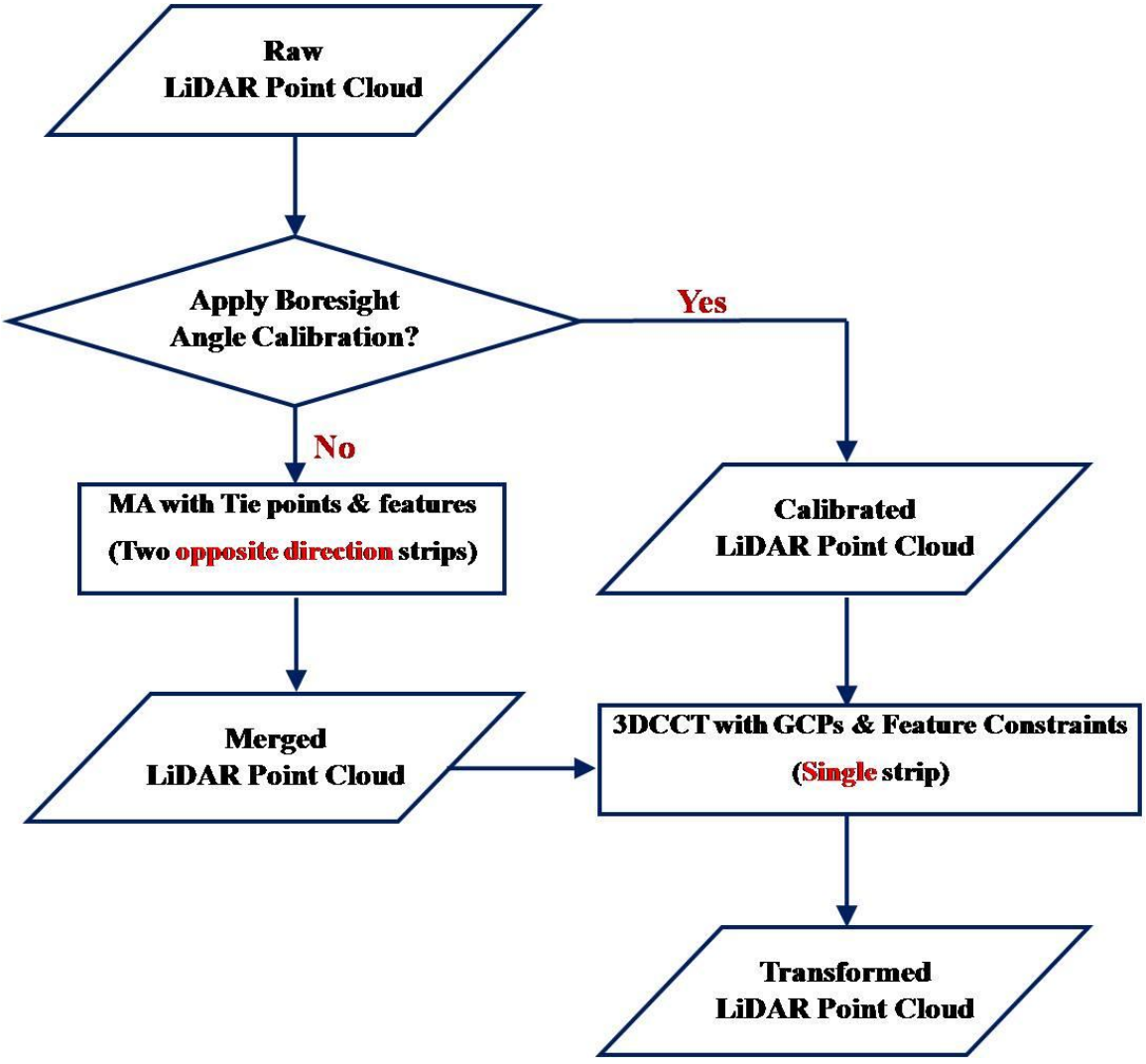

Figure 7-1: The suggested practical protocol of post-processing procedures for performance improvement of terrestrial mobile LiDAR solutions.

7.2 Recommendation for Future Works

Certain future work (not limited to) associated with this research can be suggested as follows:

1. The drawback of both 3DCCT and MA algorithms is that the identification of distinct GCPs, feature constraints, tie points and tie features in terrestrial mobile LiDAR data is a difficult task due to the irregular and sparse nature of the collected point cloud. Measurement errors possibly introduced by the identification process or the surveys of the selected targets as control points may degrade the confidence in the accuracy improvement process. In addition, it demanded much effort on preparing special test sites and carrying out field surveying. Therefore, the approach needs to be in a more economic, automatic or semi-automatic way.
2. The three boresight angle components were neither calibrated simultaneously nor during the on-board data collection stage. Moreover, other systematic errors were not considered in this research, such as, platform position and orientation, vehicle trajectory, lever-arms and laser ranges etc. A rigorous calibration methodology is desired to resolve the transformation parameters together with the biases in the system parameters in a combined adjustment model. This has a practical impact as no additional surveying campaign apart from the calibration procedures needs to be designed for LiDAR system calibration.
3. The overall quality of terrestrial mobile LiDAR solutions could be improved and the required number of GCPs may be reduced or the absence of GCPs in some areas could be compensated for by employing the tie points and features in adjacent strips.

However, more overlapped data strips will definitely increase the available data volume and redundant measurements. Therefore, an appropriate method needs to be implemented to reduce the overwhelming growth of data volume whilst improving the solution quality.

4. Due to the different accuracy level of GPS measurements, the vertical accuracy of georeferenced LiDAR coordinates is high than the horizontal direction. Hence, the 3DCCT parameters might need to be separated derived in 2D horizontal and vertical directions.

Reference

Akca D. (2010): Co-registration of Surfaces by 3D Least Squares Matching. Photogrammetry Engineering and Remote Sensing, Vol. 76, No. 3, pp. 307 – 318.

Bähr, H.; Altamimi, Z. and Heck, B. (2007): Variance Component Estimation for Combination of Terrestrial Reference Frames, Universität Karlsruhe (TH), Schriftenreihe des Studiengangs Geodäsie und Geoinformatik.

Baltsavias, E. (1999): Airborne Laser Scanning: Existing Systems and Firms and Other Resources, ISPRS Journal of Photogrammetry and Remote Sensing, 54 (2-3), pp. 164-198.

Bang, K., Habib, A. and Müller M. (2009): LiDAR System Calibration Using Overlapping Strips. Bol. Ciênc. Geodesy, v. 15, n. 5 – Special Issue on Mobile Mapping Technology, p. 725-742.

Barber, D., Mills, J., & Smith-Voysey, S. (2008). Geomatric Validation of A Ground-based Mobile Laser Scanning System. ISPRS Joirnal of Photogrammetry and Remote Sensing, 63, 128 - 141.

Besl, P. J. and N. D. McKay (1992): A Method for Registration of 3D Shapes. IEEE Transactions on Pattern Analysis and Machine Intelligence, Vol 14, No.2, 239 – 256.

Bosché Frédéric (2012): Plane-based Registration of Construction Laser Scans with 3D/4D Building. Advanced Engineering Informatics, Vol 26, pp 90 – 102.

Bretar F., Pierrot-Deseilligny M. and Roux M. (2004): Solving the Strip Adjustment Problem of 3D Airborne LiDAR Data. Geoscience and Remote Sensing Symposium, Proceedings of the IEEE IGARSS'04, Anchorage, Alaska, vol 7, pp. 4734 - 4737.

Burman, H. (2000): Adjustment of Laser Scanner Data for Correction of Orientation Errors. International Archives of Photogrammetry and Remote Sensing, Vol. XXXIII, Part B3, pp. 125-132, Amsterdam.

Caltrans (2012): Surveys Manual, California Department of Transportation, US, 2012.

Caspary, W.F: Concepts of Network and Deformation Analysis; Monograph 11, School of Surveying, UNSW, Sydney, NSW, Australia, August 2000.

Chan, T. (2011): Feature-based Boresight Self-Calibration of a Mobile Mapping System. UCGE Reports No. 20348.

Crombaghs, M., E. De Min, and R. Bruegelmann (2000): On the Adjustment of Overlapping Strips of Laser Altimeter Height Data. International Archives of Photogrammetry and Remote Sensing, 33(B3/1): 230-237.

Dold, C. and C. Brenner (2006): Registration of Terrestrial Laser Scanning Data Using Planar Patches and Image Data. The International Archives of the Photogrammetry, Remote Sensing and Spatial Information Sciences, Vol. XXXVI, Dresden, Germany, pp. 78 – 83.

Durrieu, S., Allouis, T., Fournier, R., Véga, C. and Albrech, L. (2008): Spatial Quantification of Vegetation Density from Terrestrial Laser Scanner Data for Characterization of 3D Forest Structure at Plot Level. SilviLaser 2008, Sept. 17-19, Edinburgh, UK, pp. 325-334.

Filin, S. (2001): Recovery of Systematic Biases in Laser Altimeters Using Natural Surfaces. International Archives of Photogrammetry and Remote Sensing, Vol. XXXIV, Part 3/W4, pp. 85-91.

Filin, S. (2003a): Recovery of Systematic Biases in Laser Altimetry Data Using Natural Surfaces. ISPRS Journal of Photogrammetric Engineering and Remote Sensing, 69(11): 1235–1242.

Filin, S. (2003b): Analysis and Implementation of a Laser Strip Adjustment Model. International Archives of Photogrammetry and Remote Sensing, 34 (Part 3/W13): 65–70.

Filin S. and Vosselman G. (2004): Adjustment of Airborne Laser Altimetry Strips. The International Archives of the Photogrammetry, Remote Sensing and Spatial Information Sciences, 35 (B3): 285-289.

Fitzgibbon A.W. (2003): Robust Registration of 2D and 3D Point Sets. Image and Vision Computing, Vol. 21, pp. 1145 – 1153.

Förstner, W. (1979): Ein Verfahren zur Schätzung von Varianzund Kovarianzkomponenten, Allgemeine Vermessungsnachrichten, No. 11-12, pp. 446-453.

Friess, P. (2006): Toward A Rigorous Methodology for Airborne Laser Mapping. International Calibration and Orientation Workshop EuroCOW 2006, Spain.

Glennie, C. (2007): Rigorous 3D Error Analysis of Kinematic Scanning LiDAR System. Journal of Applied Geodesy, 147-157.

Glennie, C. (2009): Kinematic Terrestrial Light-Detection and Ranging System for Scanning. Transportation Research Record, No. 2105, pp. 135-141.

Goulette, F.; Nashashibi, F.; Abuhadrous, I.; Ammoun, S. and Laurgeau, C. (2006): An Integrated On-Board Laser Range Sensing System for On-the-Way City and Road Modelling. International Archives of the Photogrammetry, Remote Sensing and Spatial Information Sciences, Paris, France, Vol. XXXVI, Part 1.

GRÄFE, G. (2008): Kinematic 3D Laser Scanning for Road or Railway Construction Surveys. 1st International Conference on Machine Control and Guidance 2008.

Grejner-Brzezinska, D. A. (2001): Mobile Mapping Technology: Ten years later (Part 1). Surveying and Land Information Systems (SaLIS), 61(2): pp. 79-94.

Gruen, A. and D. Akca (2004): Least Squares 3D Surface Matching. Proceedings of the ISPRS working group V/1, Panoramic Photogrammetry Workshop, Vol. XXXIV, Part 5/W16, Dresden.

Gruen, A. and D. Akca (2005): Least Squares 3D Surface and Curve Matching. ISPRS Journal of Photogrammetry and Remote Sensing, Vol. 59, No. 3, pp. 15 – 174.

Gueziec, A. and N. Ayache (1994): Smoothing and matching of 3-D space curves. International Journal of Computer Vision, Vol. 12, No. 1, pp.79– 104.

Haalaa, N.; Petra, M.; Cefalua, A. and Kremerb, J. (2008): Mobile LiDAR Mapping For Urban Data Capture, VSMM 2008, Digital Heritage – Proceedings of the 14th International Conference on Virtual Systems and Multimedia, pp. 95 – 100.

Habib, A. and T. Schenk (1999): A New Approach for Matching Surfaces from Laser Scanners and Optical Scanners. International Archives of Photogrammetry and Remote Sensing, Vol. 32, No. 3/W14, pp. 55– 61.

Habib, A.; Mwafag, G.; Morgan, M., and Al-Ruzouq R. (2005): Photogrammetric and LiDAR Data Registration Using Linear Features, Photogrammetric Engineering and Remote Sensing, vol. 71, no. 6, pp. 699–707.

Habib, A., K.I. Bang, S. Shin and E. Mitishita (2007): LiDAR System Self-calibration Using Planar Patches from Photogrammetric Data. MMT'07, The 5th International Symposium on Mobile Mapping Technology, Padua, Italy, 2007.

Habib, A.; K.I. Bang; A.P. Kersting and D. Lee (2009): Error Budget of LiDAR Systems and Quality Control of the Derived Point Data. Photogrammetric Engineering & Remote Sensing, Vol. 75, No. 9, September 2009, pp. 1093–1108.

Helmert, F.R. (1907): Die Ausgleichungsrechnung nach der Methode der kleinsten Quadrate. 2nd Edition, Teubner, Leipzig, Berlin.

Hofmann, S. and Brenner, C. (2009): Quality Assessment of Automatically Generated Feature Maps for Future Driver Assistance Systems. 17th ACM SIGSPATIAL International Conference on Advances in Geographic Information Systems, Seattle, Washington, USA, pp. 500–503.

Hu, Baoxin; Wang, Jianguo and Liu, Guannan (2012): Performance and Potentials of Ground LiDAR (mobile and static) in Engineering Survey and Highway Design, Highway Infrastructure Innovations Funding Program, Series Number: HIIFP-113, Ministry of Transportation of Ontario, 2012 (www.library.mto.gov.on.ca).

Hu, Baoxin; Wang, Jianguo; Leslar, Michael and Liu, Guannan (2013): Improving the Accuracy of Mobile LiDAR for Engineering Surveys. LiDAR Magazine, Vol. 3 No. 6.

Huising, E. J., and L. M. G. Pereira (1998): Errors and Accuracy Estimates of Laser Data Acquired by various Laser Scanning Systems for Topographic Applications, ISPRS Journal of Photogrammetry and Remote Sensing, 53(5), pp. 245-261.

Ingensand H. (2006): Methodological Aspects in Terrestrial Laser-scanning Technology. Proceedings of the 3rd IAG Symposium of Geodesy for Geotechnical and Structural Engineering and 12th FIG Symposium on Deformation Measurements. May 22 – 24, Baden, Austria.

International Hydrographic Organization (IHO). Chapter 3 Depth Determination. In Manual on Hydrography Publication C-13, 1st ed.; International Hydrographic Organization, International Hydrographic Bureau: Monaco, China, 2011.

Jaakkola, A.; Hyyppä, J.; Hyyppä, H. and Kukko, A. (2008): Retrieval Algorithms for Road Surface Modelling Using Laser-Based Mobile Mapping. Sensors, Vol. 8, pp. 5238–5249.

Jaakkola, A.; Hyyppä, J.; Kukko, A.; Yu, X.; Kaartinen, H.; Lehtomäki, M. and Lin, Y. (2010): A Low-Cost Multi-Sensoral Mobile Mapping System and Its Feasibility for Tree Measurements. ISPRS Journal of Photogrammetry and Remote Sensing, Vol.65, pp. 514–522.

Jaw, Jen-Jer. and Chuang, Tzu-Yi (2008): Registration of Ground-based LiDAR Point Clouds by Means of 3D Line Features. Journal of the Chinese Institute of Engineers, Vol. 31, Issue 6, pp. 303 – 308.

Kager, H. (2004): Discrepancies between Overlapping Laser Scanning Strips Simultaneous Fitting of Aerial Laser Scanner Strips. Proceedings of the International Society for Photogrammetry and Remote Sensing XXth Congress, Istanbul, 34(B/1): 555 - 560.

Keller, F. and Sternberg, H. (2013): Multi-Sensor Platform for Indoor Mobile Mapping: System Calibration and Using a Total Station for Indoor Applications. Remote Sensing, Volume 5, p. 5805-5824.

Kersting, A. P.; Zhai, R. and Habib, A. (2008): Strip Adjustment Using Conjugate Planar and Linear Features in Overlapping Strips. ASPRS 2008 Annual Conference, Portland, Oregon.

Kilian, J.; Haala, N. and Englich, M. (1996): Capture and Evaluation of Airborne Laser Scanner Data. International Archives of Photogrammetry and Remote Sensing, Vol. XXXI, B3, 383 – 388, Vienna, Austria.

Kornus, W. and Ruiz, A. (2003): Strip Adjustment of LiDAR Data, International Archives of Photogrammetry and Remote Sensing, Working Group III/3 Workshop, Dresden, Germany, International Society of Photogrammetry and Remote Sensing (ISPRS).

Krabill, W.B., J.G. Collins, L.E. Link, R.N. Swift, and M.L. Butler (1984): Airborne Laser Topographic Mapping Results. Photogrammetric Engineering & Remote Sensing, 50(6):685–694.

Kraus, K., C. Ressl and A. Roncat (2006): Least Squares Matching for Airborne Laser Scanner Data. Proceedings of the 5th International Symposium Turkish-German Joint Geodetic Days, 29 -31 March, Berlin, Germany, unpaginated CD-ROM.

Lato, M., Hutchinson, D.J., Diederichs, M.S., Ball, D., and Harrap, R. (2009): Engineering Monitoring of Rockfall Hazards Along Transportation Corridors: Using Mobile Terrestrial LiDAR. Natural Hazards and Earth System Sciences, Vol. 9, 935–946.

Lee, Jaebin; Yu, Kiyun; Kim, Yongil and Habib, Ayman F. (2007): Adjustment of Discrepancies between LiDAR Data Strips Using Linear Features. IEEE Geoscience and Remote Sensing Letters, Vol. 4, No. 3, 475 – 479, July 2007.

Leick, Alfred (2004): GPS Satellite Surveying (3rd Edition). John Wiley & Sons, ISBN 0471059307.

Lichti, D.D. and S.J. Gordon (2004): Error Propagation in Directly Georeferenced Terrestrial Laser Scanner Point Clouds for Cultural Heritage Recording. In Proceeding of FIG Working Week, Athens, Greece, May 22-27, pp. 16.

Maas, H.G. (2000): Least-squares Matching with Airborne Laser Scanning Data in a TIN Structure. International Archives of Photogrammetry and Remote Sensing, Vol. XXXIII, B3, 548 – 555, Amsterdam.

Maas, H. G. (2002): Methods for Measuring Height and Planimetry Discrepancies in Airborne Laser Scanner Data, Photogrammetric Engineering & Remote Sensing, 68(9): 933–940.

Mason, D.C., Matthew S. Horritt, Neil M. Hunter and Paul D. Bates (2007): Use of Fused Airborne Scanning Laser Altimetry and Digital Map Data for Urban Flood Modeling. Hydrological Processes. Vol. 21, Issue 11, pp. 1436-1447.

Mensi (2003) MENSI – 3D Laser Scanner/3D Scanners for Surveying Applications. http://www.mensi.com.

Morgan, Daina (2009): Using Mobile LiDAR to Survey Railway Infrastructure – Lynx Mobile Mapper, Innovative Technologies for an Efficient Geospatial Management of Earth Resources, FIG Commissions 5, 6 and SSGA Workshop, Lake Baikal, Listvyanka, Russia, 23-30 July 2009.

MTO (2006): Engineering Survey Manual, Geomatics Office, highway Standards Branch, Provicial Highways Management Division, Ministry of Transportation of Ontario (MTO), St. Catharines, Ontario, 2006.

Neter, John; Wasserman, William and Whitmore, G.A (1988): Applied Statistics, Allyn and Bacon Inc., Boston London Sydney Toronto, 1988.

Park, S.Y. and M. Subbarao (2003): A fast point-to-tangent plane technique for multi-view registration. IEEE International Conference on 3D Digital Imaging and Modeling, Banff, October 6–10, pp. 276–283.

Petrie, G. (2010): Mobile Mapping Systems - An Introduction to the Technology. Geoinformatics, 13(1), pp. 32–43.

Pfeifer, N., S. O. Elberink, and S. Filin (2005): Automatic Tie Elements Detection for Laser Scanner Strip Adjustment. International Archives of Photogrammetry and Remote Sensing, 36(3/W3): 1682-1750.

Pfeifer, N. and C. Briese (2007): Laser Scanning – Principles and Applications. Institute of Photogrammetry and Remote Sensing, Vienna University of Technology, Austria.

Pothou, A., C. Toth, S. Karamitsos and A. Georgopoulos (2007): On using QA/QC Techniques for LiDAR/IMU Boresight Misalignment. MMT'07, The 5th International Symposium on Mobile Mapping Technology, Padua, Italy, 2007.

Pothou, A., C. Toth, S. Karamitsos and A. Georgopoulos (2008): An Approach to Optimize Reference Ground Control Requirements for Estimating LiDAR/IMU Boresight Misalignment. XXI Congress ISPRS, WG-I/2, China, 2008.

Pothou, A., C. Toth, S. Karamitsos and A. Georgopoulos (2009): Spatial Distribution Requirements of Reference Ground Control for Estimating LiDAR/INS Boresight Misalignment. Special Issue on Mobile Mapping Technology, Vol. 15, No. 5, pp. 776 – 789.

Puente, I.; González-Jorge, H.; Arias, P. and Armesto, J. (2011): Land-Based Mobile Laser Scanning Systems: a Review, ISPRS workshop Laser Scanning 2011, Vol. XXXVIII – 5/W12, 2011, Calgary, Canada, 29-31 August, 2011.

Reshetyuk, Yuriy (2006): Investigation and Calibration of Pulsed Time-of-flight Terrestrial Laser Scanners. Royal Institute of Technology (KTH), Department of Transport and Economics, Division of Geodesy.

Rieger, P., Studnicka, N. and Pfennigbauer, M. (2010): Boresight Alginment Method for Mobile Laser Scanning Systems. RIEGL Laser Measurement Systems GmbH. Journal of Applied Geodesy, Volume 4, p. 13-21.

Schenk, T. (2001): Modeling and Analyzing Systematic Errors in Airborne Laser Scanners. Technical Notes in Photogrammetry, No. 19, Department of Civil and Environmental Engineering and Geodetic Science, The Ohio State University, Volume XIX, Columbus, USA, 40 pages.

Shan J. and Toth, C.K. (2008): Topographic Laser Ranging and Scanning: Principles and Processing, 616 pages, ISBN 9781420051421.

Sherif, E., A. Moussa, D.D. Lichti and N. El-Sheimy (2011): Detection of Road Curb from Mobile Terrestrial Laser Scanner Point Cloud. International Archives of the Photogrammetry, Remote Sensing and Spatial Information Sciences, Vol. XXXVIII-5/W12, Workshop, 29-31 August, Calgary, Canada

Skaloud, J. and Lichti, D. (2006): Rigorous Approach to Bore-Sight Self-Calibration in Airborne Laser Scanning. ISPRS Journal of Photogrammetry and Remote Sensing, Volume61, Issue 1, pp.47-59.

Slob, S. and R. Hack (2004): 3D Terrestrial Laser Scanning as a New Field Measurement and Monitoring Technique. Engineering Geology for Infrastructure Planning in Europe: A European Perspective, Edited by Robert Hack, Rafig Azzam, and Robert Charlier. Lecture Notes in Earth Sciences, Vol. 104, pp.179-189.

Toth, C.K. and Csanyi, N. (2001): Automating the LiDAR Boresight Misalignment. ISPRS WGII/2 Workshop on 3D Mapping from InSAR and LIDAR, Banff, Alberta, Canada, CD ROM.

Toth, C.K. (2002): Calibrating Airborne LiDAR Systems. ISPRS Commission II Symposium on Integrated Systems for Spatial Data Production, Custodian and Decision Support, IAPRS, Vol. XXXIV, part 2, pp. 475-480.

Toth, C. K., Csanyi , N., Grejner-Brzezinska, D., & Ray, J. (2005): Improvement of LiDAR Data Accuracy Using LiDAR Specific Ground Targets. ASPRS 2005 Annual Conference. Baltimore, Maryland.

Toth, C.K. and Csanyi N. (2007): Improvement of LiDAR Data Accuracy Using LiDAR-specific Ground Targets, Photogrammetric Engineering & Remote Sensing, Vol. 73, No. 4, pp. 385–396.

Toth, C. K., Paska, E., & Brzezinska, D. (2007). Using Pavement Markings to Support the QA/QC of LiDAR Data. International Archives of Photogrammetry, Remote Sensing and Spatial Information Sciences, 36, 173 – 178.

Uddin, W.; L. Yiqin, and L. D. Phillips (2001): Integration of Remote Sensing and Geospatial Technologies for Managing Transportation Infrastructure Assets. CD Proceedings Second International Symposium on Maintenance and Rehabilitation of Pavements and Technological Control. Auburn, Alabama, 2001.

Ussyshkin, Valerie (2009): Mobile Laser Scanning Technology for Surveying Applications: From Data Collection to End-Products, FIG Working Week 2009, Surveyors Key Role in Accelerated Development, Israel, 3-8 May 2008.

Vosselman, G. (2004): Strip Offset Estimation Using Linear Features. Department of Geodesy, Delft University of Technology, Netherlands.

Wyngaerd, V., J., Van Gool, L., Koch and R., Proesmans (1999): Invariant-based registration of surface patches. IEEE International Conference on Computer Vision, Kerkyra, September 20–27, pp. 301– 306.

Yen, K.S.; Akin, K.; Lofton, A.; Ravani B. and Lasky T.A.: Using Mobile Laser Scanning to Produce Digital Terrain Models of Pavement Surfaces, Report No. F/CA/RI2008/xx, 86 pages, California Department of Transportation, 2010.

Yousif, H., Li, J., Chapman, M., & Shu, Y. (2012): Accuracy Enhancement of Terrestrial Mobile LiDAR Data Using Theory of Assimilation. International Archives of Photogrammetry, Remote Sensing and Spatial Information Sciences, Commission V Mid-Term Symposium "Close Range Image Measurement Techiniques", 21- 24 June, 2010, XXXVIII, Part 5, Newcastle upon Tyne, UK.

Zampa, F. and D. Conforti (2009): Mapping with mobile LiDAR, GIM International, vol.23, no.4, pp35 – 37.

Zhang, Z. (1994): Iterative Point Matching for Registration of Freeform Curves and Surfaces. International Journal of Computer Vision, Vol. 13, No. 2, pp. 119 – 152.

Zhi, X. and L. Zhong (2008): A Progressive Quality Control to Improve the Accuracy of LiDAR Data Processing. The International Archives of the Photogrammetry, Remote Sensing and Spatial Information Sciences, Vol. XXXVII, Part B1, Beijing.

Appendix

Appendix A – The estimated ECEF coordinates (WGS84) of targets from Optech Inc. testing scene

Table A-1: The estimated ECEF coordinates (WGS84) of targets in the testing scene.

Station	X [m]	σ [mm]	Y [m]	σ [mm]	Z [m]	σ [mm]	σ_{3D} [mm]
F211	838502.4036	2.4	-4534995.7617	2.3	4391296.6050	2.2	4.0
F212	838502.3871	2.4	-4534995.6883	2.3	4391296.6941	2.2	4.0
F213	838505.0439	2.4	-4534995.3320	2.1	4391296.4984	2.0	3.8
F214	838505.0386	2.4	-4534995.2569	2.1	4391296.5798	2.0	3.8
F215	838508.2790	2.4	-4534994.8189	1.8	4391296.3773	1.7	3.4
F216	838508.2685	2.4	-4534994.7401	1.8	4391296.4628	1.7	3.4
F231	838502.0352	3.4	-4534992.0842	3.1	4391300.5644	2.8	5.4
F232	838502.0216	3.4	-4534992.0082	3.1	4391300.6380	2.8	5.4
F233	838504.6775	3.5	-4534991.6412	2.8	4391300.4159	2.5	5.1
F234	838504.6672	3.5	-4534991.5695	2.8	4391300.5076	2.5	5.1
F235	838507.9152	3.6	-4534991.1323	2.4	4391300.2739	2.1	4.8
F236	838507.9041	3.6	-4534991.0600	2.4	4391300.3568	2.1	4.8
F251	838501.7316	3.1	-4534988.3814	2.6	4391304.4690	2.3	4.7
F252	838501.7191	3.2	-4534988.3027	2.6	4391304.5573	2.3	4.7
F253	838504.5042	3.2	-4534987.9200	2.3	4391304.3484	2.0	4.4
F254	838504.4858	3.2	-4534987.8437	2.3	4391304.4290	2.0	4.4
F255	838507.5821	3.3	-4534987.4286	2.0	4391304.2233	1.7	4.2
F256	838507.5682	3.4	-4534987.3494	2.0	4391304.3066	1.7	4.3
F311	838478.1954	1.0	-4534971.8317	0.8	4391326.5077	0.8	1.5
F312	838478.0720	1.0	-4534971.8520	0.8	4391326.5143	0.8	1.5
F313	838478.0552	1.0	-4534969.7258	0.7	4391328.6501	0.7	1.4
F314	838477.9420	1.0	-4534969.7444	0.7	4391328.6492	0.7	1.4
F315	838477.9388	1.0	-4534967.7349	0.6	4391330.7280	0.7	1.4
F316	838477.8253	1.0	-4534967.7491	0.6	4391330.7306	0.7	1.4
F341	838469.6166	1.8	-4534972.9727	1.2	4391326.8034	1.3	2.5
F342	838469.5138	1.8	-4534972.9871	1.2	4391326.8089	1.3	2.5
F343	838469.4919	1.7	-4534970.9911	1.1	4391328.8271	1.2	2.4
F344	838469.3812	1.7	-4534971.0097	1.1	4391328.8253	1.2	2.4
F345	838469.3504	1.6	-4534968.8323	1.0	4391331.0643	1.1	2.2
F346	838469.2428	1.6	-4534968.8480	1.0	4391331.0706	1.1	2.2
F381	838458.8760	1.3	-4534974.3295	0.7	4391327.2541	0.8	1.7

F382	838458.7797	1.3	-4534974.3398	0.7	4391327.2543	0.9	1.7
F383	838458.7716	1.2	-4534972.3797	0.7	4391329.2194	0.9	1.7
F384	838458.6617	1.1	-4534972.3940	0.7	4391329.2262	0.9	1.6
F385	838458.6427	1.0	-4534970.1689	0.8	4391331.4710	0.9	1.6
F386	838458.5308	1.0	-4534970.1847	0.8	4391331.4792	0.9	1.6
P1001	838494.8909	3.4	-4535024.3424	3.8	4391283.9018	2.1	5.5
P1002	838493.8333	1.2	-4535010.7578	1.9	4391297.9438	3.2	3.9
P1003	838502.7729	3.7	-4535009.4845	1.7	4391297.6112	2.9	5.0
P101	838493.9069	2.7	-4535018.0379	2.6	4391280.7359	1.9	4.2
P102	838493.5383	4.2	-4535013.8194	2.0	4391285.1337	2.2	5.1
P103	838493.3383	1.1	-4535011.6866	1.9	4391287.3108	4.3	4.8
P104	838492.6412	2.0	-4535007.5582	4.4	4391291.6978	2.8	5.6
P105	838493.6595	5.9	-4535016.7623	2.4	4391279.4938	1.8	6.6
P106	838493.2982	6.7	-4535012.5418	1.9	4391283.8889	2.1	7.3
P107	838493.1816	1.1	-4535010.4379	2.0	4391286.0462	3.9	4.5
P108	838492.7363	5.9	-4535006.2218	1.9	4391290.4782	2.6	6.7
P109	838500.0231	5.4	-4535004.2859	1.4	4391292.4805	4.8	7.4
P110	838501.1309	3.8	-4535004.1964	3.2	4391292.3532	5.6	7.5
P2002	838502.5552	4.3	-4535006.6126	3.8	4391300.5747	2.4	6.2
P2003	838502.7309	4.2	-4535005.4453	3.6	4391301.7475	2.4	6.0
P2004	838502.7113	4.2	-4535005.2348	3.6	4391301.9655	2.4	6.0
P2005	838502.3371	4.2	-4535004.1381	3.5	4391303.1637	2.4	6.0
P2006	838501.0743	4.7	-4534989.7686	3.2	4391318.1391	2.2	6.1
P2007	838501.2593	4.8	-4534988.5940	3.2	4391319.3199	2.2	6.2
P2008	838501.2402	4.8	-4534988.3886	3.2	4391319.5394	2.2	6.2
P2009	838500.7390	2.2	-4534987.2578	5.0	4391320.7752	4.5	7.1
P2010	838504.0074	4.5	-4534987.5521	3.1	4391321.1272	2.2	5.9
P2011	838502.9537	3.4	-4534975.3308	2.3	4391333.8616	3.4	5.3
P201	838501.7136	3.0	-4535000.0567	2.7	4391303.8642	1.9	4.5
P202	838501.3557	3.1	-4534995.8409	2.6	4391308.2579	1.8	4.4
P203	838501.1776	3.2	-4534993.7348	2.6	4391310.4529	1.8	4.5
P204	838500.7927	3.6	-4534989.5158	2.6	4391314.8478	1.7	4.8
P205	838501.4822	3.0	-4534998.7839	2.6	4391302.6186	2.0	4.4
P206	838501.0873	3.4	-4534994.5809	2.5	4391307.0341	5.7	7.1
P207	838501.1454	3.9	-4534992.4962	2.9	4391309.0938	5.9	7.6
P208	838500.5556	3.6	-4534988.2360	2.5	4391313.6014	1.7	4.7
P209	838501.1818	4.0	-4534997.0191	3.6	4391300.9335	2.9	6.1
P210	838500.4586	3.6	-4534992.7128	4.5	4391305.4749	5.3	7.8
P211	838500.7176	2.0	-4534990.7071	5.0	4391307.4798	5.2	7.5
P212	838500.2594	5.2	-4534986.4719	3.5	4391311.9168	2.6	6.8
P213	838500.9439	4.1	-4534995.7436	3.5	4391299.6894	3.0	6.2
P214	838500.3840	1.3	-4534991.5001	5.3	4391304.1722	5.2	7.5

P215	838500.5864	1.1	-4534989.4937	3.6	4391306.2064	5.0	6.3
P216	838500.0182	5.2	-4534985.1932	3.3	4391310.6742	2.7	6.7
P3001	838485.4163	2.3	-4534977.7118	2.6	4391334.7395	1.8	3.9
P3002	838483.9661	2.4	-4534979.2419	2.9	4391332.1800	2.0	4.3
P3003	838483.6647	2.4	-4534979.2914	2.9	4391332.1989	2.0	4.3
P3004	838482.0215	2.4	-4534979.6891	2.9	4391332.0762	2.1	4.3
P301	838479.5450	2.4	-4534978.2295	2.8	4391330.4316	2.2	4.3
P302	838473.5010	2.3	-4534979.0520	3.2	4391330.7307	2.3	4.6
P303	838470.4935	2.2	-4534979.4817	3.4	4391330.8647	2.5	4.8
P308	838473.2724	2.3	-4534977.7815	3.0	4391329.4873	2.4	4.5
P309	838470.2567	2.2	-4534978.2107	3.3	4391329.6189	2.6	4.7
P311	838461.2058	2.2	-4534979.4509	4.5	4391330.0649	3.1	5.9
P312	838455.1755	3.2	-4534980.2584	3.6	4391330.3638	3.6	6.0
P313	838478.9895	3.9	-4534975.2142	3.9	4391327.4882	3.5	6.5
P314	838472.9433	3.7	-4534976.0431	4.3	4391327.7891	3.8	6.8
P315	838469.9334	3.6	-4534976.4683	1.7	4391327.9210	4.0	5.6
P316	838463.8971	3.5	-4534977.2878	2.7	4391328.2277	4.6	6.4
P318	838454.8457	5.2	-4534978.5229	3.8	4391328.6562	2.8	7.0
P319	838478.7568	3.9	-4534973.9433	3.8	4391326.2483	3.6	6.5
P320	838472.7092	3.7	-4534974.7770	4.1	4391326.5348	4.0	6.8
P322	838463.6607	3.5	-4534976.0214	5.4	4391326.9666	4.9	8.1
P324	838454.6064	5.3	-4534977.2656	3.4	4391327.4068	3.2	7.1
P304	838464.5085	1.0	-4534980.3575	5.4	4391331.0576	3.2	6.4
P305	838461.3194	1.1	-4534980.7514	2.7	4391331.1630	2.8	4.0
P306	838455.4499	2.4	-4534981.5851	5.6	4391331.4976	2.3	6.5
P307	838479.2645	3.9	-4534977.0372	2.3	4391329.1776	3.6	5.8
P317	838460.8538	1.2	-4534977.7055	3.0	4391328.3129	2.0	3.8
P321	838469.6517	1.4	-4534975.2579	1.9	4391326.6775	1.8	3.0
P323	838460.6319	1.2	-4534976.4807	2.8	4391327.1415	2.2	3.8
P4001	838444.7105	5.2	-4534984.7995	3.2	4391333.8795	4.2	7.4
P401	838444.6300	4.3	-4534984.3950	4.4	4391330.6924	3.1	6.9
P407	838444.4095	2.3	-4534983.1924	2.6	4391329.5126	2.1	4.1
P4002	838446.9870	2.7	-4535010.6127	5.0	4391307.0383	3.7	6.8
P403	838445.6644	3.7	-4534997.0832	1.8	4391317.4585	1.5	4.4
P404	838446.0989	4.6	-4535001.2425	2.4	4391313.1210	2.0	5.6
P405	838446.1780	5.2	-4535003.3946	2.9	4391310.8898	2.4	6.4
P409	838445.3991	3.7	-4534995.8540	1.7	4391316.3130	1.6	4.4
P410	838445.8768	4.6	-4535000.0317	2.3	4391311.9415	2.1	5.6
P411	838445.9790	5.3	-4535002.1841	2.8	4391309.6845	2.6	6.5
P424	838445.5408	4.7	-4534998.2262	2.2	4391310.1853	2.4	5.7
P425	838445.6262	5.3	-4535000.3745	2.6	4391307.9450	2.9	6.6
P5001	838446.9778	3.9	-4535010.5987	3.5	4391307.0308	2.4	5.8

P5002	838448.5753	4.1	-4535011.4577	3.8	4391305.8353	4.1	6.9
P5005	838453.6176	2.6	-4535014.3922	4.1	4391301.8712	4.0	6.3
P5008	838456.8966	4.9	-4535015.8305	3.5	4391299.7966	2.8	6.6
P5009	838465.6578	3.7	-4535014.6046	3.6	4391299.3692	4.3	6.7
P501	838458.7659	3.3	-4535010.5979	4.5	4391294.9626	3.5	6.6
P502	838461.7643	2.5	-4535010.1165	4.5	4391294.8697	1.9	5.5
P503	838465.0044	2.6	-4535011.3513	1.5	4391293.0028	1.7	3.4
P504	838465.2899	2.4	-4535015.5260	1.1	4391288.6574	1.2	2.9
P505	838465.5530	2.3	-4535017.6719	0.9	4391286.4142	1.0	2.7
P506	838465.9232	2.3	-4535021.8254	0.7	4391282.0871	0.8	2.5
P507	838464.7795	2.6	-4535010.1371	1.7	4391291.8263	1.6	3.5
P509	838465.3341	2.3	-4535016.4609	1.0	4391285.2320	0.9	2.7
P510	838465.7126	2.2	-4535020.6173	0.8	4391280.9052	0.7	2.4
P6001	838466.8520	4.1	-4535028.1428	3.5	4391285.1563	3.4	6.4
P6002	838494.9272	2.3	-4535024.2697	1.7	4391283.8037	3.5	4.5
P601	838470.9118	4.1	-4535022.0609	2.4	4391279.7248	3.5	5.9
P602	838471.8097	2.1	-4535021.9353	2.4	4391279.6826	5.5	6.4
P603	838485.2331	3.9	-4535021.6895	4.4	4391280.4824	3.7	6.9
P604	838488.9492	1.5	-4535021.1977	2.0	4391280.3390	2.8	3.8

Appendix B: The summary of statistic results of Optech study area

Appendix B-1: The summary of the differences between the pre-surveyed coordinates and the original LiDAR coordinates, the adjusted LiDAR coordinates through the 3DCCT derived from using 35 GCPs on five sides and 10 GCPs on side 3 only, respectively, from 14 checking GCPs on building side 3.

No.	ID	Original Differences [cm]					With 35 GCPs of all sides [cm]					With 10 GCPs of side 3 [cm]				
		N	E	U	2D_H	3D	N	E	U	2D_H	3D	N	E	U	2D_H	3D
1	P3001	1.65	3.57	1.48	3.93	4.20	1.15	-0.99	1.40	1.52	2.06	0.87	1.18	-0.78	1.47	1.66
2	P3003	-3.26	2.02	-2.60	3.84	4.63	-1.02	1.80	1.66	2.07	2.65	0.99	-1.45	-0.98	1.76	2.01
3	P302	-3.24	-0.81	-2.09	3.34	3.94	-1.35	1.87	2.01	2.31	3.06	-1.78	-1.17	1.04	2.13	2.37
4	P308	-2.68	2.72	-2.20	3.82	4.41	-0.78	1.25	1.04	1.47	1.80	-0.28	0.25	0.39	0.38	0.54
5	P309	-2.05	3.19	0.04	3.79	3.79	-2.23	1.62	1.02	2.76	2.94	-1.16	-1.71	-1.32	2.07	2.45
6	P312	-3.03	2.43	1.08	3.88	4.03	-1.13	1.58	1.57	1.94	2.50	0.78	-0.10	1.06	0.79	1.32
7	P313	2.59	2.68	-1.47	3.73	4.01	-0.88	1.88	-1.88	2.08	2.80	-0.39	1.25	-2.13	1.31	2.50
8	P315	-1.81	1.30	-2.56	2.23	3.39	-1.23	-1.60	-1.57	2.02	2.56	-1.15	-0.76	-1.44	1.38	1.99
9	P318	1.21	2.25	2.06	2.55	3.28	1.89	1.20	1.28	2.24	2.58	-1.45	1.26	0.98	1.92	2.16
10	P319	-2.37	2.18	-2.07	3.22	3.83	-0.23	1.23	-1.60	1.25	2.03	-1.18	-0.23	0.56	1.20	1.33
11	P322	-3.27	-0.03	-2.04	3.27	3.85	1.13	-0.85	1.14	1.41	1.82	-1.68	-1.49	-1.23	2.25	2.56
12	P324	-2.71	-1.72	-2.16	3.21	3.87	-0.60	-1.86	1.23	1.95	2.31	-0.58	-1.88	-2.05	1.97	2.84
13	P317	-2.91	2.21	-2.23	3.65	4.28	-1.54	0.30	1.11	1.57	1.92	-0.18	-0.28	0.30	0.33	0.45
14	P321	-3.25	-1.30	-2.79	3.50	4.48	-1.87	1.69	1.05	2.52	2.73	0.78	-1.56	0.86	1.74	1.94
Minimum		-3.27	-1.72	-2.79	2.23	3.28	-2.23	-1.86	-1.88	1.25	1.80	-1.78	-1.88	-2.13	0.33	0.45
Maximum		2.59	3.57	2.06	3.93	4.63	1.89	1.88	2.01	2.76	3.06	0.99	1.26	1.06	2.25	2.84
Mean		-1.80	1.48	-1.25	**2.33**	**2.64**	-0.62	0.65	0.68	**0.90**	**1.13**	-0.46	-0.48	-0.34	**0.66**	**0.74**
RMS		2.65	2.22	2.04	**3.46**	**4.02**	1.32	1.48	1.43	**1.98**	**2.45**	1.06	1.19	1.20	**1.59**	**1.99**
Stdev		2.03	1.72	1.67	**2.66**	**3.14**	1.21	1.38	1.31	**1.83**	**2.25**	0.99	1.13	1.19	**1.51**	**1.92**

Appendix B-2: The summary of the differences between the pre-surveyed coordinates and the adjusted LiDAR coordinates through the 3DCCT derived from using 13 building-type GCPs, 6 ground-type GCPs and 19 mixed-type GCPs, respectively, from 13 building-type checking GCPs.

No.	ID	With Building-type GCPs [cm]					With Ground-type GCPs [cm]					With Mixed-type GCPs [cm]				
		N	E	U	2D_H	3D	N	E	U	2D_H	3D	N	E	U	2D_H	3D
1	P2002	-0.27	0.84	-2.57	0.88	2.72	1.06	-1.35	0.11	1.72	1.72	1.07	0.96	-1.98	1.44	2.45
2	P2004	0.34	0.76	-0.92	0.83	1.24	0.51	-1.05	1.72	1.17	2.08	-1.68	-0.45	-0.88	1.74	1.95
3	P2006	-0.82	0.77	-0.82	1.12	1.39	-1.19	-1.79	-1.64	2.15	2.70	0.76	0.78	-0.53	1.09	1.21
4	P2007	-1.44	0.66	0.63	1.58	1.70	-2.6	-2.23	2.07	3.43	4.00	-1.71	1.16	1.11	2.07	2.35
5	P202	0.44	0.76	0.48	0.88	1.00	-2.68	-1.36	1.68	3.01	3.44	1.15	1.45	-1.88	1.85	2.64
6	P203	-1.83	-1.29	0.68	2.24	2.34	-2.15	-3.97	1.31	4.51	4.70	-1.66	-0.57	1.63	1.76	2.40
7	P205	0.36	-1.64	-1.06	1.68	1.99	-1.01	-2.59	-2.33	2.78	3.63	0.77	-2.04	-1.82	2.18	2.84
8	P207	-1.13	-1.28	0.49	1.71	1.78	-2.14	-2.6	1.47	3.37	3.67	-1.76	-1.50	1.48	2.31	2.75
9	P208	0.78	-1.07	-2.04	1.32	2.43	1.49	-1.67	-1.35	2.24	2.61	0.98	-1.23	-1.55	1.57	2.21
10	P211	1.25	-0.84	0.75	1.51	1.68	-1.36	-1.87	1.8	2.31	2.93	-0.56	-1.04	1.24	1.18	1.71
11	P213	1.19	-1.14	-1.54	1.65	2.26	-1.68	-1.89	0.46	2.53	2.57	1.14	-1.19	-1.28	1.65	2.09
12	P215	-0.77	-1.34	0.59	1.55	1.65	-0.67	1.54	2.45	1.68	2.97	-0.36	-1.48	-1.70	1.52	2.28
13	P216	0.66	-0.47	-0.83	0.81	1.16	1.49	-2.07	0.66	2.55	2.63	0.70	-1.56	-1.26	1.71	2.12
Minimum		-1.83	-1.64	-2.57	0.81	1.00	-2.68	-3.97	-2.33	1.17	1.72	-1.76	-2.04	-1.98	1.09	1.21
Maximum		1.25	0.84	0.75	2.24	2.72	1.49	1.54	2.45	4.51	4.70	1.15	1.45	1.63	2.31	2.84
Mean		-0.10	-0.41	-0.47	**0.42**	**0.63**	-0.84	-1.76	0.65	**1.95**	**2.06**	-0.09	-0.52	-0.57	**0.52**	**0.77**
RMS		0.98	1.04	1.20	**1.43**	**1.87**	1.68	2.12	1.61	**2.71**	**3.15**	1.19	1.26	1.47	**1.73**	**2.27**
Stdev		1.02	1.00	1.15	**1.42**	**1.83**	1.51	1.24	1.54	**1.95**	**2.48**	1.24	1.19	1.41	**1.72**	**2.22**

Appendix B-3: The summary of the differences between the pre-surveyed and the original LiDAR coordinates, and adjusted LiDAR coordinates through the 3DCCT derived from using GCPs only and GCPs with feature constraints, respectively, from 19 checking GCPs on building side 2.

No.	ID	Original Differences [cm]					With GCPs only [cm]					With GCPs and Features [cm]				
		N	E	U	2D_H	3D	N	E	U	2D_H	3D	N	E	U	2D_H	3D
1	P2002	-1.18	-1.78	-3.62	2.14	4.20	1.07	0.96	-1.98	1.44	2.45	0.89	-0.66	-1.67	1.11	2.00
2	P2004	-0.58	-1.45	-2.23	1.56	2.72	-1.68	-0.45	-0.88	1.74	1.95	-0.76	-0.31	-0.65	0.82	1.05
3	P2006	2.23	-2.83	-2.59	3.60	4.44	0.76	0.78	-0.53	1.09	1.21	-0.83	-0.44	-0.56	0.94	1.09
4	P2007	-4.30	1.24	-1.14	4.48	4.62	-1.71	1.16	1.11	2.07	2.35	-1.27	0.88	1.21	1.55	1.96
5	P202	-4.52	-1.28	-0.50	4.70	4.72	1.15	1.45	-1.88	1.85	2.64	-2.02	1.16	-2.08	2.33	3.12
6	P203	-3.79	-3.28	-2.65	5.01	5.67	-1.66	-0.57	1.63	1.76	2.40	-1.48	-0.97	0.85	1.77	1.96
7	P205	-1.98	-3.14	-3.01	3.71	4.78	0.77	-2.04	-1.82	2.18	2.84	0.48	-1.34	-0.87	1.42	1.67
8	P207	-1.15	-3.03	-1.00	3.24	3.39	-1.76	-1.50	1.48	2.31	2.75	-0.65	-0.71	1.16	0.96	1.51
9	P208	-0.17	-2.93	-4.69	2.93	5.53	0.98	-1.23	-1.55	1.57	2.21	-0.68	-0.55	-1.36	0.87	1.62
10	P211	-1.05	-1.42	-2.72	1.77	3.24	-0.56	-1.04	1.24	1.18	1.71	-0.45	-1.34	1.14	1.41	1.82
11	P213	-2.22	1.03	-2.75	2.45	3.68	1.14	-1.19	-1.28	1.65	2.09	-0.81	1.20	-0.85	1.45	1.68
12	P215	-1.32	1.48	1.31	1.98	2.38	-0.36	-1.48	-1.70	1.52	2.28	0.45	-1.23	-1.36	1.31	1.89
13	P216	0.94	-2.61	1.76	2.77	3.29	0.70	-1.56	-1.26	1.71	2.12	0.55	-1.21	-0.38	1.33	1.38
14	F212	-1.38	3.32	-4.30	3.60	5.61	0.98	0.98	-1.78	1.39	2.26	0.76	1.23	-0.75	1.45	1.63
15	F215	-2.87	2.84	-3.98	4.04	5.67	1.26	1.27	-1.56	1.79	2.37	0.96	1.48	-0.99	1.76	2.02
16	F231	1.60	2.98	-2.97	3.38	4.50	0.96	1.21	-1.19	1.54	1.95	0.75	0.65	-0.78	0.99	1.26
17	F236	-2.34	-1.98	1.36	3.07	3.35	-1.68	-1.11	-1.63	2.01	2.59	-0.64	-0.93	-1.13	1.13	1.60
18	F251	-2.66	2.81	-3.51	3.87	5.22	-0.84	0.88	1.39	1.22	1.85	-0.55	0.49	1.23	0.74	1.43
19	F256	-1.66	2.81	-3.56	3.26	4.83	1.16	-0.56	1.56	1.29	2.02	1.36	-0.83	1.01	1.59	1.89
Minimum		-4.52	-3.28	-4.69	1.56	2.38	-1.76	-2.04	-1.98	1.09	1.21	-2.02	-1.34	-2.08	0.74	1.05
Maximum		2.23	3.32	1.76	5.01	5.67	1.26	1.45	1.63	2.31	2.84	1.36	1.48	1.23	2.33	3.12
Mean		-1.49	-1.38	-2.15	**2.03**	**2.96**	0.04	-0.21	-0.56	**0.22**	**0.60**	-0.21	-0.18	-0.36	**0.27**	**0.45**
RMS		2.32	2.46	2.86	**3.38**	**4.42**	1.19	1.19	1.49	**1.68**	**2.24**	0.95	0.99	1.12	**1.37**	**1.77**
Stdev		1.82	2.49	1.94	**3.09**	**3.64**	1.22	1.20	1.42	**1.71**	**2.22**	0.95	1.00	1.09	**1.38**	**1.76**

Appendix B-4: The summary of the differences of between the pre-surveyed coordinates and the adjusted LiDAR coordinates through the 3DCCT derived from using 20, 10 and 5 GCPs with the same feature constraints, respectively, from 18 checking GCPs on building side 2.

No.	ID	20 GCPs + Features [cm]					10 GCPs + Features [cm]					5 GCPs + Features [cm]				
		N	E	U	2D_H	3D	N	E	U	2D_H	3D	N	E	U	2D_H	3D
1	P2002	0.87	-1.02	-0.72	1.34	1.52	0.88	-1.34	-0.86	1.60	1.82	0.91	1.28	-0.65	1.57	1.70
2	P2004	-0.67	0.64	0.90	0.93	1.29	-0.99	1.08	1.23	1.47	1.91	1.39	0.68	1.43	1.55	2.11
3	P2006	0.88	0.35	-0.28	0.95	0.99	0.98	0.88	-0.45	1.32	1.39	-1.01	0.78	-1.42	1.28	1.91
4	P2007	-1.76	0.66	1.17	1.88	2.21	-1.88	0.75	1.67	2.02	2.62	-2.01	1.67	1.93	2.61	3.25
5	P202	-1.28	0.76	1.58	1.49	2.17	-1.86	0.89	2.16	2.06	2.99	-2.45	1.52	2.03	2.88	3.53
6	P205	0.65	-1.45	-0.64	1.59	1.71	0.97	-1.88	-0.97	2.12	2.33	1.46	-2.33	-1.57	2.75	3.17
7	P207	1.30	-0.98	1.76	1.63	2.40	1.05	-1.25	1.95	1.63	2.54	1.11	-0.89	2.24	1.42	2.65
8	P211	1.04	-0.31	2.19	1.09	2.44	1.13	-0.67	2.09	1.31	2.47	0.03	-1.28	2.17	1.28	2.52
9	P213	1.48	0.34	0.59	1.52	1.63	1.56	0.65	0.58	1.69	1.79	1.78	0.8	1.29	1.95	2.34
10	P216	1.12	0.88	1.03	1.42	1.76	1.22	0.97	0.81	1.56	1.76	1.66	-1.14	-1.23	2.01	2.36
11	F212	-1.24	0.45	-0.70	1.32	1.49	-1.27	0.78	-1.47	1.49	2.09	1.29	0.95	-0.46	1.60	1.67
12	F215	0.91	1.11	-1.05	1.44	1.78	1.36	0.77	-1.10	1.56	1.91	1.69	1.68	0.52	2.38	2.44
13	F231	0.75	0.96	-0.76	1.22	1.44	1.03	1.35	-1.10	1.70	2.02	1.57	1.84	-1.68	2.42	2.94
14	F232	0.68	1.20	0.88	1.38	1.64	0.79	1.35	0.54	1.56	1.65	0.75	1.15	0.16	1.37	1.38
15	F236	-0.45	-0.88	0.57	0.99	1.14	-0.33	-0.98	0.66	1.03	1.23	1.27	1.47	1.81	1.94	2.66
16	F251	0.77	1.76	-1.87	1.92	2.68	0.87	1.89	-1.97	2.08	2.87	1.75	2.01	-1.99	2.67	3.33
17	F255	1.30	1.58	-0.56	2.05	2.12	0.60	1.62	-0.78	1.73	1.90	1.45	1.64	-0.98	2.19	2.40
18	F256	0.67	0.99	-1.26	1.20	1.74	0.97	1.01	-1.36	1.40	1.95	0.81	1.11	-0.99	1.37	1.69
Minimum		-1.76	-1.45	-1.87	0.93	0.99	-1.88	-1.88	-1.97	1.03	1.23	-2.45	-2.33	-1.99	1.28	1.38
Maximum		1.48	1.76	2.19	2.05	2.68	1.56	1.89	2.16	2.12	2.99	1.78	2.01	2.24	2.88	3.53
Mean		0.39	0.39	0.16	**0.55**	**0.57**	0.39	0.44	0.09	**0.59**	**0.60**	0.75	0.72	0.15	**1.04**	**1.05**
RMS		1.05	0.99	1.15	**1.44**	**1.84**	1.16	1.18	1.33	**1.65**	**2.12**	1.45	1.42	1.49	**2.03**	**2.52**
Stdev		1.00	0.94	1.17	**1.37**	**1.80**	1.12	1.13	1.36	**1.59**	**2.09**	1.28	1.26	1.53	**1.80**	**2.36**

Appendix C: The summary of statistic results of Black Creek Pioneer Village study area

Appendix C-1: The summary of the differences between the pre-surveyed coordinates and adjusted LiDAR coordinates through the 3DCCT derived from using 11 ground-type GCPs, 27 building-type GCPs and 38 mixed-type GCPs, respectively, from 11 ground-type checking GCPs in Study Area #1.

No.	ID	With Building type GCPs [cm]					With Ground type GCPs [cm]					With Combined type GCPs [cm]				
		N	E	U	2D_H	3D	N	E	U	2D_H	3D	N	E	U	2D_H	3D
1	Curve2	-0.95	-2.71	-1.45	2.87	3.22	-0.54	-1.21	-0.73	1.33	1.51	-0.79	-1.26	-0.96	1.49	1.77
2	Curve4	0.37	-1.47	-2.44	1.52	2.87	0.34	-1.83	1.40	1.86	2.33	1.56	-2.27	1.29	2.75	3.04
3	Curve6	1.56	-1.63	-2.87	2.26	3.65	1.33	-1.48	-0.99	1.99	2.22	1.46	-0.98	-1.38	1.76	2.24
4	Curve8	-2.67	-0.84	-1.78	2.80	3.32	1.31	-0.69	1.38	1.48	2.02	1.45	-0.98	1.24	1.75	2.14
5	R1	-1.88	-1.54	-1.76	2.43	3.00	-0.78	-0.99	-1.47	1.26	1.94	-0.68	-1.38	-1.45	1.54	2.11
6	R3	-2.67	1.36	-2.49	3.00	3.90	-2.03	1.51	-0.77	2.53	2.64	-1.44	0.99	-1.89	1.75	2.57
7	R5	-1.90	1.78	-2.55	2.60	3.64	-0.78	0.69	-0.98	1.04	1.43	-1.55	1.25	-1.45	1.99	2.46
8	R7	-2.94	-1.74	-1.68	3.42	3.81	-1.46	-1.28	-1.96	1.94	2.76	-1.88	-1.49	-2.87	2.40	3.74
9	R9	-2.28	-2.60	3.33	3.46	4.80	-0.89	-0.67	0.88	1.11	1.42	-1.21	-0.45	-0.88	1.29	1.56
10	R11	-1.20	-1.60	-2.16	2.00	2.94	-1.12	-0.46	1.37	1.21	1.83	-1.34	-0.99	1.48	1.67	2.23
11	R13	-2.60	-1.67	-2.27	3.09	3.83	-1.64	-1.08	-0.41	1.96	2.01	-1.88	-1.23	-0.48	2.25	2.30
Minimum		-2.94	-2.71	-2.87	1.52	2.87	-2.03	-1.83	-1.96	1.04	1.42	-1.88	-2.27	-2.87	1.29	1.56
Maximum		1.56	1.78	3.33	3.46	4.80	1.33	1.51	1.40	2.53	2.76	1.56	1.25	1.48	2.75	3.74
Mean		-1.56	-1.15	-1.65	**1.94**	**2.54**	-0.57	-0.68	-0.21	**0.89**	**0.91**	-0.57	-0.80	-0.67	**0.98**	**1.19**
RMS		2.07	1.79	2.32	**2.74**	**3.58**	1.21	1.16	1.20	**1.67**	**2.06**	1.43	1.28	1.51	**1.92**	**2.45**
Stdev		1.42	1.44	1.71	**2.02**	**2.65**	1.12	0.98	1.24	**1.49**	**1.93**	1.38	1.05	1.43	**1.73**	**2.24**

Appendix C-2: The summary of the differences between the pre-surveyed coordinates and the original LiDAR coordinates, the adjusted LiDAR coordinates through the 3DCCT derived from using GCPs only and GCPs with feature constraints, respectively, from 38 checking GCPs in Study Area #1.

No.	ID	Original Differences [cm]					With GCPs only [cm]					With GCPs and Features [cm]				
		N	E	U	2D_H	3D	N	E	U	2D_H	3D	N	E	U	2D_H	3D
1	Rex2	1.35	-2.58	6.55	2.91	7.17	0.55	-0.88	0.88	1.04	1.36	0.45	0.78	1.22	0.90	1.52
2	Rex4	-2.20	-1.52	6.32	2.67	6.86	-0.78	-0.99	0.46	1.26	1.34	0.41	-0.97	1.22	1.05	1.61
3	Rex6	1.12	0.53	6.65	1.24	6.76	0.78	0.55	0.88	0.95	1.30	0.64	0.27	0.79	0.69	1.05
4	TrafficA3	-2.45	1.13	4.73	2.70	5.45	-0.93	0.96	-1.93	1.34	2.35	-0.89	0.90	-0.93	1.27	1.57
5	TrafficA7	1.24	1.66	5.54	2.07	5.91	0.65	1.49	0.76	1.63	1.79	0.56	1.42	0.93	1.53	1.79
6	SWTraffic2	1.03	0.53	6.26	1.16	6.37	0.64	0.49	-0.89	0.81	1.20	0.22	0.36	-0.23	0.42	0.48
7	SWTraffic4	2.23	-2.34	3.34	3.23	4.65	1.52	-1.33	-1.54	2.02	2.54	0.55	-0.76	0.63	0.94	1.13
8	YUSignA2	-2.74	-2.65	6.24	3.81	7.31	-0.96	-1.13	-0.95	1.48	1.76	-0.75	-0.99	-0.82	1.24	1.49
9	YUSignA4	1.05	-3.71	4.74	3.86	6.11	1.23	-1.29	-1.44	1.78	2.29	1.04	-1.15	-1.31	1.55	2.03
10	YUSignA7	-2.70	-0.39	5.84	2.73	6.45	-0.87	-1.21	-1.29	1.49	1.97	-0.69	-0.85	-1.21	1.09	1.63
11	YUMap1	0.62	-3.86	4.15	3.91	5.70	0.44	-1.56	-1.38	1.62	2.13	0.24	1.33	-0.98	1.35	1.67
12	YUMap2	0.56	-3.36	5.36	3.41	6.35	1.03	-0.98	-1.34	1.42	1.95	0.17	0.78	-1.88	0.80	2.04
13	YUMap6	2.40	2.76	5.59	3.66	6.68	0.98	-0.98	-1.78	1.39	2.26	2.03	1.23	-1.64	2.37	2.89
14	StopSign3	0.21	0.00	3.33	0.21	3.34	-0.78	-0.65	-2.66	1.02	2.85	0.09	-0.35	-3.03	0.36	3.05
15	StopSign4	0.57	-2.51	6.10	2.57	6.62	0.78	-0.98	0.82	1.25	1.50	0.46	-0.86	0.25	0.98	1.01
16	StopSign6	0.96	-3.62	6.45	3.75	7.46	-0.98	-1.23	-0.88	1.57	1.80	0.84	-0.97	0.59	1.28	1.41
17	StopSign8	-2.23	-2.71	6.50	3.51	7.39	-1.20	1.36	-0.83	1.81	1.99	1.43	-0.98	0.64	1.73	1.85
18	Building1	-2.88	-2.23	5.53	3.64	6.62	-1.44	-1.69	0.45	2.22	2.27	-1.37	-1.56	0.29	2.08	2.10
19	Building4	-2.23	1.37	5.06	2.62	5.70	-1.36	0.94	2.36	1.65	2.88	-1.93	0.94	0.73	2.15	2.27
20	Building5	-2.13	2.03	5.83	2.94	6.53	1.03	1.39	-0.44	1.73	1.79	1.83	1.59	0.75	2.42	2.54
21	YUSignB1	2.41	1.64	6.61	2.92	7.22	1.78	1.14	-0.99	2.11	2.33	0.13	0.98	-0.48	0.99	1.10
22	YUSignB3	0.61	0.63	6.20	0.88	6.26	-0.94	0.56	0.98	1.09	1.47	-0.79	0.36	1.16	0.87	1.45
23	RexW2	-3.67	3.32	-4.05	4.95	6.39	-1.43	1.68	-1.66	2.21	2.76	-0.42	0.84	-0.27	0.94	0.98
24	RexW4	-4.20	0.39	6.39	4.22	7.66	-1.34	0.69	-1.86	1.51	2.39	-1.02	0.57	0.79	1.17	1.41

25	RexW6	-2.23	-2.06	3.48	3.04	4.62	-1.35	-1.39	1.67	1.94	2.56	-0.68	-0.86	-0.79	1.10	1.35
26	YUSignC4	-2.59	-1.19	6.59	2.85	7.18	-1.34	-1.69	1.26	2.16	2.50	-0.48	-1.58	0.74	1.65	1.81
27	YUSignC6	-2.23	-4.16	5.88	4.72	7.54	-1.89	-1.65	-1.46	2.51	2.90	-1.00	-0.99	-1.08	1.41	1.77
28	Curve2	-0.78	-2.27	6.16	2.40	6.61	-0.79	-1.26	-0.96	1.49	1.77	-0.89	-0.71	-0.84	1.14	1.41
29	Curve4	1.63	-3.90	5.59	4.23	7.01	1.56	-2.27	1.29	2.75	3.04	-0.67	-0.89	-0.78	1.11	1.36
30	Curve6	2.03	-1.23	5.30	2.37	5.81	1.46	-0.98	-1.38	1.76	2.24	-1.27	-1.46	-1.21	1.94	2.28
31	Curve8	-2.53	-0.47	5.45	2.57	6.03	1.45	-0.98	1.24	1.75	2.14	0.13	-0.62	0.88	0.63	1.08
32	R1	-0.85	-2.34	4.11	2.49	4.81	-0.68	-1.38	-1.45	1.54	2.11	-0.04	-1.29	-1.11	1.29	1.70
33	R3	-2.39	2.87	4.57	3.73	5.90	-1.44	0.99	-1.89	1.75	2.57	-1.43	0.89	-1.55	1.68	2.29
34	R5	-2.59	2.14	3.06	3.36	4.54	-1.55	1.25	-1.45	1.99	2.46	-1.45	0.25	-1.93	1.47	2.43
35	R7	-3.08	-2.55	2.29	4.00	4.61	-1.88	-1.49	-2.87	2.40	3.74	-0.77	-0.98	-1.59	1.25	2.02
36	R9	-2.45	-2.26	5.03	3.33	6.03	-1.21	-0.45	-0.88	1.29	1.56	-0.99	-0.18	-0.69	1.01	1.22
37	R11	-2.69	-2.16	2.56	3.45	4.30	-1.34	-0.99	1.48	1.67	2.23	-0.73	-0.49	0.66	0.88	1.10
38	R13	-3.41	-1.58	-3.30	3.76	5.00	-1.88	-1.23	-0.48	2.25	2.30	-1.75	-1.24	-1.05	2.14	2.39
Minimum		-4.20	-4.16	-4.05	0.21	3.34	-1.89	-2.27	-2.87	0.81	1.20	-1.93	-1.58	-3.03	0.36	0.48
Maximum		2.41	3.32	6.65	4.95	7.66	1.78	1.68	2.36	2.75	3.74	2.03	1.59	1.22	2.42	3.05
Mean		-0.93	-0.96	4.79	**1.34**	**4.97**	-0.33	-0.45	-0.53	**0.56**	**0.77**	-0.23	-0.19	-0.35	**0.30**	**0.46**
RMS		2.20	2.34	5.32	**3.21**	**6.22**	1.23	1.22	1.41	**1.73**	**2.24**	0.98	0.97	1.12	**1.38**	**1.78**
Stdev		2.02	2.16	2.35	**2.95**	**3.78**	1.20	1.15	1.33	**1.66**	**2.13**	0.96	0.97	1.08	**1.36**	**1.74**

Appendix C-3: The summary of the differences between the pre-surveyed coordinates and the adjusted LiDAR coordinates through the 3DCCT derived from using GCPs with 10 features, 4 horizontal directional features and 6 vertical directional features, respectively, from 38 checking GCPs in Study Area #1.

No.	ID	With All Feature Constraints [cm]					With Only Vertical Features [cm]					With Only Horizontal Features [cm]				
		N	E	U	2D_H	3D	N	E	U	2D_H	3D	N	E	U	2D_H	3D
1	Rex2	0.45	0.78	1.22	0.90	1.52	0.06	0.86	1.35	0.86	1.60	0.53	0.98	1.20	1.11	1.64
2	Rex4	0.41	-0.97	1.22	1.05	1.61	0.01	-1.14	0.83	1.14	1.41	0.46	-1.12	1.19	1.21	1.70
3	Rex6	0.64	0.27	0.79	0.69	1.05	1.32	0.46	0.52	1.40	1.49	0.98	0.35	0.76	1.04	1.29
4	TrafficA3	-0.89	0.90	-0.93	1.27	1.57	-1.17	0.75	-1.23	1.39	1.86	-0.88	1.00	-1.13	1.33	1.75
5	TrafficA7	0.56	1.42	0.93	1.53	1.79	0.29	1.27	1.08	1.30	1.69	0.57	1.45	0.90	1.56	1.80
6	SWTraffic2	0.22	0.36	-0.23	0.42	0.48	-0.04	0.24	-0.78	0.24	0.82	0.21	0.54	-0.27	0.58	0.64
7	SWTraffic4	0.55	-0.76	0.63	0.94	1.13	1.13	-1.22	0.70	1.66	1.80	0.60	-0.74	1.30	0.95	1.61
8	YUSignA2	-0.75	-0.99	-0.82	1.24	1.49	-1.09	-1.34	-0.99	1.73	1.99	-0.65	-1.01	-0.87	1.20	1.48
9	YUSignA4	1.04	-1.15	-1.31	1.55	2.03	0.70	-1.31	-0.99	1.49	1.78	1.14	-1.03	-1.67	1.54	2.27
10	YUSignA7	-0.69	-0.85	-1.21	1.09	1.63	-1.01	-1.00	-1.09	1.42	1.79	-0.60	-0.72	-1.26	0.94	1.57
11	YUMap1	0.24	1.33	-0.98	1.35	1.67	-0.20	0.57	-1.13	0.60	1.28	0.38	0.68	-2.20	0.78	2.33
12	YUMap2	0.17	0.78	-1.88	0.80	2.04	-0.27	1.35	-1.58	1.38	2.10	0.32	0.68	-1.95	0.75	2.09
13	YUMap6	2.03	1.23	-1.64	2.37	2.89	1.61	1.26	-1.35	2.04	2.45	1.68	1.01	-1.71	1.96	2.60
14	StopSign3	0.09	-0.35	-3.03	0.36	3.05	-0.26	-0.46	-3.30	0.53	3.34	0.17	-0.78	-3.59	0.80	3.68
15	StopSign4	0.46	-0.86	0.25	0.98	1.01	0.10	-1.23	0.27	1.23	1.26	0.53	-0.99	0.45	1.12	1.21
16	StopSign6	0.84	-0.97	0.59	1.28	1.41	0.49	-1.45	0.98	1.53	1.82	0.92	-1.21	0.54	1.52	1.61
17	StopSign8	1.43	-0.98	0.64	1.73	1.85	1.07	-1.35	0.78	1.72	1.89	1.50	-1.23	0.59	1.94	2.03
18	Building1	-1.37	-1.56	0.29	2.08	2.10	-1.67	-1.60	0.46	2.31	2.36	-1.20	-1.45	0.19	1.88	1.89
19	Building4	-1.93	0.94	0.73	2.15	2.27	-2.57	0.87	0.88	2.71	2.85	-1.75	0.56	0.64	1.84	1.95
20	Building5	1.83	1.59	0.75	2.42	2.54	1.41	1.48	1.10	2.04	2.32	1.15	1.64	0.68	2.00	2.12
21	YUSignB1	0.13	0.98	-0.48	0.99	1.10	1.75	1.05	-0.64	2.04	2.14	0.25	1.01	-0.54	1.04	1.17
22	YUSignB3	-0.79	0.36	1.16	0.87	1.45	1.62	0.56	1.13	1.71	2.05	-1.23	0.35	1.38	1.28	1.88
23	RexW2	-0.42	0.84	-0.27	0.94	0.98	-0.64	1.23	-1.03	1.39	1.73	-0.41	0.95	-0.24	1.03	1.06
24	RexW4	-1.02	0.57	0.79	1.17	1.41	-1.34	0.36	0.77	1.39	1.59	-0.91	1.04	0.81	1.38	1.60

25	RexW6	-0.68	-0.86	-0.79	1.10	1.35	-1.13	-1.23	-1.13	1.67	2.02	-1.02	-1.39	-1.89	1.72	2.56
26	YUSignC4	-0.48	-1.58	0.74	1.65	1.81	-0.75	-1.72	1.23	1.88	2.24	-0.42	-1.43	0.70	1.49	1.65
27	YUSignC6	-1.00	-0.99	-1.08	1.41	1.77	-0.27	-1.45	-1.13	1.47	1.86	-1.25	-1.05	-1.13	1.63	1.99
28	Curve2	-0.89	-0.71	-0.84	1.14	1.41	-1.22	-1.23	-0.57	1.73	1.82	-0.79	-1.24	-0.89	1.47	1.72
29	Curve4	-0.67	-0.89	-0.78	1.11	1.36	0.07	-1.17	-0.98	1.17	1.53	-0.56	-1.01	0.39	1.15	1.22
30	Curve6	-1.27	-1.46	-1.21	1.94	2.28	-1.46	-1.60	-0.94	2.17	2.36	-1.27	-0.56	-1.24	1.39	1.86
31	Curve8	0.13	-0.62	0.88	0.63	1.08	0.02	-0.78	0.89	0.78	1.18	0.07	-0.35	0.86	0.36	0.93
32	R1	-0.04	-1.29	-1.11	1.29	1.70	-0.10	-1.30	-0.99	1.30	1.64	-0.12	-0.98	-1.67	0.99	1.94
33	R3	-1.43	0.89	-1.55	1.68	2.29	-1.45	0.98	-0.68	1.75	1.88	-1.54	0.98	-1.55	1.83	2.39
34	R5	-1.45	0.25	-1.93	1.47	2.43	-1.41	0.21	-2.13	1.43	2.56	-1.58	0.44	-2.23	1.64	2.77
35	R7	-0.77	-0.98	-1.59	1.25	2.02	-0.99	-1.49	-1.64	1.79	2.43	-0.95	-1.15	-1.99	1.49	2.49
36	R9	-0.99	-0.18	-0.69	1.01	1.22	-1.31	-0.22	-0.86	1.33	1.58	-1.25	-0.23	-1.35	1.27	1.85
37	R11	-0.73	-0.49	0.66	0.88	1.10	-1.44	-1.13	0.69	1.83	1.96	-0.80	-0.55	1.33	0.97	1.65
38	R13	-1.75	-1.24	-1.05	2.14	2.39	-1.53	-1.25	-0.84	1.98	2.15	-1.83	-0.76	-1.03	1.98	2.23
Minimum		-1.93	-1.58	-3.03	0.36	0.48	-2.57	-1.72	-3.30	0.24	0.82	-1.83	-1.45	-3.59	0.36	0.64
Maximum		2.03	1.59	1.22	2.42	3.05	1.75	1.48	1.35	2.71	3.34	1.68	1.64	1.38	2.00	3.68
Mean		-0.23	-0.19	-0.35	**0.30**	**0.46**	-0.31	-0.35	-0.32	**0.46**	**0.57**	-0.25	-0.19	-0.43	**0.32**	**0.54**
RMS		0.98	0.97	1.12	**1.38**	**1.78**	1.12	1.13	1.16	**1.59**	**1.97**	0.98	0.97	1.35	**1.38**	**1.93**
Stdev		0.96	0.97	1.08	**1.36**	**1.74**	1.09	1.09	1.13	**1.54**	**1.91**	0.96	0.97	1.29	**1.36**	**1.88**

Appendix C-4: The summary of the differences between the pre-surveyed coordinates and the adjusted LiDAR coordinates through the 3DCCT derived from using 23 GCPs, 16 GCPs and 8 GCPs with the same feature constraints, respectively, from 38 checking GCPs in the Study Area #1.

No.	ID	With 23 GCPs + Features [cm]					With 16 GCPs + Features [cm]					With 8 GCPs + Features [cm]				
		N	E	U	2D_H	3D	N	E	U	2D_H	3D	N	E	U	2D_H	3D
1	Rex2	0.56	1.03	1.25	1.17	1.71	0.78	1.03	1.27	1.29	1.81	0.50	0.95	0.78	1.07	1.33
2	Rex4	0.54	-1.17	1.25	1.29	1.80	0.66	-1.34	1.31	1.49	1.99	0.43	-1.88	0.98	1.93	2.16
3	Rex6	0.77	0.45	0.98	0.89	1.33	0.56	0.56	0.97	0.79	1.25	0.98	0.09	1.34	0.98	1.66
4	TrafficA3	-0.90	0.79	-1.17	1.20	1.67	-1.45	0.72	-1.34	1.62	2.10	-0.69	0.73	-2.12	1.00	2.35
5	TrafficA7	0.58	1.31	0.67	1.43	1.58	0.66	1.23	0.80	1.40	1.61	0.77	1.25	0.52	1.47	1.56
6	SWTraffic2	0.28	0.24	-0.14	0.37	0.39	0.35	0.14	0.02	0.38	0.38	0.47	0.19	-0.43	0.51	0.66
7	SWTraffic4	0.65	-0.88	1.23	1.09	1.65	0.79	-0.87	1.38	1.18	1.81	1.44	-1.65	2.04	2.19	2.99
8	YUSignA2	-0.68	-1.21	-1.35	1.39	1.94	-0.55	-1.34	-1.43	1.45	2.04	-0.48	-1.23	-1.23	1.32	1.80
9	YUSignA4	1.10	-1.25	-1.36	1.67	2.15	1.23	-1.42	-1.56	1.88	2.44	1.31	-1.29	-1.75	1.84	2.54
10	YUSignA7	-0.78	-0.95	-1.76	1.23	2.15	-1.46	-1.13	-1.83	1.85	2.60	-2.41	-0.99	-1.63	2.61	3.07
11	YUMap1	0.28	0.88	-1.24	0.92	1.55	0.43	1.21	-1.45	1.28	1.94	0.53	2.24	-1.34	2.30	2.66
12	YUMap2	0.22	0.98	-1.98	1.00	2.22	0.36	0.89	-2.10	0.96	2.31	0.46	2.75	-0.88	2.79	2.92
13	YUMap6	1.87	1.25	-1.98	2.25	3.00	2.02	1.23	-2.30	2.37	3.30	1.45	2.13	-1.87	2.58	3.18
14	StopSign3	0.16	-0.42	-2.25	0.45	2.29	0.27	-0.62	-2.34	0.68	2.44	0.38	-0.48	-1.56	0.61	1.68
15	StopSign4	0.53	-0.67	0.14	0.85	0.87	0.64	-0.89	0.10	1.10	1.10	0.74	-1.56	0.58	1.73	1.82
16	StopSign6	0.92	-1.23	0.49	1.54	1.61	0.67	-1.45	0.46	1.60	1.66	0.88	-1.78	0.44	1.99	2.03
17	StopSign8	1.50	-1.14	0.55	1.88	1.96	1.60	-1.56	0.51	2.23	2.29	1.71	-1.56	0.49	2.31	2.37
18	Building1	-1.45	-1.45	0.24	2.05	2.06	-1.34	-1.70	0.45	2.16	2.21	-2.98	-1.62	1.36	3.39	3.65
19	Building4	-2.02	1.01	0.42	2.26	2.30	-1.78	0.76	0.43	1.94	1.98	-1.78	0.87	0.63	1.98	2.08
20	Building5	1.87	1.53	0.48	2.42	2.46	1.67	1.30	0.33	2.12	2.14	1.78	1.48	0.89	2.31	2.48
21	YUSignB1	0.56	1.10	-0.79	1.23	1.47	0.78	0.86	-0.93	1.16	1.49	1.23	1.06	-1.68	1.62	2.34
22	YUSignB3	-0.89	0.20	-0.15	0.91	0.92	-0.98	0.38	-0.23	1.05	1.08	-2.45	0.14	1.14	2.45	2.71
23	RexW2	-0.72	1.21	-1.25	1.41	1.88	-0.58	1.45	-1.45	1.56	2.13	-0.48	1.88	-2.45	1.94	3.13
24	RexW4	-1.53	0.29	0.95	1.56	1.82	-1.52	0.88	1.35	1.76	2.22	-1.78	0.26	1.89	1.80	2.61
25	RexW6	-0.99	-1.16	-1.80	1.53	2.36	-1.23	-1.35	-1.06	1.83	2.11	-1.78	-2.17	-1.64	2.81	3.25

26	YUSignC4	-0.89	-1.70	0.41	1.92	1.96	-0.99	-1.86	0.98	2.11	2.32	-2.34	-1.73	1.78	2.91	3.41
27	YUSignC6	-1.45	-0.98	-1.41	1.75	2.25	-1.56	-1.23	-1.47	1.99	2.47	0.36	-1.72	-1.36	1.76	2.22
28	Curve2	-0.76	-0.76	-1.18	1.07	1.60	-0.89	-1.23	-1.26	1.52	1.97	-0.57	-1.89	-1.66	1.97	2.58
29	Curve4	0.55	-1.14	-0.02	1.27	1.27	0.99	-0.98	1.17	1.39	1.82	0.75	-1.74	0.78	1.89	2.05
30	Curve6	-1.45	-1.61	-1.25	2.17	2.50	-1.72	-0.89	-1.08	1.94	2.22	-2.22	-1.64	-1.98	2.76	3.40
31	Curve8	0.30	-0.81	1.23	0.86	1.50	0.37	-0.85	2.03	0.93	2.23	0.40	-1.67	1.56	1.72	2.32
32	R1	-1.13	-1.50	-1.31	1.88	2.29	-1.23	-1.50	-1.79	1.94	2.64	0.23	-1.51	-1.57	1.53	2.19
33	R3	-1.23	1.41	-1.60	1.87	2.46	-1.34	1.34	-2.07	1.90	2.81	-1.45	1.40	-1.67	2.02	2.62
34	R5	-1.23	0.34	-2.02	1.28	2.39	-1.18	0.45	-2.10	1.26	2.45	-1.19	-0.01	-2.51	1.19	2.78
35	R7	-0.89	-1.68	1.67	1.90	2.53	-1.50	-1.58	1.46	2.18	2.62	-1.52	-1.68	-2.45	2.27	3.34
36	R9	-1.16	-0.50	-0.80	1.26	1.50	-1.34	-0.33	-0.89	1.38	1.64	-2.45	-0.49	-1.47	2.50	2.90
37	R11	-0.85	-0.68	1.05	1.09	1.51	-1.01	-0.72	1.21	1.24	1.73	-1.49	-1.51	1.89	2.12	2.84
38	R13	-1.89	-1.57	-0.37	2.46	2.48	-1.50	-1.38	-0.67	2.04	2.15	-1.50	-1.58	-1.46	2.18	2.62
Minimum		-2.02	-1.70	-2.25	0.37	0.39	-1.78	-1.86	-2.34	0.38	0.38	-2.98	-2.17	-2.51	0.51	0.66
Maximum		1.87	1.53	1.67	2.46	3.00	2.02	1.45	2.03	2.37	3.30	1.78	2.75	2.04	3.39	3.65
Mean		-0.25	-0.27	-0.37	**0.37**	**0.53**	-0.27	-0.31	-0.35	**0.41**	**0.54**	-0.34	-0.42	-0.41	**0.54**	**0.68**
RMS		1.07	1.09	1.21	**1.53**	**1.95**	1.15	1.14	1.35	**1.62**	**2.11**	1.42	1.49	1.53	**2.06**	**2.56**
Stdev		0.96	0.97	1.08	**1.36**	**1.74**	1.13	1.11	1.32	**1.59**	**2.06**	1.40	1.45	1.49	**2.01**	**2.50**

Appendix C-5: The summary of the differences between the pre-surveyed coordinates, the original LiDAR coordinates, and the adjusted LiDAR coordinates through the 3DCCT derived from using 68 GCPs from all the segments and 23 GCPs from Segment #1 only, respectively, from 23 checking GCPs with Segment #1 in Study Area #2.

No.	ID	Original Differences [cm]					With 68 GCPs of Run 1 [cm]					With 23 GCPs of Section 1[cm]				
		N	E	U	2D_H	3D	N	E	U	2D_H	3D	N	E	U	2D_H	3D
1	L41	-2.59	-3.27	3.21	4.17	5.26	-1.21	-1.01	1.34	1.58	2.07	-1.03	-1.01	0.84	1.44	1.67
2	L45	-3.35	-1.95	4.12	3.88	5.66	-0.98	-0.96	1.89	1.37	2.34	-0.76	0.47	1.63	0.89	1.86
3	L46	-3.11	-2.13	4.40	3.77	5.79	-1.73	-1.13	1.51	2.07	2.56	-1.52	0.27	1.32	1.54	2.03
4	L49	-3.42	-3.16	3.35	4.66	5.74	-1.64	-1.76	1.46	2.41	2.81	-0.67	-0.76	0.63	1.01	1.19
5	L50	-2.20	-2.95	4.49	3.68	5.81	-1.14	-0.97	1.62	1.50	2.21	-1.60	-0.52	0.96	1.68	1.94
6	R10	-2.03	-2.24	4.81	3.02	5.68	-1.67	0.78	1.95	1.84	2.68	-1.42	0.20	1.23	1.43	1.89
7	R12	-1.91	2.89	4.25	3.46	5.48	1.56	0.98	1.41	1.84	2.32	-1.29	0.85	1.26	1.54	1.99
8	R14	-2.25	-3.62	3.59	4.26	5.57	-1.52	-2.02	1.79	2.53	3.10	-0.73	-1.21	0.88	1.41	1.66
9	R16	-3.29	-2.77	-3.16	4.30	5.34	-1.19	-1.89	-1.14	2.23	2.51	-0.89	-1.24	-1.03	1.53	1.84
10	R17	-1.14	-3.61	-3.48	3.79	5.14	-0.36	1.86	-1.18	1.89	2.23	-0.63	-0.94	-0.94	1.13	1.47
11	R19	3.24	-2.40	3.90	4.03	5.61	1.21	-1.56	-1.56	1.97	2.52	0.88	-1.33	-1.21	1.59	2.00
12	R21	-1.32	-2.62	4.55	2.93	5.41	-1.18	-1.67	0.88	2.04	2.23	-0.69	-0.15	0.83	0.71	1.09
13	R22	-1.60	-2.89	4.74	3.30	5.78	-1.25	1.03	1.89	1.62	2.49	-0.68	0.92	1.68	1.14	2.03
14	R25	-3.75	2.41	2.16	4.46	4.95	-1.88	1.84	0.89	2.63	2.78	-1.65	1.53	0.60	2.25	2.33
15	R26	-3.83	2.68	4.99	4.67	6.84	-1.46	-0.69	1.12	1.61	1.97	-0.78	0.75	0.78	1.08	1.33
16	R29	-3.40	-3.74	2.64	5.05	5.70	-1.08	-0.82	-1.29	1.36	1.87	-0.48	-1.25	-0.78	1.34	1.55
17	R30	2.01	-3.04	4.69	3.64	5.94	1.38	-1.24	0.80	1.86	2.02	1.29	-0.64	1.20	1.44	1.87
18	R200	-1.01	-3.29	5.73	3.44	6.68	-0.64	-0.68	-1.83	0.93	2.05	-0.34	-0.89	-1.62	0.95	1.88
19	R203	2.83	-2.35	3.29	3.68	4.94	1.02	-1.32	-1.63	1.67	2.33	1.88	-1.98	-1.55	2.73	3.14
20	R204	-1.05	-1.98	4.33	2.24	4.88	-0.66	-0.91	-0.85	1.12	1.41	-0.49	0.36	-0.65	0.61	0.89
21	R205	2.31	-1.75	5.14	2.90	5.90	2.07	-0.67	0.98	2.18	2.39	2.03	0.79	2.13	2.18	3.05
22	R208	-1.90	-2.20	4.87	2.91	5.67	-1.15	-1.10	0.90	1.59	1.83	-0.85	-1.12	1.29	1.41	1.91
23	R210	-3.76	-3.18	5.32	4.92	7.25	-0.36	0.87	-1.33	0.94	1.63	0.88	-0.88	-1.45	1.24	1.91
Minimum		-3.83	-3.74	-3.48	2.24	4.88	-1.88	-2.02	-1.83	0.93	1.41	-1.65	-1.98	-1.62	0.61	0.89
Maximum		3.24	2.89	5.73	5.05	7.25	2.07	1.86	1.95	2.63	3.10	2.03	1.53	2.13	2.73	3.14
Mean		-1.59	-2.05	3.56	**2.59**	**4.41**	-0.60	-0.57	0.42	**0.83**	**0.93**	-0.41	-0.34	0.35	**0.54**	**0.64**
RMS		2.67	2.82	4.24	**3.88**	**5.75**	1.34	1.31	1.44	**1.88**	**2.36**	1.16	1.02	1.25	**1.54**	**1.98**
Stdev		2.17	1.95	2.34	**2.92**	**3.74**	1.19	1.17	1.37	**1.67**	**2.16**	1.06	0.93	1.19	**1.41**	**1.85**

Appendix C-6: The summary of the differences between the pre-surveyed coordinates and the adjusted LiDAR coordinates using the GCPs at the different separations of 25m, 100m and 200m with the same feature constraints, respectively, from 59 checking GCPs in Study Area #2.

No.	ID	With 25m Interval [cm]					With 100m Interval [cm]					With 200m Interval [cm]				
		N	E	U	2D_H	3D	N	E	U	2D_H	3D	N	E	U	2D_H	3D
1	L41	-1.21	-0.23	0.34	1.23	1.28	-1.53	-0.37	1.41	1.57	2.11	-2.56	-1.36	2.45	2.90	3.80
2	L43	-1.64	-0.16	1.46	1.65	2.20	-1.83	-0.31	1.61	1.86	2.46	-1.45	-1.45	2.05	2.05	2.90
3	L44	-0.73	-0.73	1.51	1.03	1.83	-1.13	-0.88	1.78	1.43	2.28	-1.67	-0.87	1.78	1.88	2.59
4	L45	-0.98	-0.96	1.39	1.37	1.95	-1.52	-1.25	1.57	1.97	2.52	-2.25	-1.67	2.26	2.80	3.60
5	L46	-1.84	-0.97	1.62	2.08	2.64	-1.91	-1.19	1.71	2.25	2.83	-2.57	-1.67	2.56	3.06	3.99
6	L47	-0.67	-0.88	0.95	1.11	1.46	-0.84	-1.23	1.17	1.49	1.89	-2.38	-1.13	2.16	2.63	3.41
7	L48	-1.56	0.98	1.41	1.84	2.32	1.71	1.13	1.65	2.05	2.63	1.67	0.98	2.56	1.94	3.21
8	L49	-1.08	-0.28	-0.69	1.12	1.31	-1.38	-0.38	-0.78	1.43	1.63	-1.56	-1.78	-2.03	2.37	3.12
9	L50	-0.89	-0.89	-1.46	1.26	1.93	-1.75	-0.89	-1.57	1.96	2.51	-2.04	-1.83	-0.56	2.74	2.80
10	R197	-0.93	0.86	-1.29	1.27	1.81	-1.04	0.99	-1.36	1.44	1.98	-1.45	1.57	-1.67	2.14	2.71
11	R198	1.21	-0.56	-1.26	1.33	1.83	1.43	-0.65	-1.68	1.57	2.30	1.98	-1.56	-2.08	2.52	3.27
12	R199	-0.98	-0.67	0.88	1.19	1.48	-1.12	-0.93	0.98	1.46	1.75	-2.03	-0.78	1.67	2.17	2.74
13	R200	-1.25	1.42	1.89	1.89	2.67	-1.41	1.45	2.01	2.02	2.85	-2.23	1.97	1.69	2.98	3.42
14	R201	-1.38	0.84	0.89	1.62	1.84	-2.56	1.23	1.14	2.84	3.06	-2.98	1.33	2.67	3.26	4.22
15	R202	-2.02	-0.69	1.12	2.13	2.41	-2.63	-1.13	1.51	2.86	3.24	-2.27	-1.68	1.93	2.82	3.42
16	R203	-2.02	1.63	1.79	2.60	3.15	-2.03	1.99	1.89	2.84	3.41	-2.45	1.46	1.56	2.85	3.25
17	R204	1.38	-1.24	0.80	1.86	2.02	1.68	-1.35	0.89	2.16	2.33	1.56	-1.68	1.67	2.29	2.84
18	R205	-0.64	-0.68	-1.83	0.93	2.05	-0.68	-0.98	-1.89	1.19	2.23	-2.03	1.98	-1.19	2.84	3.08
19	R206	1.88	-1.32	-1.63	2.30	2.82	1.35	-0.89	-1.93	1.62	2.52	1.98	-0.45	-2.28	2.03	3.05
20	R207	-0.66	-0.91	0.45	1.12	1.21	-0.98	-1.13	0.65	1.50	1.63	-1.98	-1.71	1.87	2.62	3.22
21	R208	1.07	-0.67	0.98	1.26	1.60	2.23	-1.26	1.56	2.56	3.00	1.56	1.56	2.06	2.21	3.02
22	R209	-1.50	-1.10	0.90	1.86	2.07	-0.77	-1.45	1.26	1.64	2.07	-1.78	-0.78	1.99	1.94	2.78
23	R210	-0.36	0.87	-2.33	0.94	2.51	-0.64	1.23	-1.65	1.39	2.16	-1.31	0.34	-2.56	1.35	2.90
24	R221	-0.65	2.94	0.90	3.01	3.14	-0.89	1.21	1.13	1.50	1.88	-0.98	1.47	2.67	1.77	3.20
25	R222	0.07	0.74	-1.47	0.74	1.65	-1.66	1.28	-1.78	2.10	2.75	1.67	0.98	-1.01	1.94	2.18
26	R223	-0.78	-0.66	0.85	1.02	1.33	-1.21	-0.89	0.78	1.50	1.69	-1.45	-0.98	1.45	1.75	2.27
27	R224	-0.55	0.78	0.84	0.95	1.27	-1.28	1.23	1.24	1.78	2.17	-2.00	2.21	2.53	2.98	3.91
28	R225	-0.07	0.56	1.77	0.56	1.86	-0.50	0.99	2.70	1.11	2.92	-1.22	1.60	0.89	2.01	2.20
29	R226	-0.29	0.39	0.76	0.49	0.90	-0.38	0.52	1.37	0.64	1.51	-1.38	1.89	0.91	2.34	2.51
30	R227	-0.83	0.40	-1.67	0.92	1.91	-0.81	0.78	-1.12	1.12	1.59	-1.85	1.78	-1.85	2.57	3.16

31	R228	0.37	0.56	0.49	0.67	0.83	0.35	0.72	1.21	0.80	1.45	-0.60	0.88	0.56	1.07	1.20
32	L27	0.80	-0.46	0.85	0.92	1.25	0.87	-0.76	0.96	1.16	1.50	0.29	-1.10	0.52	1.14	1.25
33	L29	0.24	-0.18	0.96	0.30	1.01	0.82	-0.56	1.56	0.99	1.85	0.50	-0.45	0.49	0.67	0.83
34	L31	-0.25	-0.67	0.88	0.72	1.13	-0.46	-0.81	1.21	0.93	1.53	-0.88	0.71	0.67	1.13	1.31
35	L32	0.36	-0.56	-1.89	0.67	2.00	0.91	-0.78	-0.78	1.20	1.43	0.05	-0.87	-1.10	0.87	1.40
36	L35	0.44	-0.73	-1.34	0.85	1.59	0.31	-0.69	-1.38	0.76	1.57	-0.71	-1.54	-2.20	1.70	2.78
37	L1	-0.56	-0.45	0.85	0.72	1.11	-0.36	-0.98	0.97	1.04	1.43	-0.75	0.67	0.82	1.01	1.30
38	L2	-0.22	0.75	1.01	0.78	1.28	-0.78	1.03	0.45	1.29	1.37	-0.27	1.78	1.98	1.80	2.68
39	L3	-0.74	0.78	0.92	1.08	1.42	-0.88	1.05	-0.56	1.37	1.48	-2.80	0.25	0.88	2.81	2.95
40	L4	-0.64	0.66	0.85	0.92	1.25	-0.59	0.99	0.97	1.15	1.51	-0.98	1.98	0.81	2.21	2.35
41	L5	0.65	0.68	0.57	0.94	1.10	1.45	0.78	1.29	1.65	2.09	2.85	1.03	1.53	3.03	3.39
42	L6	-0.49	1.36	-1.45	1.45	2.05	-0.78	1.26	-1.58	1.48	2.17	-0.87	1.62	-0.44	1.84	1.89
43	L7	-0.29	0.98	-1.61	1.02	1.91	-1.37	1.18	-0.48	1.81	1.87	-0.37	0.67	-0.66	0.77	1.01
44	L8	-0.36	0.95	0.80	1.02	1.29	0.67	1.25	-0.67	1.42	1.57	0.87	1.75	0.76	1.95	2.10
45	L9	-0.35	0.74	0.74	0.82	1.10	-0.53	1.27	1.28	1.38	1.88	0.63	1.67	1.10	1.78	2.10
46	L10	0.70	-0.78	-1.45	1.05	1.79	0.79	-0.92	-1.16	1.21	1.68	0.26	-0.45	-0.19	0.52	0.55
47	L11	0.34	-0.56	0.37	0.66	0.75	0.54	-0.49	0.52	0.73	0.90	-0.42	0.38	0.34	0.57	0.66
48	L12	0.29	0.93	0.25	0.97	1.01	0.37	1.27	-0.78	1.32	1.54	0.21	1.81	0.21	1.82	1.83
49	L13	0.38	0.89	-0.87	0.97	1.30	0.65	1.78	-0.72	1.89	2.03	0.69	1.87	-0.90	1.99	2.19
50	L14	0.67	1.39	0.77	1.54	1.72	0.98	1.04	0.92	1.43	1.70	1.45	1.66	0.73	2.20	2.32
51	L15	0.80	0.38	0.85	0.89	1.23	0.81	1.06	1.00	1.33	1.67	0.68	0.98	0.80	1.19	1.44
52	L16	0.33	1.28	0.59	1.32	1.45	0.56	1.39	0.74	1.50	1.67	-0.46	0.76	0.53	0.89	1.03
53	L17	1.45	-0.56	-1.66	1.55	2.27	0.98	-0.65	-1.50	1.18	1.91	1.30	0.39	-0.72	1.36	1.54
54	L18	0.45	1.43	-1.15	1.50	1.89	-0.78	1.89	0.77	2.04	2.18	-0.67	1.45	-0.07	1.60	1.60
55	L19	1.80	-0.68	-0.90	1.92	2.12	0.48	-0.36	-2.45	0.60	2.52	0.62	0.37	1.82	0.72	1.96
56	L20	0.45	0.76	0.31	0.88	0.94	0.65	1.38	0.56	1.53	1.62	0.09	1.89	0.81	1.89	2.06
57	L21	0.87	0.86	0.68	1.22	1.40	0.78	1.04	0.74	1.30	1.50	0.64	1.54	-0.02	1.67	1.67
58	L22	-0.29	0.78	0.35	0.83	0.90	-0.56	1.17	0.45	1.30	1.37	-0.54	1.78	1.92	1.86	2.67
59	L25	0.56	0.93	0.64	1.09	1.26	1.23	1.45	1.35	1.90	2.33	2.01	2.13	2.46	2.93	3.82
Minimum		-2.02	-1.32	-2.33	0.30	0.75	-2.63	-1.45	-2.45	0.60	0.90	-2.98	-1.83	-2.56	0.52	0.55
Maximum		1.88	2.94	1.89	3.01	3.15	2.23	1.99	2.70	2.86	3.41	2.85	2.21	2.67	3.26	4.22
Mean		-0.21	0.17	0.19	**0.27**	**0.33**	-0.29	0.22	0.36	**0.36**	**0.51**	-0.55	0.43	0.67	**0.70**	**0.97**
RMS		0.95	0.93	1.17	**1.33**	**1.77**	1.19	1.10	1.33	**1.62**	**2.09**	1.56	1.41	1.60	**2.10**	**2.64**
Stdev		0.93	0.92	1.16	**1.31**	**1.75**	1.16	1.08	1.29	**1.59**	**2.05**	1.47	1.35	1.46	**2.00**	**2.48**

Appendix C-7: The summary of the differences between the pre-surveyed coordinates and the adjusted LiDAR coordinates through the 3DCCT using a single strip, through the MA process using two strips acquired in the opposite driving directions and in the same direction, respectively, from 38 checking GCPs in Study Area #1.

No.	ID	With Singe Strip [cm]					With Opposite Direction Strips [cm]					With Same Direction Strips [cm]				
		N	E	U	2D_H	3D	N	E	U	2D_H	3D	N	E	U	2D_H	3D
1	Rex2	0.45	0.78	1.22	0.90	1.52	0.55	-0.77	0.87	0.95	1.29	0.77	-0.85	0.93	1.15	1.48
2	Rex4	0.41	-0.97	1.22	1.05	1.61	-0.38	-0.79	0.67	0.88	1.10	-0.68	-1.56	0.67	1.70	1.83
3	Rex6	0.64	0.27	0.79	0.69	1.05	0.79	0.66	0.74	1.03	1.27	0.45	0.34	0.29	0.56	0.63
4	TrafficA3	-0.89	0.90	-0.93	1.27	1.57	-0.47	0.93	-1.76	1.04	2.05	-0.79	0.39	-1.67	0.88	1.89
5	TrafficA7	0.56	1.42	0.93	1.53	1.79	0.56	0.69	0.73	0.89	1.15	0.86	1.44	0.69	1.68	1.81
6	SWTraffic2	0.22	0.36	-0.23	0.42	0.48	0.66	0.82	-1.53	1.05	1.86	0.67	0.96	-0.64	1.17	1.33
7	SWTraffic4	0.55	-0.76	0.63	0.94	1.13	0.48	-0.45	-0.55	0.66	0.86	0.88	-0.45	-0.62	0.99	1.17
8	YUSignA2	-0.75	-0.99	-0.82	1.24	1.49	-0.37	-0.71	-0.87	0.80	1.18	-0.45	-0.63	-0.45	0.77	0.90
9	YUSignA4	1.04	-1.15	-1.31	1.55	2.03	0.51	-0.73	-0.93	0.89	1.29	1.16	-0.83	-1.34	1.43	1.96
10	YUSignA7	-0.69	-0.85	-1.21	1.09	1.63	-0.36	-0.78	-0.63	0.86	1.07	-1.67	-1.32	-1.04	2.13	2.37
11	YUMap1	0.24	1.33	-0.98	1.35	1.67	0.97	1.01	-0.57	1.40	1.51	1.45	-1.25	-0.78	1.91	2.07
12	YUMap2	0.17	0.78	-1.88	0.80	2.04	0.68	-0.83	-1.33	1.07	1.71	0.77	-0.29	-1.86	0.82	2.03
13	YUMap6	2.03	1.23	-1.64	2.37	2.89	1.49	-1.14	-1.69	1.88	2.53	0.73	-1.22	-1.24	1.42	1.89
14	StopSign3	0.09	-0.35	-3.03	0.36	3.05	0.73	-0.34	-1.89	0.81	2.05	0.69	-0.58	-2.02	0.90	2.21
15	StopSign4	0.46	-0.86	0.25	0.98	1.01	0.85	-0.79	0.56	1.16	1.29	0.74	-0.75	0.56	1.05	1.19
16	StopSign6	0.84	-0.97	0.59	1.28	1.41	0.95	-1.43	0.61	1.72	1.82	0.44	-1.11	0.33	1.19	1.24
17	StopSign8	1.43	-0.98	0.64	1.73	1.85	-1.05	-0.86	0.83	1.36	1.59	-1.73	-1.33	1.41	2.18	2.60
18	Building1	-1.37	-1.56	0.29	2.08	2.10	-1.31	-1.34	0.61	1.87	1.97	-1.45	-1.45	0.75	2.05	2.18
19	Building4	-1.93	0.94	0.73	2.15	2.27	-1.39	0.42	0.33	1.45	1.49	-1.58	0.68	0.44	1.72	1.78
20	Building5	1.83	1.59	0.75	2.42	2.54	0.83	0.97	1.27	1.28	1.80	1.48	1.56	1.73	2.15	2.76
21	YUSignB1	0.13	0.98	-0.48	0.99	1.10	-0.69	1.34	-0.45	1.51	1.57	0.78	1.22	-0.33	1.45	1.49
22	YUSignB3	-0.79	0.36	1.16	0.87	1.45	-0.45	0.79	0.55	0.91	1.06	-0.88	0.39	0.67	0.96	1.17
23	RexW2	-0.42	0.84	-0.27	0.94	0.98	-0.57	0.72	-0.93	0.92	1.31	-0.93	0.52	-1.23	1.07	1.63
24	RexW4	-1.02	0.57	0.79	1.17	1.41	-1.23	0.68	1.14	1.41	1.81	-0.66	0.64	0.96	0.92	1.33
25	RexW6	-0.68	-0.86	-0.79	1.10	1.35	-1.34	-0.86	0.99	1.59	1.87	-0.85	0.77	1.37	1.15	1.79
26	YUSignC4	-0.48	-1.58	0.74	1.65	1.81	-1.14	1.49	-0.69	1.88	2.00	-1.09	0.55	-0.56	1.22	1.34

27	YUSignC6	-1.00	-0.99	-1.08	1.41	1.77	-0.99	-0.71	1.56	1.22	1.98	-0.65	-0.79	1.35	1.02	1.69
28	Curve2	-0.89	-0.71	-0.84	1.14	1.41	-0.66	-0.77	-0.74	1.01	1.26	-0.98	-0.74	-0.67	1.23	1.40
29	Curve4	-0.67	-0.89	-0.78	1.11	1.36	-0.45	-0.82	-0.52	0.94	1.07	-0.55	-0.79	-0.82	0.96	1.26
30	Curve6	-1.27	-1.46	-1.21	1.94	2.28	-0.88	-0.23	-1.03	0.91	1.37	-0.91	-0.45	-1.15	1.02	1.53
31	Curve8	0.13	-0.62	0.88	0.63	1.08	1.15	-0.56	0.69	1.28	1.45	1.33	-0.67	0.88	1.49	1.73
32	R1	-0.04	-1.29	-1.11	1.29	1.70	-0.15	-0.69	-1.03	0.71	1.25	-0.38	-0.91	-1.19	0.99	1.55
33	R3	-1.43	0.89	-1.55	1.68	2.29	-1.01	0.44	-0.83	1.10	1.38	-1.20	0.69	-1.11	1.38	1.77
34	R5	-1.45	0.25	-1.93	1.47	2.43	-1.04	0.63	-1.14	1.22	1.67	-0.98	0.92	-1.56	1.34	2.06
35	R7	-0.77	-0.98	-1.59	1.25	2.02	-0.67	-0.62	-1.25	0.91	1.55	-0.82	-0.33	-1.29	0.88	1.56
36	R9	-0.99	-0.18	-0.69	1.01	1.22	-0.60	-0.39	-0.58	0.72	0.92	-0.51	-0.55	-1.66	0.75	1.82
37	R11	-0.73	-0.49	0.66	0.88	1.10	-0.77	-0.58	0.51	0.96	1.09	-0.72	-0.77	0.57	1.05	1.20
38	R13	-1.75	-1.24	-1.05	2.14	2.39	-1.35	-0.84	-0.83	1.59	1.79	-0.53	-0.91	-0.93	1.05	1.40
Minimum		-1.93	-1.58	-3.03	0.36	0.48	-1.39	-1.43	-1.89	0.66	0.86	-1.73	-1.56	-2.02	0.56	0.63
Maximum		2.03	1.59	1.22	2.42	3.05	1.49	1.49	1.56	1.88	2.53	1.48	1.56	1.73	2.18	2.76
Mean		-0.23	-0.19	-0.35	**0.30**	**0.46**	-0.21	-0.17	-0.24	**0.27**	**0.36**	-0.21	-0.25	-0.28	**0.32**	**0.43**
RMS		0.98	0.97	1.12	**1.38**	**1.78**	0.87	0.83	0.98	**1.20**	**1.55**	0.97	0.91	1.09	**1.32**	**1.72**
Stdev		0.96	0.97	1.08	**1.36**	**1.74**	0.85	0.82	0.97	**1.19**	**1.53**	0.96	0.88	1.07	**1.30**	**1.69**

Appendix C-8: The summary of the differences between the pre-surveyed coordinates and the adjusted LiDAR coordinates through the 3DCCT using a single strip, through the MA process using two strips acquired in the opposite directions and in the same direction, respectively, from 23 checking GCPs on Segment 1 in Study Area #2.

No.	ID	With Singe Strip [cm]					With Opposite Direction Strips [cm]					With Same Direction Strips [cm]				
		N	E	U	2D_H	3D	N	E	U	2D_H	3D	N	E	U	2D_H	3D
1	L41	-1.03	-1.01	0.84	1.44	1.67	-0.46	-1.23	0.46	1.31	1.39	-0.59	-1.03	0.76	1.19	1.41
2	L45	-0.76	0.47	1.63	0.89	1.86	-0.51	-0.98	1.48	1.10	1.85	-0.78	-0.67	1.79	1.03	2.06
3	L46	-1.52	0.27	1.32	1.54	2.03	-0.73	0.34	0.63	0.81	1.02	-0.98	0.46	0.61	1.08	1.24
4	L49	-0.67	-0.76	0.63	1.01	1.19	-0.93	1.03	1.41	1.39	1.98	-0.88	0.31	1.45	0.93	1.72
5	L50	-1.60	-0.52	0.96	1.68	1.94	-0.98	-0.33	1.03	1.03	1.46	-1.56	-0.56	0.99	1.66	1.93
6	R10	-1.42	0.20	1.23	1.43	1.89	-0.66	0.88	0.96	1.10	1.46	-1.29	0.65	1.13	1.44	1.83
7	R12	-1.29	0.85	1.26	1.54	1.99	-0.93	0.93	0.97	1.32	1.63	-0.65	0.88	0.78	1.09	1.34
8	R14	-0.73	-1.21	0.88	1.41	1.66	-0.51	-0.78	-0.98	0.93	1.35	-0.73	-1.06	-1.23	1.29	1.78
9	R16	-0.89	-1.24	-1.03	1.53	1.84	-0.96	-0.83	-0.98	1.27	1.60	-0.98	-0.98	-1.23	1.39	1.85
10	R17	-0.63	-0.94	-0.94	1.13	1.47	-0.53	-1.34	-0.79	1.44	1.64	-0.65	-0.68	-0.98	0.94	1.36
11	R19	0.88	-1.33	-1.21	1.59	2.00	1.15	-1.11	-1.03	1.60	1.90	1.27	-1.56	-1.00	2.01	2.25
12	R21	-0.69	-0.15	0.83	0.71	1.09	-0.67	-0.67	0.87	0.95	1.29	-0.81	-0.34	0.74	0.88	1.15
13	R22	-0.68	0.92	1.68	1.14	2.03	-0.34	0.73	1.42	0.81	1.63	-0.77	0.66	1.34	1.01	1.68
14	R25	-1.65	1.53	0.60	2.25	2.33	-1.28	1.23	1.34	1.78	2.22	-0.65	1.25	0.78	1.41	1.61
15	R26	-0.78	0.75	0.78	1.08	1.33	-0.71	0.79	0.34	1.06	1.12	-0.75	0.87	0.55	1.15	1.27
16	R29	-0.48	-1.25	-0.78	1.34	1.55	-0.66	-1.01	-0.45	1.21	1.29	-0.64	-1.17	0.44	1.33	1.40
17	R30	1.29	-0.64	1.20	1.44	1.87	0.84	-0.78	0.97	1.15	1.50	0.94	-0.83	1.45	1.25	1.92
18	R200	-0.34	-0.89	-1.62	0.95	1.88	-0.28	-0.61	-1.35	0.67	1.51	-0.55	-1.22	-1.53	1.34	2.03
19	R203	1.88	-1.98	-1.55	2.73	3.14	1.18	-0.92	-0.75	1.50	1.67	1.56	-1.88	-1.31	2.44	2.77
20	R204	-0.49	0.36	-0.65	0.61	0.89	-0.75	0.38	0.49	0.84	0.97	-0.69	0.38	0.39	0.79	0.88
21	R205	2.03	0.79	2.13	2.18	3.05	1.24	0.38	1.05	1.30	1.67	1.66	0.85	1.88	1.86	2.65
22	R208	-0.85	-1.12	1.29	1.41	1.91	-0.37	-0.82	1.19	0.90	1.49	-0.59	-1.08	1.44	1.23	1.89
23	R210	0.88	-0.88	-1.45	1.24	1.91	1.36	-0.91	-1.42	1.64	2.17	0.99	-0.99	-1.13	1.40	1.80
Minimum		-1.65	-1.98	-1.62	0.61	0.89	-1.28	-1.34	-1.42	0.67	0.97	-1.56	-1.88	-1.53	0.79	0.88
Maximum		2.03	1.53	2.13	2.73	3.14	1.36	1.23	1.48	1.78	2.22	1.66	1.25	1.88	2.44	2.77
Mean		-0.41	-0.34	0.35	**0.54**	**0.64**	-0.28	-0.24	0.30	**0.37**	**0.48**	-0.35	-0.34	0.35	**0.49**	**0.60**
RMS		1.16	1.02	1.25	**1.54**	**1.98**	0.89	0.92	1.07	**1.28**	**1.67**	1.01	1.01	1.19	**1.43**	**1.86**
Stdev		1.06	0.93	1.19	**1.41**	**1.85**	0.81	0.86	1.01	**1.18**	**1.55**	0.92	0.92	1.13	**1.30**	**1.72**

Appendix C-9: The summary of the differences between the pre-surveyed coordinates and the original LiDAR coordinates, the adjusted LiDAR coordinates through the 3DCCT using single strip and through the MA process using two strips acquired in the opposite driving directions after the preliminary boresight angle calibration, respectively, from 38 checking GCPs in Study Area #1.

No.	ID	Original Differences (after BA) [cm]					Refinement w. single strip (after BA) [cm]					Refinement w. two strips (after BA)[cm]				
		N	E	U	2D_H	3D	N	E	U	2D_H	3D	N	E	U	2D_H	3D
1	Rex2	1.05	-1.69	-0.98	1.99	2.22	0.33	0.68	0.88	0.76	1.16	0.35	0.98	0.75	1.04	1.28
2	Rex4	-1.88	1.68	2.28	2.52	3.40	0.24	-0.68	1.13	0.72	1.34	-0.29	0.66	-0.57	0.72	0.92
3	Rex6	1.54	-0.97	2.55	1.82	3.13	0.78	0.67	0.96	1.03	1.41	-0.36	1.02	0.68	1.08	1.28
4	TrafficA3	-2.03	0.66	1.73	2.13	2.75	-0.67	0.88	-0.68	1.11	1.30	0.55	0.53	-1.56	0.76	1.74
5	TrafficA7	-1.55	1.13	2.74	1.92	3.34	0.44	1.12	1.13	1.20	1.65	-1.01	-0.46	0.60	1.11	1.26
6	SWTraffic2	-0.88	-0.97	2.13	1.31	2.50	0.32	0.64	0.67	0.72	0.98	0.38	-0.68	-1.13	0.78	1.37
7	SWTraffic4	1.83	1.34	2.48	2.27	3.36	0.15	-0.65	0.45	0.67	0.80	0.22	0.65	-1.15	0.69	1.34
8	YUSignA2	-2.04	-1.13	2.64	2.33	3.52	-0.64	-0.77	0.38	1.00	1.07	-0.28	-1.55	-0.98	1.58	1.86
9	YUSignA4	0.98	-2.65	-3.98	2.83	4.88	0.87	-0.87	-0.87	1.23	1.51	0.98	-0.38	-0.78	1.05	1.31
10	YUSignA7	-2.15	0.97	-1.12	2.36	2.61	-0.54	-0.65	-1.45	0.85	1.68	-0.13	-0.78	1.13	0.79	1.38
11	YUMap1	1.53	-1.22	1.97	1.96	2.78	0.44	0.87	-1.23	0.97	1.57	-0.55	0.65	-0.45	0.85	0.96
12	YUMap2	0.97	-1.99	1.44	2.21	2.64	0.28	0.55	-0.44	0.62	0.76	0.33	-0.75	-0.98	0.82	1.28
13	YUMap6	1.45	-2.65	1.19	3.02	3.25	1.64	0.88	-0.88	1.86	2.06	0.78	-0.38	-1.16	0.87	1.45
14	StopSign3	-0.65	-1.13	2.13	1.30	2.50	0.11	-1.68	-1.23	1.68	2.09	0.55	0.45	-1.09	0.71	1.30
15	StopSign4	-0.98	-1.44	2.10	1.74	2.73	0.77	-0.78	-1.26	1.10	1.67	0.98	-0.66	0.88	1.18	1.47
16	StopSign6	0.46	-1.97	2.78	2.02	3.44	0.35	-0.64	0.64	0.73	0.97	0.38	-1.13	0.98	1.19	1.54
17	StopSign8	-1.76	1.83	1.25	2.54	2.83	0.87	-0.79	0.88	1.18	1.47	-0.79	-0.44	0.73	0.90	1.16
18	Building1	-1.37	1.67	2.97	2.16	3.67	-0.46	-1.23	0.95	1.31	1.62	-0.88	-0.71	0.83	1.13	1.40
19	Building4	-1.89	1.06	2.18	2.17	3.07	-1.21	0.34	0.31	1.26	1.29	-1.05	0.31	0.27	1.09	1.13
20	Building5	-1.46	1.03	2.67	1.79	3.21	0.78	-1.11	0.65	1.36	1.50	0.65	-0.68	0.97	0.94	1.35
21	YUSignB1	1.33	0.98	2.16	1.65	2.72	0.33	-1.65	-0.87	1.68	1.89	-0.45	-1.98	-0.66	2.03	2.14
22	YUSignB3	0.97	-0.96	2.97	1.36	3.27	-0.54	0.68	1.03	0.87	1.35	0.88	0.55	0.43	1.04	1.12
23	RexW2	-1.68	-2.29	-1.87	2.84	3.40	-0.38	0.55	-1.65	0.67	1.78	-0.38	0.38	-1.28	0.54	1.39
24	RexW4	-2.33	1.65	2.96	2.86	4.11	-0.87	0.67	0.48	1.10	1.20	-0.79	0.18	1.33	0.81	1.56
25	RexW6	-2.45	-1.93	2.97	3.12	4.31	-0.64	-0.66	-0.66	0.92	1.13	-0.69	-0.38	0.35	0.79	0.86
26	YUSignC4	1.66	-2.13	0.56	2.70	2.76	-0.37	-1.13	-0.88	1.19	1.48	-0.93	0.79	-0.78	1.22	1.45

27	YUSignC6	1.13	-2.88	1.87	3.09	3.61	-0.78	-0.57	-1.24	0.97	1.57	0.66	-0.66	1.13	0.93	1.47
28	Curve2	0.96	1.19	2.67	1.53	3.08	-0.65	-0.66	-1.13	0.93	1.46	0.13	-0.38	-0.88	0.40	0.97
29	Curve4	0.64	-2.87	2.11	2.94	3.62	-0.54	0.65	-0.88	0.85	1.22	0.39	0.83	-1.13	0.92	1.46
30	Curve6	-1.55	1.98	2.13	2.51	3.30	-0.66	0.68	-1.33	0.95	1.63	-0.62	0.33	-0.98	0.70	1.21
31	Curve8	-1.67	-1.15	2.97	2.03	3.60	0.23	-0.54	0.45	0.59	0.74	0.75	-0.68	0.93	1.01	1.37
32	R1	0.99	-2.65	-1.87	2.83	3.39	0.38	-0.68	-0.58	0.78	0.97	0.38	-0.99	1.23	1.06	1.62
33	R3	-1.38	1.64	2.16	2.14	3.04	-0.84	0.41	0.74	0.93	1.19	-0.78	0.35	0.68	0.85	1.09
34	R5	-1.67	-2.03	-1.44	2.63	3.00	-1.01	0.24	-0.98	1.04	1.43	0.78	0.78	-1.25	1.10	1.67
35	R7	-1.67	-2.02	1.76	2.62	3.16	-0.87	-0.98	1.33	1.31	1.87	-0.98	-0.78	-1.69	1.25	2.10
36	R9	-2.33	1.65	3.63	2.86	4.62	-0.67	-0.46	-0.78	0.81	1.13	-0.33	-0.66	-0.45	0.74	0.86
37	R11	1.65	1.88	-2.68	2.50	3.67	-0.55	-0.61	-0.38	0.82	0.90	-0.67	-0.45	0.38	0.81	0.89
38	R13	-2.38	1.69	1.18	2.92	3.15	-1.15	-0.83	-0.99	1.42	1.73	-0.85	-0.67	0.66	1.08	1.27
Minimum		-2.45	-2.88	-3.98	1.30	2.22	-1.21	-1.68	-1.65	0.59	0.74	-1.05	-1.98	-1.69	0.40	0.86
Maximum		1.83	1.98	3.63	3.12	4.88	1.64	1.12	1.33	1.86	2.09	0.98	1.02	1.33	2.03	2.14
Mean		-0.49	-0.39	1.46	**0.62**	**1.59**	-0.12	-0.21	-0.19	**0.25**	**0.31**	-0.07	-0.18	-0.11	**0.19**	**0.22**
RMS		1.58	1.75	2.31	**2.36**	**3.30**	0.69	0.82	0.94	**1.07**	**1.43**	0.66	0.76	0.95	**1.00**	**1.38**
Stdev		1.52	1.73	1.82	**2.31**	**2.93**	0.69	0.80	0.93	**1.06**	**1.41**	0.66	0.74	0.96	**1.00**	**1.38**

Appendix C-10: The summary of the differences between the pre-surveyed coordinates and the original LiDAR coordinates, the adjusted LiDAR coordinates through the 3DCCT using single strip and through the MA process using two strips acquired in the opposite driving directions after the preliminary boresight angle calibration, respectively, from 23 checking GCPs in Study Area #2.

No.	ID	Original Differences (after BA) [cm]					Refinement w. single strip (after BA) [cm]					Refinement w. two strips (after BA)[cm]				
		N	E	U	2D_H	3D	N	E	U	2D_H	3D	N	E	U	2D_H	3D
1	L41	-2.44	-2.98	2.73	3.85	4.72	-0.88	-0.83	0.73	1.21	1.41	-0.49	-0.74	0.98	0.89	1.32
2	L45	-2.59	1.47	1.69	2.98	3.42	0.36	0.59	0.92	0.69	1.15	-0.55	0.68	0.88	0.87	1.24
3	L46	-3.38	-2.08	2.07	3.97	4.48	-0.78	0.47	1.22	0.91	1.52	-0.67	0.69	1.01	0.96	1.39
4	L49	-2.95	-1.99	0.82	3.56	3.65	-0.37	-0.33	0.82	0.50	0.96	-0.39	-0.88	0.75	0.96	1.22
5	L50	2.88	-1.95	2.41	3.48	4.23	-1.05	0.44	-1.26	1.14	1.70	-0.98	0.67	-0.93	1.19	1.51
6	R10	-1.99	2.12	2.19	2.91	3.64	-0.93	0.45	1.35	1.03	1.70	-0.73	0.73	1.23	1.03	1.61
7	R12	-0.89	1.85	2.14	2.05	2.97	-1.02	-1.41	0.47	1.74	1.80	-0.83	-0.48	0.69	0.96	1.18
8	R14	0.94	-0.88	-1.61	1.29	2.06	0.38	-0.98	0.52	1.05	1.17	0.84	-0.67	0.98	1.07	1.45
9	R16	0.78	-1.93	-0.75	2.08	2.21	-0.73	-1.06	-0.89	1.29	1.56	-0.62	-0.71	-1.22	0.94	1.54
10	R17	-1.04	-0.64	1.48	1.22	1.92	1.04	-0.62	-0.73	1.21	1.41	0.87	-0.89	-0.51	1.24	1.35
11	R19	1.47	-1.78	2.05	2.31	3.09	0.57	-0.98	-0.88	1.13	1.44	0.69	-1.04	-0.98	1.25	1.59
12	R21	-1.09	-0.82	2.69	1.36	3.02	-0.66	0.58	0.66	0.88	1.10	-0.41	0.69	0.42	0.80	0.91
13	R22	-0.31	1.25	2.64	1.29	2.94	-0.97	0.73	1.17	1.21	1.69	-0.57	0.62	1.02	0.84	1.32
14	R25	-1.53	2.47	2.38	2.91	3.76	-1.05	1.11	0.48	1.53	1.60	-0.79	0.78	0.88	1.11	1.42
15	R26	0.91	0.92	2.65	1.29	2.95	-0.53	0.57	1.03	0.78	1.29	-0.64	0.88	1.29	1.09	1.69
16	R29	-0.62	-1.51	-2.01	1.63	2.59	-0.92	-1.34	-0.67	1.63	1.76	-0.59	-0.92	-1.33	1.09	1.72
17	R30	0.56	-1.38	0.88	1.49	1.73	0.67	0.48	1.05	0.82	1.33	0.58	0.33	0.64	0.67	0.92
18	R200	-1.14	-1.22	-1.15	1.67	2.03	-0.68	-0.66	-1.17	0.95	1.51	-0.49	-0.57	-1.01	0.75	1.26
19	R203	2.09	-1.77	-2.38	2.74	3.63	0.89	-0.88	-0.63	1.25	1.40	0.83	-0.78	-0.57	1.14	1.27
20	R204	-0.61	-1.08	1.65	1.24	2.06	-0.28	0.68	-0.48	0.74	0.88	-0.57	0.41	-1.38	0.70	1.55
21	R205	1.71	-1.33	2.99	2.17	3.69	1.09	-0.35	0.82	1.14	1.41	1.03	-0.31	0.77	1.08	1.32
22	R208	-0.75	-0.63	1.91	0.98	2.15	-0.64	-0.78	0.93	1.01	1.37	-0.51	-0.77	0.87	0.92	1.27
23	R210	1.45	-0.52	-1.89	1.54	2.44	0.71	-0.44	-1.16	0.84	1.43	0.77	-0.59	-1.09	0.97	1.46
Minimum		-3.38	-2.98	-2.38	0.98	1.73	-1.05	-1.41	-1.26	0.50	0.88	-0.98	-1.04	-1.38	0.67	0.91
Maximum		2.88	2.47	2.99	3.97	4.72	1.09	1.11	1.35	1.74	1.80	1.03	0.88	1.29	1.25	1.72
Mean		-0.37	-0.63	1.11	**0.73**	**1.33**	-0.25	-0.20	0.19	**0.32**	**0.37**	-0.18	-0.12	0.15	**0.22**	**0.27**
RMS		1.74	1.65	2.08	**2.40**	**3.17**	0.84	0.84	0.96	**1.19**	**1.53**	0.75	0.77	1.01	**1.08**	**1.48**
Stdev		1.71	1.53	1.77	**2.29**	**2.90**	0.76	0.78	0.91	**1.09**	**1.42**	0.68	0.72	0.98	**0.99**	**1.39**

Appendix D: The figures and tables of example checking points

Appendix D-1: Study Area #1 - Categorization of ground control points

The performance of accuracy improvement was evaluated using the checking GCPs through the comparison against using different types and the mixed-types of GCPs. Figure D-1 presents the scatter plot of 38 checking GCPs (27 building-type & 11 ground-type) in study area #1. By taking the enlarged snapshots of two checking points "Building4" (building-type) and "R5" (ground-type) as examples, the adjusted LiDAR coordinates using the same type GCPs was the closest to the pre-surveyed coordinates (red dot) in 3D, while the adjusted coordinates on the basis of the 7 parameters determined using the different types of the GCPs were the furthest, and using the mixed types of the GCPs (cyan diamond) fell in between. With respect to the pre-surveyed coordinates as references, the differences of the LiDAR coordinates were calculated and used as errors in performance evaluation. The error results (Table D-1) based on 11 ground-type GCPs were the biggest (i.e., 3.80cm in 3D) for the building-type checking GCP "Building4". Similarly, the errors based on 27 building-type GCPs were the largest (i.e., 3.64cm in 3D) for the ground-type checking GCP "R5". The performance improvement became significant up to around 2cm in 3D if the checking GCPs were the same type with the used GCPs in the corresponding 3D conformal transformation.

Table D-2: The differences between the pre-surveyed coordinates and the adjusted LiDAR coordinates using 11 ground-type GCPs, 27 building-type GCPs and 38 mixed-type GCPs, respectively, from the checking points "Building4(B4)" and "R5".

ID	With Building-type GCPs [cm]					With Ground-type GCPs [cm]					With Mixed-type GCPs [cm]				
	N	E	2D	U	3D	N	E	2D	U	3D	N	E	2D	U	3D
B4	-0.78	0.58	0.97	1.05	1.43	-1.98	1.06	2.25	3.06	3.80	-1.36	0.94	1.65	2.36	2.88
R5	-1.90	1.78	2.60	-2.55	3.64	-0.78	0.69	1.04	-0.98	1.43	-1.55	1.25	1.99	-1.45	2.46

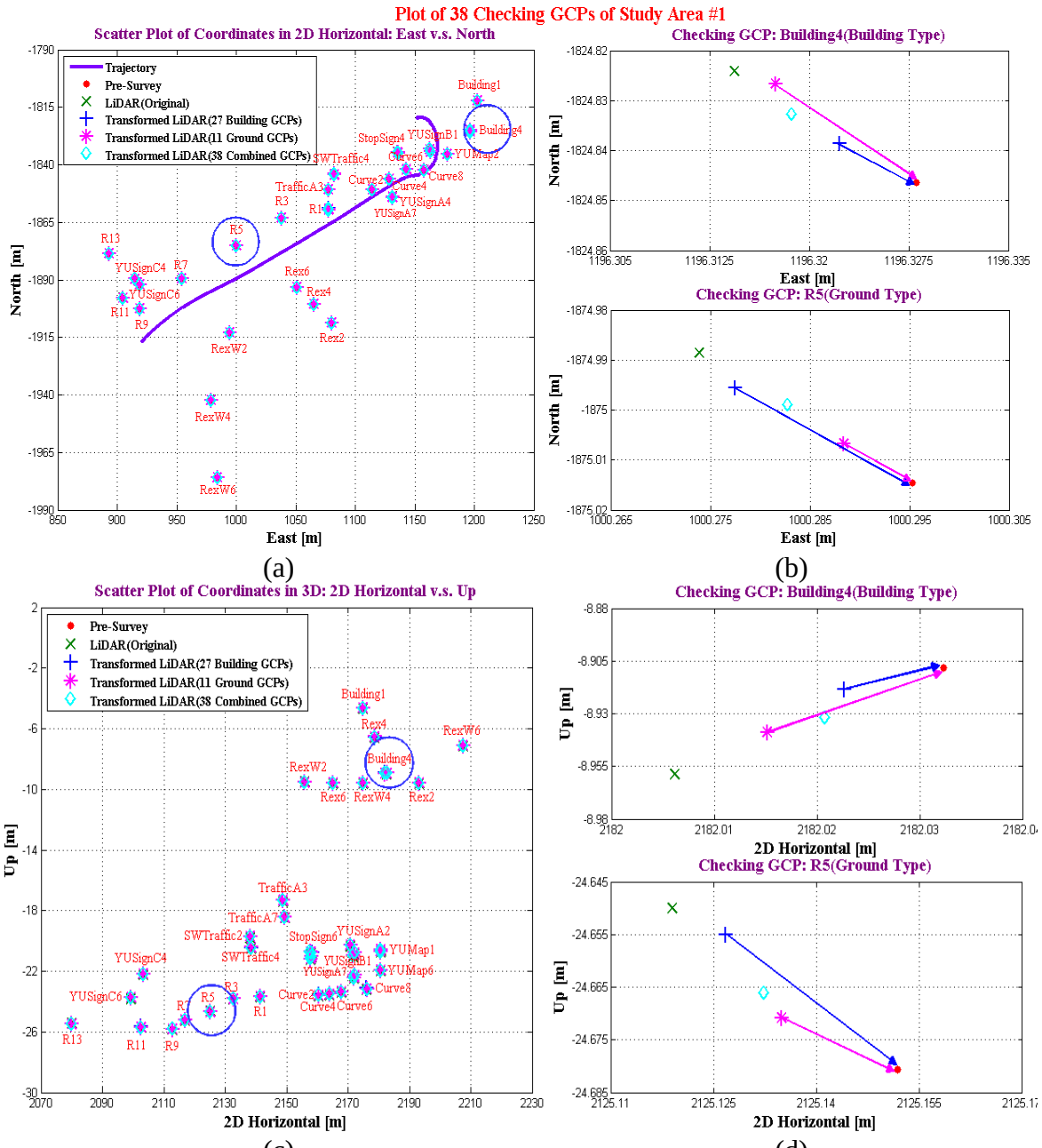

Figure D-1: Scatter plot of 38 checking GCPs (27 building-type & 11 ground-type) in Study Area #1. The adjusted LiDAR coordinates using 11 ground-type GCPs, 27 building-type GCPs and 38 mixed-type GCPs were presented in pink star, green cross and cyan diamond, respectively: (a) & (c) 2D horizontal and vertical; (b) & (d) Close-up details of "B4" and "R5".

Appendix D-2: Study Area #1 – Utilization of Feature Constraints

The accuracy improvement through the 38 checking GCPs aided by line and planar features was analyzed and presented in Figure D-2 in both 2D horizontal and vertical direction. By taking the enlarged snapshots of two checking points "SWTraffic4" (building-type) and "R11" (ground-type) as examples, the adjusted LiDAR coordinates using 7 conformal transformation parameters based on the GCPs with the feature constraints (pink star) were closer to the pre-surveyed coordinates (red dot) comparing with the adjusted LiDAR coordinates using 7 conformal transformation parameters estimated only from the GCPs (blue cross) horizontally and vertically. By considering the pre-surveyed coordinates as reference coordinates, the differences were used to assess the errors in the adjusted LiDAR data. Based on the numerical results in Table D-2, the errors using GCPs incorporating with feature constraints together were much smaller than using only GCPs. The performance was improved by around 1cm in 3D.

Table D-3: The differences between the pre-surveyed coordinates and the adjusted LiDAR coordinates using GCPs only and GCPs with feature constraints, respectively, from checking points "SWTraffic4" (building-type) and "R11" (ground-type).

ID	Original Differences [cm]					With GCPs only [cm]					With GCPs and Features [cm]				
	N	E	2D	U	3D	N	E	2D	U	3D	N	E	2D	U	3D
SW4	2.23	-2.34	3.23	3.34	4.65	1.52	-1.33	2.02	-1.54	2.54	0.55	-0.76	0.94	0.63	1.13
R11	-2.69	-2.16	3.45	2.56	4.30	-1.34	-0.99	1.67	1.48	2.23	-0.73	-0.49	0.88	0.66	1.10

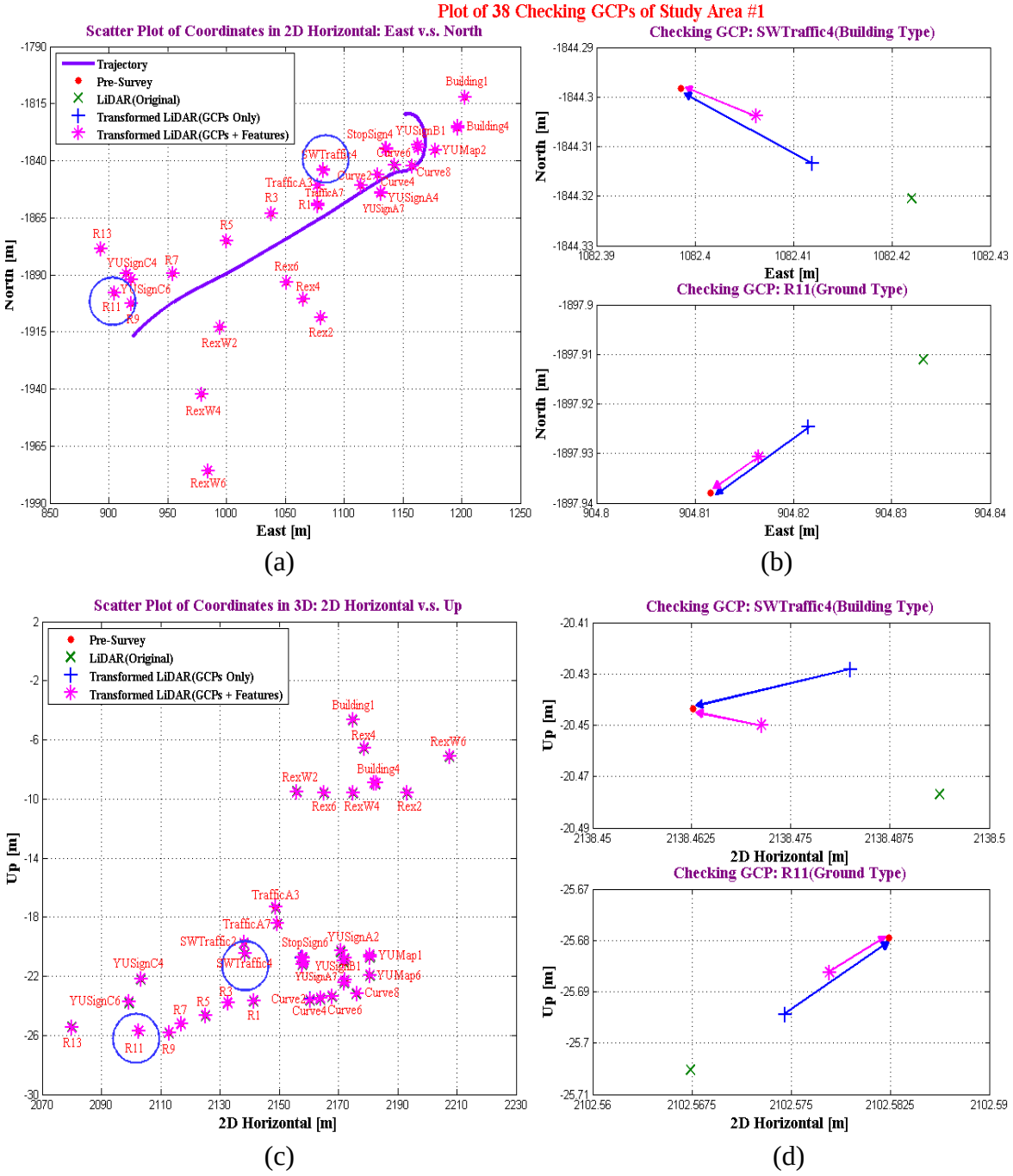

Figure D-2: Scatter plot of 38 checking GCPs (27 building-type & 11 ground-type) in Study Area #1. The adjusted LiDAR coordinates using 38 mixed-type GCPs with the features and only GCPs were presented in pink star and blue cross, respectively: (a) & (c) 2D horizontal and vertical; (b) & (d) Close-up details of "SWTraffic4" (building-type) and "R11"(ground-type).

Appendix D-3: Study Area #1 – Usage Optimization of Ground Control Points

The scatter plot of 38 checking GCPs in the test scene in both 2D horizontal and vertical direction is as in Figure D-3. By taking the enlarged snapshots of two checking points "SWTraffic4" and "R11" as examples, the adjusted LiDAR coordinates using the 7 conformal transformation parameters derived from 38 GCPs (i.e., 50%), 23 GCPs (i.e., 30%) and 16 GCPs (i.e., 20%), respectively, were close to each other, and had the similar discrepancies to the pre-surveyed coordinates (red dot). However, the adjusted LiDAR coordinates using the 7 conformal transformation parameters derived only form 8 GCPs (i.e., 10%) were further away. By considering the pre-surveyed coordinates as references, the differences of the adjusted LiDAR coordinates for the checking points were analysed in details. Based on the numerical results in Table D-3, the coordinate differences from the results using 8 GCPs was the biggest ones. However, the performance of the results based on 16 GCPs was only degraded by around 5mm in 3D comparing with the results based on 38 GCPs.

Table D-4: The differences between the pre-surveyed coordinates and the adjusted LiDAR coordinates using 38, 16 and 8 GCPs, respectively, from checking points "SWTraffic4 (SW4)" and "R11".

ID	With 38 GCPs + Features [cm]					With 16 GCPs + Features [cm]					With 8 GCPs + Features [cm]				
	N	E	2D	U	3D	N	E	2D	U	3D	N	E	2D	U	3D
SW4	0.55	-0.76	0.94	0.63	1.13	0.79	-0.87	1.18	1.38	1.81	1.44	-1.65	2.19	2.04	2.99
R11	-0.73	-0.49	0.88	0.66	1.10	-1.01	-0.72	1.24	1.21	1.73	-1.49	-1.51	2.12	1.89	2.84

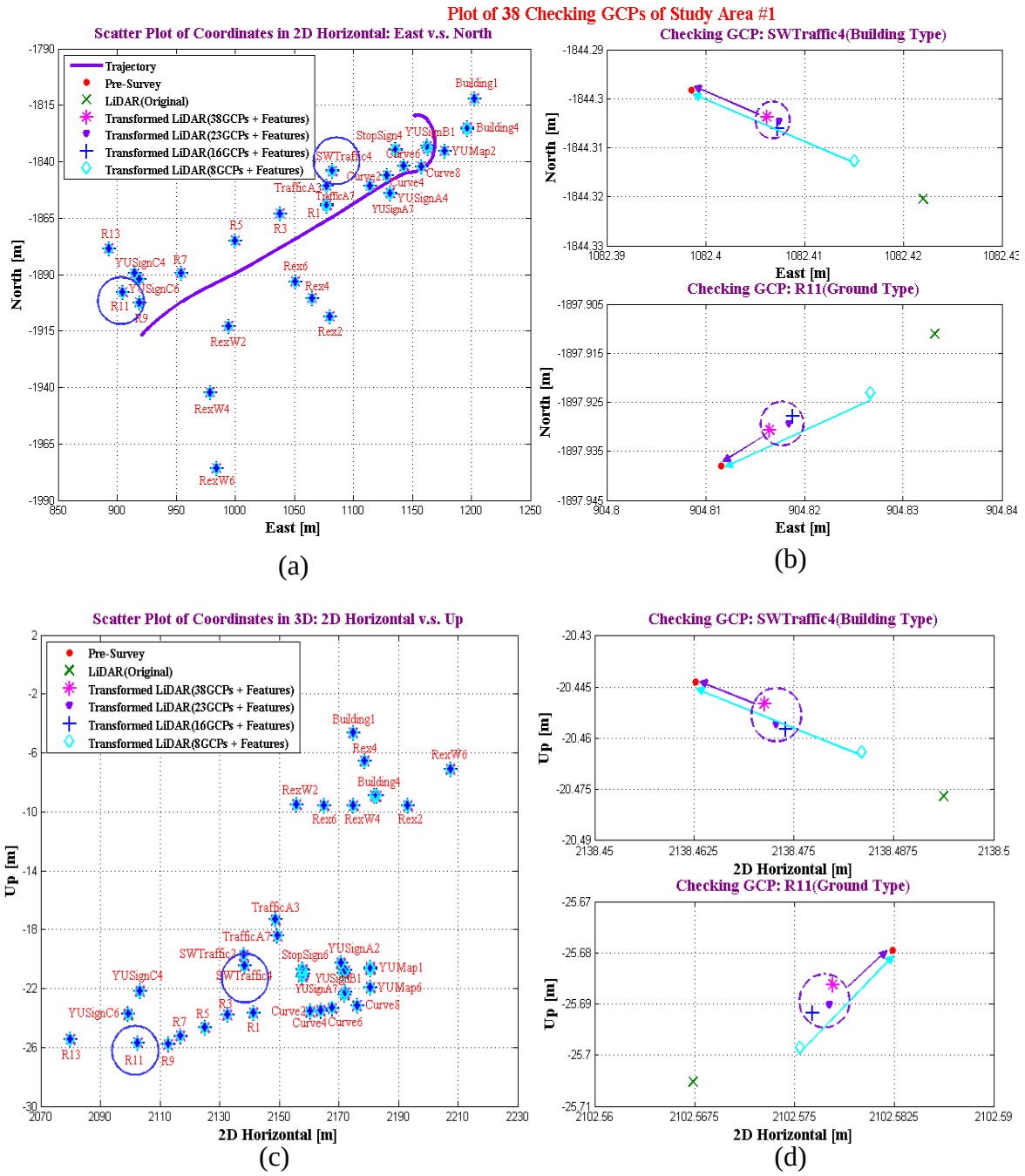

Figure D-3: Scatter plot of 38 checking GCPs in Study Area #1. The adjusted LiDAR coordinates using 38 GCPs, 23 GCPs, 16 GCPs and 8GCPs (out of 76 GCPs in total) aided by the same feature constraints were presented in pink star, purple triangle, blue cross and cyan diamond, respectively: (a) & (c) 2D horizontal and vertical; (b) Close-up details of "SWTraffic4" and "R11".